AT's 27569

NASA CR-72870
UARL L930845-81

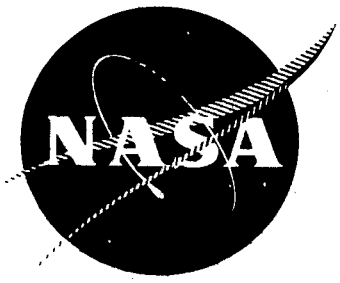

(NASA-CR-72870) SYSTEMATIC TWO-DIMENSIONAL CASCADE TESTS. VOLUME 3: SLOTTED DOUBLE CIRCULAR-ARC HYDROFOILS R.M. Columbo, et al (United Aircraft Corp.) 1 May 1972 190 p CSCL 20D G3/12

N72-24366

Unclas 28623

SYSTEMATIC TWO-DIMENSIONAL CASCADE TESTS

VOL. 3 - SLOTTED DOUBLE CIRCULAR-ARC HYDROFOILS

by

R. M. Colombo and T. A. Murrin

UNITED AIRCRAFT RESEARCH LABORATORIES

Prepared for

NATIONAL AERONAUTICS AND SPACE ADMINISTRATION

NASA Lewis Research Center
Contract NAS3-4184

Werner R. Britsch, LeRC Project Manager
Liquid Rocket Technology Branch

NOTICE

This report was prepared as an account of Government-sponsored work. Neither the United States, nor the National Aeronautics and Space Administration (NASA), nor any person acting on behalf of NASA:

A.) Makes any warranty or representation, expressed or implied, with respect to the accuracy, completeness, or usefulness of the information contained in this report, or that the use of any information, apparatus, method, or process disclosed in this report may not infringe privately-owned rights; or

B.) Assumes any liabilities with respect to the use of, or for damages resulting from the use of, any information, apparatus, method or process disclosed in this report.

As used above, "person acting on behalf of NASA" includes any employee or contractor of NASA, or employee of such contractor, to the extent that such employee or contractor of NASA or employee of such contractor prepares, disseminates, or provides access to any information pursuant to his employment or contract with NASA, or his employment with such contractor.

1. Report No.	2. Government Accession No.	3. Recipient's Catalog No.
CR-72870		

4. Title and Subtitle	5. Report Date
SYSTEMATIC TWO-DIMENSIONAL CASCADE TESTS VOL. 3 - SLOTTED DOUBLE CIRCULAR-ARC HYDROFOILS	May 1, 1972 6. Performing Organization Code

7. Author(s)	8. Performing Organization Report No.
R. M. Colombo and T. A. Murrin	UARL L930845-81 10. Work Unit No.

9. Performing Organization Name and Address	11. Contract or Grant No.
United Aircraft Research Laboratories East Hartford, Connecticut 06108	NAS3-4184 13. Type of Report and Period Covered

12. Sponsoring Agency Name and Address	13. Type of Report and Period Covered / 14. Sponsoring Agency Code
National Aeronautics and Space Administration Washington, D. C. 20546	Contractor Report

15. Supplementary Notes

Project Manager, Werner R. Britsch, Liquid Rocket Technology Branch, NASA Lewis Research Center, Cleveland, Ohio

16. Abstract

Performance parameters are presented in Vol. 3 for cascades of slotted double circular-arc hydrofoils tested over a range of systematically introduced variables in a rectilinear cascade tunnel which uses water as the test medium. Cascade configurations included various combinations of an inlet flow angle [β_1 = 50, 60 and 70 deg (0.8727, 1.0472 and 1.2217 radians)], a cascade solidity (σ = 0.75, 1.00 and 1.50), a hydrofoil camber angle [ϕ = 20, 30, 40 and 45 deg (0.3491, 0.5236, 0.6981 and 0.7854 radians)] and angles of incidence between positive and negative stall. The slot was positioned at the 45 percent chord station and the slot exit width was 0.047-in. (11.94×10^{-4} meters). Tests were also performed with the slot positioned at the 35 percent chord station and with slot widths of 0.063 and 0.094-in. (16.00×10^{-4} and 23.88×10^{-4} meters). These data were correlated to indicate the effects of slot location and slot width on minimum loss incidence and deviation angles. In addition, a comparison is presented of the performance parameters for cascades of slotted and unslotted hydrofoils. In Vols. 1 and 2 performance parameters and hydrofoil static pressure distributions are presented for double and multiple circular-arc hydrofoils, respectively, and the incidence and deviation angles corresponding to minimum total pressure loss coefficient are correlated. In addition, the turning angles are presented in a format which permits the determination of turning angles for arbitrary cascade configurations. Comparisons of the minimum loss incidence and deviation angles and the hydrofoil pressure distributions for multiple and double circular-arc hydrofoils are presented in Vol. 2

17. Key Words (Suggested by Author(s))	18. Distribution Statement
Cascades Circular-arc hydrofoils Slotted	Unclassified-unlimited

19. Security Classif. (of this report)	20. Security Classif. (of this page)	21. No. of Pages	Price*
Unclassified	Unclassified	188	$3.00 ~~$3.00~~

* For sale by the National Technical Information Service, Springfield, Virginia 22151

PRECEDING PAGE BLANK NOT FILMED

NASA CR-72870
UARL L930845-81

CONTRACTOR REPORT

SYSTEMATIC TWO-DIMENSIONAL CASCADE TESTS

VOL. 3 - SLOTTED DOUBLE CIRCULAR-ARC HYDROFOILS

by

R. M. Colombo and T. A. Murrin

UNITED AIRCRAFT RESEARCH LABORATORIES
East Hartford, Connecticut 06108

Prepared for

NATIONAL AERONAUTICS AND SPACE ADMINISTRATION

May 1, 1972

CONTRACT NAS3-4184

NASA Lewis Research Center
Cleveland, Ohio

Werner R. Britsch, Project Manager
Liquid Rocket Technology Branch

PRECEDING PAGE BLANK NOT FILMED

FOREWORD

The experimental investigation described herein was conducted by the Research Laboratories of the United Aircraft Corporation under Contract NAS3-4184 with the National Aeronautics and Space Administration. The work was performed under the management of the NASA Project Manager, Mr. Werner R. Britsch, Liquid Rocket Technology Branch, NASA Lewis Research Center. Technical direction was provided by Mr. L. J. Herrig, Special Projects Division, NASA Lewis Research Center.

PRECEDING PAGE BLANK NOT FILMED

Report CR-72870

Systematic Two-Dimensional Cascade Tests

Vol. 3 - Slotted Double Circular-Arc Hydrofoils

TABLE OF CONTENTS

TABLE OF CONTENTS
(concluded)

LIST OF ILLUSTRATIONS

LIST OF ILLUSTRATIONS
(concluded)

Figure

ABSTRACT

Performance parameters are presented in Vol. 3 for cascades of slotted double circular-arc hydrofoils tested over a range of systematically introduced variables in a rectilinear cascade tunnel which uses water as the test medium. Cascade configurations included various combinations of an inlet flow angle [β_{1N} = 50, 60 and 70 deg (0.8727, 1.0472 and 1.2217 radians)], a cascade solidity (σ = 0.75, 1.00 and 1.50), a hydrofoil camber angle [ϕ = 20, 30, 40 and 45 deg (0.3491, 0.5236, 0.6981 and 0.7854 radians)], and angles of incidence between positive and negative stall. On each hydrofoil used in the systematic tests, the slot was located at the 45 percent chord station and the slot exit width was 0.047-in. (11.94 x 10^{-4} meters). Slot evaluation tests were also performed with the slot located at the 35 percent chord station and with slot widths of 0.063 and 0.094-in. (16.00 x 10^{-4} and 23.88 x 10^{-4} meters). These data were correlated to indicate the effects of slot location and slot width on minimum loss incidence and deviation angles. In addition, a comparison is presented of the performance parameters of cascades of slotted and unslotted hydrofoils.

In Vols. 1 and 2, performance parameters and hydrofoil static pressure distributions are presented for double and multiple circular-arc hydrofoils, respectively, and the incidence and deviation angles corresponding to minimum total pressure loss coefficient are correlated. In addition, the turning angles are presented in a form which makes it possible to determine the turning angles for arbitrary cascade configurations. Comparisons of the minimum loss incidence and deviation angles and the hydrofoil pressure distributions for multiple and double circular-arc hydrofoils are presented in Vol. 2

SUMMARY

Cascade performance parameters as related to the flow turning angles, total pressure loss and static pressure rise are presented as functions of incidence angle for a particular slot configuration installed in various double circular-arc hydrofoils arranged in various cascade configurations. The 6 percent thickness ratio hydrofoils had camber angles of 20, 30 40 and 45 degrees (0.3491, 0.5236, 0.6981 and 0.7854 radians), the inlet flow angles were 50, 60 and 70 degrees (0.8727, 1.0472 and 1.2217 radians) and the cascade solidities were 0.75, 1.00 and 1.50. Comparison and summary plots are presented which illustrate the effect of slot wall convergence, slot location, slot geometry and slot width on cascade turning angles and total pressure loss coefficients. The incidence and deviation angles for the slotted hydrofoils were correlated at minimum total pressure loss coefficient.

The results presented indicate that installing a well-designed slot in a hydrofoil may improve the hydrofoil performance in cascades by increasing the range of unstalled incidence angles, providing greater flow turning angles at high incidence angles and providing turning angles which generally increase linearly with increasing incidence angle.

INTRODUCTION

In order to meet future demands for high efficiency, low weight and improved cavitation characteristics in pumping equipment, continued refinement is required in the accuracy and range of applicability of both the experimental data and the analytical procedures which form the basis for modern pump design techniques. For many applications involving high flow rates, such as in large liquid fuel rocket engines, the above performance requirements are best satisfied by multi-stage axial-flow pumps. At the present time, one of the more successful techniques for the selection of blade geometries for the various radial stations in axial-flow machinery is based upon the use of data obtained from experiments in two-dimensional, rectilinear cascades.

A substantial amount of the cascade data, compiled by a number of investigators to support axial-flow compressor development, can be applied to pump design. However, these data are deficient in two important respects: 1) the inlet flow angle range to which the data apply does not include all conditions of interest in pump design, for example, large inlet angles relative to the axial direction; and 2) information relative to cavitation performance of the blade elements is not available.

A water tunnel was designed and erected at the United Aircraft Research Laboratories (UARL) in which cascade tests may be performed under cavitating and noncavitating conditions throughout a range of cascade variables. Under Contract NAS3-4184, with the National Aeronautics and Space Administration, certain modifications were made to the facility to increase the degree of control over the test section flow, and an experimental program was initiated to determine the two-dimensional turning and loss performance of a series of slotted and unslotted circular-arc type hydrofoils when tested with various combinations of flow angles relative to the cascade inlet plane, flow angles relative to the blade mean line (incidence angle) and spacings between adjacent hydrofoils. The broad range of these test variables enabled the correlation of a design reference point and the presentation of the test data in the form of carpet plots which are useful for design evaluations. In addition, these data extend the available compilation of two-dimensional cascade data to include both other fluids and higher inlet flow angles. The data therefore provide the means for correlating liquid and air cascade data and extending the range of fundamental empirical data as required for blade element design of axial-flow turbomachinery.

Results from cascade tests with a family of double circular-arc hydrofoils are presented in Vol. 1 (NASA CR-72498) of this report series, results from cascade tests with a family of multiple circular-arc hydrofoils are presented in Vol. 2 (NASA CR-72499) and results from cascade tests with a family of slotted double circular-arc hydrofoils are reported herein, in Vol. 3. The slotted hydrofoil tests were undertaken in an effort to determine experimentally

the effects upon cascade performance of slot variations such as convergence, chordwise location, geometries and width. The goal of the test program was to establish a slot geometry which would permit an increase in the range of incidence angles for low loss and higher turning angles than those for unslotted hydrofoils.

TEST APPARATUS

UARL Cascade Water Tunnel

Basic Considerations

In a rectilinear cascade, a linear two-dimensional array of blades is used to simulate the blade geometry at a discrete radial location in a three-dimensional axial-flow machine. Measurements can then be obtained for determining the static pressure rise, total pressure loss coefficient and flow turning angle for this blade profile and blade spacing at various incidence angles. By testing cascades which simulate different radial stations, the flow characteristics through the blade rows in an axial-flow stage may be approximated by stacking the two-dimensional performance measurements of the blade elements.

A basic goal in the design of a cascade test section is to provide a flow in the cascade test apparatus which approximates the two-dimensional flow that would exist in an infinite array of blades having infinite span. This requires that means be provided in the test equipment to control wall boundary layer development and to contour the walls confining the flow so that the interference produced by the walls is minimized. Additional design specifications related to cascade performance testing are that the test apparatus have the flexibility to accommodate various cascade geometries and that the blade Reynolds number be greater than 2.5×10^5 to minimize the possibility of laminar separation from the blade surfaces.

Facility Configuration

Overall design of the water tunnel was largely dictated by the requirements for determining cascade cavitation coefficients and avoiding cavitation elsewhere in the test loop. The facility was therefore designed as a vertical, variable-pressure, closed loop arranged such that the main components of the test section are accessible from ground level. The test section is oriented such that the inlet plane of the cascade is horizontal to eliminate hydrostatic pressure gradients along the length of the cascade, which would otherwise affect the uniformity of cavitation inception on the individual blades in the cascade. In order to provide sufficient net positive suction head at the pump inlets to prevent pump cavitation, the water circulating pumps are located at the lowest point in the test loop.

A drawing of the water tunnel is shown in Figure 1. In this vertical flow circuit, the flow is discharged from the pumps, diffused and turned in a system of ducts and settled in a rectangular chamber containing both a honeycomb flow straightener and graded-porosity screens for reducing large scale turbulence.

Subsequent guide vane sections provide the required flow alignment and a means for attachment between the settling chamber and interchangeable cascade inlet nozzles. The flow is first accelerated by the inlet nozzle, then passed through the cascade test section and finally discharged into a large plenum tank from which the flow completes the circuit to the circulating pumps.

The flow is accelerated to the prescribed velocity relative to the test section by means of one of the four interchangeable nozzles which were designed for inlet flow angles of 50, 60, 70 and 75 deg (0.8727, 1.0472, 1.2217 and 1.3090 radians) as measured relative to the axial direction, which is normal to the cascade inlet plane. [The 75-deg (1.3090 radians) nozzle was not used during the program with the slotted double circular-arc hydrofoils.] The design of the nozzles was greatly influenced by factors related to cavitation testing. The horizontal orientation of the cascade inlet plane required the nozzle to accelerate the flow downward to the cascade plane from the region of low static head which is present at the top of the inlet ducting. Therefore, the maximum vertical distance between the blade leading edge plane and the top of the inlet ducting was limited to the dynamic head at the test section. This insured lower static pressure at the cascade than at the top of the ducting, thereby minimizing the possibility of cavitation in this ducting. However, this dimension placed design restrictions on not only the maximum length available for the inlet nozzle but also the maximum height of the inlet cross section. The height, and a width which was restricted by the diameter of the plenum tank, limited the area contraction ratios of the relatively short inlets to 9.08, 11.4, 11.1 and 14.2 for the 50, 60, 70 and 75-deg (0.8727, 1.0472, 1.2217 and 1.3090 radians) nozzles, respectively. The contours for the nozzle walls were selected from an analysis of minimum length, two-dimensional contractions for accelerating flow (Ref. 1). Installations of the 50 and 70-deg (0.8727 and 1.2217 radians) inlet nozzles with the test section assembly are shown in Figure 2. Each of the inlet flow nozzles was provided with a window in the upper wall, aligned with the window at the top of the plenum tank, through which the central portion of the cascade could be observed. The windows provided the capability for observing and photographing cavitation using the available high intensity, short duration strobe lighting system. However, cavitation effects were not investigated with the slotted hydrofoils.

The cascade test section assembly is supported from the fixed head of a 10-ft (3.05 meters) diameter plenum tank. The plenum tank has an operating pressure range between one and 100 psia (6894.76 and 689475.72 newtons/meter^2) as required for establishing the desired cavitating or noncavitating test conditions and contains windows at the sides and top for observation of the test equipment or degree of cavitation during the tests. Enclosing the test section assembly within a removable pressure shell (plenum tank) affords the advantages of: 1) allowing complete accessibility of the test section when the plenum is open; 2) permitting relatively light-weight construction of the test section assembly,

since immersion of the test section in the test fluid insures that the differential pressures on the test section walls are low throughout the operating pressure range of the tunnel; 3) minimizing the problem of air and water leakage in a test section which incorporates both interchangeable parts and variable geometry end walls and yet operates over a wide range of test pressures.

The three main flow pumps were fabricated from zinc-free bronzes and stainless steel. Each pump is driven by a 10 hp (7457.00 watts) motor and is capable of delivering water flows at a rate of 1700 gpm (6.44 meters^3/minute) with a head rise of 16 ft (4.88 meters).

Contamination of the water used in the facility is minimized by special water processing equipment. In addition, the facility is constructed primarily of stainless steel to avoid solid particle shedding. Solid particles contained in the test medium are removed by various filters, one of which provides continuous three-micron (3×10^{-6} meters) filtration at a flow rate of 100 gpm (0.38 meters^3/minute). Dissolved minerals are removed from the test water by a commercial ion-exchange type demineralizer which provides water comparable to distilled water in conductivity, a measure of dissolved mineral content. The conductivity of the water from this unit was approximately 1 micromho centimeter. Dissolved gases may be removed by a cold-water deaerator which can reduce the gas content to three parts per million.

Cascade Test Section

The test section (Figure 3) was designed to establish both a uniform flow along the cascade inlet plane and a periodic (blade-to-blade) flow downstream of the cascade. These are necessary conditions to insure that the flow about each blade is identical; accomplishment of these goals provides a flow which is representative of the flow through an infinite cascade. Approximations of flow uniformity and periodicity are achieved by removal of the wall boundary layers and by contouring the cascade end walls to minimize undesirable perturbation of the mainstream flow.

The boundary layer which develops along the walls of the inlet nozzle is removed upstream of the test section by means of step-type slots located on all four walls of the nozzle (Figure 3). The boundary layer flow intercepted by each of the four step slots is ducted through individual throttling valves to a common pump. Within the test section, porous side walls are used for removal of boundary layer flow in the immediate vicinity of the cascade as required for the simulation of two-dimensional flow through the cascade (Ref. 2). A porous wall assembly consists essentially of a rectangular plenum with an interchangeable porous metal wall which is fabricated from sintered woven wire mesh. A photograph of a porous side wall assembly with the blades installed is presented in Figure 4.

Perturbations of flow streamlines (to obtain uniformity) are accomplished by means of variable geometry end walls located at each end of the cascade as shown in Figure 3. These end walls are comprised of three sections, a flexible wall which connects the rigid inlet nozzle end wall to an adjustable end wall, an adjustable end wall which is analogous to one surface of a cascade blade and a tailboard which extends downstream from the adjustable end wall. Actuation of these end wall sections enables independent adjustment of: 1) the gap between the end blades of the cascade and the adjustable end wall, 2) the angle of the adjustable end wall, 3) the angle of the tailboard. The convex, flexible end wall is porous (Figure 3) to permit removal of the end wall boundary layer, thereby decreasing any tendency toward flow separation from this surface. Flow through the flexible porous wall and each porous side wall is independently controlled.

Blade aspect ratio and the number of blades to incorporate into a cascade assembly are selected somewhat arbitrarily. An aspect ratio of two was chosen as a compromise between the structural problem of blade bowing or bending that would be associated with high aspect ratio blades, and the undesirable three-dimensional flow effects that would occur with low aspect ratio blades. A compromise was also made between the large number of blades desired for simulation of the infinite cascade and the practical considerations of cost and test section size. Based upon general information obtained from previous experimental testing at UARL with a cascade tunnel which used air as the test medium and from the experimental evidence from NACA cascade tests (Ref. 3), it was decided to establish five blades as the minimum number to be included at the highest blade spacing (4 in.) (10.16×10^{-2} meters) considered in the current test program. These considerations, together with a specified minimum blade-chord Reynolds number of 5×10^5 and the selection of a 3-in. (7.62×10^{-2} meters) blade chord established a minimum test section velocity of 22 ft (6.71 meters) per second. With a 5100 gpm (19.31 meters^3/minute) facility pumping capability, the maximum cascade inlet flow area for each of the inlet flow angles was known. In order to remain within these limits, a test section of rectangular cross section having a 6-in. (15.24×10^{-2} meters) span with a 24-in. (60.96×10^{-2} meters) length was selected for the 50 and 60-deg (0.8727 and 1.0472 radians) inlet nozzles and a test section having a 6-in. (15.24×10^{-2} meters) span with a 36-in. (91.44×10^{-2} meters) length was selected for the 70 and 75-deg (1.2217 and 1.3090 radians) inlet nozzles.

The remaining considerations involved in selecting the test section configuration were primarily associated with the requirement that the facility accommodate configuration changes with relative ease. For this purpose, the design included interchangeable side wall components, to simplify changes in the blade spacing, and remote actuators to permit adjustment of blade incidence angle, flexible end wall contour and tailboard angle without the need for opening the large plenum tank.

Hydrofoil Profiles

Basic Profile

The basic test profile was a double circular-arc, for which both upper and lower surfaces are defined by circular arcs. These profiles are described by the camber angle (ϕ), which is the acute angle formed by the intersection of tangents to the profile meanline at the leading and trailing edges, and by the ratio of the maximum profile thickness to the chord length. The profiles of the hydrofoils for this slotted blade test program (Figure 5) included camber angles of 20, 30, 40 and 45 deg (0.3491, 0.5236, 0.6981 and 0.7854 radians) with a maximum thickness ratio of 6 percent. Coordinates of the profiles are presented in Table I. The 3-in. (7.62×10^{-2} meters) chord, 6-in. (15.24×10^{-2} meters) span hydrofoil blades were fabricated from stainless steel and were polished to a surface finish of 8 microinches (0.20×10^{-6} meters) (rms). The leading and trailing edge radii were 0.10 percent of the blade chord. The blades were supported in the test section by stub shafts welded to the blade ends at the leading edge (Figure 4) to simplify remote adjustment of incidence.

Static Pressure Instrumentation

Static pressure instrumentation was installed in two hydrofoils of each camber angle for obtaining surface pressure distributions for a range of cascade test variables. Twelve 0.022-in. (5.59×10^{-4} meters) diameter orifices were drilled in the suction surface of one hydrofoil and 12 also in the pressure surface of the other hydrofoil at the locations shown in Figure 6. Pressure was led out by means of stainless steel tubing laid in grooves milled into both the blade surface opposite the instrumented surface and along one of the stub shafts. The grooves were filled with an epoxy cement, and the surface was refinished to the original contour. Instrumented hydrofoils are shown in Figure 7. Static pressure instrumentation was also installed in the slotted blades; however, several of the static pressure leads were eliminated as necessitated for the installation of the slots.

Slot Configurations

Two different slot configurations were tested in one cascade configuration to provide a comparison of the cascade performance obtained with slots having parallel and converging walls. Slot A (Figure 8a) had a mean line which penetrated the blade suction surface at the 35 percent chordal station and formed an angle of 23 degrees with a tangent line at that point. The slot walls were parallel with a width of 0.063 inches (16.00×10^{-4} meters). The upstream wall of the slot was faired into the blade pressure surface with a radius of 0.20 inches (50.80×10^{-4} meters). The downstream wall of the slot was faired

into the pressure surface with a radius of 0.031 inches (7.87×10^{-4} meters) and into the suction surface with a radius of 0.20 inches (50.80×10^{-4} meters). Slot B had walls which converged toward the blade suction surface with an included angle of 8 degrees (0.1396 radians). The slot geometry was identical to that described below for Slot 1 with a slot discharge width of 0.063 inches (16.00×10^{-4} meters). The slot geometry is indicated by Figure 8b.

The three slot configurations systematically tested under this program are indicated in Figure 8b. Slot 1 had a mean line which penetrated the blade suction surface at the 35 percent chord station and was inclined at an angle of 23 deg (0.4014 radians) relative to a tangent at that point. The slot walls converged toward the suction surface, each wall making an angle of 4 deg (0.0698 radians) with the mean line. The upstream wall of the slot was faired into the blade pressure surface with a radius of 0.20 inches (50.80×10^{-4} meters). The downstream wall of the slot was faired into the pressure surface with a radius of 0.031 inches (7.87×10^{-4} meters) and faired into the suction surface with a radius of 0.20 inches (50.80×10^{-4} meters). Slot 2 was identical to Slot 1 with the exception that the slot mean line penetrated the blade suction surface at the 45 percent chord station. Slot 3 had the same mean line location as Slot 2 and was similar with the exceptions that the downstream wall was faired into the blade pressure surface with a radius of 0.050 inches (12.70×10^{-4} meters) and into the blade suction surface with a radius of 0.50 inches (127.00×10^{-4} meters).

The slot discharge width (w), measured normal to the slot mean line, was a variable in each slot configuration; each configuration was tested with discharge widths of 0.047, 0.063, and 0.094 inches (11.94×10^{-4}, 16.00×10^{-4} and 23.88×10^{-4} meters). For those hydrofoils which were not instrumented for pressure distribution measurements, the slots extended across the span of the hydrofoils to within 0.140 inches (35.56×10^{-4} meters) from each end. The slots in the instrumented hydrofoil extended to within 0.77 inches (195.58×10^{-4} meters) from the pressure leadout end of the hydrofoil. A photograph of slotted hydrofoils is presented in Figure 9.

Instrumentation

The performance of a cascade of hydrofoils was determined from static and total pressures and flow directions measured both upstream and downstream of the cascade. Static pressures were measured by means of sidewall orifices which were spaced at one inch intervals along the length of the cascade. This arrangement of orifices provided an indication of the degree of uniformity of both the inlet and exit flows and therefore was useful for adjusting test section flow conditions as well as for indicating the cascade static pressure rise. Total pressures and flow angles were measured by means of two-dimensional, directional

wedge and Kiel-wedge probes as shown in Figure 10; these probes provided a capability of measuring flow angle to an accuracy of $\pm 1/4$ deg (0.0044 radians). The designation "wedge" refers to the probe cross section at the pressure sensing location. The probes were traversed along the length of the cascade to within one gap from the end walls and could also be remotely positioned in the spanwise direction. The upstream probe and the upstream static pressure orifices were located in a plane which was 0.6 chord length (axially) upstream of the plane of leading edges. The axial position of the downstream probe traversing plane was varied so that the streamwise distance between the blade trailing edge plane and the probe was between one and two chord lengths for all cascade configurations.

An automatic data acquisition system (Figure 11) was used to record cascade performance data by storing the data on paper tape. The tape-stored data were then processed by a high-speed digital computer. The data recorded from the upstream and downstream measurement stations included total pressure and flow angles, which were continuously acquired during traverses of the probes, and local static pressure which were acquired from the pressure orifices arranged along the length of the cascade. The pressures and flow angles were also visually displayed while testing using strip chart recorders for readout of probe traverse data and both a multi-tube mercury manometer and an x-y plotter for indication of the individual wall static pressures.

PROCEDURES

Test Program

The test program was established to determine, experimentally, an optimum slot configuration for specified variations in slot location and shape and also the performance of cascades of slotted double circular-arc profiles when operated over a range of incidence angles with various inlet flow angles and cascade solidities. Incidence angle is defined as the difference between the inlet flow angle and the angle of the tangent to the profile mean line at the leading edge (Figure 12). For the double circular-arc profiles, the incidence angle (i) is related to angle-of-attack (α), which is a reference angle used by many investigators (e.g., Refs. 2 and 3) through the expression

$$i = \alpha - \phi/2 \text{ (deg)}$$

The broad range of test variables included in this investigation enables the correlation or comparison of these experimental data throughout regions of interest to both axial-flow pump and compressor designers. The test configurations, which consisted of various combinations of inlet flow angles

[β_{1N} = 50, 60 and 70 deg (0.8727, 1.0472 and 1.2217 radians)] and cascade solidities (σ = 0.75, 1.00 and 1.50) with slotted double circular-arc profiles having camber angles of 20, 30, 40 and 45 deg (0.3491, 0.5236, 0.6981 and 0.7854 radians) (Figure 5), are presented in Table II. The 50 and 60-deg (0.8727 and 1.0472 radians) inlet flow angles are within the range of cascade tests which had been conducted by other investigators for the development of axial-flow compressors and therefore provide a means for comparing and correlating these water cascade slotted hydrofoil data with cascade data for unslotted blades obtained from other test programs wherein air was used as the test medium. The data from tests with the 70 deg (1.2217 radians) inlet flow angle are in the range of interest for pump design and are also of importance for extrapolating the correlations of compressor cascade data to this higher inlet flow angle.

Each of the cascade configurations, represented by a particular profile shape, inlet flow angle and cascade solidity, was tested over an incidence angle range which included the points of positive and negative stall, where stall is defined as the point at which the total pressure loss coefficient is double the minimum value. The maximum incidence range for the tests conducted under this slotted blade program was established by the incidence angles where the total pressure loss coefficient was approximately equal to $\bar{\omega}$ min + 0.04.

Test Procedure

The test procedure for each set of cascaded hydrofoils involved extensive iterative adjustments of the various flow control devices to achieve the best approximation to the desired two-dimensional flow in the cascade. At the start of this procedure, the hydrofoils were set at an angle estimated to be close to the incidence angle corresponding to the point of blade minimum total pressure loss coefficient. The flow velocity was then adjusted to provide a Reynolds number (Re_c), based upon the chord length, of approximately 5 x 10^5. The results from various cascade tests (e.g., Refs. 2 and 3) indicated that this value of Re_c was well above the critical Reynolds number range. Therefore, extensive laminar separation from the hydrofoil surfaces was unlikely, and the effects of Reynolds number on the cascade performance parameters was expected to be minor. The endwall geometries and boundary layer control flow rates were then progressively adjusted to produce uniform distributions of inlet and exit wall static pressures and essentially constant inlet flow angles along the full length of the cascade.

After a relatively uniform inlet flow distribution was obtained (inlet flow angle constant to within $\pm$0.8 deg (0.0140 radians) of the value at the center of the cascade), the distributions of exit flow angle and total pressure were examined in the same manner; the porous endwall flow rate and tailboard

settings were adjusted accordingly to improve periodicity of the exit flow. A calculation was then made to determine if the dynamic pressure ratio across the cascade was within ± 0.05 of the value computed from an approximation of the two-dimensional continuity equation which is defined by:

$$\left(\frac{q_2}{q_1}\right)_{2D} = \left[\frac{1}{2}\left(\frac{\cos\beta_1}{\cos\beta_2} + \sqrt{\left(\frac{\cos\beta_1}{\cos\beta_2}\right)^2 + 2\bar{\omega}}\right)\right]^2 \qquad (1)$$

where:

$$\bar{\omega} = \frac{1}{s}\int_0^s \frac{\Delta P}{q_1}\, dy \qquad (2)$$

These terms are defined in Appendix I.

Equation (1) was used to estimate the adjustments required to control the sidewall boundary layer thickness, thereby eliminating spanwise divergence or convergence of the streamlines and producing effective two-dimensional flow. If required, an appropriate change in sidewall flow removal rate was made, and the inlet flow was resurveyed since changes in blade loading affect the inlet flow field. An iterative procedure for evaluating and modifying upstream and downstream flow fields was thus established. A minimum of three complete iteration cycles was required for the first test of a cascade configuration before both upstream and downstream flow fields were acceptably uniform or before it had become obvious that significant improvements in flow uniformity could not be obtained. The time required for the iteration procedure varied from a minimum of approximately three hours to a maximum of about eight hours.

After obtaining the data for an initial test point of a configuration, subsequent test points were established by changing the blade-chord angle in approximately 2-deg (0.0349 radians) increments until an incidence angle range was covered which included minimum loss incidence angle and values of incidence angle corresponding to the minimum total pressure loss coefficient plus 0.04. Each additional test point required an iterative procedure of flow adjustment identical to that described for the initial test point except that only one iteration was generally required. Approximately two hours were required to establish the flow uniformity and obtain the data for each additional test point.

In addition to the downstream surveys of exit flow angle and total pressure loss at mid-span, flow angle and loss surveys were also obtained at the 5, 10, 20 and 40 percent span stations along the slotted hydrofoils. However,

these surveys were obtained only for incidence angles near minimum and maximum loss coefficients.

The distributions of total pressure and flow angle obtained between the cascade sidewalls and midstream with the 60 deg (1.0472 radians) inlet nozzle installed are presented in Figure 13 for three camber angles and three solidities. These total pressure loss distributions show that a wall boundary layer on the order of one-inch (25.4×10^{-4} meters) thick had developed at the downstream measuring station. This boundary layer was evident for both extremes of the incidence angle range and also for an incidence angle near the point of minimum loss. However, the limited number of measurements obtained provide only a gross representation of the boundary layer profile making it difficult to establish with certainty the incidence effects upon the boundary layer thickness. A variation of turning angle across the semi-span of the hydrofoil is also indicated in Figure 13. The general trend indicated is for the turning to: 1) increase at stations near the wall for the lowest incidence angle; 2) remain fairly constant across the semi-span for the low loss incidence angles; 3) decrease near the wall for the highest incidence angle. Here again, the specific position across the span where the turning angle changes from the value at mid-span cannot be established because of the limited number of test points obtained near the wall. Although the slots did not extend to the cascade sidewalls, these distributions of total pressure loss coefficient and exit flow angle show that the spanwise flow distribution was reasonably uniform, indicating that the main stream flow was not unduly influenced by the sidewall boundary layer.

A great variation in flow removal was required for cascade boundary layer control throughout the extremes of incidence angle between positive and negative stall. During tests of highly cambered hydrofoils at incidence angles approaching positive stall, the porous wall boundary layer control system was required to remove a substantial portion of the main stream flow to achieve two-dimensional flow conditions. Under conditions of severe separation or in the range of the highest static pressure ratios, the two-dimensional condition could not always be achieved even though maximum flow was being removed by the porous wall boundary layer control system.

During tests of low-cambered hydrofoils at incidence angles approaching negative stall, the boundary layer control system was required to remove only a small portion of the main stream flow to achieve two-dimensionality. For some low static pressure ratio conditions, two-dimensionality was often achieved without the use of the porous wall boundary layer control system. Extreme low static pressure ratio conditions were encountered for which it was impossible to achieve two-dimensional flow even though this boundary layer control system was not utilized.

Although some of the test conditions near the extreme angles of incidence were not two-dimensional as defined, test points were obtained in this

region in order to provide data which may be useful for achieving a reasonably meaningful extrapolation of the two-dimensional data. Some of the data in the low loss regions are also reported as being non two-dimensional. However, these test points were determined to be two-dimensional within the required limits through a comparison of experimental and theoretical values of the q_2/q_1 ratios which were computed by hand at the time the tests were being conducted. Subsequent computer computations using the tape-stored data resulted in a difference between the experimental and theoretical values of q_2/q_1 which slightly exceeded the allowable value of ± 0.05. Nonetheless, these values are reported as non two-dimensional data. It should be noted that many of the indicated non two-dimensional data points near stall were within a few percentage points of being classified "two-dimensional" as defined in this report.

Data Reduction Procedure

The measurements of cascade static pressures, total pressures and flow angles were stored on paper tape by the data acquisition system (Figure 11) and were later converted to cascade performance parameters by a computer program. This program computed and tabulated the flow angle and wall static pressure distributions along the entire cascade and also the hydrofoil wake parameters for each wake traversed. The equations and methods used in calculating the cascade performance parameters are outlined in Appendix I; the significance of the various terms in these expressions may be determined by reference to Figure 12 which is a schematic presentation of the cascade nomenclature.

The computed distributions of pressure and flow angle were then examined to determine the uniformity and periodicity of the flow for the particular test configuration. In addition, the pressure and flow angle distributions over the two central gaps of the cascade were averaged to give representative values for inlet and exit flow angles, total pressure loss coefficient, momentum thickness ratio and inlet and exit static pressures. The diffusion factors and deviation angles for each cascade were determined from the averaged inlet and exit flow angles.

PRESENTATION OF RESULTS

The effectiveness of the various slot configurations was determined from the total pressure loss coefficient and turning angle characteristics of the cascade configurations. The effects of the slots on these characteristics are presented for the 30, 40 and 45 deg (0.5236, 0.6981, and 0.7854 radians) camber hydrofoils with solidities of 0.75, 1.00 and 1.50 and an inlet flow angle

of 60 deg (1.0472 radians). The performance comparison of parallel and convergent wall slots is shown in Figure 14; the effects of slots located at the 35 and 45 percent chord stations are shown in Figure 15; the effects of differences in the slot geometry are shown in Figure 16 and the effects of variations in slot width are shown in Figure 17.

For the test configurations with Slot 3 and a slot width of 0.047 in. (11.94×10^{-4} meters), the characteristics of the performance parameters, $\overline{\omega}$, θ, D, θ^*/s, $\Delta p/q_1$) are presented as functions of incidence angle (deg) in Figures 18 through 41; the order of presentation is shown in Table II. Since the average inlet flow angle (β_1) as determined from flow surveys at the upstream measuring station were often slightly different from the fixed inlet nozzle angles (β_{1N}), these average inlet flow angles are also presented for each test point in Figures 18 through 41. Prior to fairing curves through the parameter test points, the data were cross plotted and compared for the purpose of evaluating trends and disclosing possible experimental errors; corrections were made in accordance with the results obtained from checking the data, or when necessary, by repeating a test point. By means of these smoothing processes, curves were developed and presented which reflect greater precision in the numerical values of the performance than could be achieved by simply fairing the curves through the actual test points. However, because of this procedure, the faired curves do not necessarily pass through the plotted data points.

Static pressure distributions along the surfaces of the hydrofoils were obtained for various cascades of slotted and unslotted 20, 30, 40 and 45 deg (0.3491, 0.5236, 0.6981 and 0.7854 radians) camber hydrofoils. Representative results from these tests are presented in Figures 42 through 46. The 30, 40 and 45 deg (0.5236, 0.6981 and 0.7854 radians) camber hydrofoils were tested in solidities of 0.75, 1.00 and 1.50 with an inlet flow angle of 60 deg (1.0472 radians); the 20 and 30 deg (0.3491 and 0.5236 radians) camber hydrofoils were also tested in solidities of 0.75, 1.00 and 1.50 but with an inlet flow angle of 70 deg (1.2217 radians). The five static pressure distribution tests presented on each of these figures represent test points near minimum loss incidence, near minimum loss incidence ± 4 deg and near the maximum and minimum incidence points. Several of the pressure distributions for unslotted hydrofoils are presented in Figure 47 for comparison with slotted hydrofoil pressure distributions at a solidity of 1.00.

DISCUSSION

Slot Configuration Evaluation

In the slot configuration evaluation, the slot variables - slot wall convergence, slot location, slot geometry, slot width - were experimentally

investigated to determine their individual effects upon cascade loss and turning angle performance.

Slot Wall Convergence

The slot wall convergence effect was determined from tests of a zero degree convergence or parallel wall slot (Slot A, Figure 8a) and an eight degree (0.1396 radians) convergent wall slot (Slot B, Figure 8b) both having the same mean line angle, slot exit width, slot location and slot-wall to blade-surface blending radii. The single cascade configuration tested with these slots consisted of 40 deg (0.6981 radians) camber double circular-arc hydrofoils arranged in a cascade with a solidity of 1.00 and an inlet flow angle of 60 deg (1.0472 radians).

The total pressure loss coefficients and turning angles obtained with the parallel and convergent slot walls are shown in Figure 14. These results show that the turning angles were nearly the same for the two different slots. However, the total pressure losses for the convergent slot were substantially lower throughout the range of incidence tested. On the basis of these results, all subsequent slots evaluated in the test program had an eight degree (0.1396 radians) wall convergence angle.

Slot Location

The slot location effect refers to the chordwise position of the slot opening along the suction surface of the hydrofoil. The comparison in Figure 15 is made between slots located at the 35 percent chord station (Slot 1) and 45 percent chord station (Slot 2) for the same cascade configuration. The curves presented in Figure 15 show the total pressure loss coefficient and turning angle characteristics for cascades of slotted 30, 40 and 45 deg (0.5236, 0.6981 and 0.7854 radians) camber hydrofoils with solidities of 0.75, 1.00 and 1.50.

Solidity Equals 0.75

For cascades of 30 deg (0.5236 radians) camber hydrofoils, Figure 15a shows that the lowest value of total pressure loss coefficient and the lowest minimum loss incidence angles were obtained with Slot 1; it also shows that the turning angle characteristics were very similar for the two slot locations. Because of the loss characteristics indicated in Figure 15a, Slot 1 would be more effective for the incidence angle range below 6 deg (0.1047 radians) and Slot 2 would be more effective for the incidence angle range above 6 deg (0.1047 radians).

For cascades of 40 deg (0.6981 radians) camber hydrofoils, Figure 15d shows that Slot 2 resulted in a lower minimum total pressure loss coefficient, lower losses at incidence angles less than -5 deg (=0.0873 radians) and slightly higher losses at incidence angles greater than -5 deg (-0.0873 radians). The

turning angles for the two slots were nearly the same at incidence angles less than minimum loss incidence; at higher incidence angles, the turning was higher for Slot 2.

For cascades of 45 deg (0.7854 radians) camber hydrofoils, Figure 15g shows that Slot 2 provided lower minimum total pressure loss coefficients and higher turning angles throughout the range of operation. The performance of Slot 2 was clearly an improvement over that obtained for Slot 1.

In summary, the loss coefficient curves presented in Figure 15 (a, d, g) show that the minimum total pressure loss coefficients increased with increasing camber angle but the rate of increase in loss coefficient was lower for the Slot 2 configuration.

Solidity Equals 1.00

For cascades of 30 deg (0.5236 radians) camber hydrofoils, Figure 15b shows that a slightly lower value of minimum total pressure loss coefficient was obtained with Slot 1; however, higher turning was obtained with Slot 2 throughout the test range of incidence. The loss characteristic shows that Slot 1 operated with lower losses than Slot 2 at incidence angles less than -3 1/2 deg (-0.0611 radians) and with higher losses than Slot 2 at higher incidence angles.

For cascades of 40 deg (0.6981 radians) camber hydrofoils, Figure 15e shows that Slot 2 had lower total pressure loss coefficients below i = 5 deg (0.0873 radians) and higher turning angles below i = -2 deg (-0.0349 radians).

For cascades of 45 deg (0.7854 radians) camber hydrofoils, Figure 15h shows that lower losses and higher turning angles were obtained with Slot 2 for incidence angles less than -3 deg (-0.0524 radians).

As indicated by the loss coefficient curves in Figure 15 (b, e, h), the minimum total pressure loss coefficients increased with increasing camber for Slot 1 and decreased slightly with increasing camber for Slot 2.

Solidity Equals 1.50

For cascades of 30 deg (0.5236 radians) camber hydrofoils, Figure 15c shows that the lowest values of total pressure loss coefficient and lowest minimum loss incidence angles were obtained with Slot 1. However, the turning angle characteristic for Slot 2 indicates appreciably higher turning angles throughout the test range of operation. The total pressure loss coefficient and turning angle characteristics shown in Figure 15c indicated that Slot 2 is more effective than Slot 1 especially in the range of incidence angles greater than minimum loss incidence.

For cascades of 40 deg (0.6981 radians) hydrofoils, Figure 15f shows that the lowest value of minimum total pressure loss coefficient was obtained with Slot 1 and that the losses were lower in the incidence range between -6 and +1 deg (-0.1047 and +0.0175 radians). Slot 2 provided lower losses in the incidence ranges -10 to -6 deg (-0.1745 to -0.1047 radians) and +1 to +6 deg (+0.0175 to +0.1047 radians). The turning angle characteristics were very similar for the two slot locations.

For cascades of 45 deg (0.7854 radians) camber hydrofoils, Figure 15i shows that Slot 2 provided the lowest minimum total pressure loss coefficient and also provided higher turning angles throughout the test range of operation. The performance of Slot 2 was clearly an improvement over that obtained for Slot 1.

As functions of camber angle, the minimum total pressure loss coefficients for Slot 1 first decreased then increased sharply as camber was increased; for Slot 2, the minimum loss coefficients showed little change as camber was increased from 30 to 40 deg (0.5236 to 0.6981 radians) but then decreased slightly as camber was increased to 45 deg (0.7854 radians).

Slot Geometry

Slot geometry refers to the radii used for the various corners (Figure 8b). It was presumed in the design of the slots that corner radii, especially the slot lip radius and the radius which blends the downstream wall of the slot into the hydrofoil suction surface, could have a significant effect upon the cascade turning angle and total pressure loss performance of a slot. In order to investigate the effects of these radii, changes in the slot shape were introduced by combining a slot lip radius of 0.031-in. (7.87×10^{-4} meters) with a Coanda radius of 0.20-in. (50.8×10^{-4} meters) (Slot 2) and a slot lip radius of 0.05-in. (12.70×10^{-4} meters) with a Coanda radius of 0.50-in. (127.0×10^{-4} meters) (Slot 3). The effects on cascade loss and turning angle performance of these slot geometries with 30 and 45 deg (0.5236 and 0.7854 radians) camber hydrofoils at solidities of 0.75, 1.00 and 1.50 are presented in Figure 16.

Solidity Equals 0.75

For cascades of 30 deg (0.5236 radians) camber hydrofoils, Figure 16a shows that Slot 3 provided the lower minimum total pressure loss coefficient and also lower losses throughout most of the operating range of incidence; the turning angles for Slot 3 were higher throughout this range of tests. For cascades of 40 deg (0.6981 radians) camber hydrofoils, Figure 16d shows that Slot 3 provided a lower value of minimum total pressure loss coefficient, lower losses over most of the test range of incidence and higher turning angles throughout

the entire test range of incidence. For cascades of 45 deg (0.7854 radians) camber hydrofoils, Figure 16g shows that the values for minimum total pressure loss coefficient for Slots 2 and 3 were nearly equal; however, outside of a narrow range of incidence near that for minimum loss coefficient, the loss coefficients for Slot 3 were lower than those for Slot 2. Slot 3 provided greater turning angles throughout the test range of incidence.

Solidity Equals 1.00

For cascades of 30 deg (0.5236 radians) camber hydrofoils, Figure 16b shows that Slot 3 provided the lower minimum total pressure loss coefficient and also lower loss coefficients within the incidence range above approximately -3 deg (-0.05236 radians). The turning angles for Slot 3 were higher than those for Slot 2 throughout the test range of incidence. For cascades of 40 deg (0.6981 radians) camber hydrofoils, Figure 16e shows that Slot 2 provided the lower minimum total pressure loss coefficient and also lower loss coefficients for the incidence ranges below -4 1/2 deg (-0.0785 radians) and above 1 deg (0.0175 radians). Slot 3 provided higher turning angles throughout the test range of incidence. For cascades of 45 deg (0.7854 radians) camber hydrofoils, Figure 16h shows that Slot 2 provided lower total pressure loss coefficients and Slot 3 provided higher turning angles throughout the test range of incidence.

Solidity Equals 1.50

For cascades of 30 deg (0.5236 radians) camber hydrofoils, Figure 16c shows that Slot 2 provided lower total pressure loss coefficients throughout the test range of incidence; however, Slot 3 provided higher turning angles throughout. For cascades of 40 deg (0.6981 radians) camber hydrofoils, Figure 16f shows that Slot 2 provided lower losses except within the range of highest incidence and Slot 3 provided generally higher turning angles. For cascades of 45 deg (0.7854 radians) camber hydrofoils, Figure 16i shows that Slot 2 provided the lower minimum total pressure loss coefficient and lower losses in the incidence range between approximately -6 and +2 deg (-0.1047 and +0.0349 radians); Slot 3 provided higher turning angles over the test range of incidence above -9 deg (-0.1571 radians).

Slot Width

The slot width effect was investigated by testing slots which differed only in the width of the slot opening in the suction surface of the hydrofoil. Three slot widths [0.047, 0.063 and 0.094-in. (11.94×10^{-4}, 16.00×10^{-4} and 23.88×10^{-4} meters)] were tested with Slots 1, 2 and 3. The effects of Slot 3 with 0.047 and 0.094-in. (11.94×10^{-4} and 23.88×10^{-4} meters) slot widths on the profile loss coefficients and turning angles of 30, 40 and 45 deg (0.5236, 0.6981 and 0.7854 radians) camber hydrofoils in cascades with solidities of 0.75, 1.00 and 1.50 are compared in Figure 17.

Solidity Equals 0.75

For cascades of 30 deg (0.5236 radians) camber hydrofoils, Figure 17a shows that the 0.047 in. (11.94×10^{-4} meters) wide slot provided the lower total pressure loss coefficient throughout the test range of incidence; however, the slope of the turning angle characteristic was slightly lower than that for the 0.094 in. (23.88×10^{-4} meters) wide slot. For cascades of 40 deg (0.6981 radians) camber hydrofoils, Figure 17d shows that the 0.047 in. (11.94×10^{-4} meters) wide slot provided the lower minimum total pressure loss coefficient, lower loss coefficients over almost the entire test range of incidence and higher turning angles through the test range. For cascades of 45 deg (0.7854 radians) camber hydrofoils, Figure 17g shows that the 0.047 in. (11.94×10^{-4} meters) wide slot provided the lower minimum total pressure loss coefficient, lower total pressure loss coefficients over the test range up to an incidence angle of 5-1/2 deg (0.0960 radians) and higher turning angles throughout the test range of incidence. In general, the loss characteristic with incidence for the 0.047-in. (11.94×10^{-4} meters) wide slot was somewhat broader than that for the 0.094-in. (23.88×10^{-4} meters) wide slot.

Solidity Equals 1.00

For cascades of 30 deg (0.5236 radians) camber hydrofoils, Figure 17b shows that the 0.093 in. (23.87×10^{-4} meters) wide slot provided lower total pressure loss coefficients for the range of incidence between i = -10 and -2 deg (-0.1745 and -0.0349 radians) and also provided higher turning angles throughout the test range of incidence. For cascades of 40 deg (0.6981 radians) camber hydrofoils, Figure 17e shows that the 0.093 in. (23.88×10^{-4} meters) wide slot provided lower total pressure loss coefficients at incidence angles greater than -6 deg (-0.1047 radians); the 0.047 in. (11.94×10^{-4} meters) wide slot provided lower total pressure loss coefficients at incidence angles less than -6 deg (-0.1047 radians) and also provided higher turning angles throughout the test range of operation. For cascades of 45 deg (0.7854 radians) camber hydrofoils, Figure 17h shows that the 0.047 (11.94×10^{-4} meters) wide slot provided lower total pressure loss coefficients only for incidence angles less than -7 deg (-0.1222 radians) and provided higher turning angles for the range of operation below i = -4 deg (-0.0698 radians).

Solidity Equals 1.50

For cascades of 30 deg (0.5236 radians) camber hydrofoils, Figure 17c shows that the 0.094 in. (23.88×10^{-4} meters) wide slot provided the lower total pressure loss coefficients at incidence angles above -2 deg (-0.0349 radians) but the 0.047 in. (11.94×10^{-4} meters) wide slot provided higher turning angles throughout the test range of incidence. For cascades of 40 deg (0.6981 radians) camber hydrofoils, Figure 17f shows that the 0.047 in. (11.94×10^{-4} meters)

wide slot provided lower total pressure loss coefficients at incidence angles less than that for minimum loss; as incidence was increased beyond the point of minimum loss, loss coefficients for the 0.047 in. (11.94×10^{-4} meters) wide slot were greater than those for the 0.094 in. (23.88×10^{-4} meters) wide slot. Turning angles for the 0.047 in. (11.94×10^{-4} meters) wide slot were higher throughout the test range of incidence. For cascades of 45 deg (0.7854 radians) camber hydrofoils, Figure 17i shows that the 0.047 in. (11.94×10^{-4} meters) wide slot provided lower total pressure loss coefficients only at incidence angles below -4 1/2 deg (-0.0785 radians); the 0.094 in. (23.88×10^{-4} meters) wide slot provided lower total pressure loss coefficients at incidence angles above -4 1/2 deg (-0.0785 radians) and provided higher turning angles throughout the test range of incidence.

Cascade Performance

The cascade performance parameters (total pressure loss coefficient, turning angle, static pressure rise coefficient, diffusion factor, deviation angle and wake momentum thickness ratio) vary in a systematic manner with changes in cascade geometry (incidence angle and solidity) and hydrofoil profile shape (camber angle). Some of the characteristics which may be observed for these parameters are discussed briefly in the following sections. The slot configuration evaluation indicated that Slot 3 generally resulted in better turning and loss characteristics. Therefore, the performance characteristics which are presented in Figures 18 through 41 were obtained using cascades of hydrofoils with Slot 3. The basis for evaluating the slotted blade performance characteristics is the performance of cascades of unslotted hydrofoils presented in Ref. 4. Typical examples of the comparison of cascade total pressure loss coefficient and turning angle for slotted and unslotted hydrofoils are presented in Figure 48. The comparisons are for the 30, 40 and 45 deg (0.5236, 0.6981 and 0.7854 radians) camber hydrofoils with solidities of 0.75, 1.00 and 1.50 and an inlet flow angle of 60 deg (1.0472 radians) and for the 20 and 30 deg (0.3491 and 0.5236 radians) camber hydrofoils with a solidity of 1.00 and an inlet flow angle of 70 deg (1.2217 radians).

Total Pressure Loss Coefficient

The total pressure loss coefficients varied with incidence in a manner similar to that of the unslotted hydrofoils. That is, each curve indicated higher losses as the incidence is varied in either direction from a minimum loss incidence angle. The values of minimum total pressure loss coefficient tended to increase with increasing camber, solidity and inlet flow angle.

As indicated by Figure 48, the minimum loss incidence angles for the slotted hydrofoils were higher than those for the unslotted hydrofoils [except

for $\emptyset$ = 45 deg (0.7854 radians), σ = 1.50, β_1 = 60 deg (1.0472 radians)]. Because of this shift in the operating characteristic, the slotted hydrofoils performed with lower losses than unslotted hydrofoils at the same incidence angle within the incidence range toward positive stall. Very high losses are exhibited by these slotted hydrofoils at σ = 1.50 indicating that slots may provide more performance potential when used at solities less than 1.50. Although the minimum total pressure loss coefficients for these slotted hydrofoils were greater than those for unslotted hydrofoils, it may be presumed that some reduction in the minimum total pressure loss coefficient may be achieved through further optimization of the slots.

Turning Angle

Turning angles obtained with slotted hydrofoils varied almost linearly with increasing incidence for all test configurations; none of the test configurations exhibited the reduction in the rate-of-increase of turning with increasing incidence which characterizes the stall region for cascades of unslotted hydrofoils having camber angles greater than 20 deg (0.3491 radians) (Ref. 4).

Static Pressure Rise Coefficient

For two-dimensional cascade flow in the absence of separation, the static pressure rise across the cascade is largely a function of the flow turning angle. Therefore, as a result of the high turning produced by the slotted hydrofoils in the high incidence region, the slotted hydrofoil cascades developed static pressure rise coefficients as high as 0.5 and 0.6.

Diffusion Factor

Diffusion (D) factors, (Ref. 5), also a function of turning angle, increased with increasing incidence angles for all slotted hydrofoil cascades and gave no indication of stall even at high positive incidence. For inlet flow angles of 60 and 70 deg (1.0472 and 1.2217 radians), diffusion factors at the incidence angle for minimum total pressure loss coefficient were often much greater than 0.50, the design value. This was especially true for high solidity cascades with highly cambered hydrofoils. For example, as shown in Figure 39, a diffusion factor of 0.68 was obtained at minimum loss incidence for a cascade of 30 deg (0.5236 radians) camber hydrofoils with a solidity of 1.00 and an inlet flow angle of 70 deg (1.2217 radians). The maximum diffusion factor for this cascade was 0.75.

Hydrofoil Pressure Distributions

Pressure distributions for the slotted blades (Figures 42 through 47) are discontinuous in the region of the slot because the pressure leads had to be eliminated for slot installation. In addition, efforts to install pressure leads to measure pressures within the slots were not always successful. Therefore, the most significant information that can be derived from these pressure distributions is relative to the pressure distribution over the suction surface downstream of the 50 percent chord station. Within this region, the most distinctive characteristic of these slotted hydrofoil pressure distributions is that there is no indication of flow separation for positive stall incidence. This evidence that flow has not separated from the slotted hydrofoils within the test range of incidence accounts for the continually increasing turning angles with increasing incidence.

The pressure distributions for the unslotted hydrofoils, which are presented in Figure 47, show a much different characteristic near the trailing edge at the highest incidence angle; the pressure coefficient on the suction surface is relatively constant indicating that separation has occurred. With separation, it would be anticipated that the slope of the turning angle characteristic would decrease with increasing incidence.

CORRELATION OF TEST RESULTS

A reference point which may be used as the basis for evaluating cascade configuration performance or for developing empirical cascade performance prediction systems is the incidence angle at which minimum loss occurs. Using minimum loss as the reference point, it is possible to develop correlations for both incidence and deviation angles.

A correlation of incidence and deviation angles presented in Ref. 4 expressed the incidence and deviation angles, expressed in degrees, as

$$i = i_{\bullet} + n\phi$$

and

$$\delta^{\circ} = \delta_{\bullet}^{\circ} + m\phi$$

where $i_{\bullet}$ and $\delta_{\bullet}^{\circ}$ are the values of incidence and deviation at minimum loss for the zero degree camber hydrofoil and n and m are the respective rates of change of incidence and deviation with camber angle.

For the correlation of the slotted double circular-arc hydrofoils, it was assumed that the minimum loss incidence and deviation angles were linear functions of the minimum loss incidence and deviation angles of unslotted double circular-arc hydrofoils. Therefore, in equation form, the minimum loss incidence and deviation angles for slotted (subscript s) double circular-arc hydrofoils are presented in terms of minimum loss incidence and deviation for unslotted (subscript $\bullet$) double circular-arc hydrofoils by the expression

$$i_s = i_\bullet + k\phi^2$$

where

$$k = \frac{i_\bullet - i_s}{\phi^2}$$

and

$$\delta_s^\circ = \delta_\bullet^\circ + (\ell + 0.35\phi)$$

where

$$\ell = \delta_s^\circ - \delta_\bullet^\circ \text{ at } \phi = 0$$

For these definitions, the angles are expressed in degrees.

The minimum loss incidence angles for zero degree unslotted hydrofoils ($i_\bullet$), the slope factor (n) and the slope factor (k) are presented in Figures 49, 50 and 51; the minimum loss deviation angles for zero degree unslotted hydrofoils ($\delta_\bullet^\circ$), the slope factor (m) and the slope intercept factor (ℓ) are presented in Figures 52, 53 and 54. Figures 49, 50, 52 and 53 were obtained from Ref. 4

CONCLUDING REMARKS

An experimental test program was completed for the purpose of optimizing a slot configuration within the limits of the selected slot variables and determining the performance characteristics of cascades of hydrofoils modified by the inclusion of this optimum slot. The most beneficial slot location was selected as the 45 percent chord station because lower losses and higher turning were generally realized with the slot at this station. However, the question still remains of whether further reduction in loss and higher turning may be gained by placing the slot downstream of the 45 percent chord station.

The slot geometry incorporating a 0.5-in. (127×10^{-4} meters) Coanda radius on the suction surface and a 0.05-in. (12.70×10^{-4} meters) slot lip radius on the pressure surface was selected as being the better slot geometry

because it also provided generally higher turning angles and also lower losses for the lower solidity cascades. However, additional information is required on the effects on cascade performance of various convergence angles within the slot and the effects of a small lip radius with a large Coanda radius. A slot width of 0.047-in. (11.94×10^{-4} meters) provided somewhat lower losses and higher turning angles than were obtained with the 0.094-in. (23.88×10^{-4} meters) slot width; this was more evident at low solidity. Some further reduction in loss may be possible with a smaller slot width which would result in a smaller boundary layer displacement thickness downstream of the slot.

As a result of installing slots in hydrofoils, the loss and turning performance characteristics appear to shift to a range of incidence other than that predicted for unslotted hydrofoils. Therefore, to obtain a desired turning angle with low loss for a prescribed inlet flow angle, the design blade chord angle of a slotted hydrofoil may differ from that of the unslotted hydrofoil. In order to determine the blade chord angle settings for prescribed turning and inlet flow angles, some data are required from testing cascades of slotted hydrofoils through an incidence variation for which blade chord angles are fixed and inlet flow angles are varied in small increments.

Another effect of slots on the cascade performance of these hydrofoils was that of preventing flow separation and the consequent fall-off in turning angle even when the hydrofoils were operating at the highest incidence angle in the test range. The slot flow evidently had sufficient momentum to energize the boundary layer downstream of the slot and therefore to prevent separation. The high losses evident at the high incidence angle range are apparently due to the boundary layer which had been thickened by the flow from the slot; there is no evidence from the surface pressure distribution data that separation caused the high losses. The permissible high turning angles available with slotted hydrofoils introduces the possibility of reducing the number of blades per stage by using low solidity slotted blades in place of higher solidity unslotted blades. However, some trade-off in loss may be anticipated from such a substitution of blading. This high turning capability also introduces the possibility of reducing the number of axial flow stages by allowing higher stage turning angles.

A characteristic of the slotted hydrofoils used in this test program was that of causing greater losses at the minimum loss incidence than those for unslotted hydrofoils, especially as solidity was increased. As shown in Figure 48, the minimum losses for the slotted hydrofoils at a solidity of 1.50 were on the order of twice the minimum losses for the unslotted hydrofoils. Figure 48 also indicates that, from the standpoint of loss only, these slot configurations are more beneficial when used in low solidity cascades. This also suggests the possibility that slots may permit efficient turning at solidities less than 0.75.

Although significant improvements in both cascade turning angle characteristics and low-loss range of incidence have been achieved through

the application of slots to this family of double circular-arc hydrofoils, further improvements in their cascade performance appear feasible through refinements in the slot design and chordal location. Obviously, the superposition of both slot geometry and location variables upon a reasonable set of cascade variables represents an extensive and therefore costly experimental test program. A practical approach to effecting a cost reduction without compromising such a comprehensive program is to first analytically assess the effects of the slot geometry variables upon various cascade flow fields and then follow this with an experimental test program to evaluate the cascade turning and loss characteristics of so-determined optimum slot configurations, especially at off-design conditions where mathematical analysis may be invalid. However, in this endeavor it must be recognized that the analytical procedure used for slot evaluations in cascades must include a realistic description of the boundary layer flows, particularly in the vicinity of the slot. The suggested effort to continue the development of slots will provide results having application to axial flow turbomachinery development for pumps, fans and compressors.

APPENDIX I

Equations for Data Reduction

For the acquisition of data, the test procedures were established to: 1) exclude turning angle measurements within the wake regions, 2) measure flow angles and total pressures only at the mid-span position and 3) adjust the flow conditions to provide effective two-dimensional flow through the cascade. An expression based upon the continuity equation was derived for determining the two-dimensional dynamic pressure ratio to provide a reference for estimating the two-dimensionality of the test data. This expression,

$$\left(\frac{q_2}{q_1}\right)_{2D} = \left[\frac{1}{2}\left(\frac{\cos\beta_1}{\cos\beta_2} + \sqrt{\left(\frac{\cos\beta_1}{\cos\beta_2}\right)^2 + 2\bar{\omega}}\right)\right]^2 \qquad (1)$$

is an approximation to the two-dimensional continuity equation in which the integrations are performed for a sine-squared variation of total pressure and a sine variation of angle across a blade wake. This approximation, which includes wake blockage effects on the exit flow area, is valid within experimental error if 1) the total pressure loss coefficient, $\bar{\omega}$, is less than 0.10, 2) the flow angle variations from the mean exit flow angle are less than 15 deg (0.2618 radians), and 3) the width of the wakes at the measuring station are less than the blade spacing. This expression was derived using the methods prescribed in Ref. 2. Effective two-dimensional flow was assumed when the average experimental dynamic pressure ratio was within ± 0.05 of the value computed by the above expression using the average measured exit flow angle.

The total pressure loss coefficient, $\bar{\omega}$, is the nondimensionalized total pressure loss across a blade wake averaged across the blade spacing and is expressed by the formula

$$\bar{\omega} = \frac{1}{s}\int_0^s \frac{P_1 - P_2}{q_1}\, dy \qquad (2)$$

The experimental dynamic pressure ratio is expressed as

$$\left(\frac{q_2}{q_1}\right)_E = \frac{P_1 - p_2}{P_1 - p_1} \qquad (3)$$

APPENDIX I
(continued)

An expression developed in Ref. 6 to relate the total pressure loss coefficient to the wake momentum thickness (θ^*) and wake shape factor (H) at the downstream measuring station is given by

$$\bar{\omega} = 2\left(\frac{\theta^*}{c}\right)_2 \frac{\sigma}{\cos\beta_2}\left(\frac{\cos\beta_1}{\cos\beta_2}\right)^2 \left\{ \frac{\frac{2H_2}{3H_2-1}}{\left[1-\left(\frac{\theta^*}{c}\right)_2 \frac{\sigma H_2}{\cos\beta_2}\right]^3} \right\} \qquad (4)$$

which indicates the contributions by the cascade geometry terms, σ, β_1, β_2, and the aerodynamic terms: θ^*, H (the contribution of the expression within the braces was stated in Ref. 6 to be very small). For the presentation of cascade characteristics, the momentum thickness is ratioed to the blade spacing, and the total pressure loss coefficient expression is given by

$$\bar{\omega} = \frac{2}{\cos\beta_2}\left(\frac{\theta^*}{s}\right)_2\left(\frac{\cos\beta_1}{\cos\beta_2}\right)^2 \left\{ \frac{\frac{2H_2}{3H_2-1}}{\left[1-\left(\frac{\theta^*}{s}\right)_2 \frac{H_2}{\cos\beta_2}\right]^3} \right\} \qquad (5)$$

The momentum thickness ratio was calculated from the expression

$$\frac{\theta^*}{s} = \frac{1}{s}\int_{\delta\ell y}^{\delta uy}\left(1-\frac{V}{V_0}\right)\frac{V}{V_0}\,dy \qquad (6)$$

where the limits of integration are the wake boundaries. This expression, by inclusion of the Bernoulli equation, becomes

$$\frac{\theta^*}{s} = \frac{1}{s}\int_{\delta\ell y}^{\delta uy}\left[\sqrt{1-\frac{\Delta P}{q_2}} - \left(1-\frac{\Delta P}{q_2}\right)\right] dy \qquad (7)$$

In Ref. 7, it was stated that a factor to be used for wake thickness correlations is the diffusion of blade surface velocities because of the contribution of this diffusion to the wake shape. A diffusion factor (D) developed in Ref. 5 is expressed for incompressible flow as

$$D = \left(1 - \frac{\cos\beta_1}{\cos\beta_2}\right) + \frac{\cos\beta_1}{2\sigma}\left(\tan\beta_1 - \tan\beta_2\right) \qquad (8)$$

The significance of this diffusion factor is restricted to the region of minimum loss.

APPENDIX II

List of Symbols

A	Flow area, sq. in.
c	Hydrofoil chord length, in.
Cp	Pressure coefficient, $Cp = \frac{p_{local} - p_1}{P_1 - p_1}$
D	Diffusion factor, $D = \left(1 - \frac{\cos\beta_1}{\cos\beta_2}\right) + \frac{\cos\beta_1}{2\sigma}(\tan\beta_1 - \tan\beta_2)$
H	Boundary layer form factor, $H = \delta^*/\theta^*$
i	Incidence angle, angle between inlet-flow direction and tangent to meanline at leading edge, deg, $i = \beta_1 - \left(\gamma^\circ + \frac{\phi}{2}\right)$, $\therefore i = \alpha - \frac{\phi}{2}$
k	Slope factor in slotted blade incidence angle relation, $k = (i_{unslotted} - i_{slotted})/\phi^2$
ℓ	Slope factor in slotted blade deviation angle relation, $\ell = (\delta^\circ_{\ slotted} - \delta^\circ_{\ unslotted})$ at $\phi = 0$
m	Slope factor in unslotted blade deviation angle relation, $m = (\delta^\circ - \delta_\bullet{}^\circ)/\phi$
n	Slope factor in unslotted blade incidence angle relation, $n = (i - i_\bullet)/\phi$
P	Total pressure, lb/sq. in.
p	Static pressure, lb/sq. in.
Δp	Static pressure difference, $p_2 - p_1$, lb sq. in.
q	Dynamic pressure, lb/sq. in.

Re_c Reynolds number based on chord length, $Re_c = \frac{Vc}{\nu}$

r Radius, in.

s Blade spacing, in.

t Maximum profile thickness, in.

V Velocity, ft/sec

w Slot opening width on suction surface, in.

X Chordal station, % chord

y Coordinate normal to axis, in.

α Angle-of-attack, angle between inlet-flow direction and blade-chord angle, $\alpha = \beta_1 - \gamma^\circ$ deg

β Flow angle, angle between flow direction and axial direction, deg

γ° Blade chord angle, angle between blade chord and axial direction, deg

δ Wake full thickness

δ° Deviation angle, angle between exit-flow direction and tangent to blade mean camber line at trailing edge, $\delta^\circ = i + \phi - \theta$, deg

δ^* Boundary layer displacement thickness, $\delta^* = \int_{\delta_{\ell y}}^{\delta_{uy}} \left(1 - \frac{V}{V_o}\right) dy$

θ Turning angle, $\theta = \beta_1 - \beta_2$, deg

θ^* Wake momentum-defect thickness, $\theta^* = \int_{\delta_{\ell y}}^{\delta_{uy}} \left(1 - \frac{V}{V_o}\right) \frac{V}{V_o} dy$

ν Kinematic viscosity, sq. ft/sec

ρ Density, slugs/cu. ft.

σ Solidity, ratio of chord to spacing

ϕ Camber angle, difference between tangent angles at leading and trailing edges, deg

$\overline{\omega}$ Total pressure loss coefficient

Subscripts

E Experimental

ly Wake boundary from lower surface

N Nominal

∞ Free stream

uy Wake boundary from upper surface

1 Station at cascade inlet

2 Station at cascade exit

2D Two-dimensional

$\bullet$ Value for zero degree camber hydrofoil

REFERENCES

1. Lin, T. C.: Ducts for Accelerated Flow. ASME Proceedings of the Second U. S. National Congress on Mechanics, June 1954.

2. Emery, J. C., L. J. Herrig, J. R. Erwin and A. R. Felix: Systematic Two-Dimensional Cascade Tests of NACA 65-Series Compressor Blades at Low Speeds. NACA Report 1368, 1958.

3. Erwin, J. R. and J. C. Emery: Effect of Tunnel Configuration and Testing Technique on Cascade Performance. NACA Report 1016, 1951.

4. Taylor, William E., T. A. Murrin and R. M. Colombo: Systematic Two-Dimensional Cascade Tests, Vol. 1 - Double Circular-Arc Hydrofoils, NASA CR-72498, December 19, 1969.

5. Lieblein, S., F. C. Schwenk and R. L. Broderick: Diffusion Factor for Estimating Losses and Limiting Blade Loadings in Axial-Flow Compressor Blade Elements. NACA RM E53D01, 1953.

6. Lieblein, S. and W. H. Roudebush: Theoretical Loss Relations for Low-Speed, Two-Dimensional Cascade Flow. NACA Report TN 3662, March 1956.

7. Johnsen, I. A. and R. O. Bullock (Editors): Aerodynamic Design of Axial-Flow Compressors. NASA Report SP-36, 1965.

8. McNally, William D. and James E. Crouse: Fortran Program for Computing Coordinates of Circular-Arc Single and Tandem Turbomachinery Blade Sections on a Plane. NASA TN D-6020, 1970.

9. Katsanis, Theodore and William D. McNally: FORTRAN Program for Calculating Velocities on a Blade-to-Blade Stream Surface of a Tandem Blade Turbomachine. NASA TN D-5044, 1969.

10. Taylor, William, T. A. Murrin and R. M. Colombo: Systematic Two-Dimensional Cascade Tests, Vol. 2 - Multiple Circular-Arc Hydrofoils, NASA CR-72499, April 6, 1970.

TABLE I

Coordinates for Basic Double Circular-Arc Profiles

Camber Angle (Deg)	20	30	40	45
(Radians)	0.3491	0.5236	0.6981	0.7854
Thickness Ratio (%)	6	6	6	6
Chordal Station (% Chord)	y/c upper surface (%)			
0.0	0.10	0.10	0.10	0.10
8.33	2.29	3.00	3.77	4.15
16.67	4.14	5.41	6.74	7.41
25.00	5.56	7.25	9.01	9.87
33.33	6.57	8.55	10.58	11.59
41.67	7.18	9.33	11.54	12.61
50.00	7.38	9.58	11.84	12.95
58.33	7.18	9.33	11.54	12.61
66.67	6.57	8.55	10.58	11.59
75.00	5.56	7.25	9.01	9.87
83.33	4.14	5.41	6.74	7.41
91.67	2.29	3.00	3.77	4.15
100.00	0.10	0.10	0.10	0.10
	y/c lower surface (%)			
0.0	-0.10	-0.10	-0.10	-0.10
8.33	0.42	1.10	1.80	2.15
16.67	0.76	2.00	3.26	3.89
25.00	1.03	2.69	4.40	5.23
33.33	1.22	3.19	5.19	6.19
41.67	1.33	3.48	5.68	6.76
50.00	1.38	3.58	5.84	6.95
58.33	1.33	3.48	5.68	6.76
66.67	1.22	3.19	5.19	6.19
75.00	1.03	2.69	4.40	5.23
83.33	0.76	2.00	3.26	3.89
91.67	0.42	1.10	1.80	2.15
100.00	-0.10	-0.10	-0.10	-0.10

TABLE II

Index to Cascade Test Configurations

(Slot 3 - Figure 8b)

Inlet Flow Angle (Deg)	Inlet Flow Angle (Radians)	Camber (Deg)	Camber (Radians)	Solidity	Figure Number
50	0.8727	30	0.5236	0.75	18
				1.00	19
				1.50	20
50	0.8727	40	0.6981	0.75	21
				1.00	22
				1.50	23
50	0.8727	45	0.7854	0.75	24
				1.00	25
				1.50	26
60	1.0472	30	0.5236	0.75	27
				1.00	28
				1.50	29
60	1.0472	40	0.6981	0.75	30
				1.00	31
				1.50	32
60	1.0472	45	0.7854	0.75	33
				1.00	34
				1.50	35
70	1.2217	20	0.3491	0.75	36
				1.00	37
				1.50	38
70	1.2217	30	0.5236	0.75	39
				1.00	40
				1.50	41

PRECEDING PAGE BLANK NOT FILMED

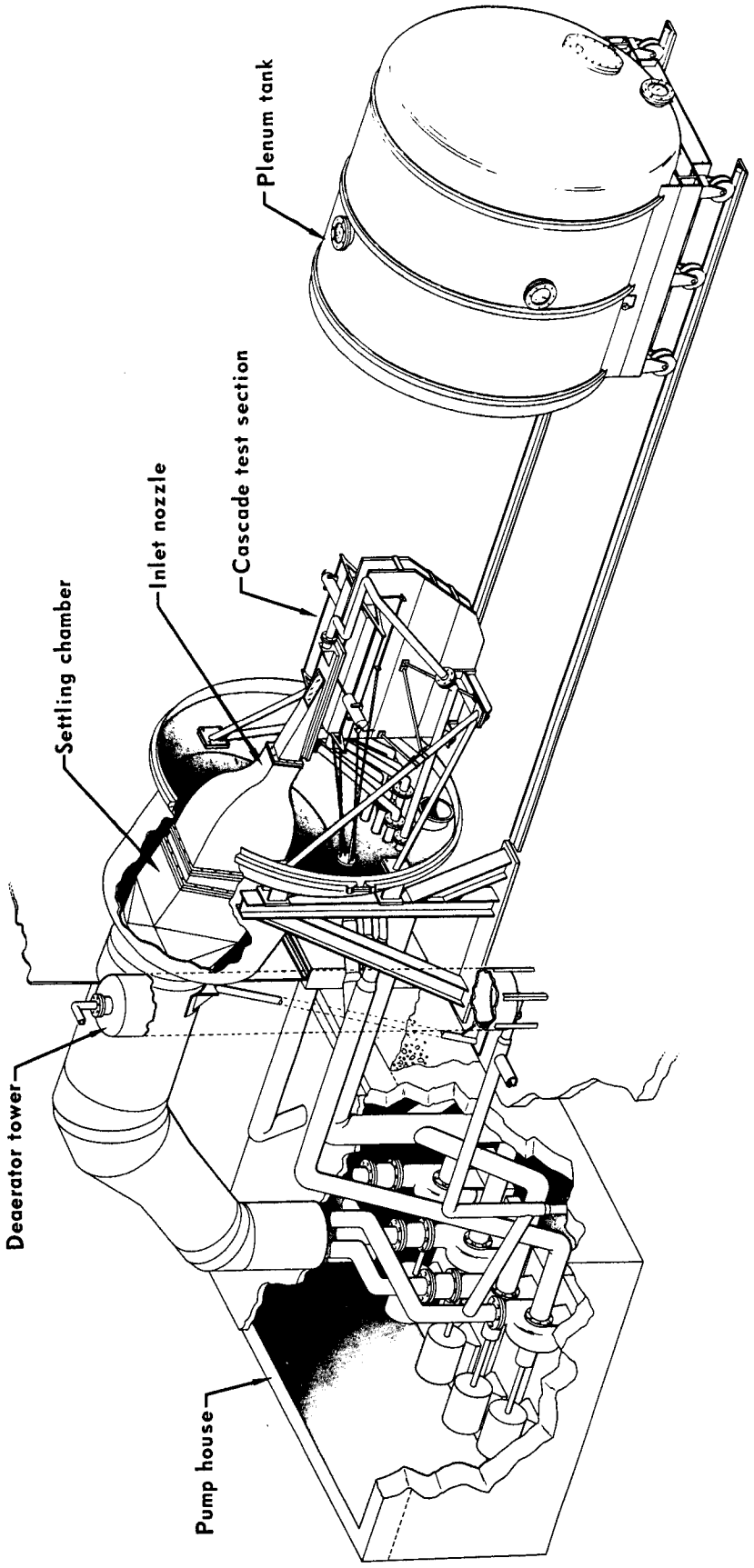

Figure 1.- Cascade water tunnel

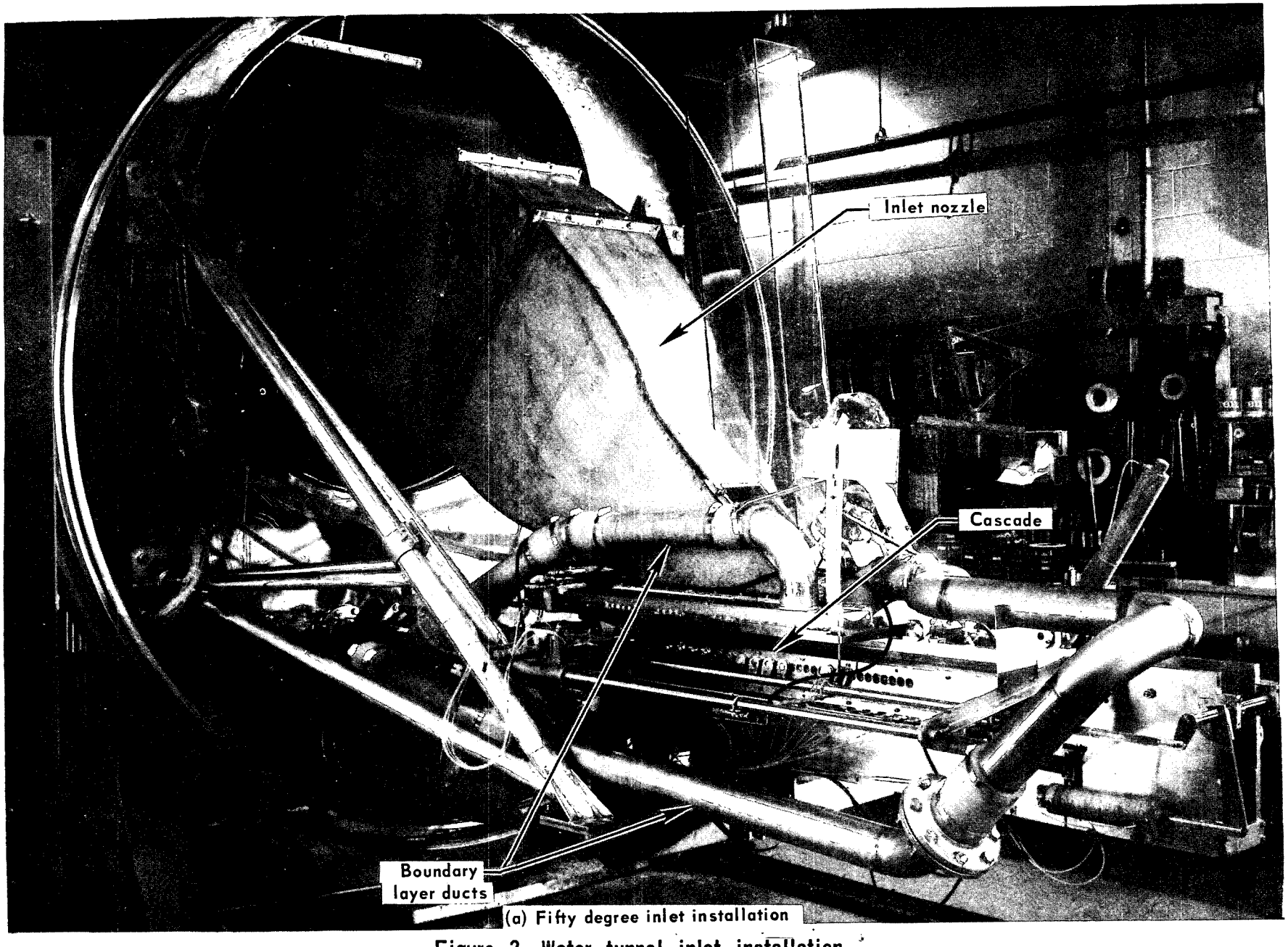

Figure 2. Water tunnel inlet installation.

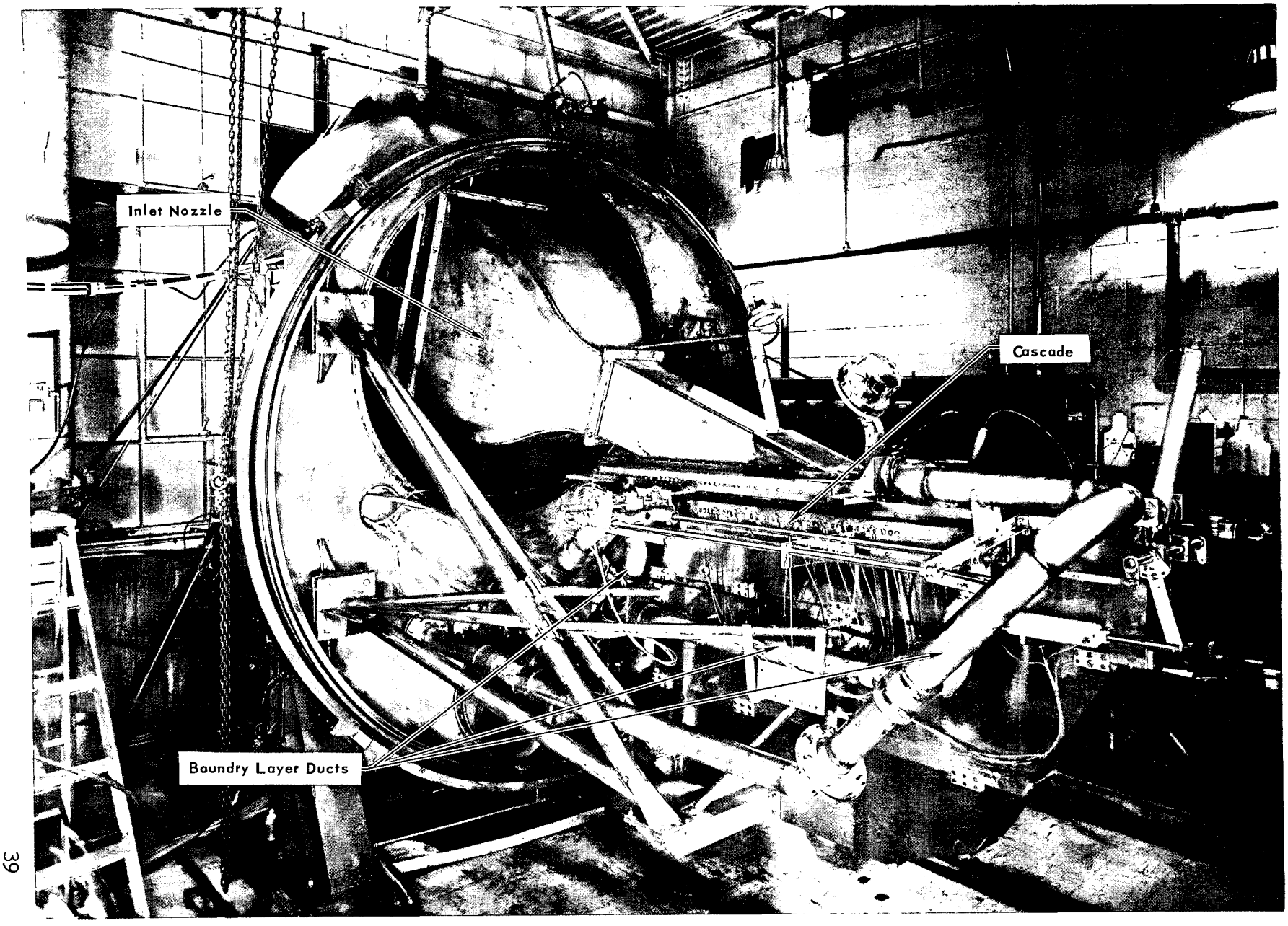

(b) Seventy degree inlet installation

Figure 2. – Concluded.

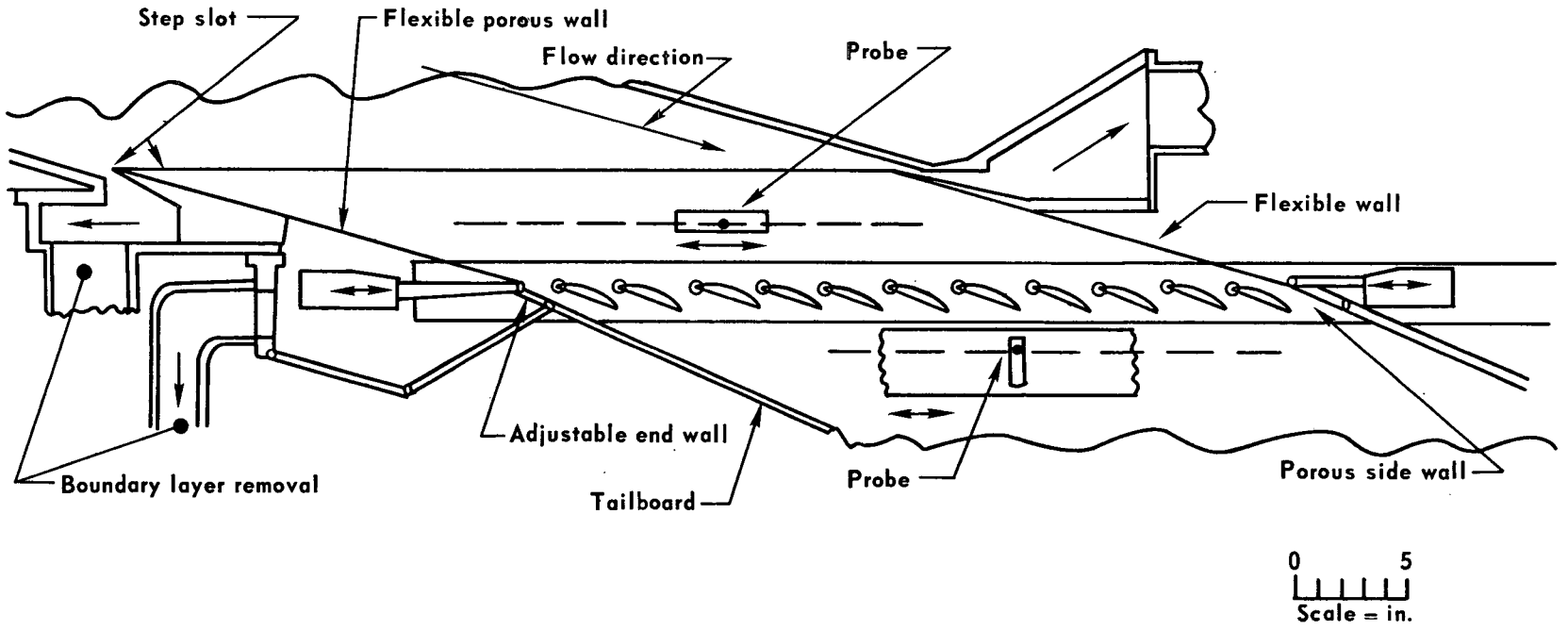

Figure 3. – Cascade test section

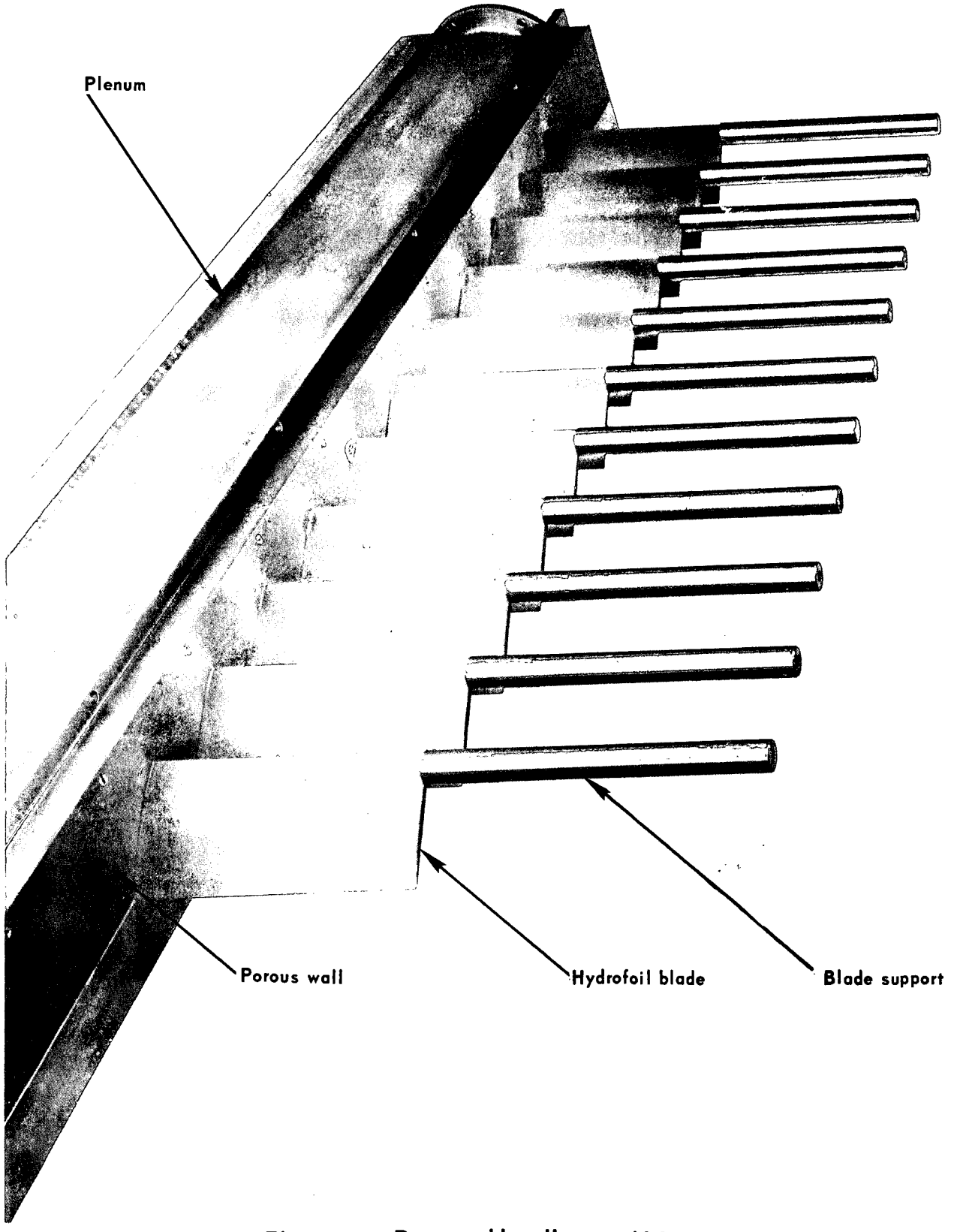

Figure 4. – Porous sidewall assembly.

(a) $\Phi = 20$, $t/c = 0.06$

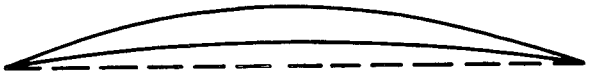

(b) $\Phi = 30$, $t/c = 0.06$

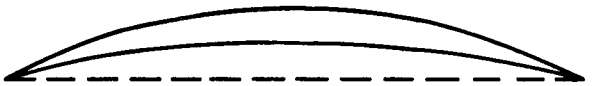

(c) $\Phi = 40$, $t/c = 0.06$

(d) $\Phi = 45$, $t/c = 0.06$

Figure 5. – Double circular–arc profiles.

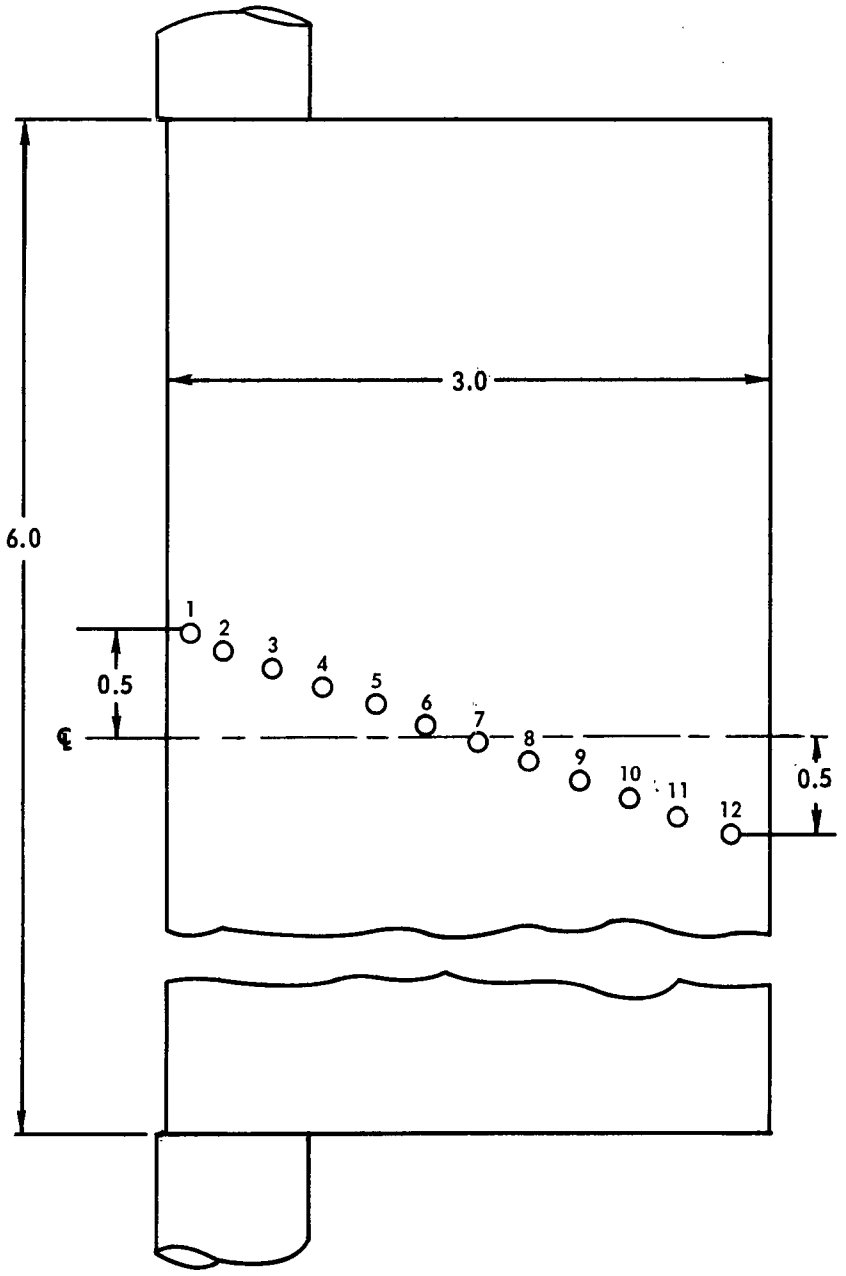

NO.	X	% CHORD
1	0.125	4.16
2	0.250	8.33
3	0.500	16.67
4	0.750	25.00
5	1.000	33.33
6	1.250	41.60
7	1.500	50.00
8	1.750	58.33
9	2.000	66.67
10	2.250	75.00
11	2.500	83.33
12	2.750	91.67

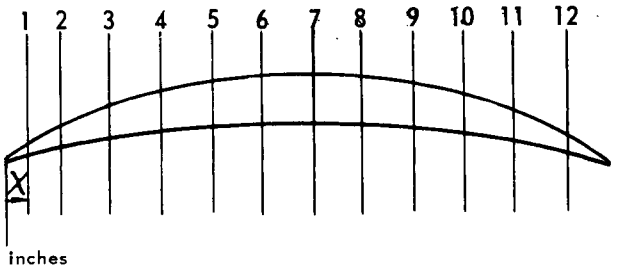

Note: All dimensions are in inches

Figure 6 . – Location of static pressure instrumentation – suction and pressure surfaces.

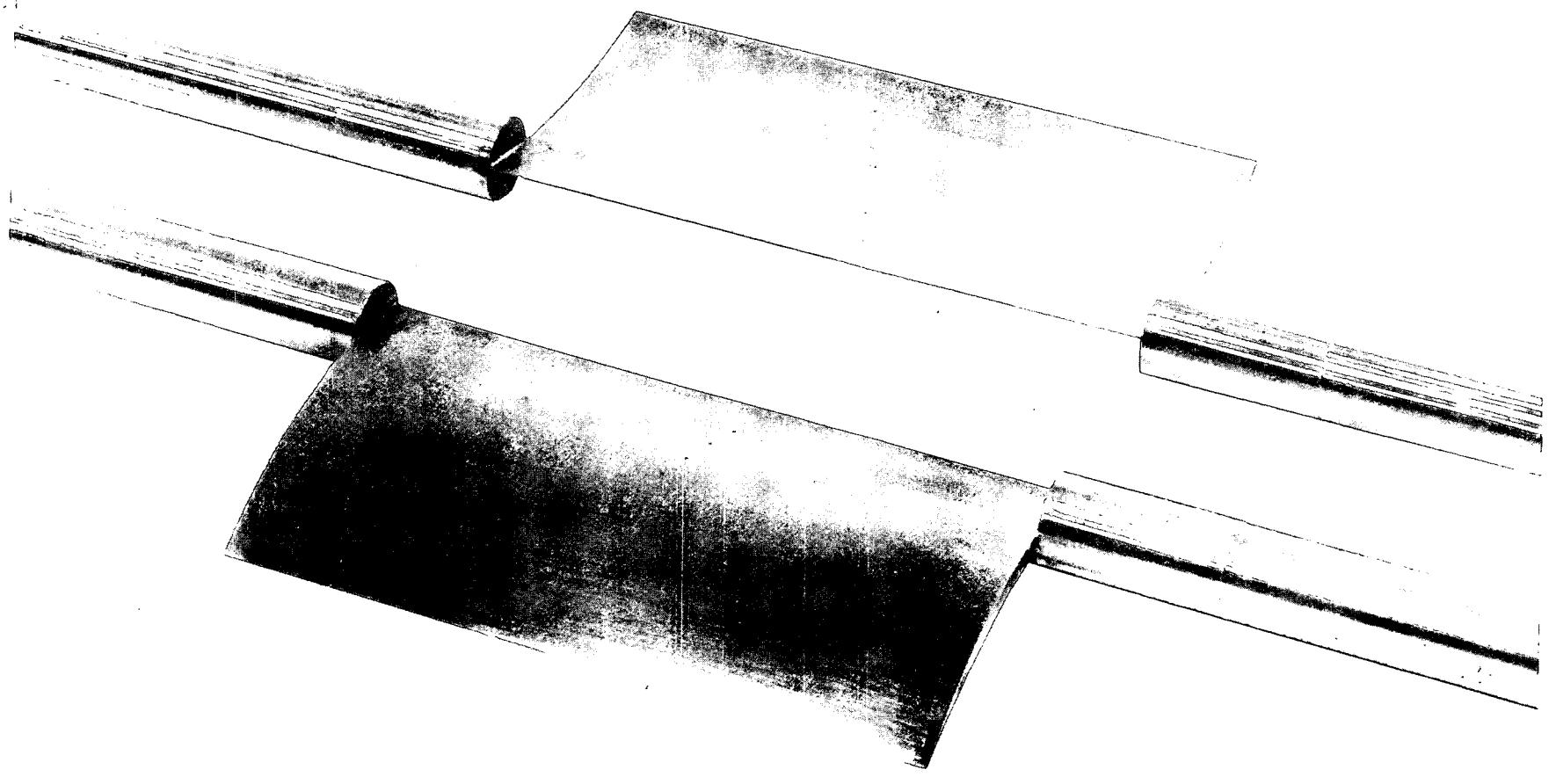

Figure 7. – Static pressure instrumentation in 40–deg camber double circular–arc hydrofoils.

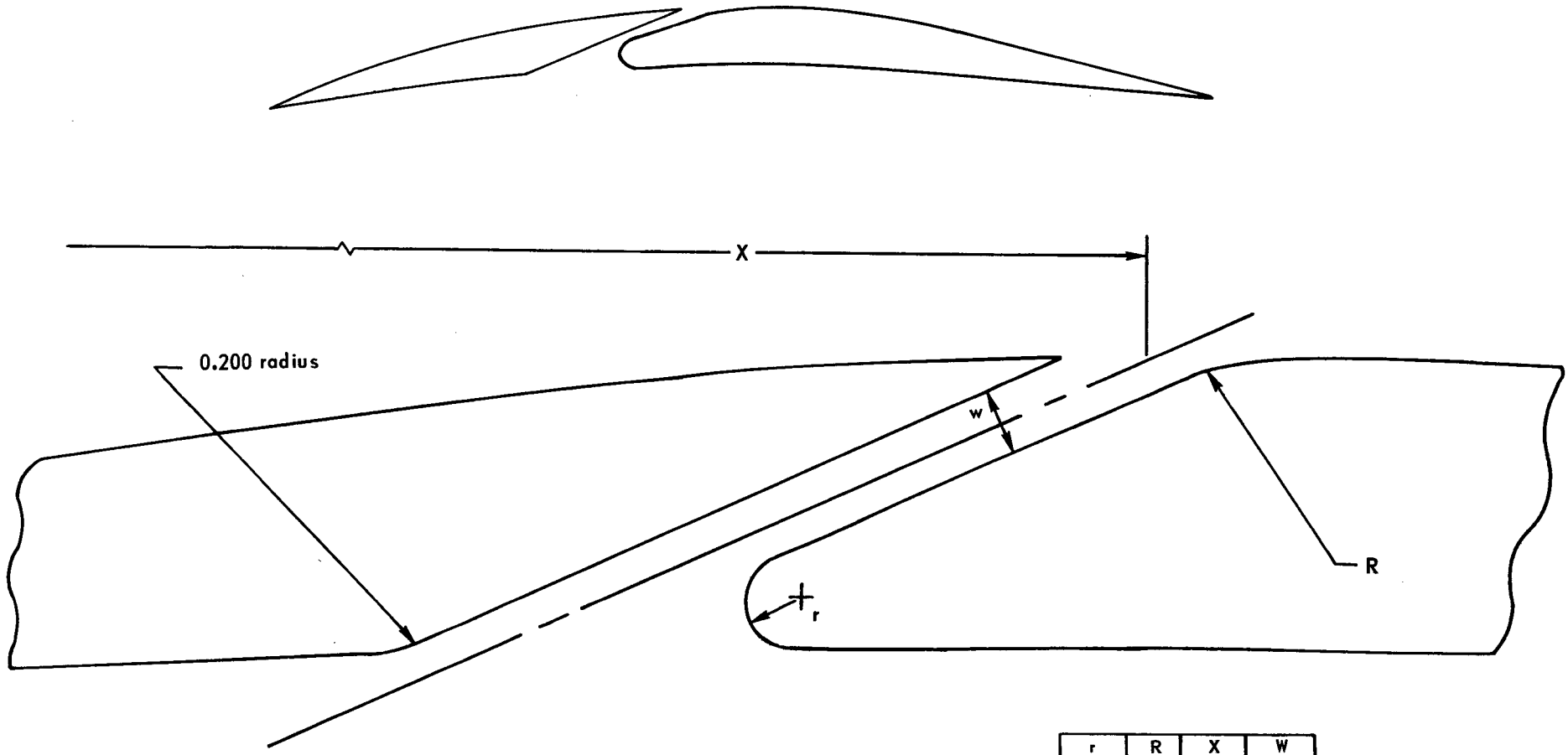

r	R	X	W
0.031	0.2	35	0.063

a. Parallell wall slot

Figure 8. – Slot configuration for double circular–arc hydrofoils.

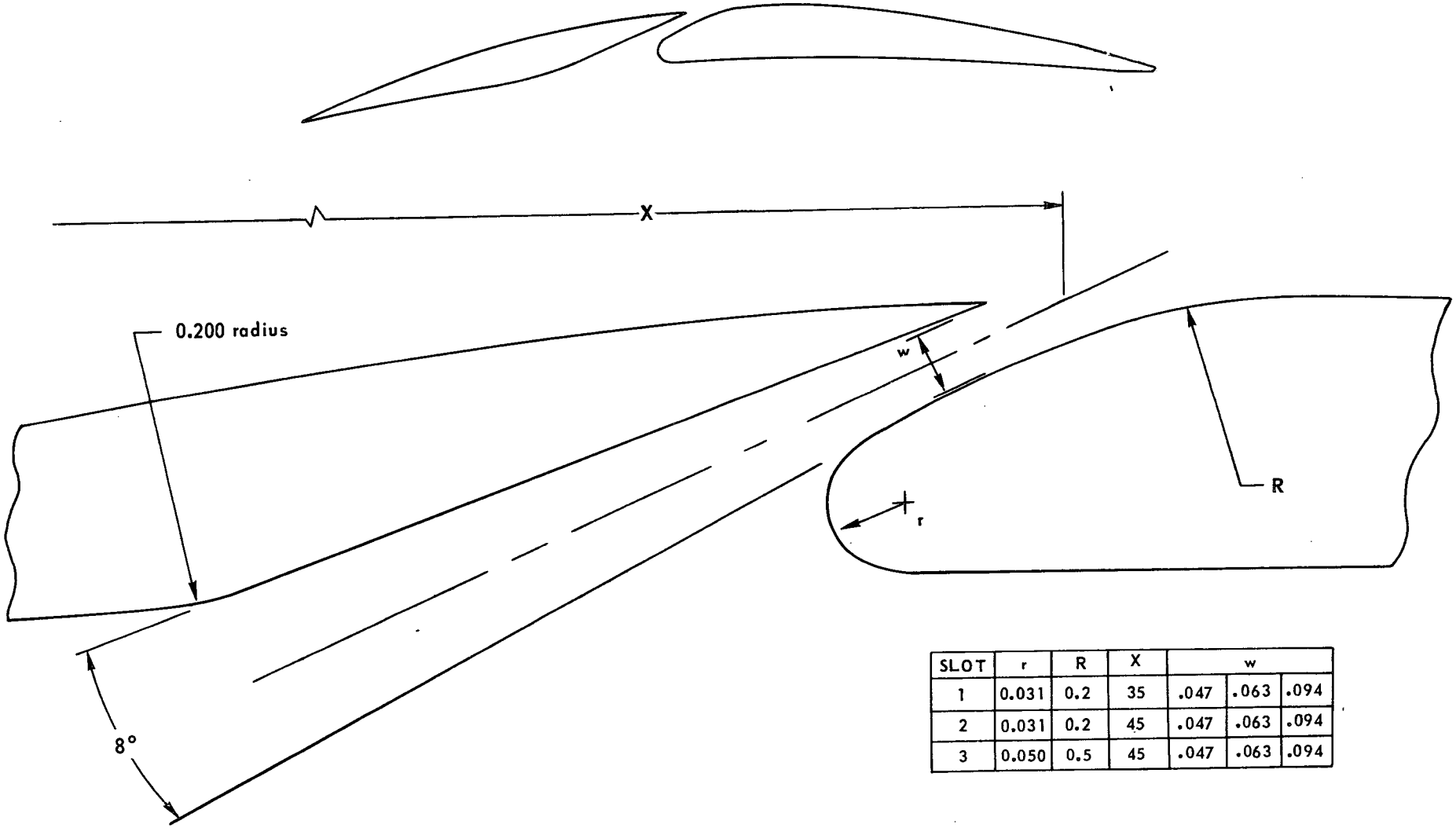

SLOT	r	R	X	w		
1	0.031	0.2	35	.047	.063	.094
2	0.031	0.2	45	.047	.063	.094
3	0.050	0.5	45	.047	.063	.094

b. Converging wall slot

Figure 8 . – Concluded.

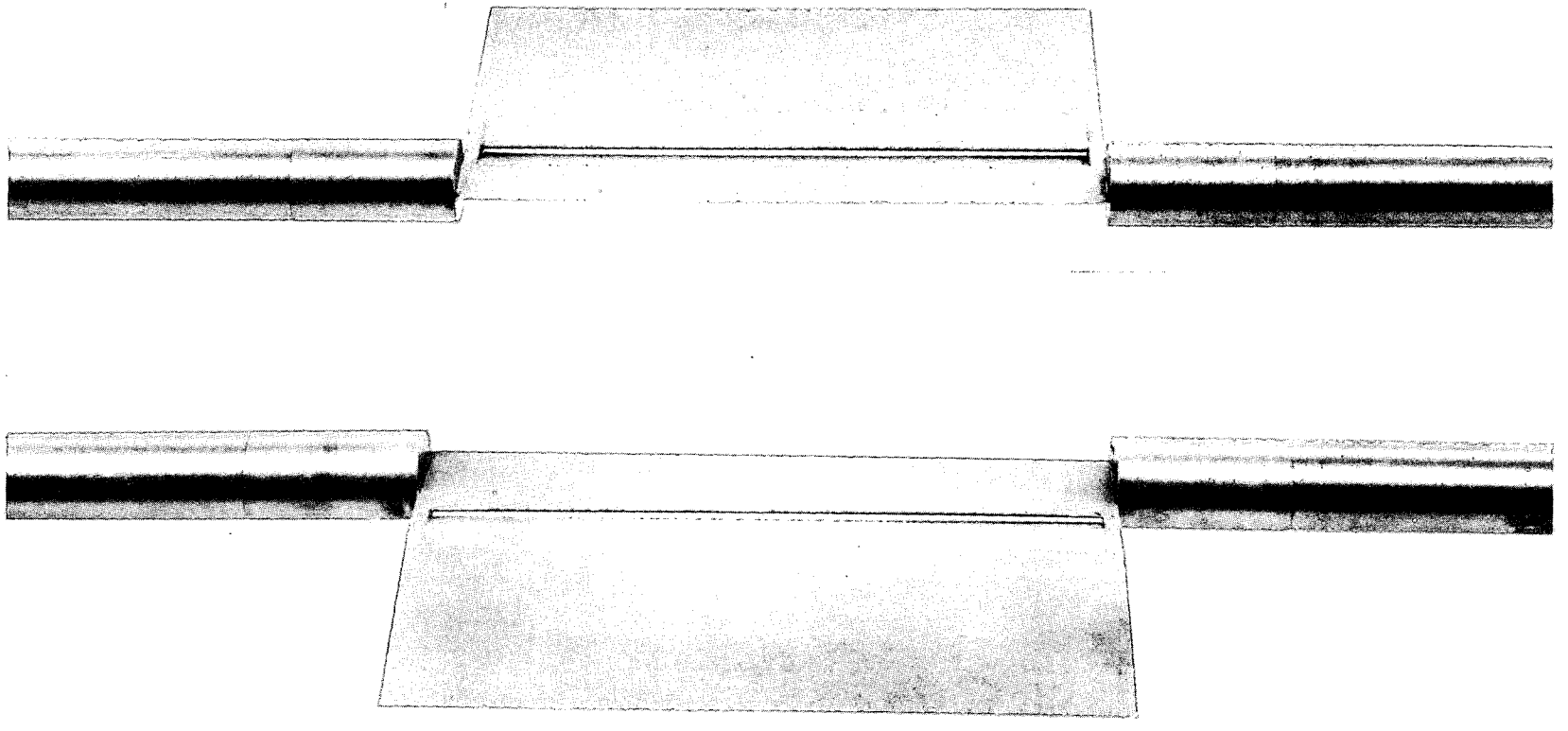

Figure 9. – Slotted double circular–arc hydrofoils.

a. Wedge (upstream)

b. Kiel–wedge combination
(downstream)

Figure 10. –Directional probes

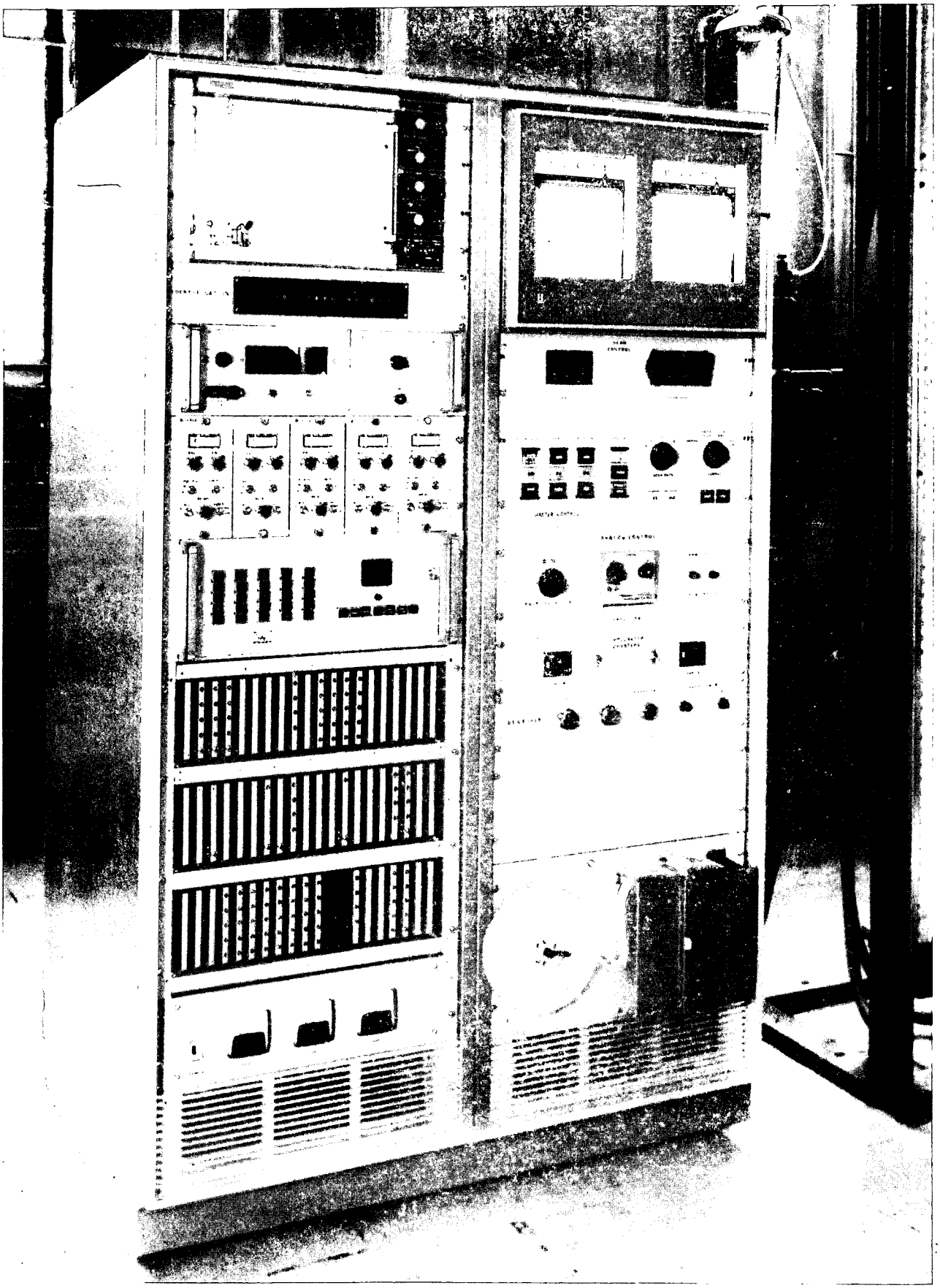

Figure 11. – Data acquisition system.

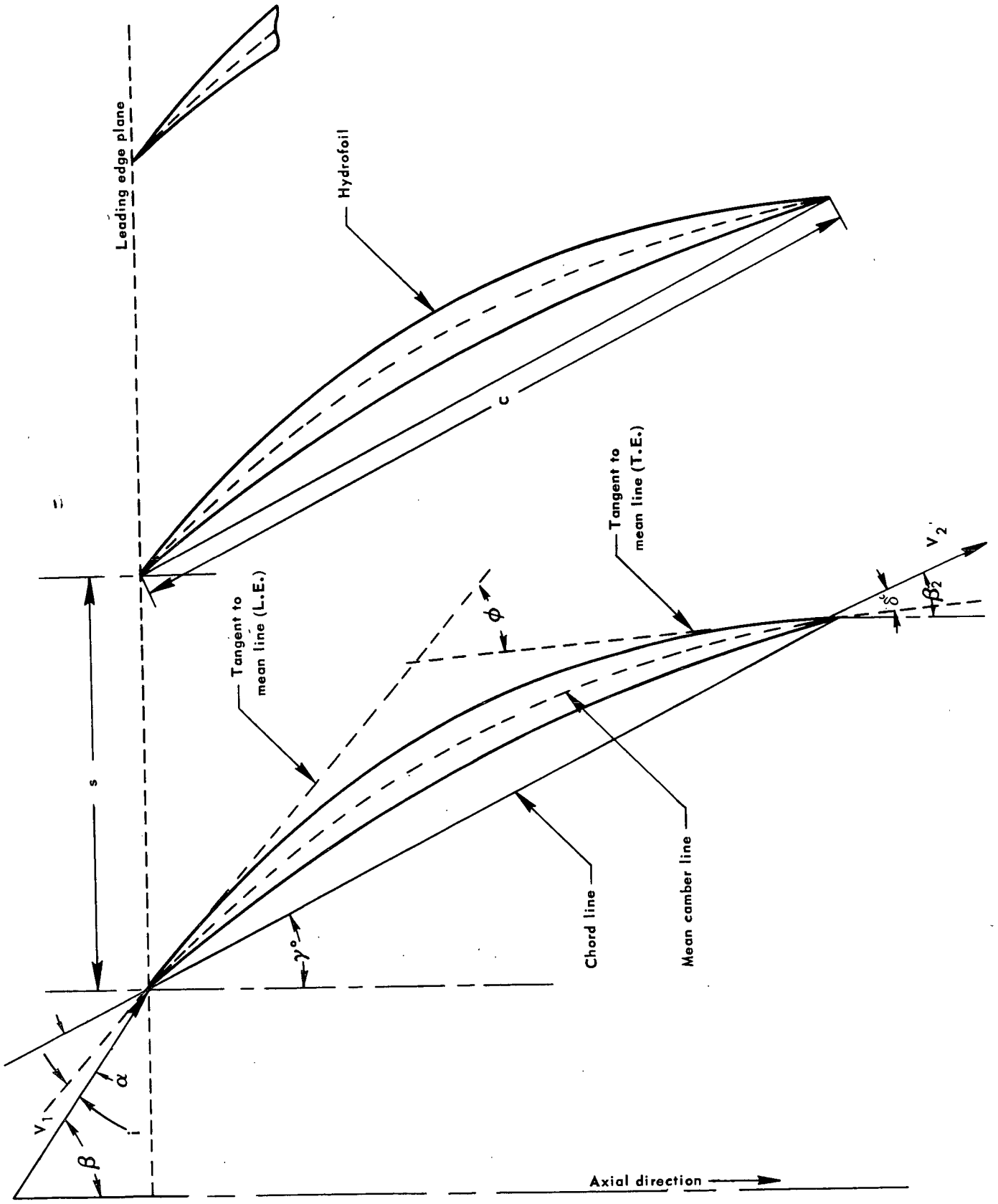

Figure 12. — Cascade nomenclature.

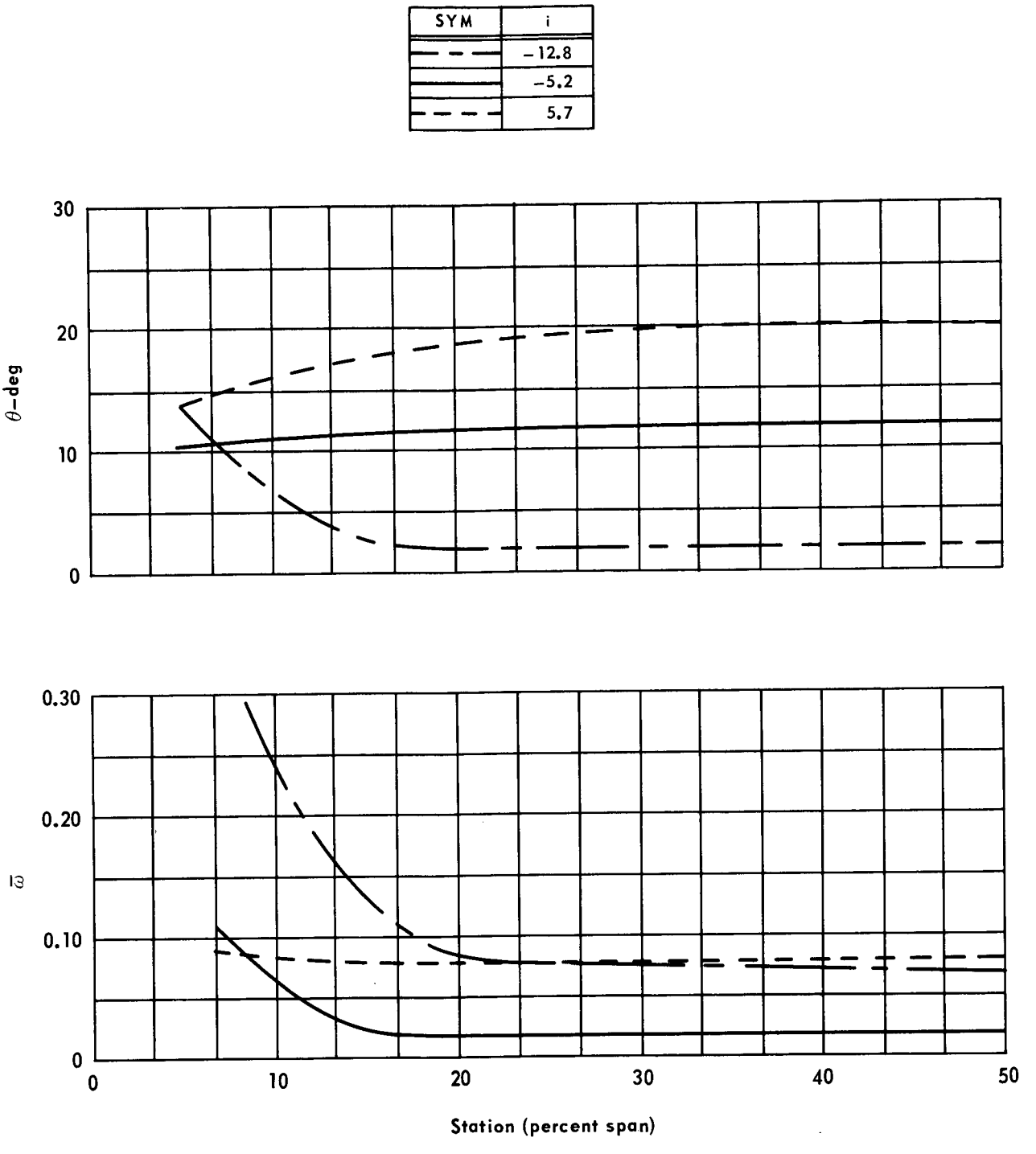

Cascade configuration: $\beta_{1N} = 60$, $\sigma = 0.75$

(a) Slotted double circular-arc profile: $\phi = 30$, t/c = 0.06

Figure 13.- Cascade characteristics as a function of spanwise station for various incidence angles.

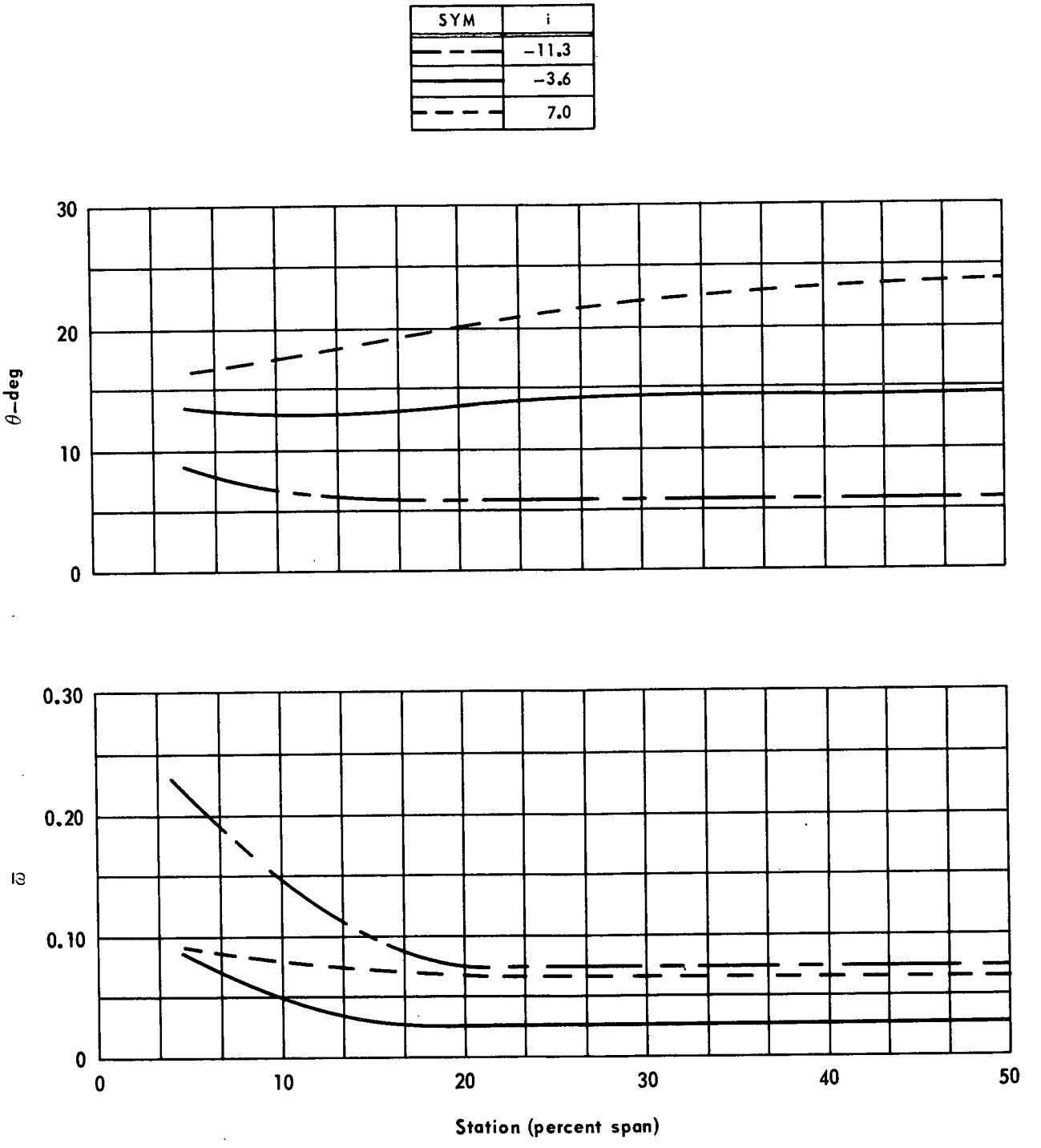

(b) Cascade configuration: $\beta_{IN} = 60$, $\sigma = 1.00$

Slotted double circular-arc profile: $\phi = 30$, t/c = 0.06

Figure 13. – Continued.

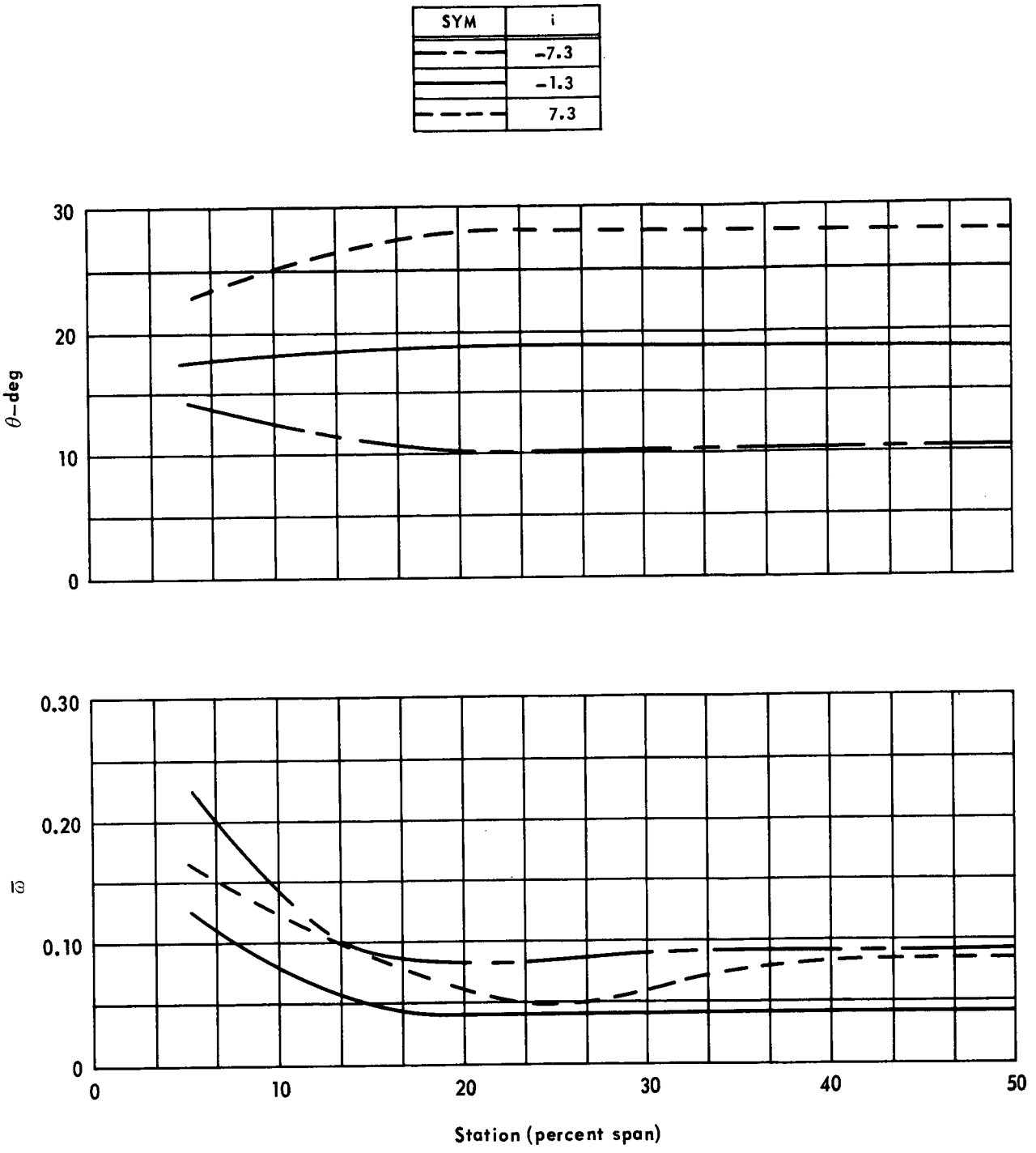

(c) Cascade configuration: $\beta_{IN} = 60$, $\sigma = 1.50$

Slotted double circular-arc profile: $\phi = 30$, $t/c = 0.06$

Figure 13. – Continued.

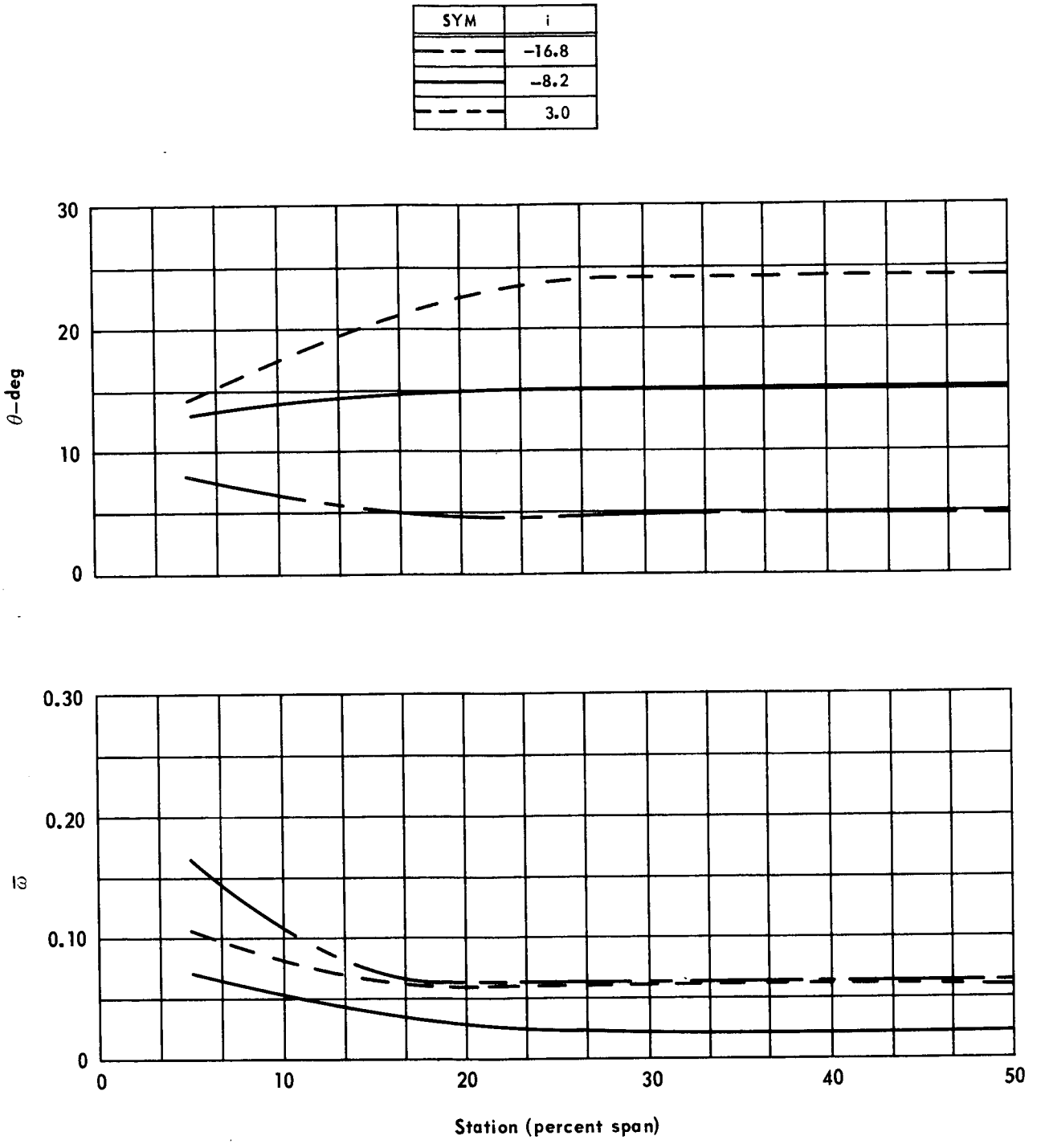

(d) Cascade configuration: $\beta_{IN} = 60$, $\sigma = 0.75$

Slotted double circular-arc profile: $\phi = 40$, $t/c = 0.06$

Figure 13. – Continued.

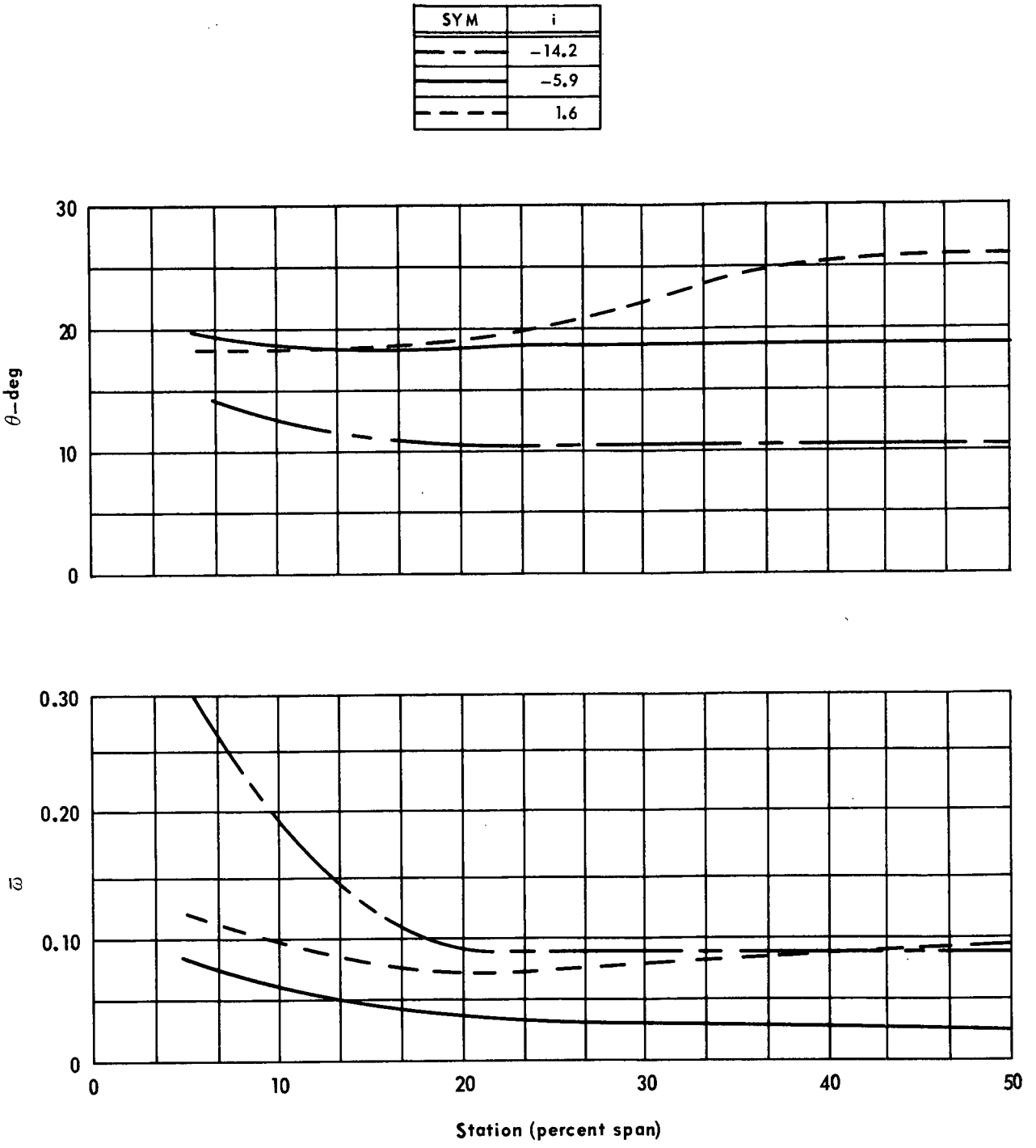

(e) Cascade configuration: $\beta_{IN} = 60$, $\sigma = 1.00$

Slotted double circular-arc profile: $\phi = 40$, $t/c = 0.06$

Figure 13. – Continued.

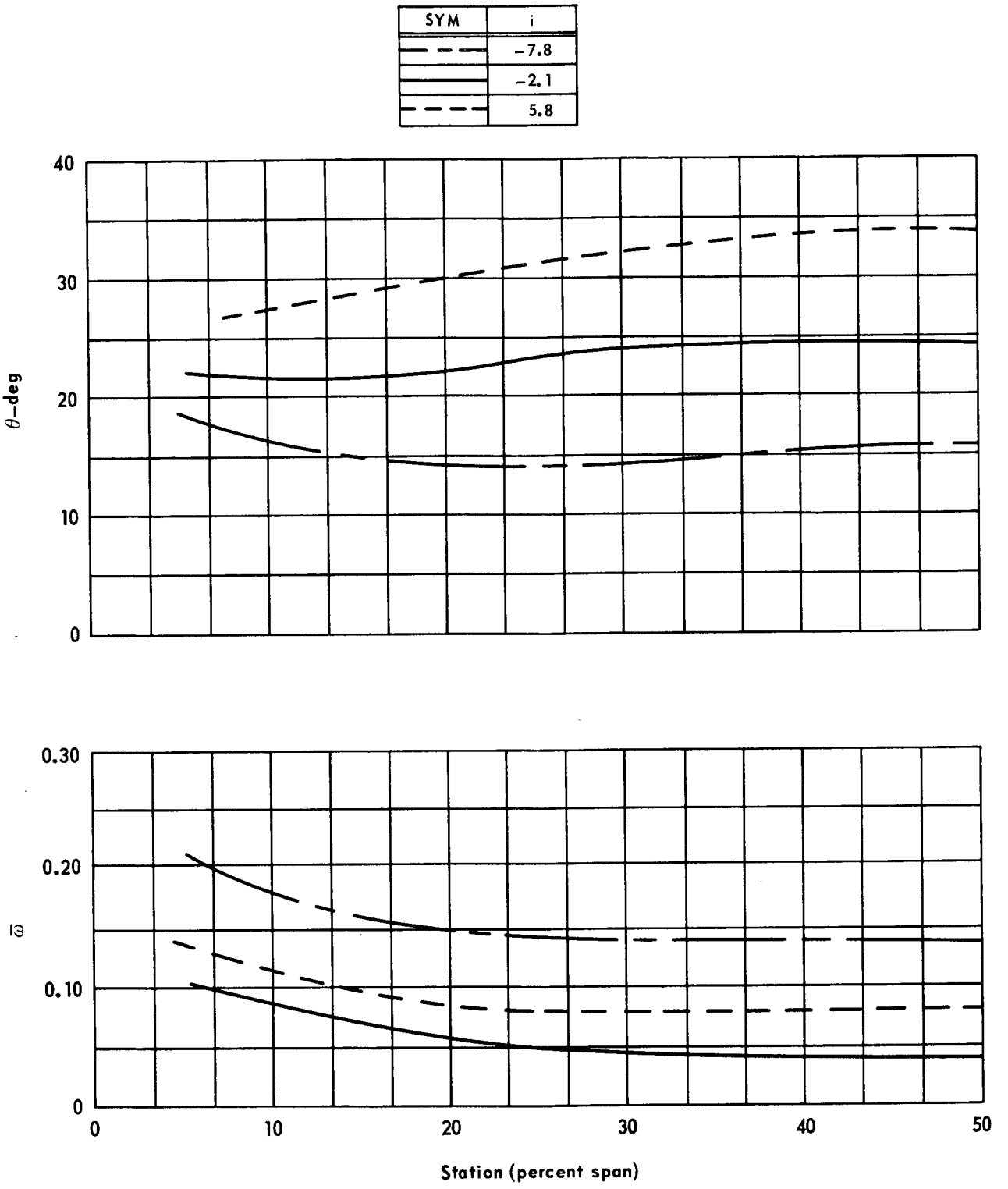

(f) Cascade configuration: $\beta_{1N} = 60$, $\sigma = 1.50$

Slotted double circular-arc profile: $\phi = 40$, $t/c = 0.06$

Figure 13. – Continued.

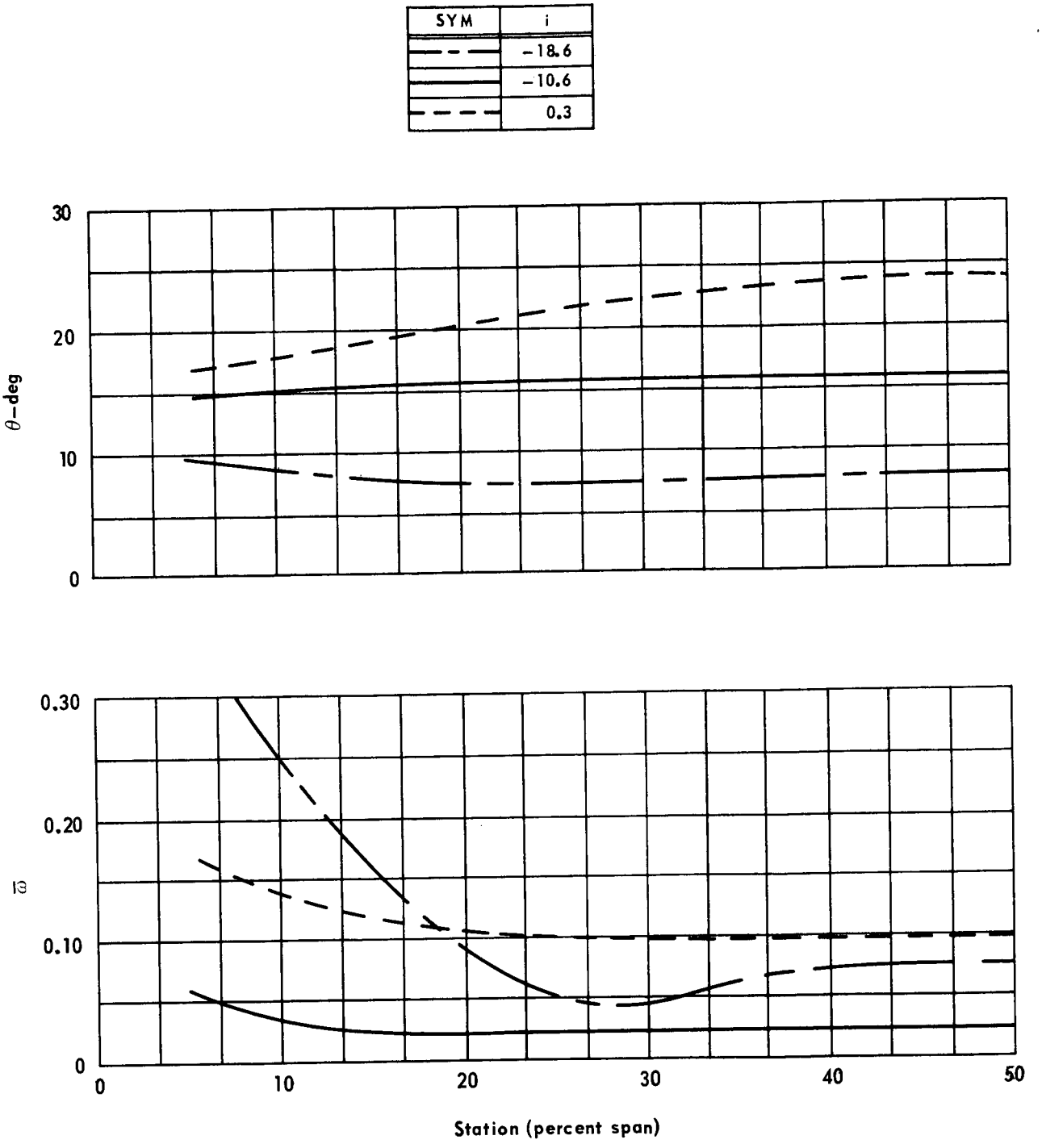

(g) Cascade configuration: $\beta_{IN} = 60$, $\sigma = 0.75$

Slotted double circular-arc profile: $\phi = 45$, $t/c = 0.06$

Figure 13. – Continued.

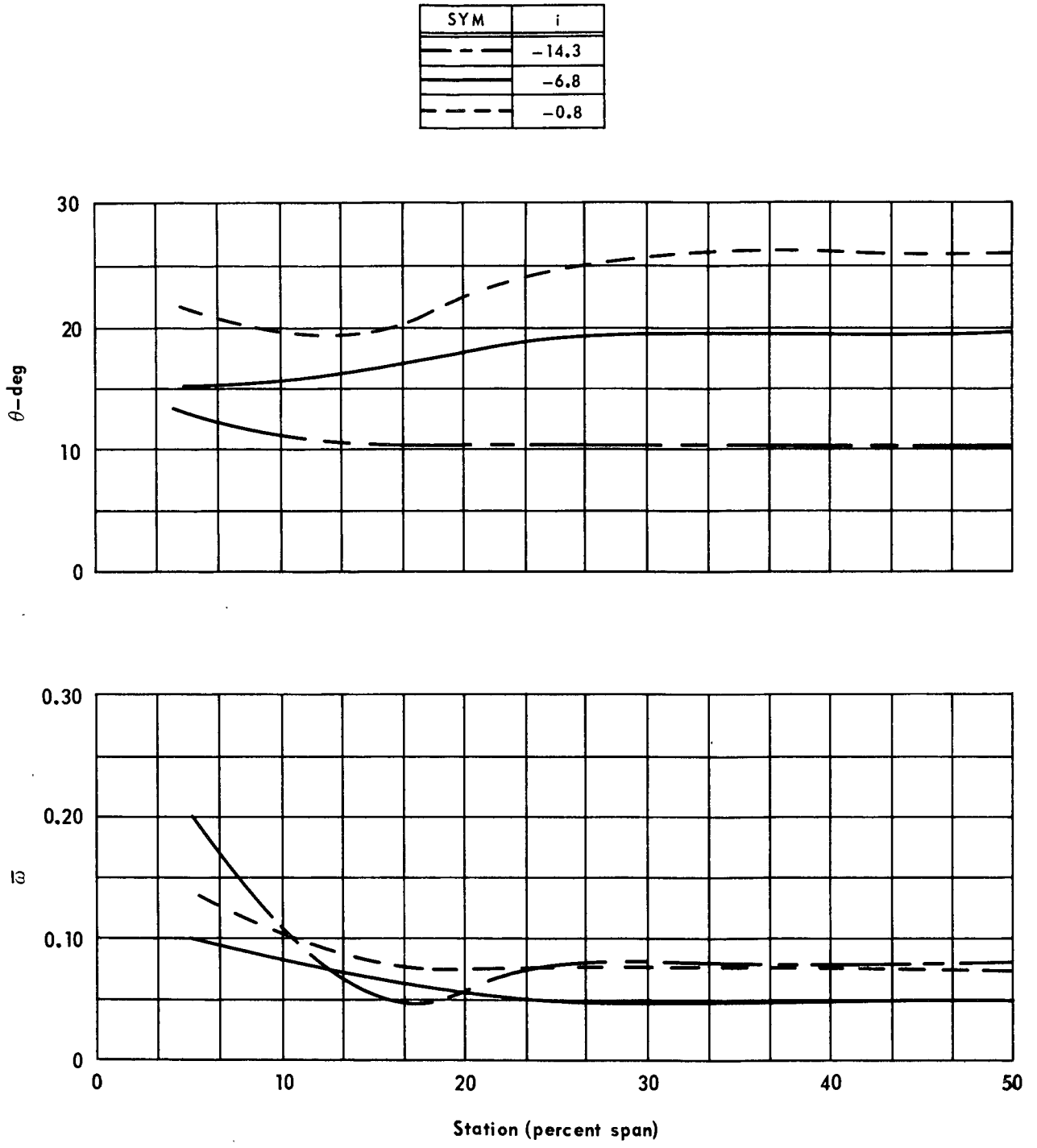

(h) Cascade configuration: $\beta_{IN} = 60$, $\sigma = 1.00$

Slotted double circular-arc profile: $\phi = 45$, $t/c = 0.06$

Figure 13. – Continued.

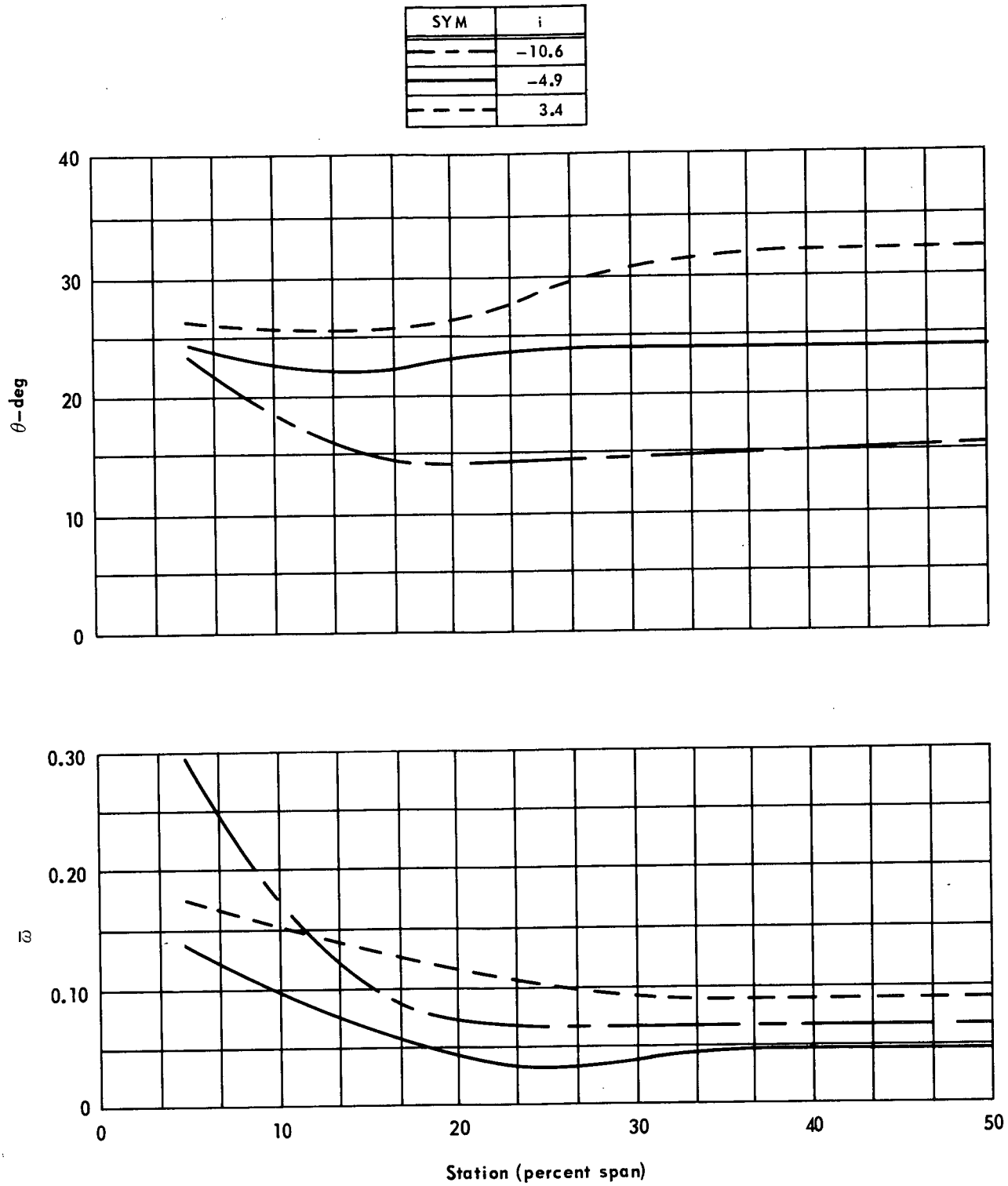

(i) Cascade configuration: $\beta_{IN} = 60$, $\sigma = 1.50$

Slotted double circular-arc profile: $\phi = 45$, $t/c = 0.06$

Figure 13. – Concluded.

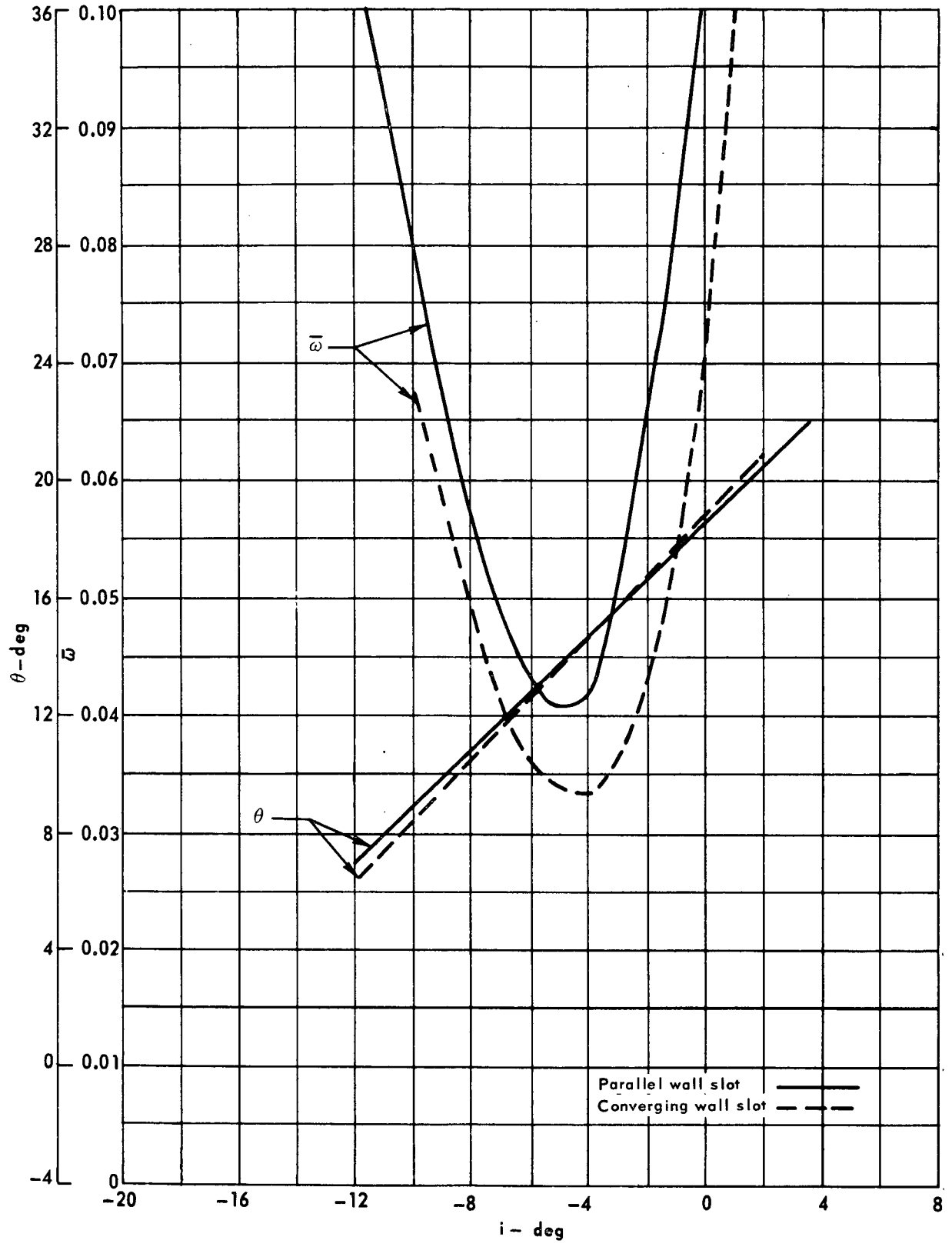

Cascade configuration : $\beta_{1N} = 60$, $\sigma = 1.00$

Double circular-arc profile : $\phi = 40$, $t/c = 0.06$

Figure 14. – Slot wall convergence effect.

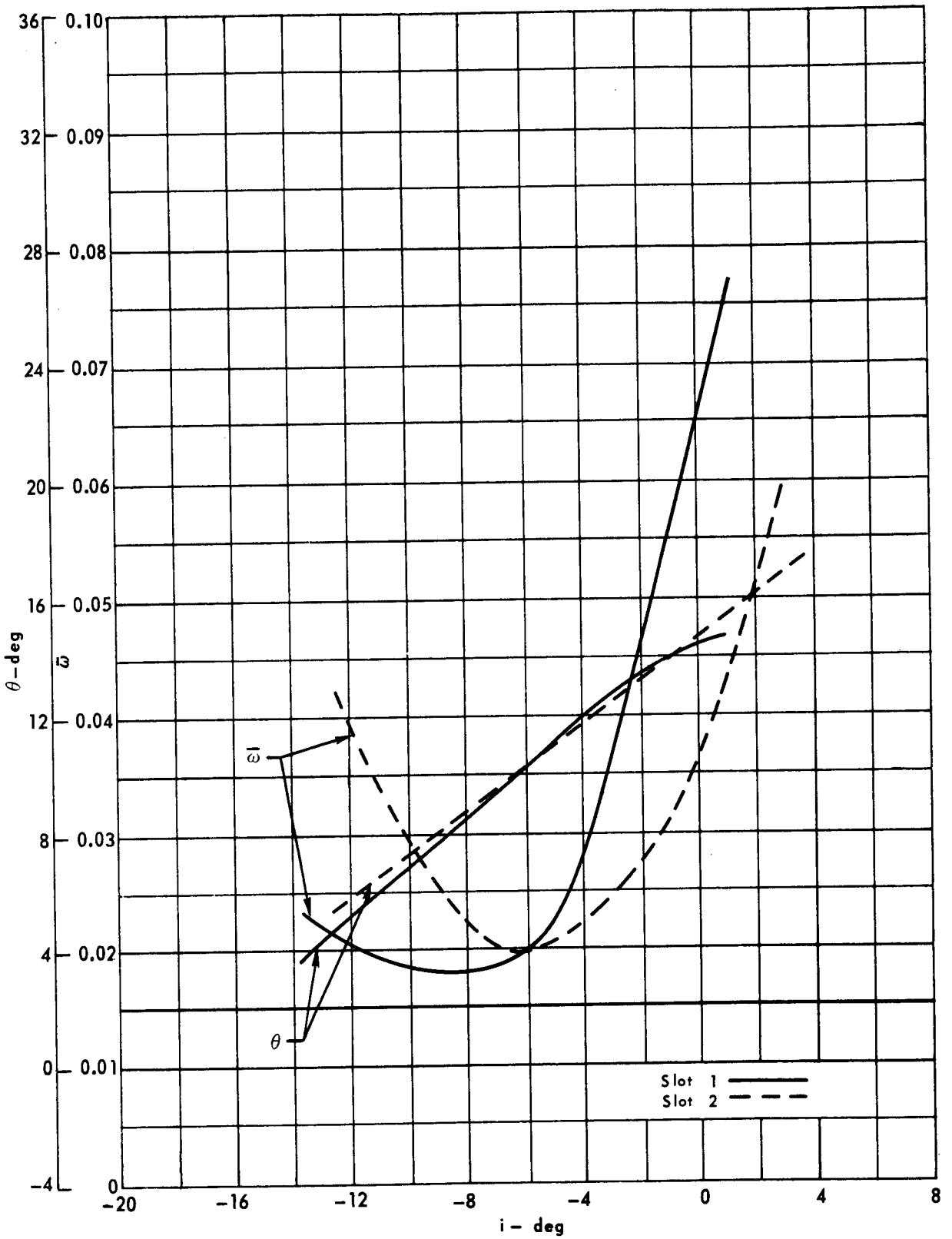

(a) Cascade configuration : $\beta_{1N} = 60$, $\sigma = 0.75$

Double circular-arc profile : $\phi = 30$, $t/c = 0.06$

Figure 15. – Slot location effect.

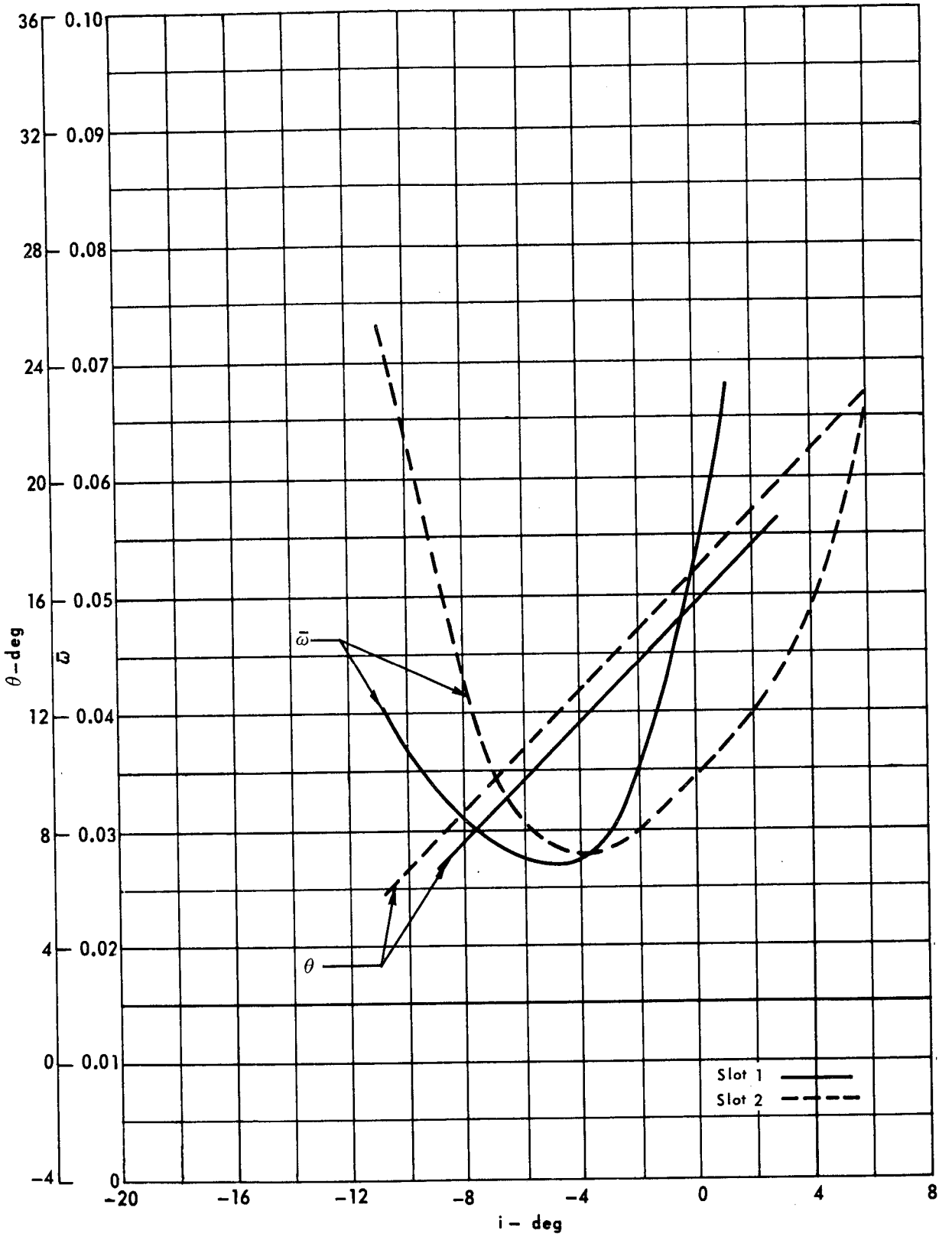

(b) Cascade configuration : $\beta_{1N} = 60$, $\sigma = 1.00$

Double circular–arc profile : $\phi = 30$, $t/c = 0.06$

Figure 15. – Continued.

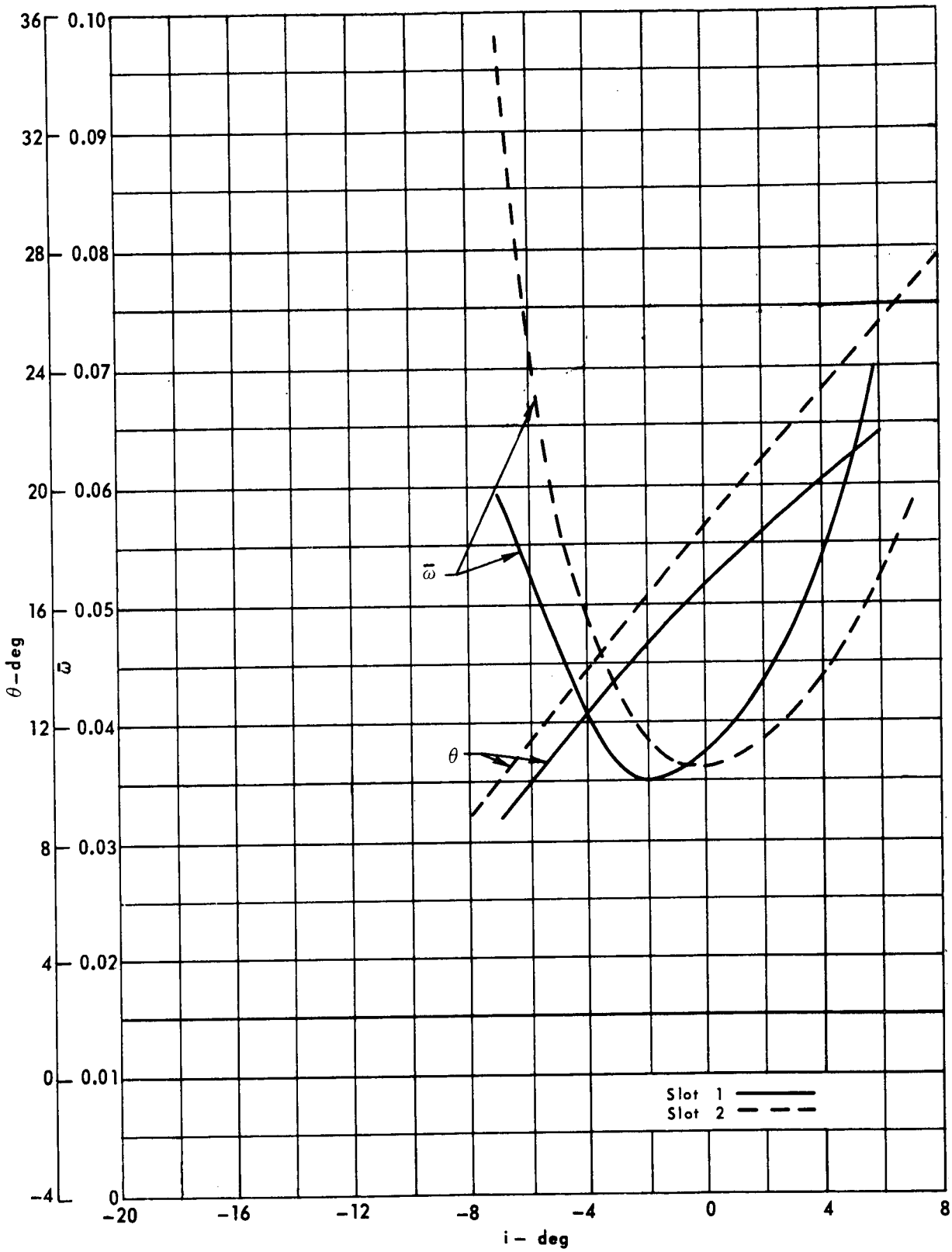

(c) Cascade configuration : $\beta_{1N} = 60$, $\sigma = 1.50$

Double circular–arc profile : $\phi = 30$, $t/c = 0.06$

Figure 15. – Continued.

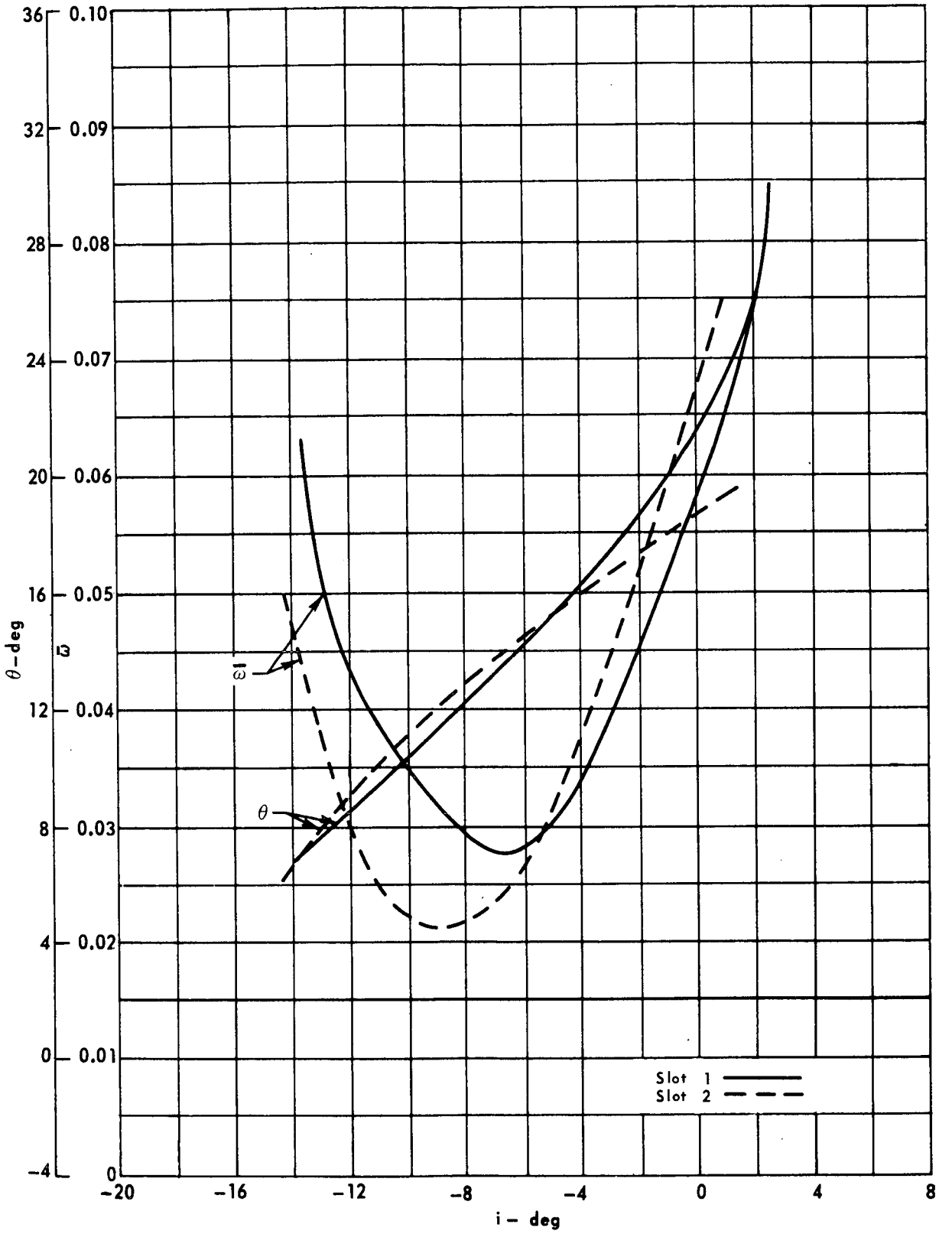

(d) Cascade configuration : $\beta_{1N} = 60$, $\sigma = 0.75$

Double circular-arc profile : $\phi =$ 40 , t/c = 0.06

Figure 15. – Continued.

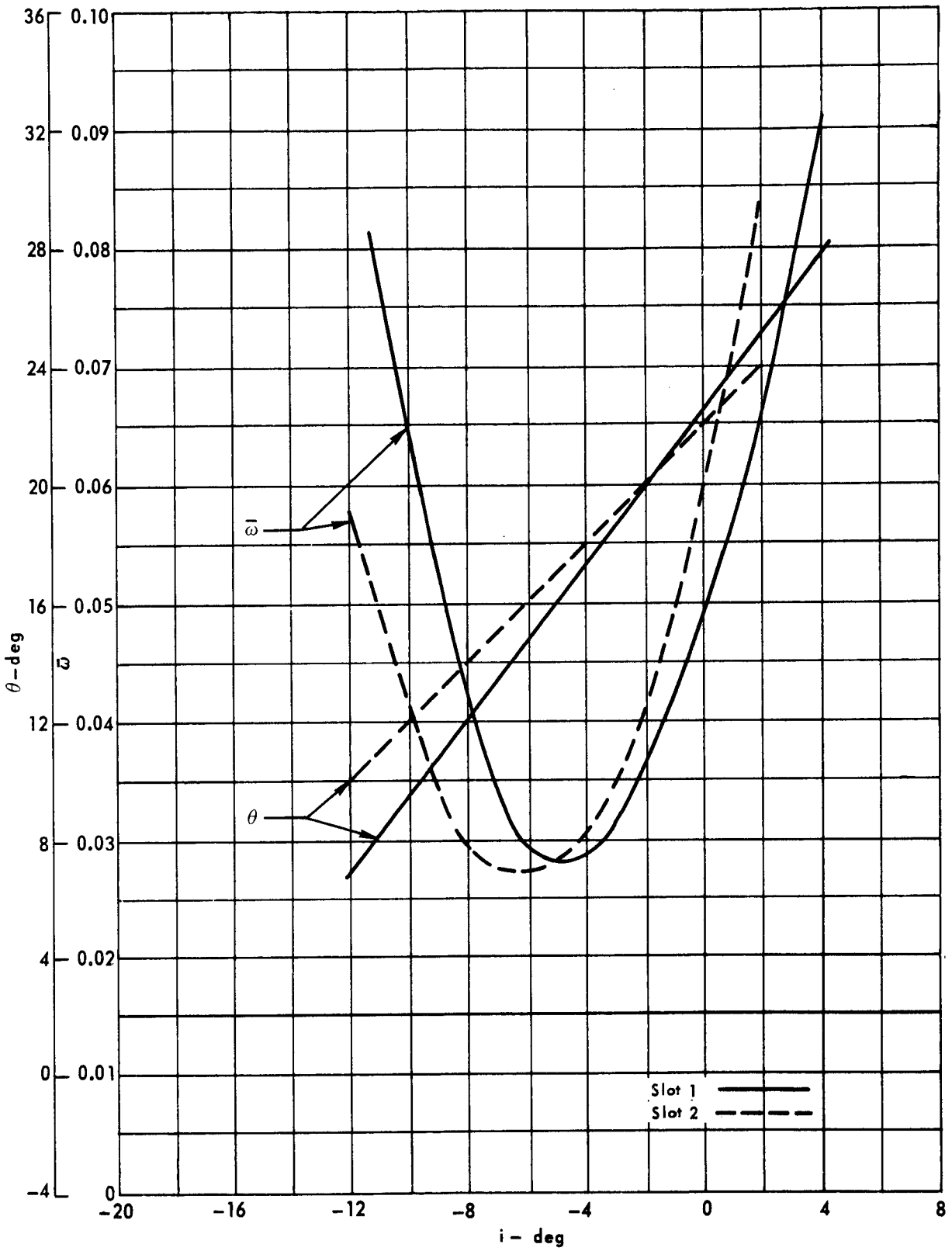

(e) Cascade configuration : $\beta_{1N} = 60$, $\sigma = 1.00$

Double circular–arc profile : $\phi = 40$, $t/c = 0.06$

Figure 15. – Continued.

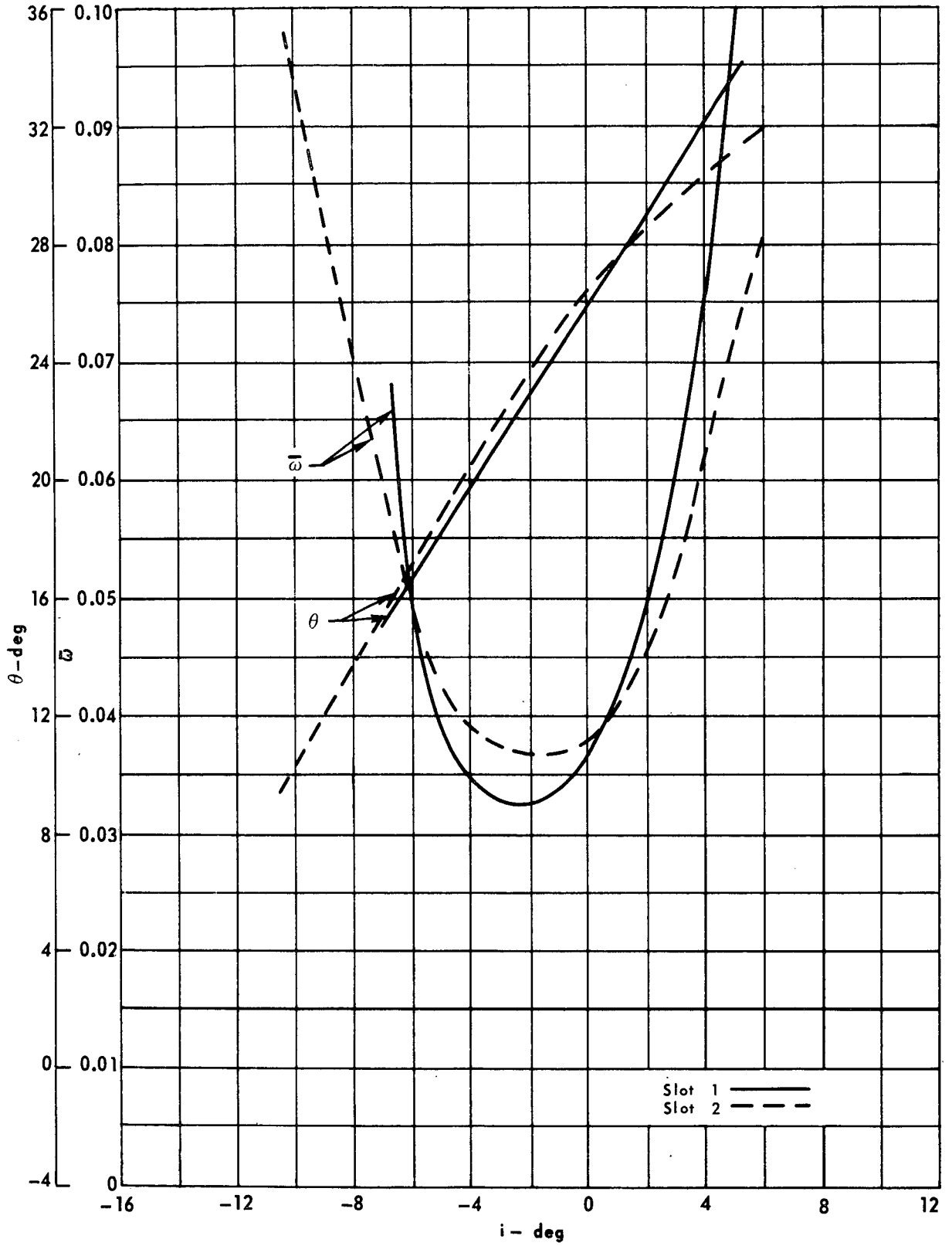

(f) Cascade configuration : $\beta_{1N} = 60$, $\sigma = 1.50$

Double circular-arc profile : $\phi = 40$, $t/c = 0.06$

Figure 15. – Continued.

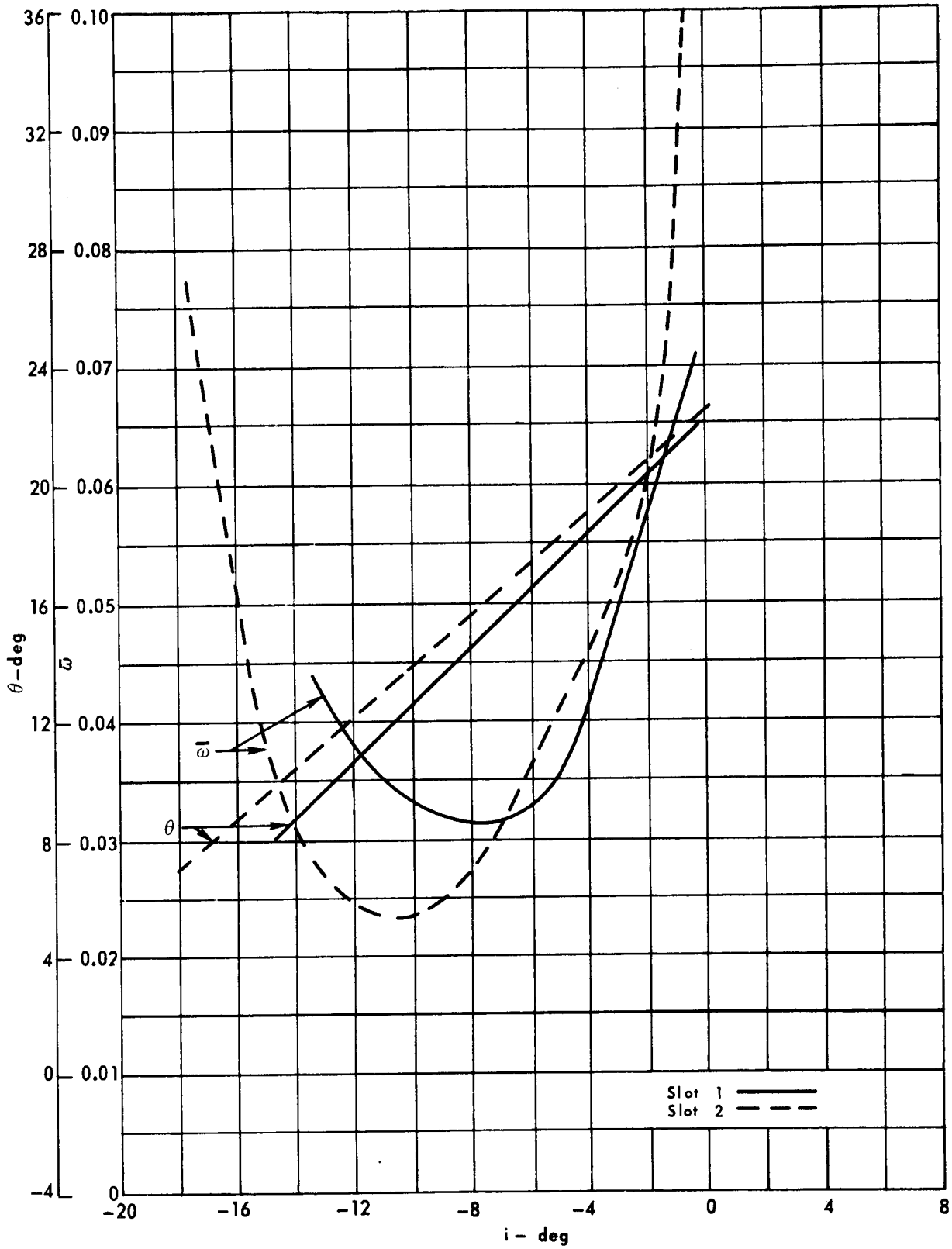

(g) Cascade configuration : $\beta_{1N} = 60$, $\sigma = 0.75$

Double circular-arc profile : $\phi = 45$, $t/c = 0.06$

Figure 15. – Continued.

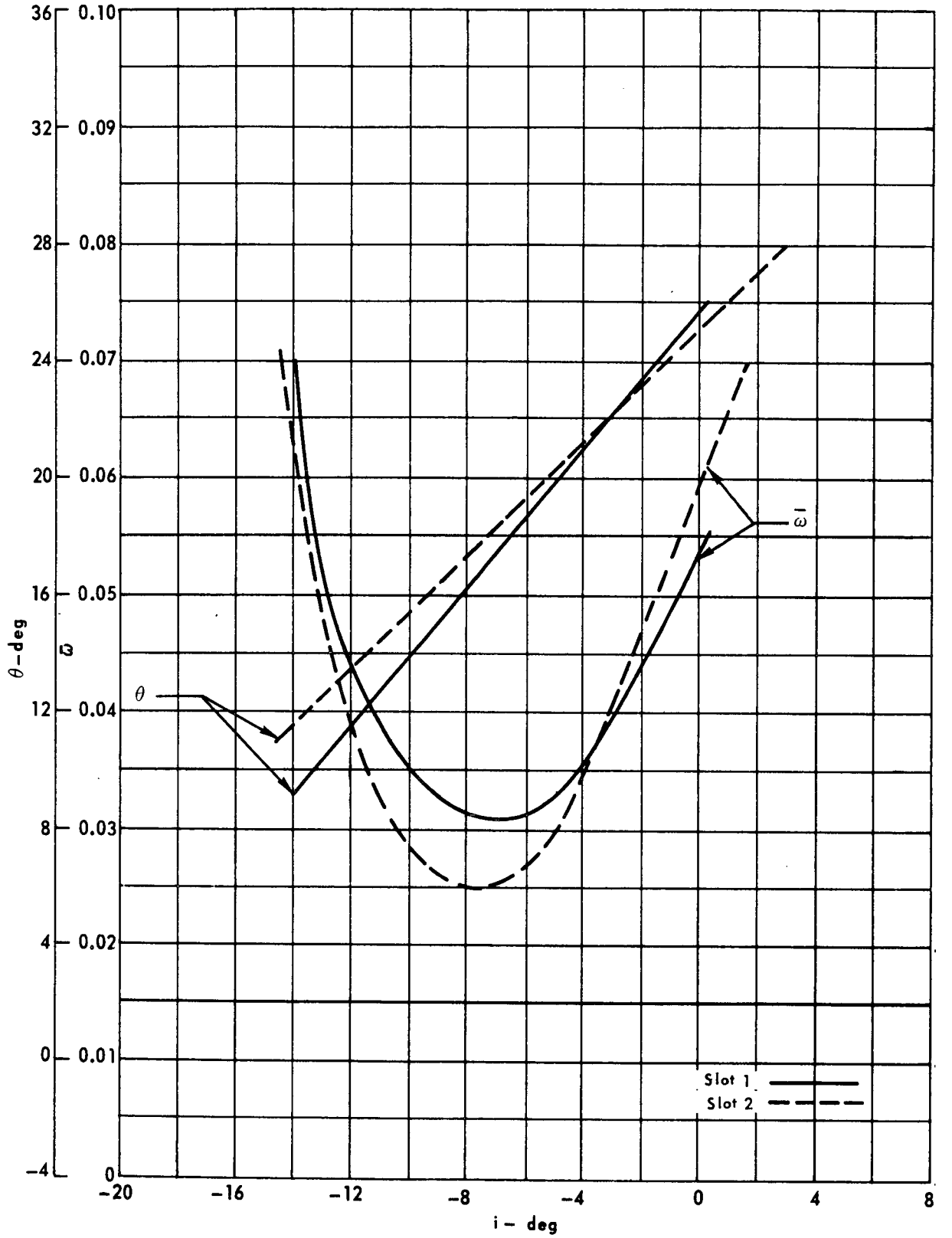

(h) Cascade configuration : $\beta_{1N} = 60$, $\sigma = 1.00$

Double circular-arc profile : $\phi = 45$, $t/c = 0.06$

Figure 15. – Continued.

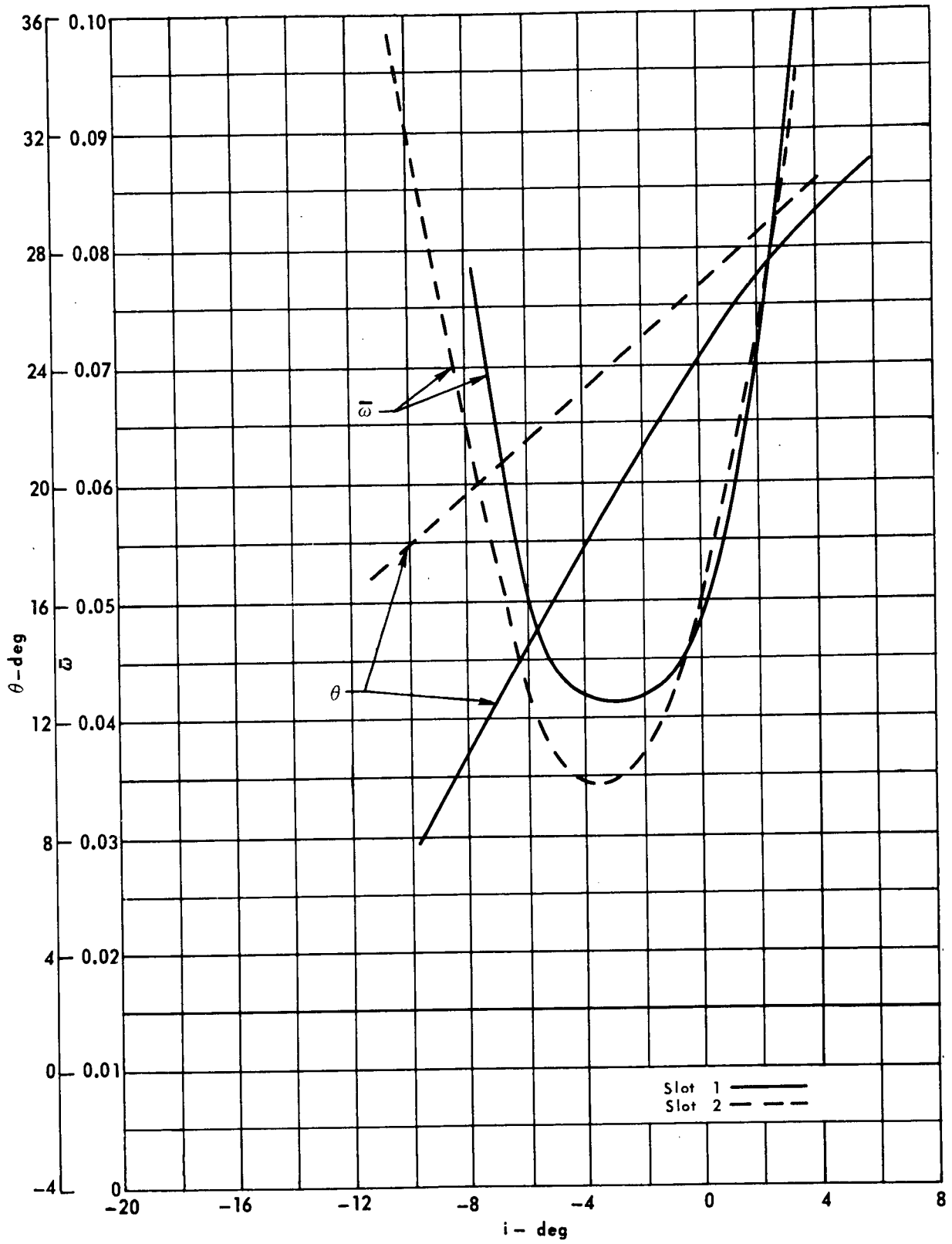

(i) Cascade configuration : $\beta_{1N} = 60$, $\sigma = 1.50$

Double circular–arc profile : $\phi = 45$, $t/c = 0.06$

Figure 15. – Concluded.

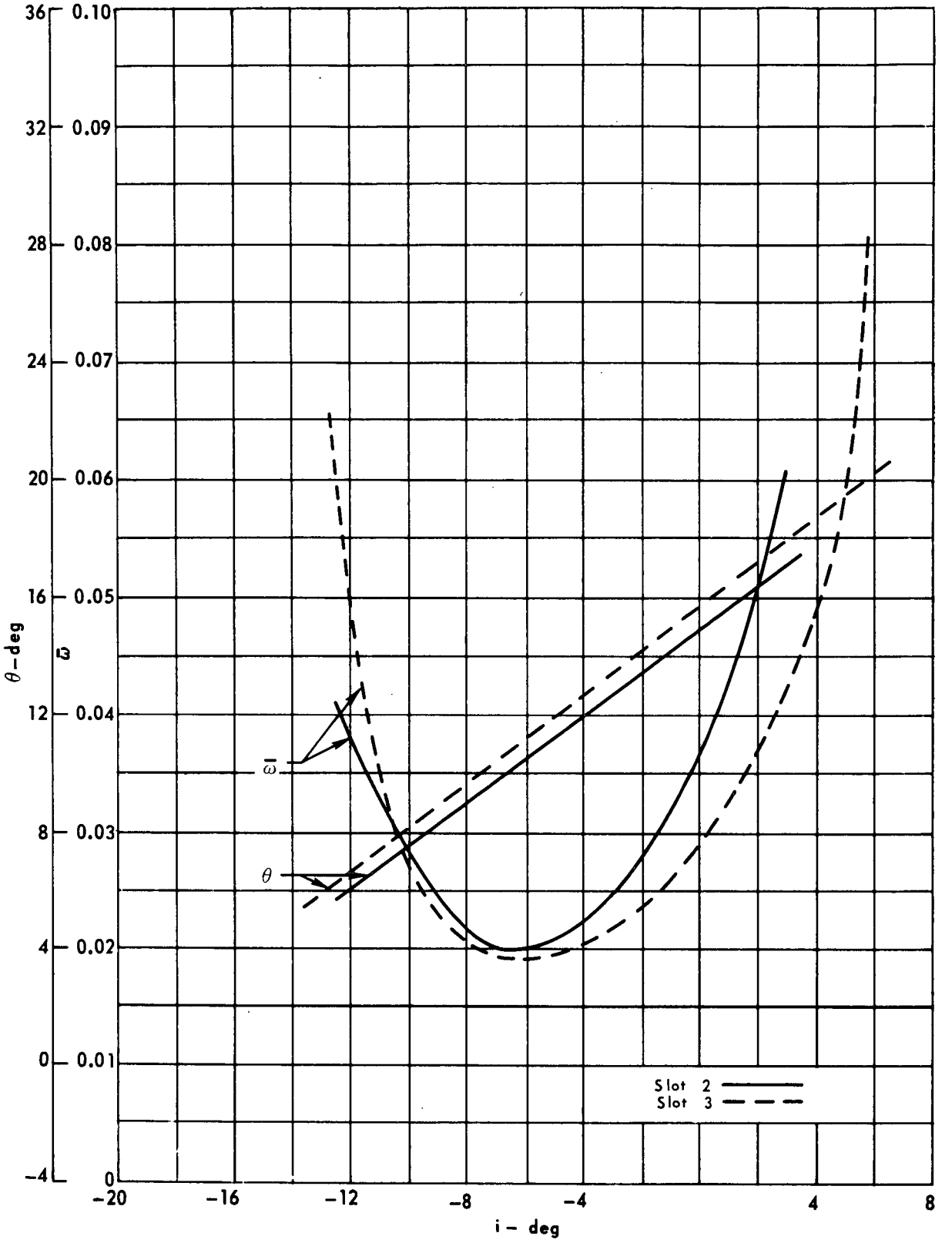

(a) Cascade configuration : $\beta_{1N} = 60$, $\sigma = 0.75$

Double circular–arc profile : $\phi = 30$, $t/c = 0.06$

Figure 16. – Slot geometry effect.

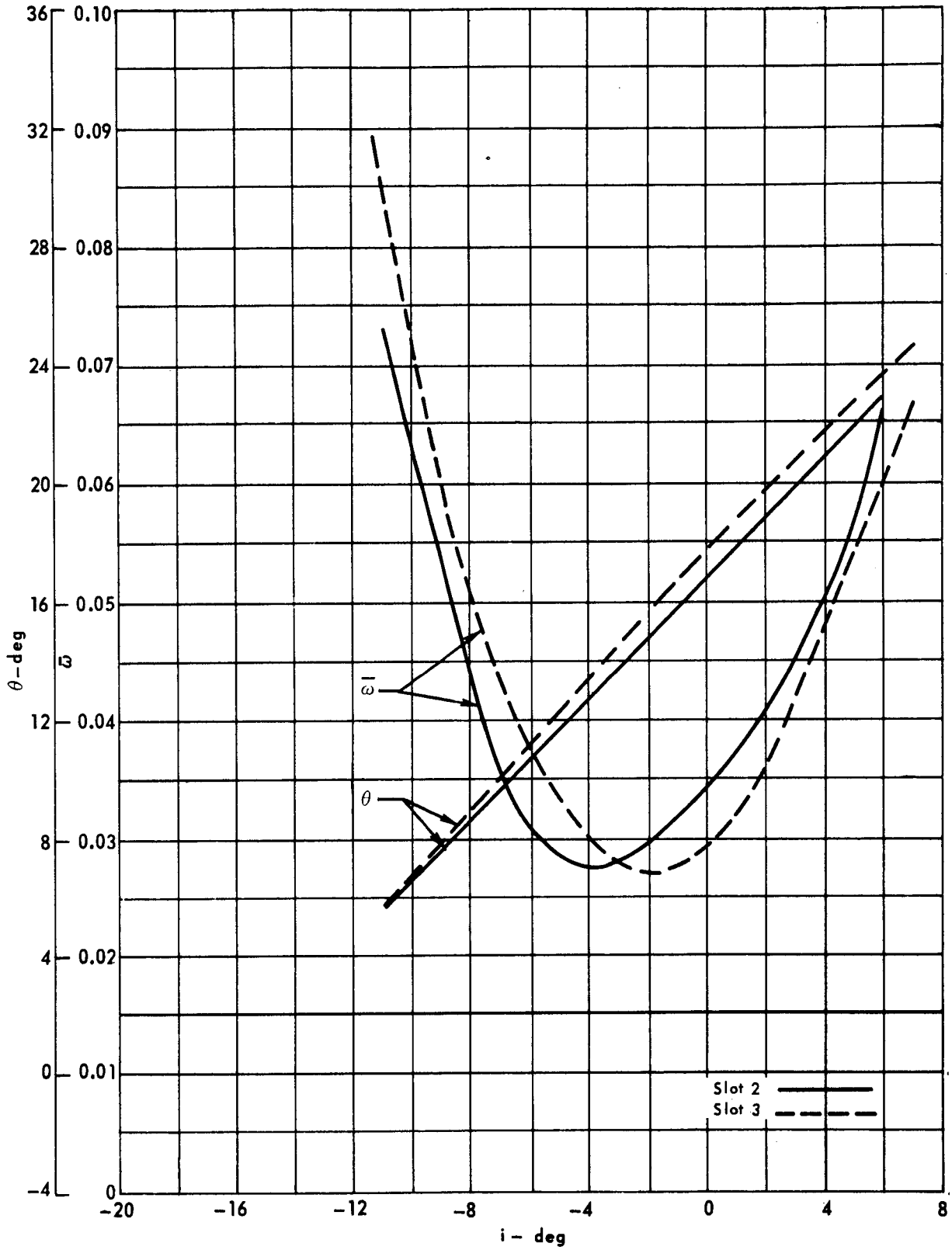

Cascade configuration : $\beta_{1N} = 60$, $\sigma = 1.00$

(b)

Double circular-arc profile : $\phi = 30$, $t/c = 0.06$

Figure 16. – Continued.

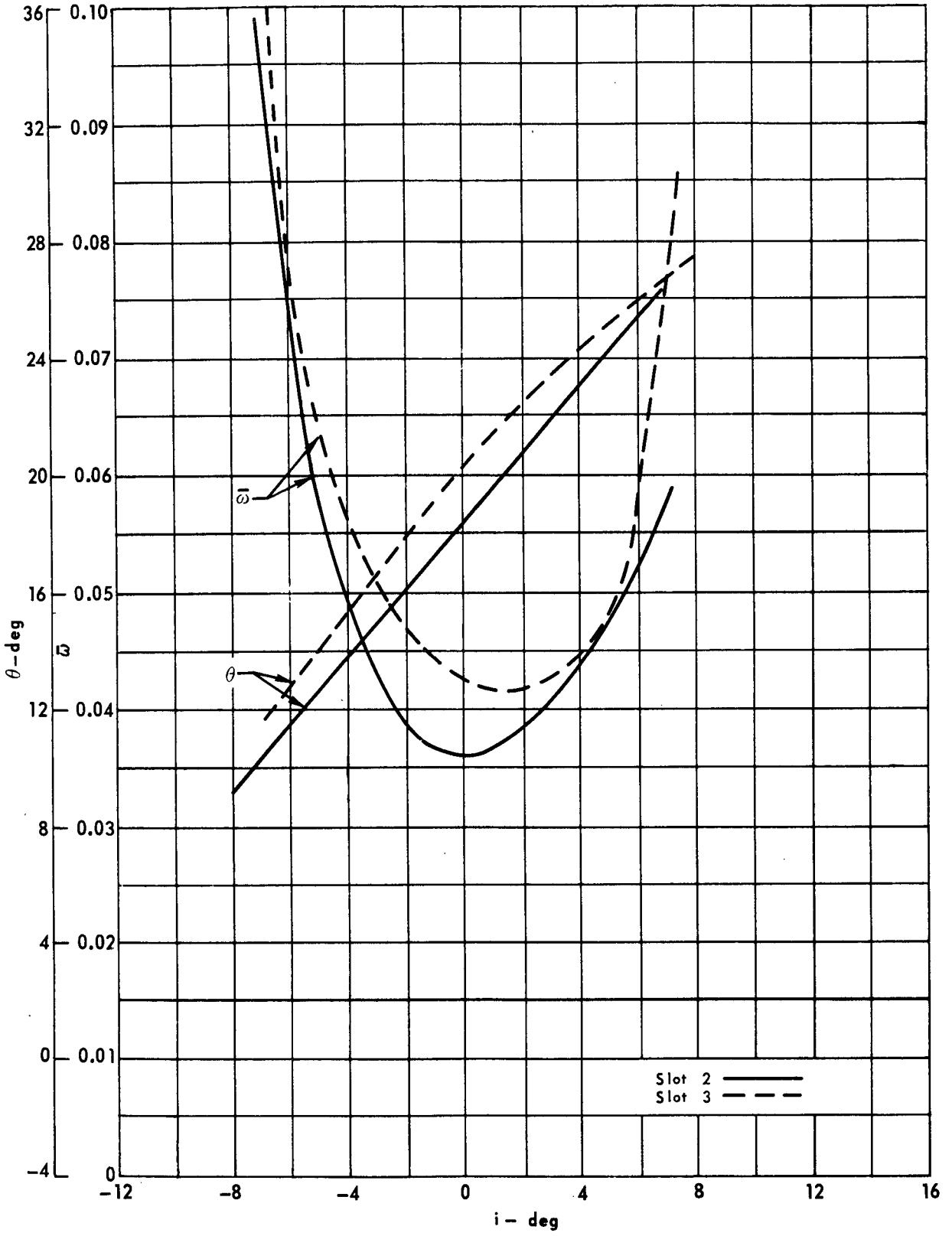

(c) Cascade configuration : $\beta_{1N} = 60$, $\sigma = 1.50$

Double circular–arc profile : $\phi = 30$, t/c =0.06

Figure 16. – Continued.

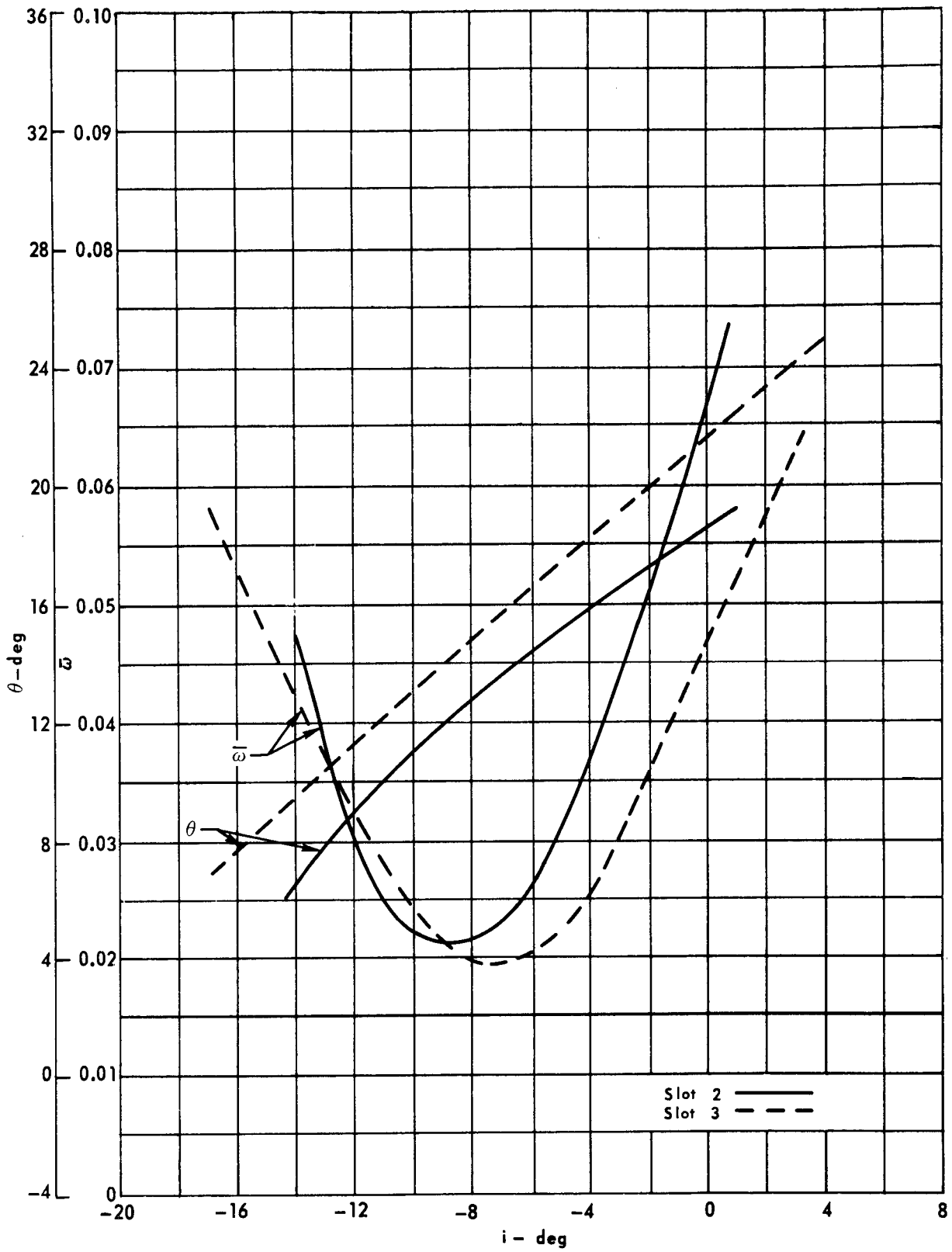

(d) Cascade configuration : $\beta_{1N} = 60$, $\sigma = 0.75$

Double circular-arc profile : $\phi = 40$, $t/c = 0.06$

Figure 16. – Continued.

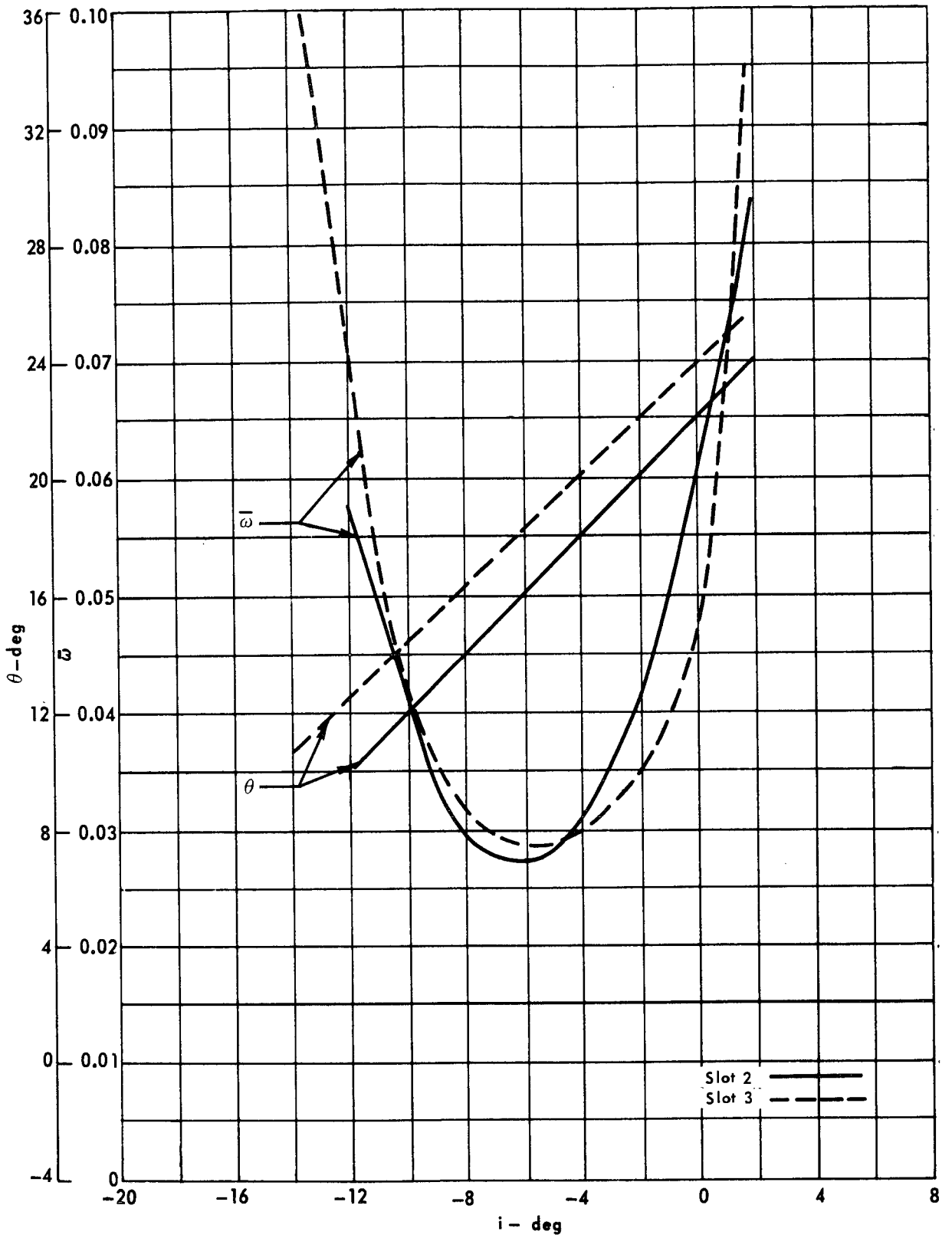

(e) Cascade configuration : $\beta_{1N} = 60$, $\sigma = 1.00$

Double circular–arc profile : $\phi = 40$, t/c = 0.06

Figure 16. – Continued.

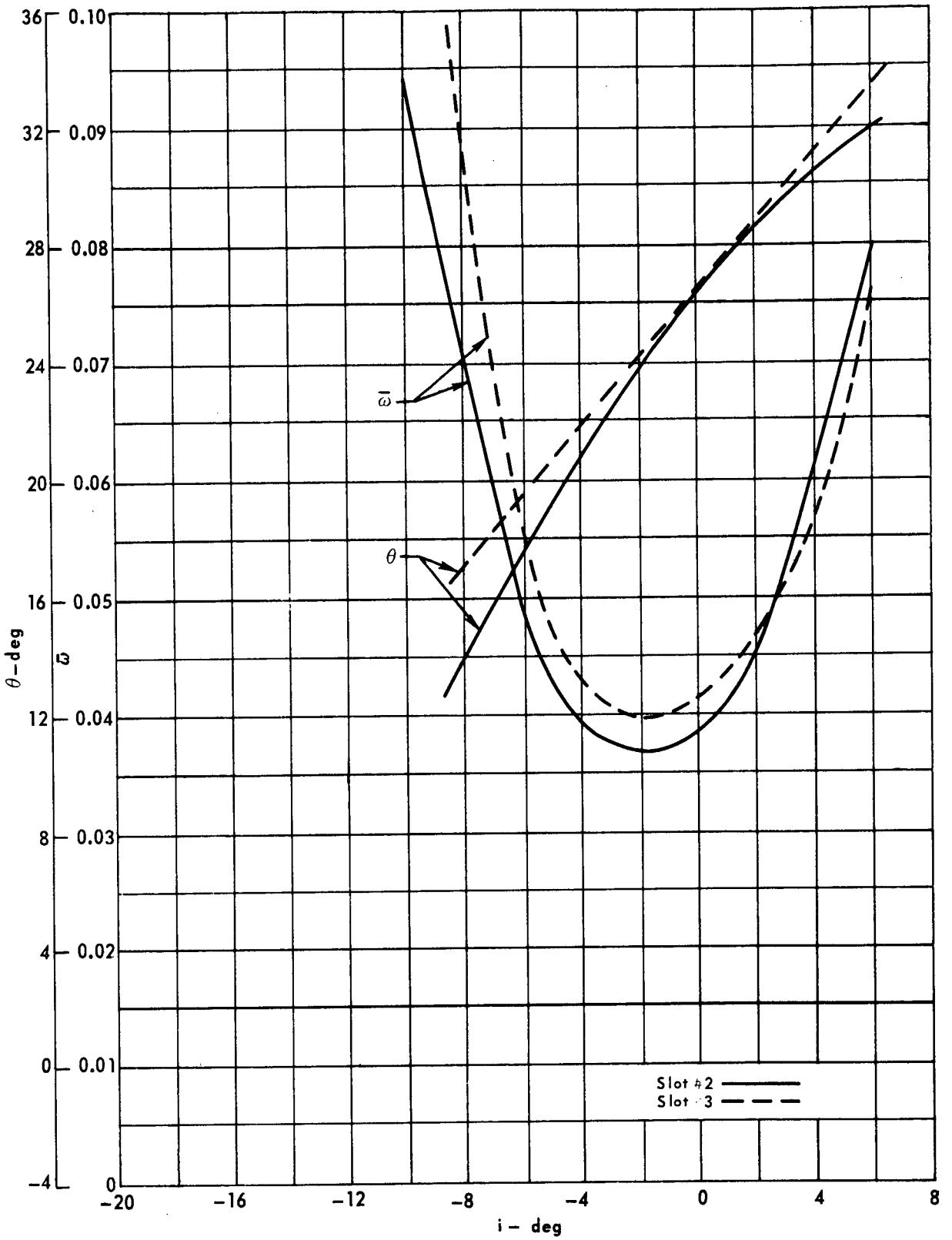

(f) Cascade configuration : $\beta_{1N} = 60$, $\sigma = 1.50$

Double circular-arc profile : $\phi = 40$, $t/c = 0.06$

Figure 16. – Continued.

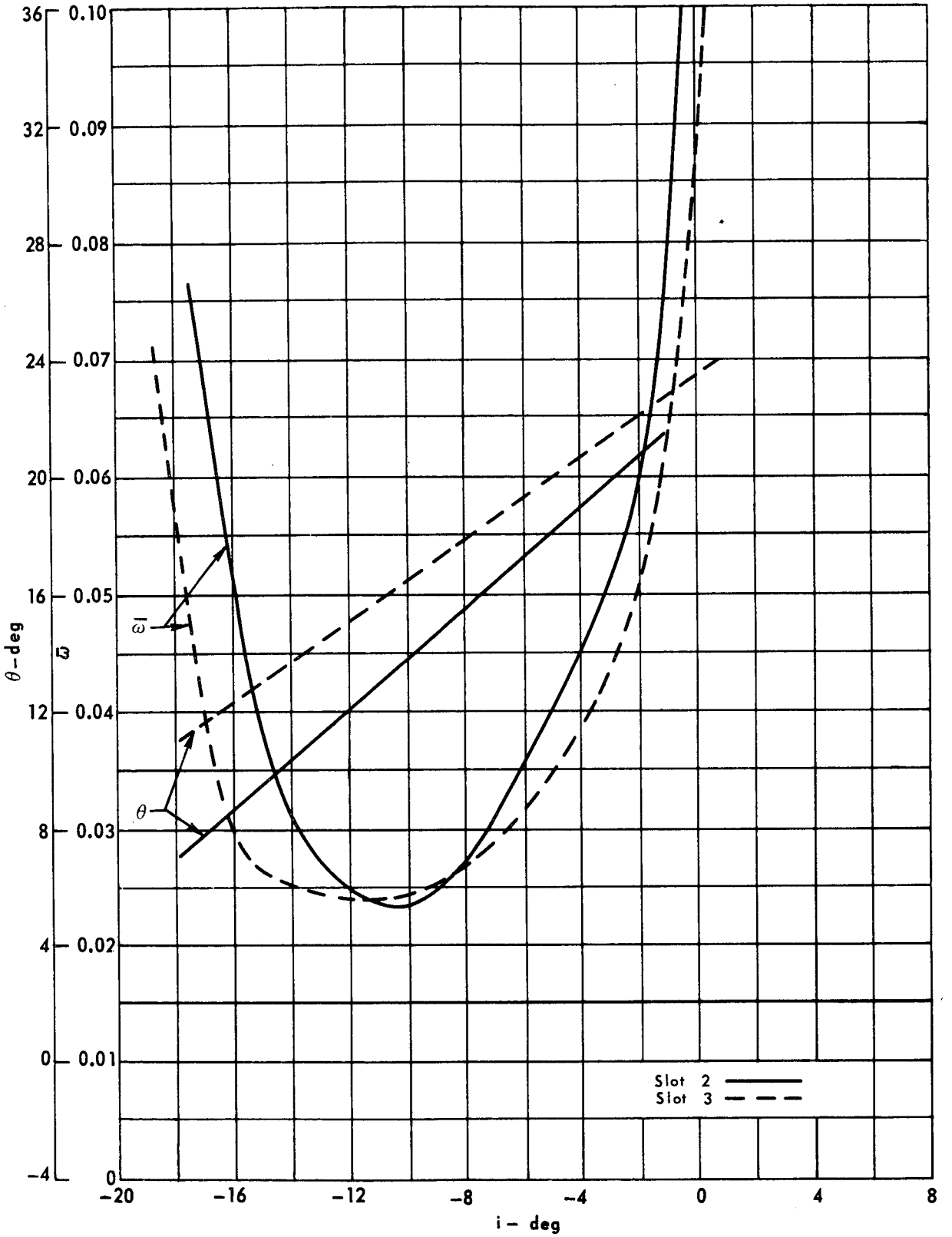

(g) Cascade configuration : $\beta_{1N} = 60$, $\sigma = 0.75$

Double circular-arc profile : $\phi = 45$, $t/c = 0.06$

Figure 16. – Continued.

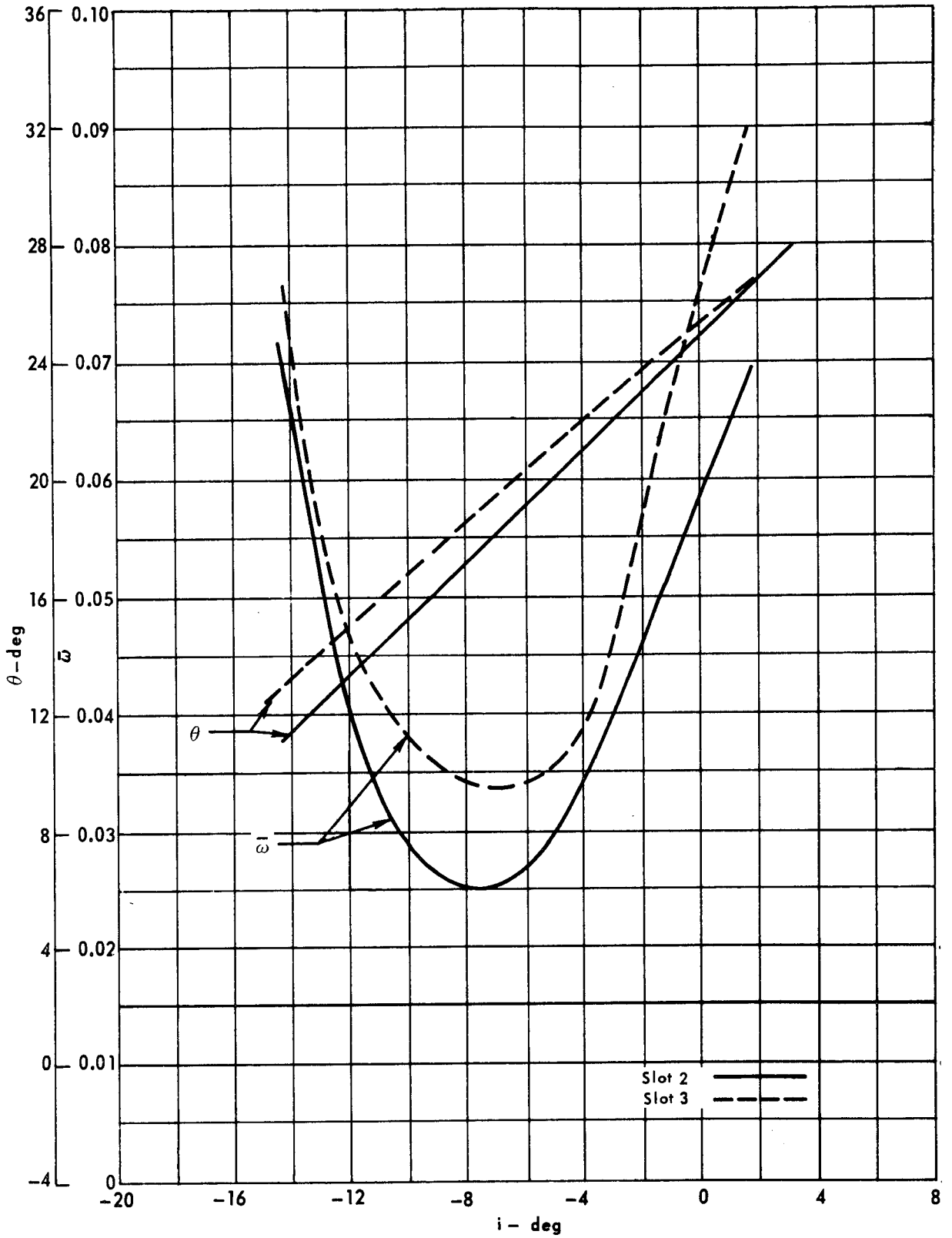

(h) Cascade configuration : $\beta_{1N} = 60$, $\sigma = 1.00$

Double circular–arc profile : $\phi = 45$, $t/c = 0.06$

Figure 16. – Continued.

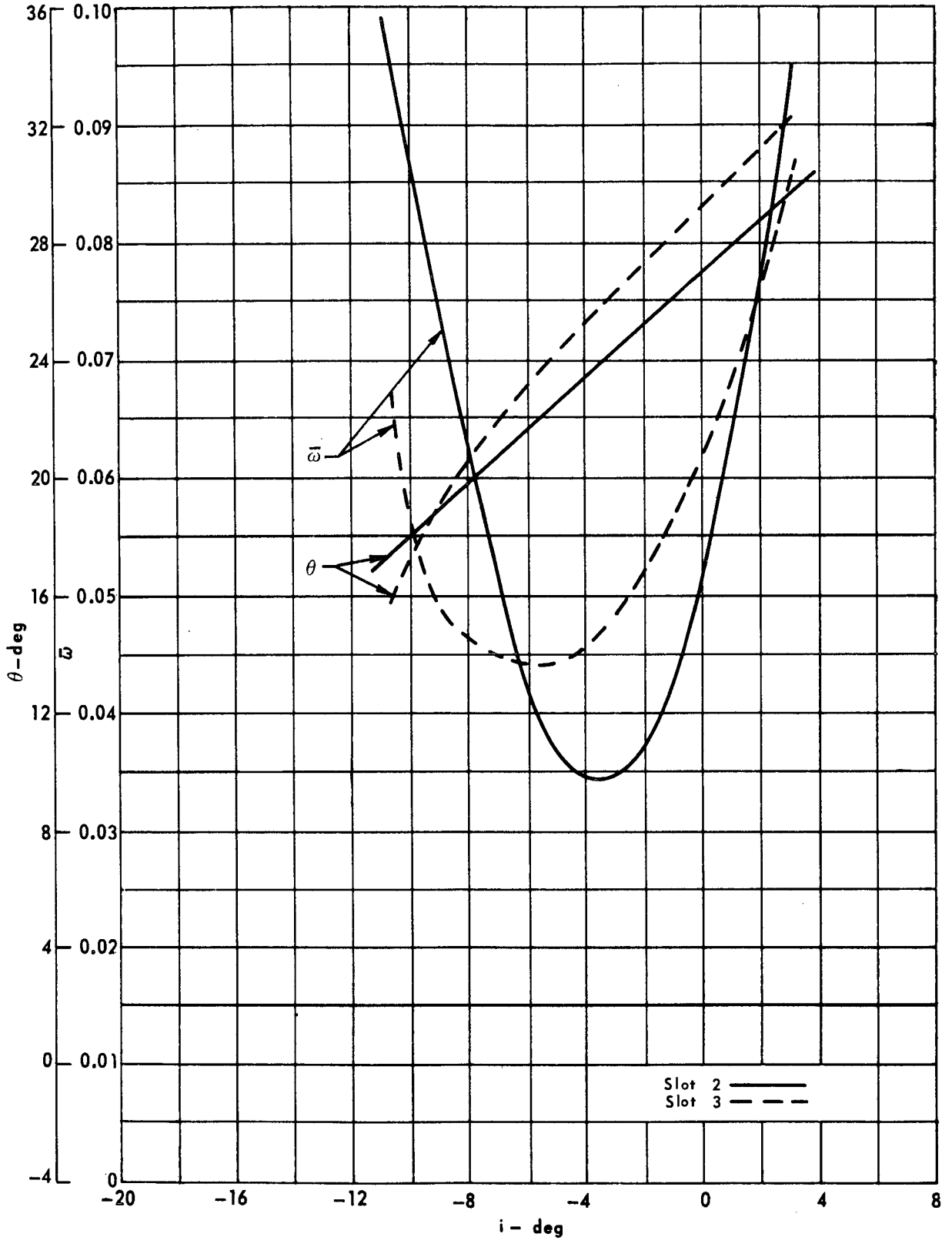

(i) Cascade configuration : $\beta_{1N} = 60$, $\sigma = 1.50$

Double circular–arc profile : $\phi = 45$, $t/c = 0.06$

Figure 16. – Concluded.

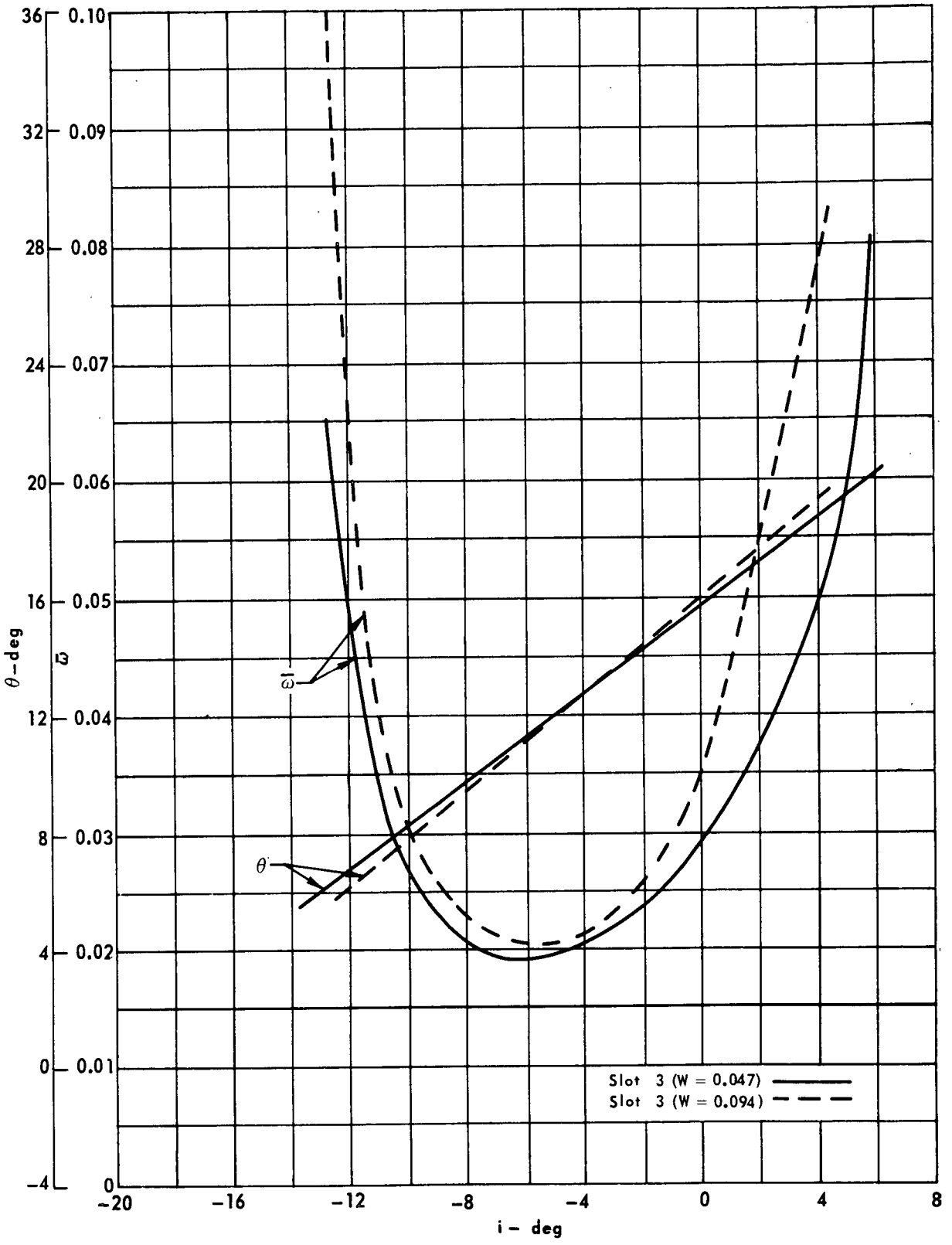

(a) Cascade configuration : $\beta_{1N} = 60$, $\sigma = 0.75$

Double circular-arc profile : $\phi = 30$, $t/c = 0.06$

Figure 17. – Slot width effect.

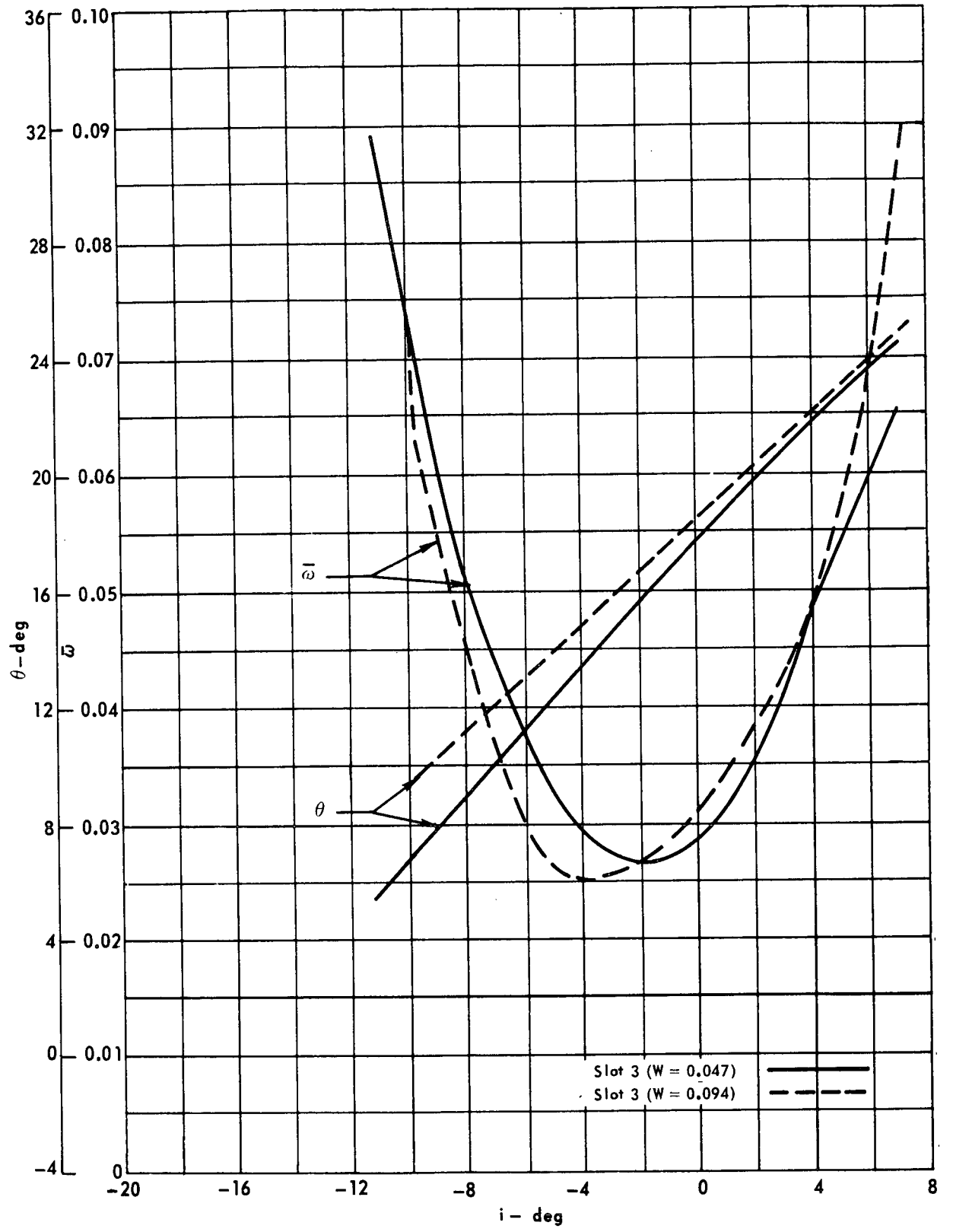

(b) Cascade configuration : $\beta_{1N} = 60$, $\sigma = 1.00$

Double circular-arc profile : $\phi = 30$, $t/c = 0.06$

Figure 17. – Continued.

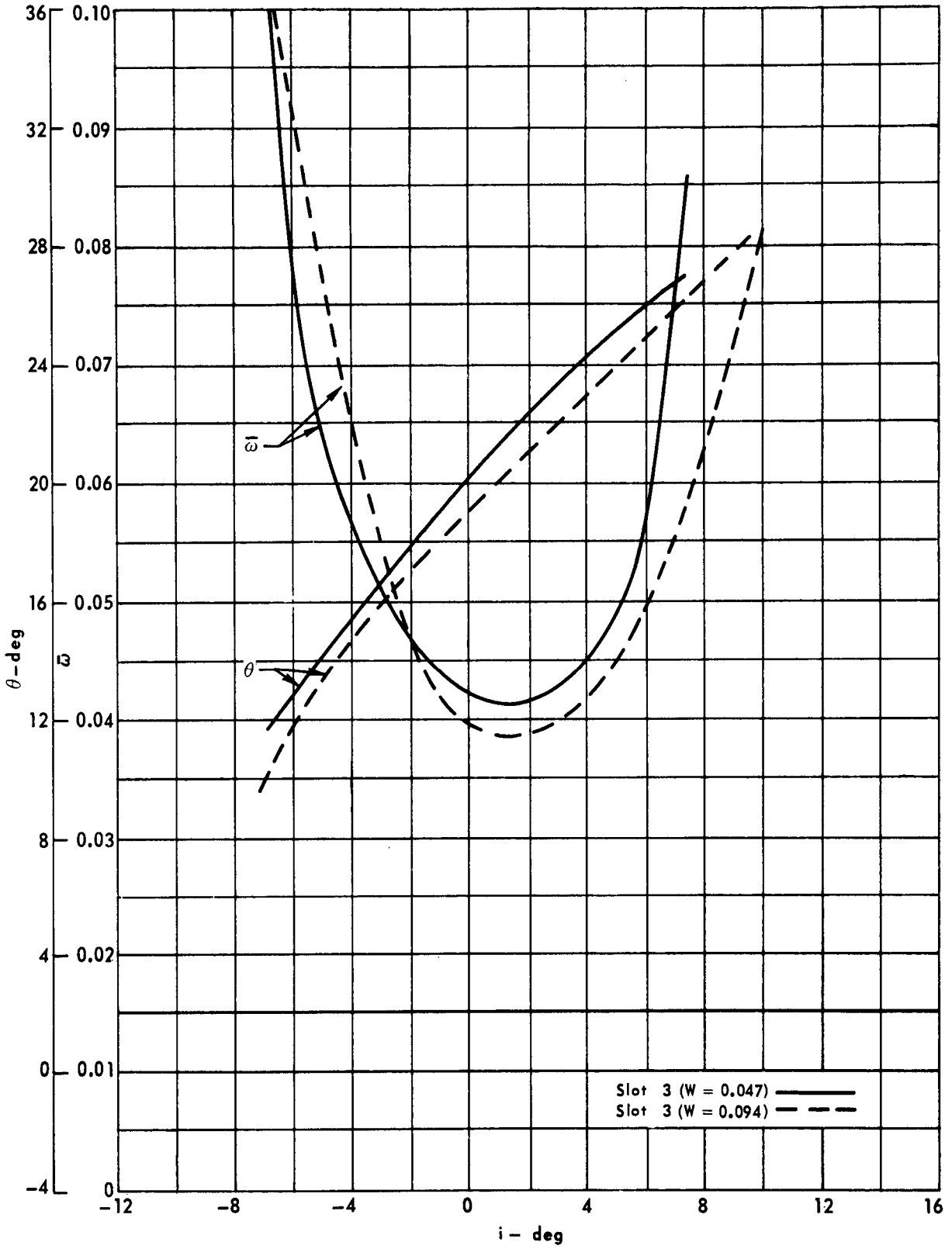

(c) Cascade configuration : $\beta_{1N} = 60$, $\sigma = 1.50$

Double circular-arc profile : $\phi = 30$, $t/c = 0.06$

Figure 17. – Continued.

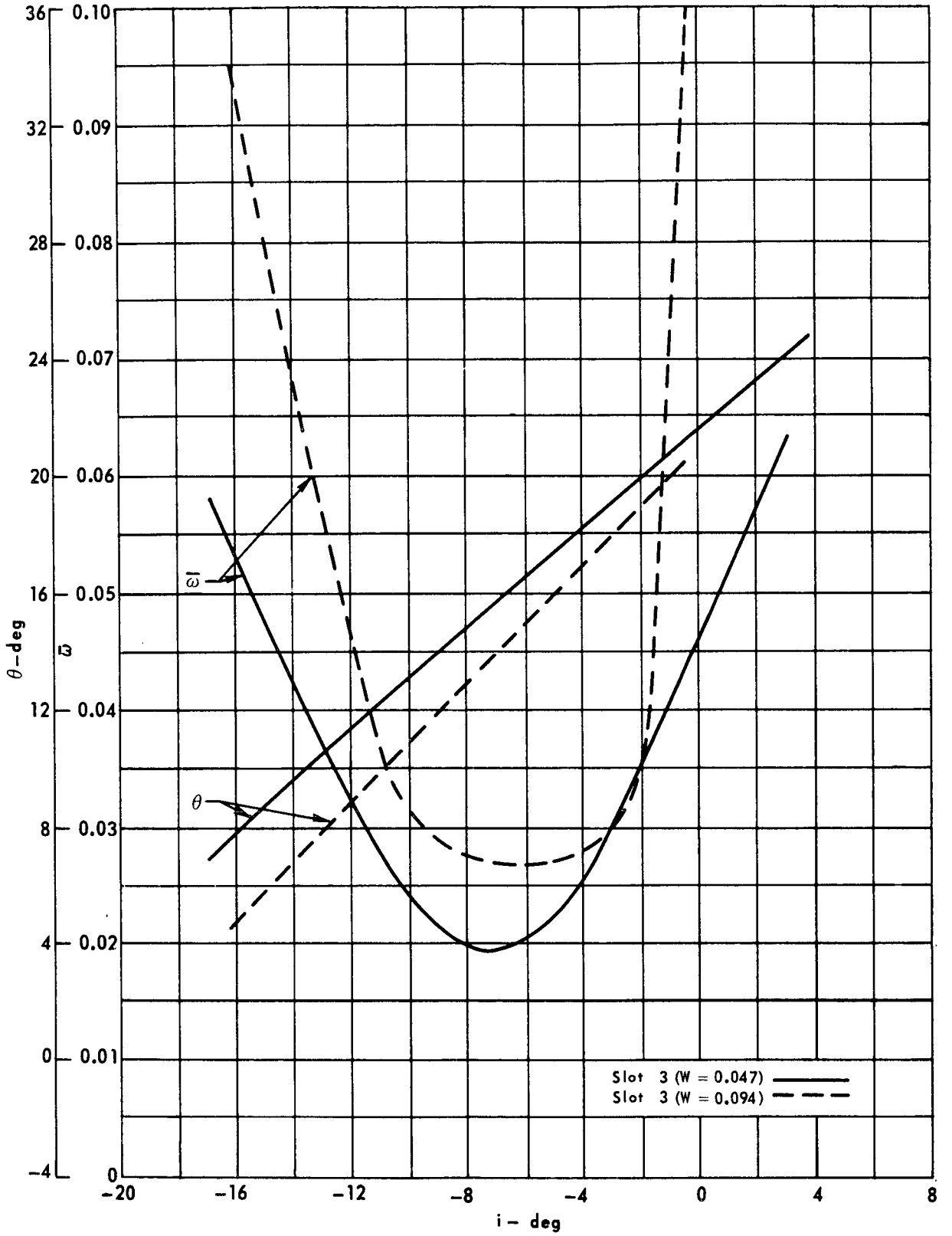

(d) Cascade configuration : $\beta_{1N} = 60$, $\sigma = 0.75$

Double circular-arc profile : $\phi = 40$, t/c = 0.06

Figure 17. – Continued.

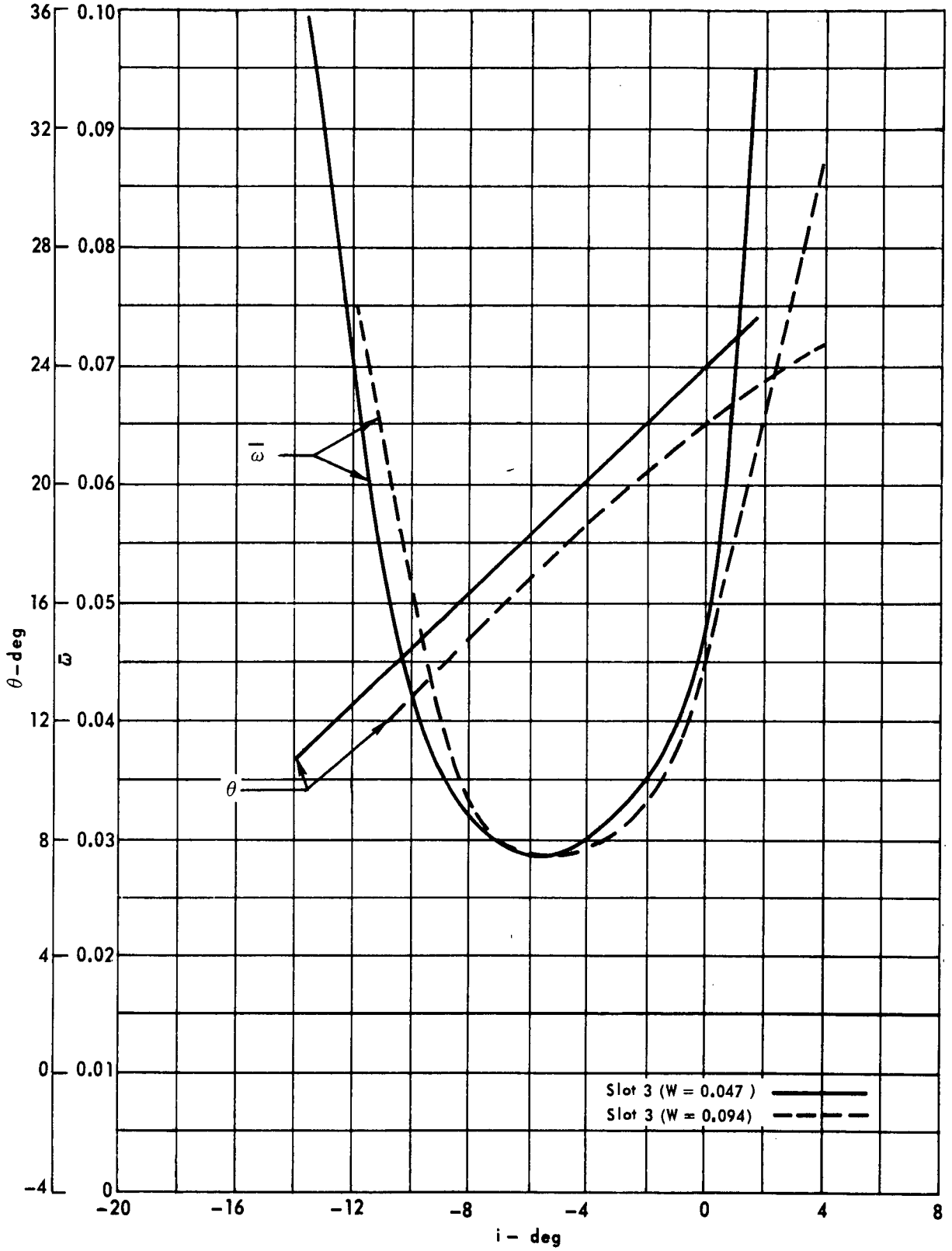

(e) Cascade configuration : $\beta_{1N} = 60$, $\sigma = 1.00$

Double circular-arc profile : $\phi = 40$, $t/c = 0.06$

Figure 17. – Continued.

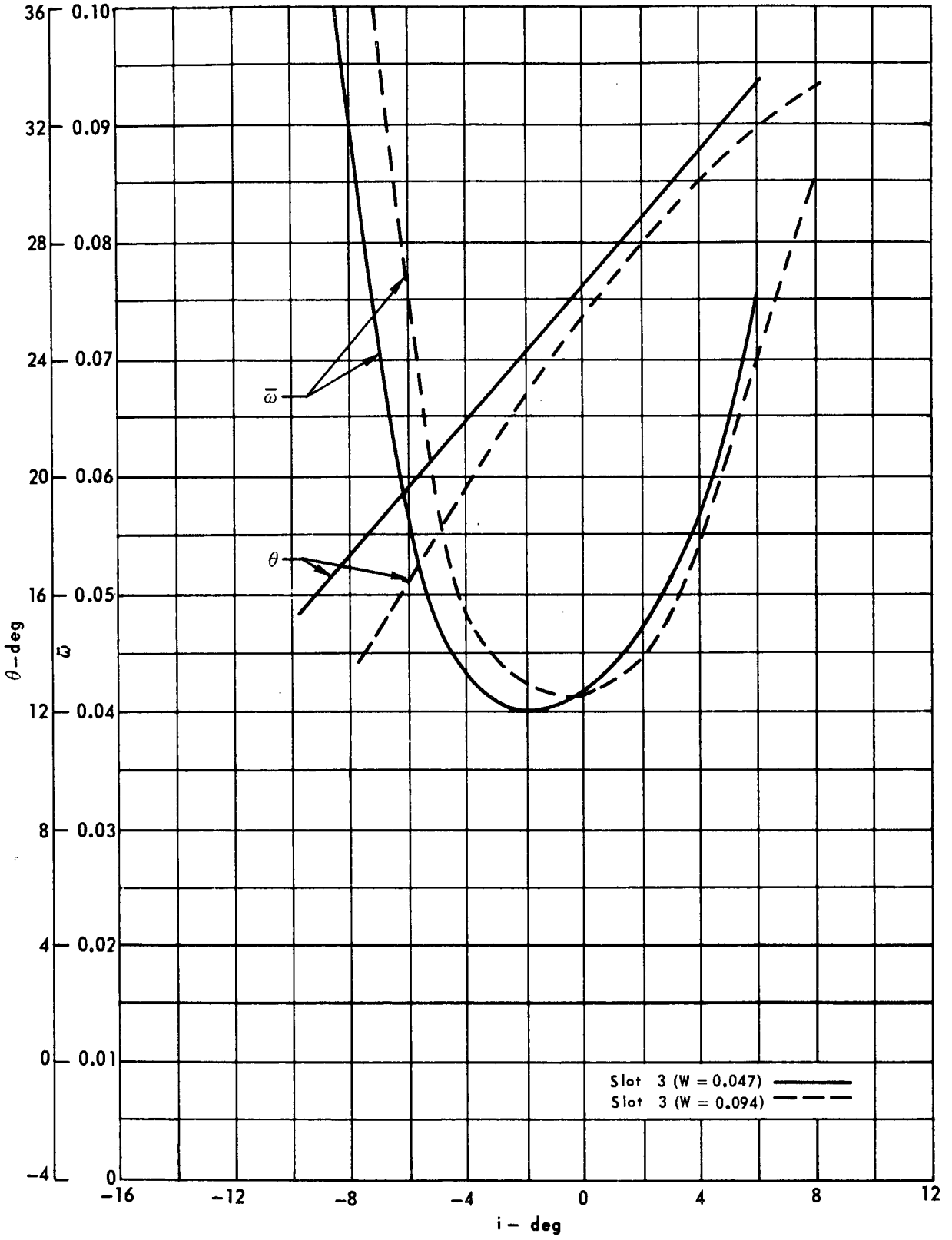

(f) Cascade configuration : $\beta_{1N} = 60$, $\sigma = 1.50$

Double circular-arc profile : $\phi = 40$, $t/c = 0.06$

Figure 17. – Continued.

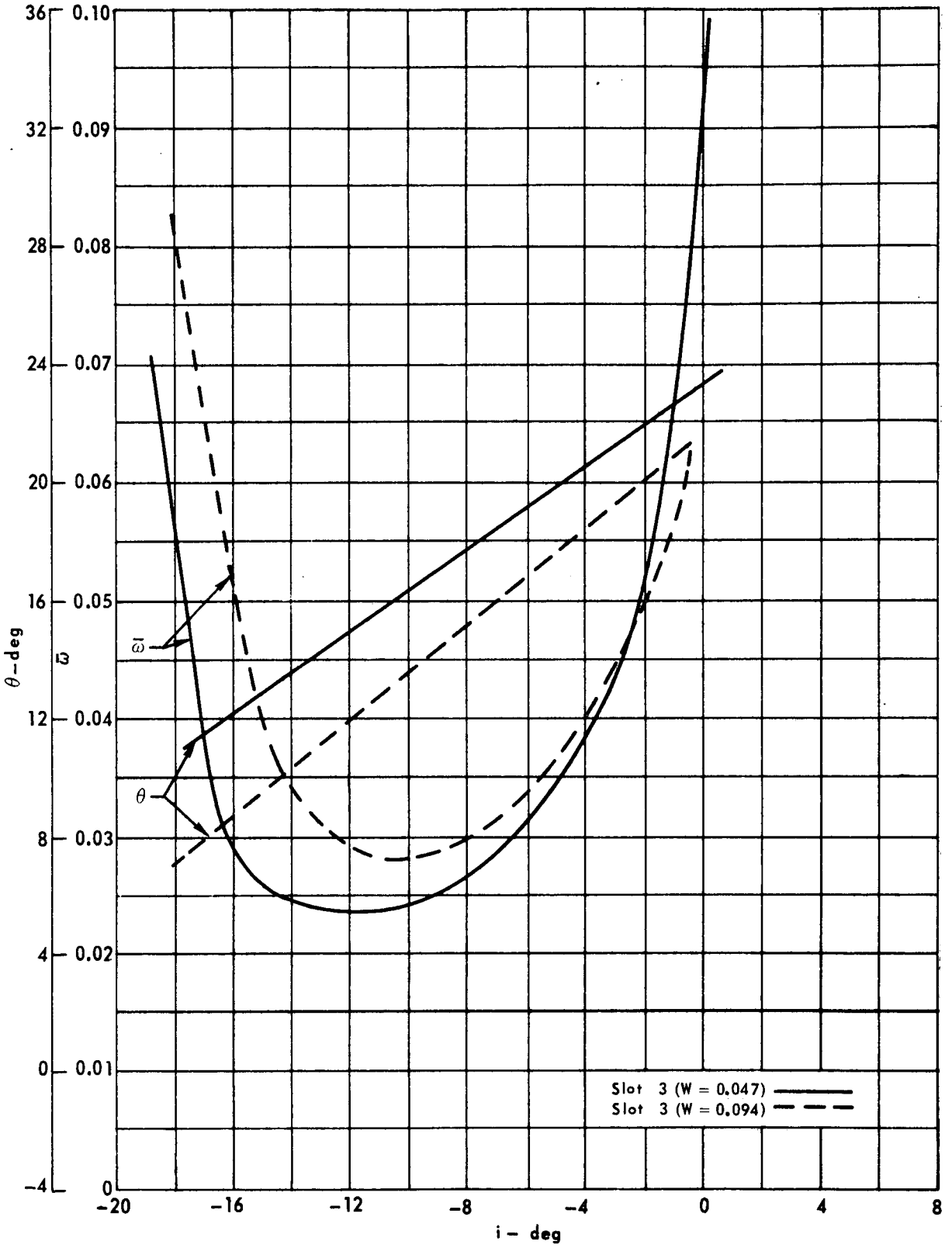

(g) Cascade configuration : $\beta_{1N} = 60$, $\sigma = 0.75$

Double circular-arc profile : $\phi = 45$, $t/c = 0.06$

Figure 17. – Continued.

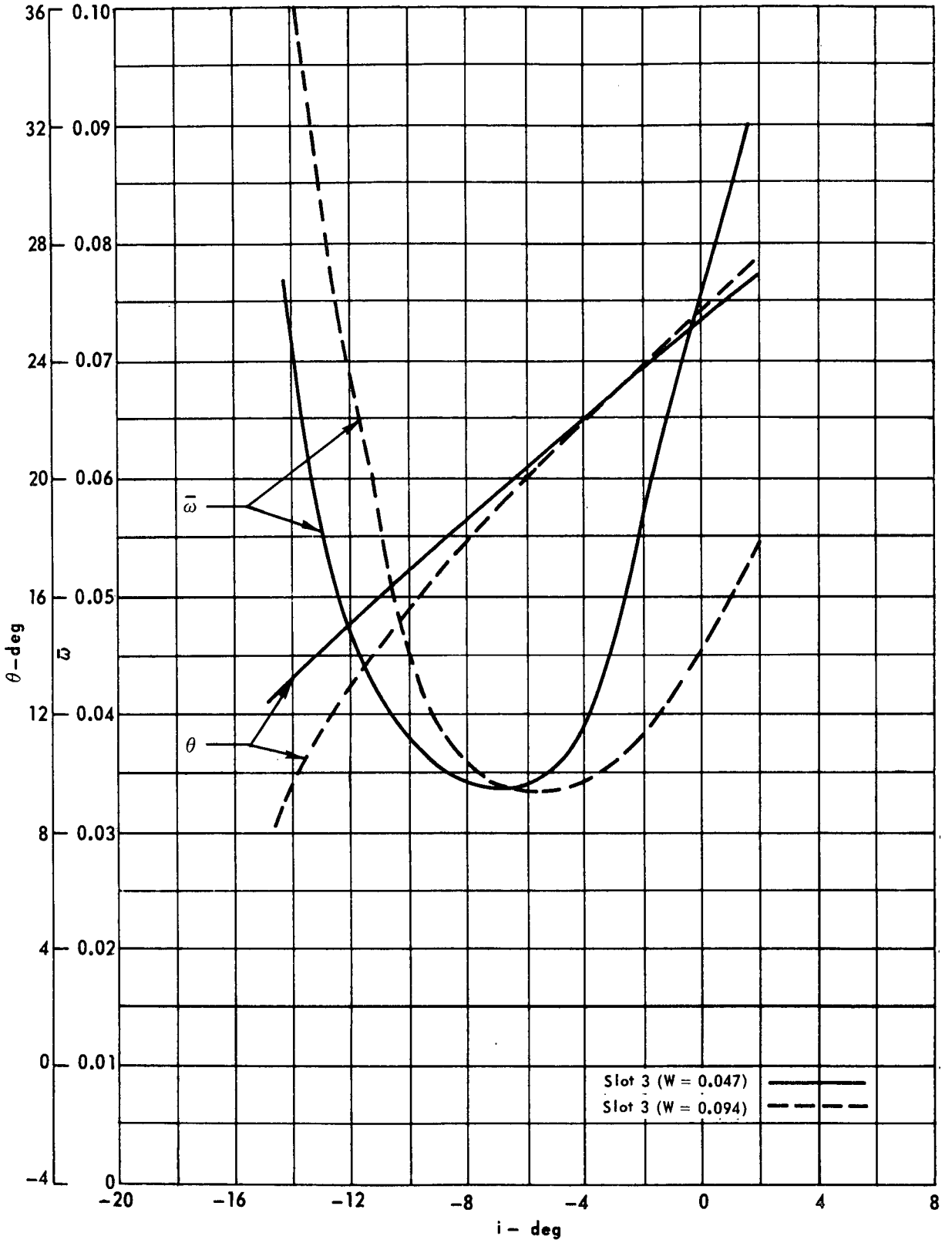

(h) Cascade configuration : $\beta_{1N} = 60$, $\sigma = 1.00$

Double circular-arc profile : $\phi = 45$, $t/c = 0.06$

Figure 17. – Continued.

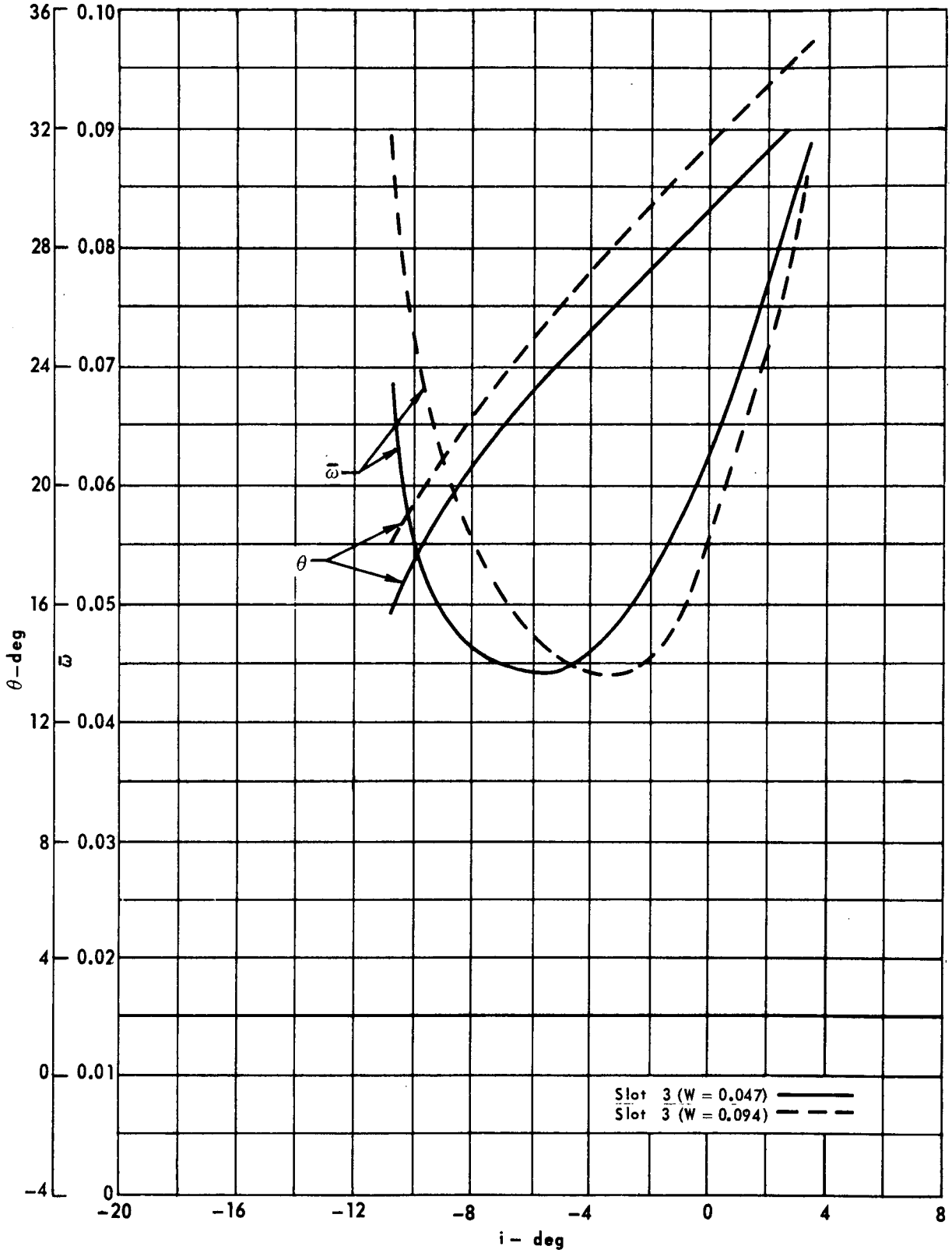

(i) Cascade configuration : $\beta_{1N} = 60$, $\sigma = 1.50$

Double circular–arc profile : $\phi = 45$, $t/c = 0.06$

Figure 17. – Concluded.

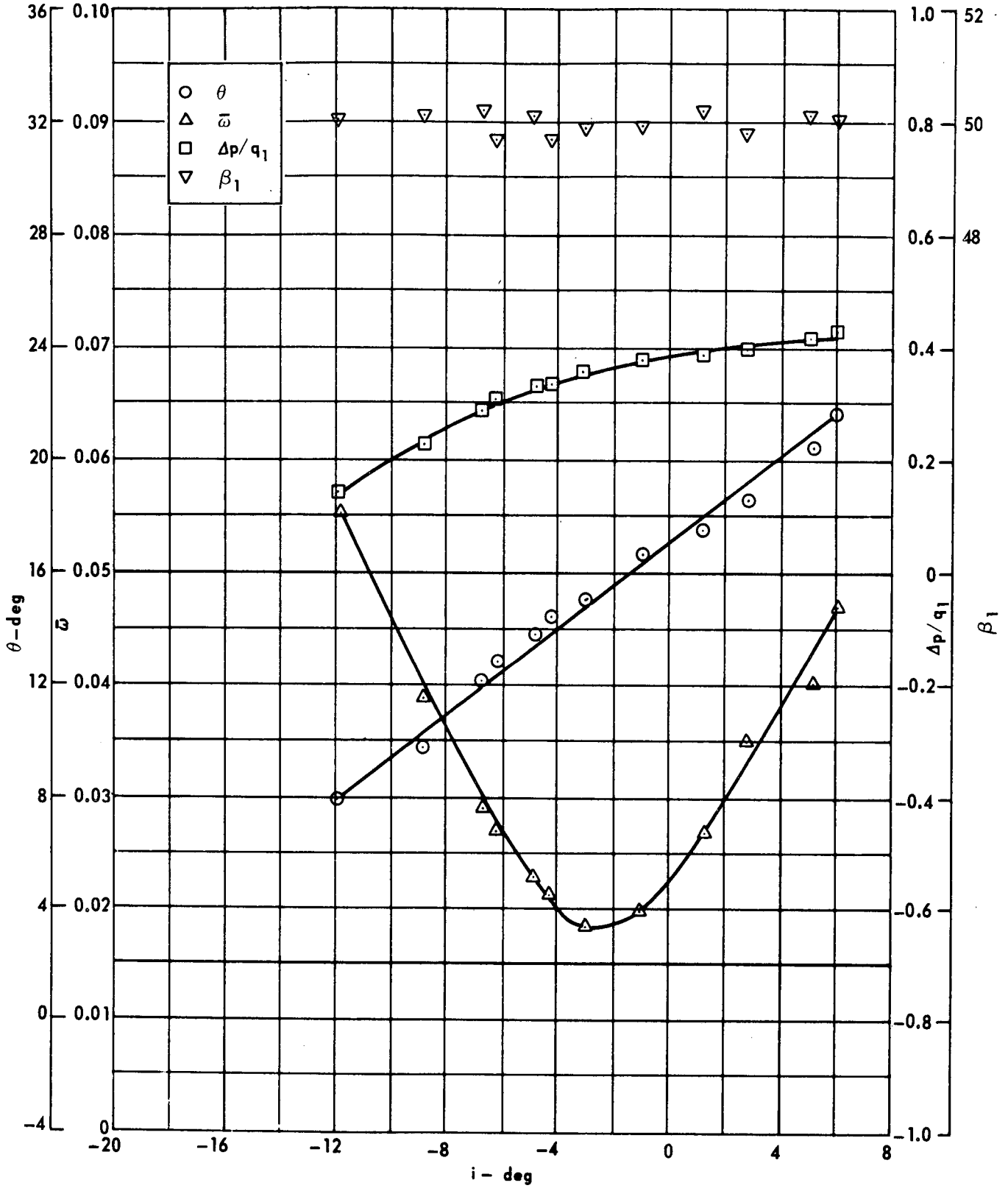

Cascade configuration : $\beta_{1N} = 50$, $\sigma = 0.75$

Double circular-arc profile : $\phi = 30$, $t/c = 0.06$

(a) $\theta, \bar{\omega}, \Delta p/q_1, \beta_1$

Figure 18. – Cascade characteristics as functions of incidence .

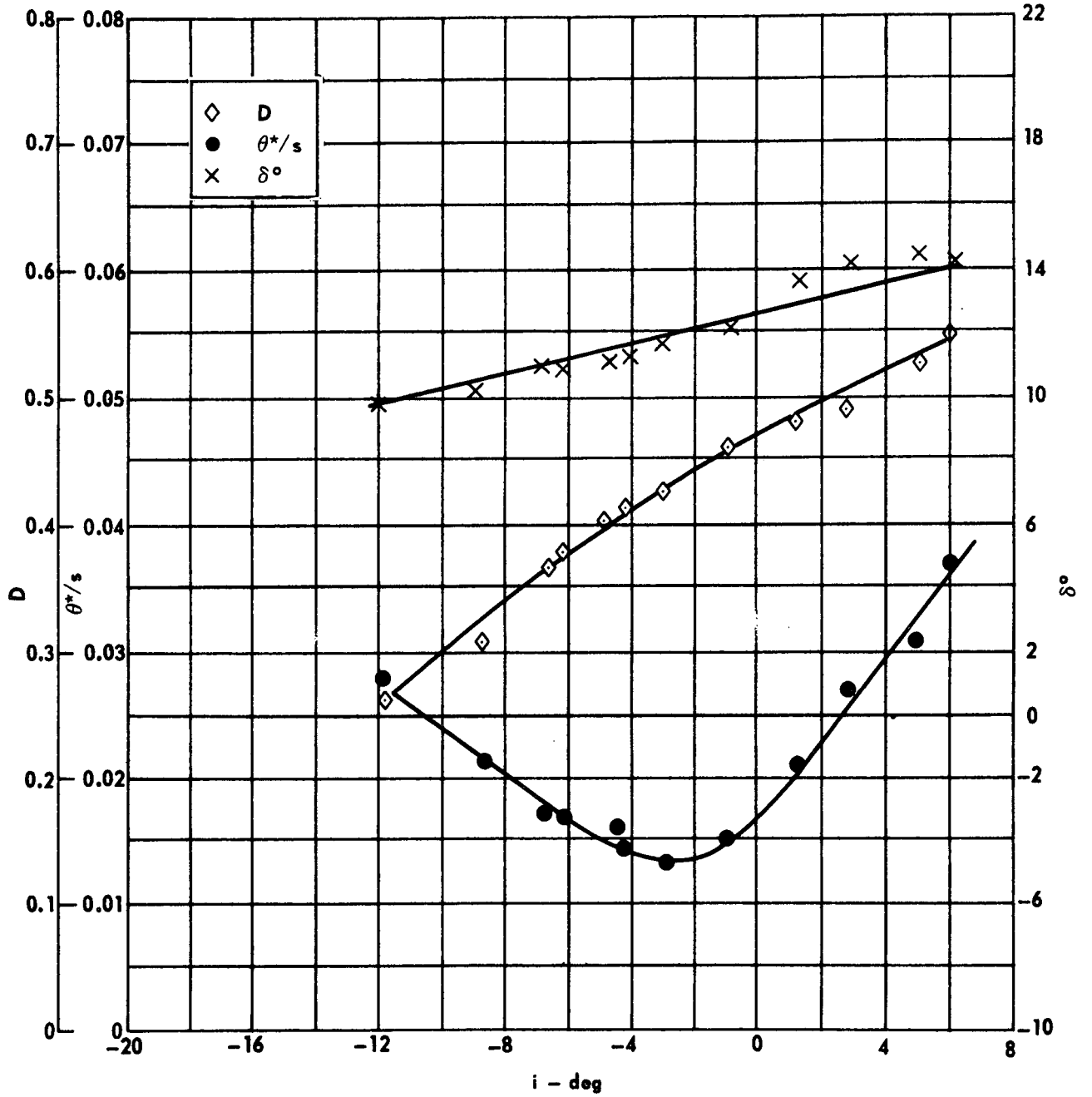

Cascade configuration : $\beta_{1N} = 50$, $\sigma = 0.75$

Double circular–arc profile : $\phi = 30$, $t/c = 0.06$

(b) D, θ^*/s, $\delta°$

Figure 18. – **Concluded.**

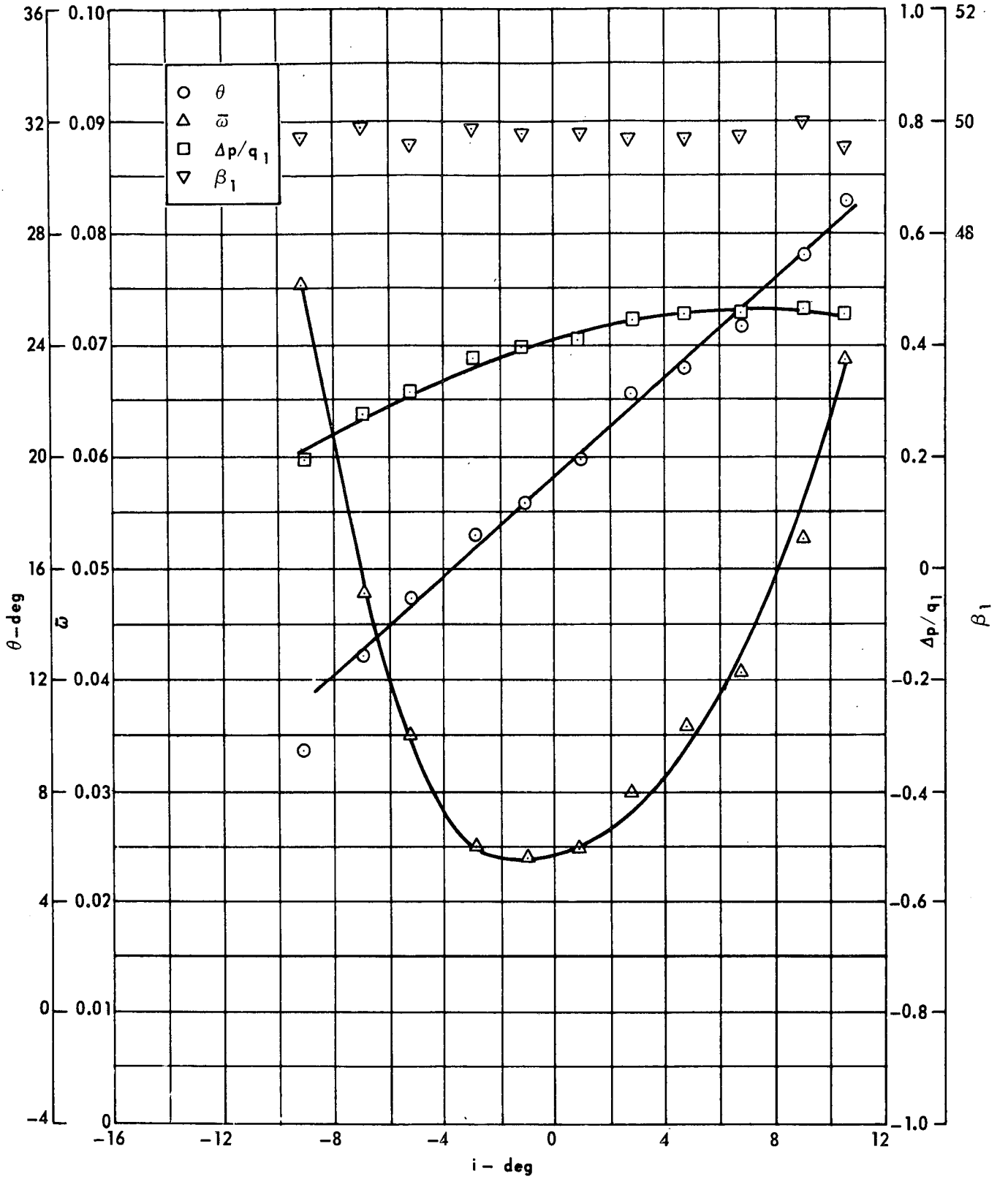

Cascade configuration : $\beta_{1N} = 50$, $\sigma = 1.00$

Double circular–arc profile : $\phi = 30$, $t/c = 0.06$

(a) $\theta, \bar{\omega}, \Delta p/q_1, \beta_1$

Figure 19. – Cascade characteristics as functions of incidence .

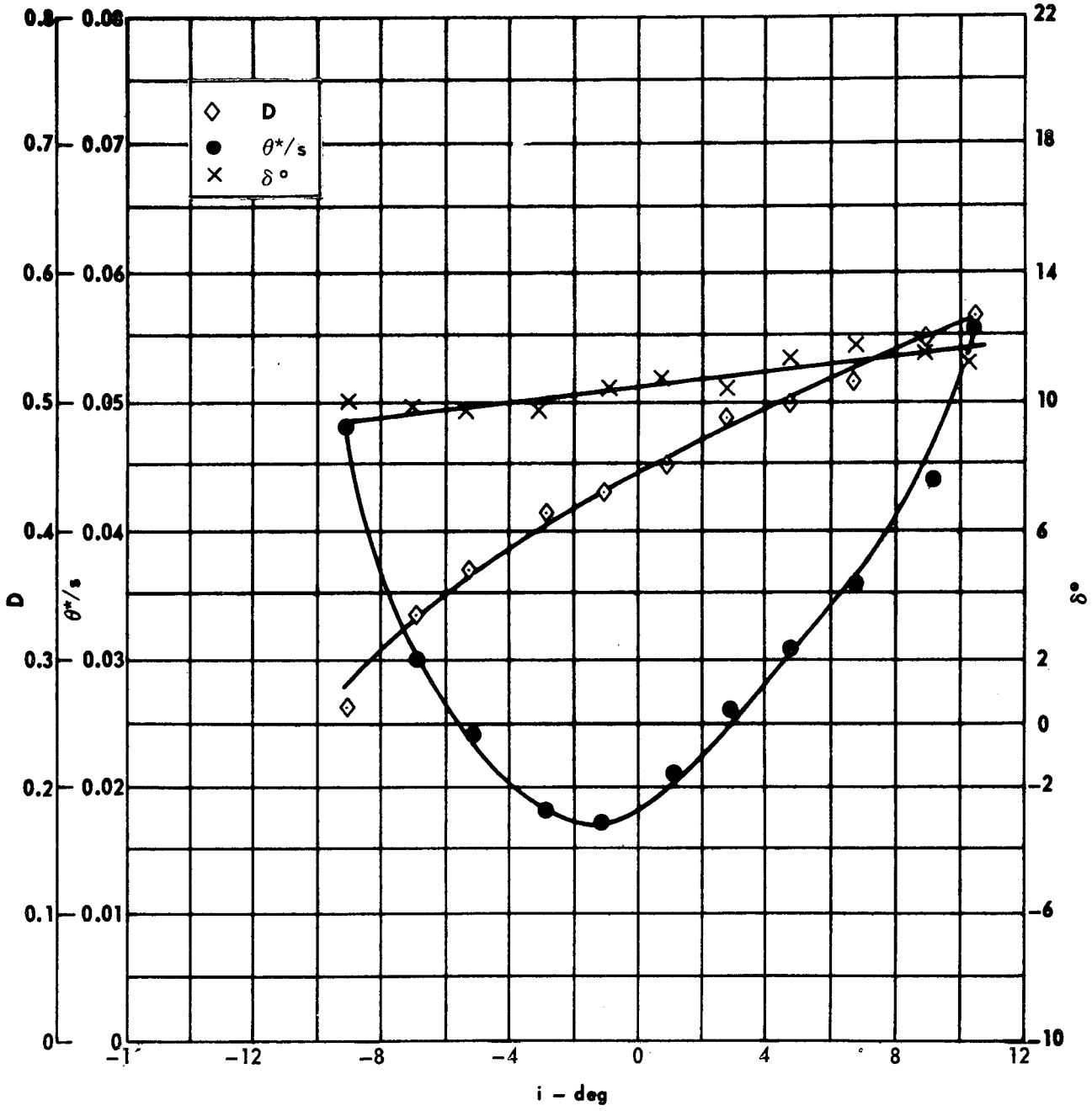

Cascade configuration : $\beta_{1N} = 50$, $\sigma = 1.00$

Double circular-arc profile : $\phi = 30$, $t/c = 0.06$

(b) D, θ^*/s, δ°

Figure 19. – **Concluded.**

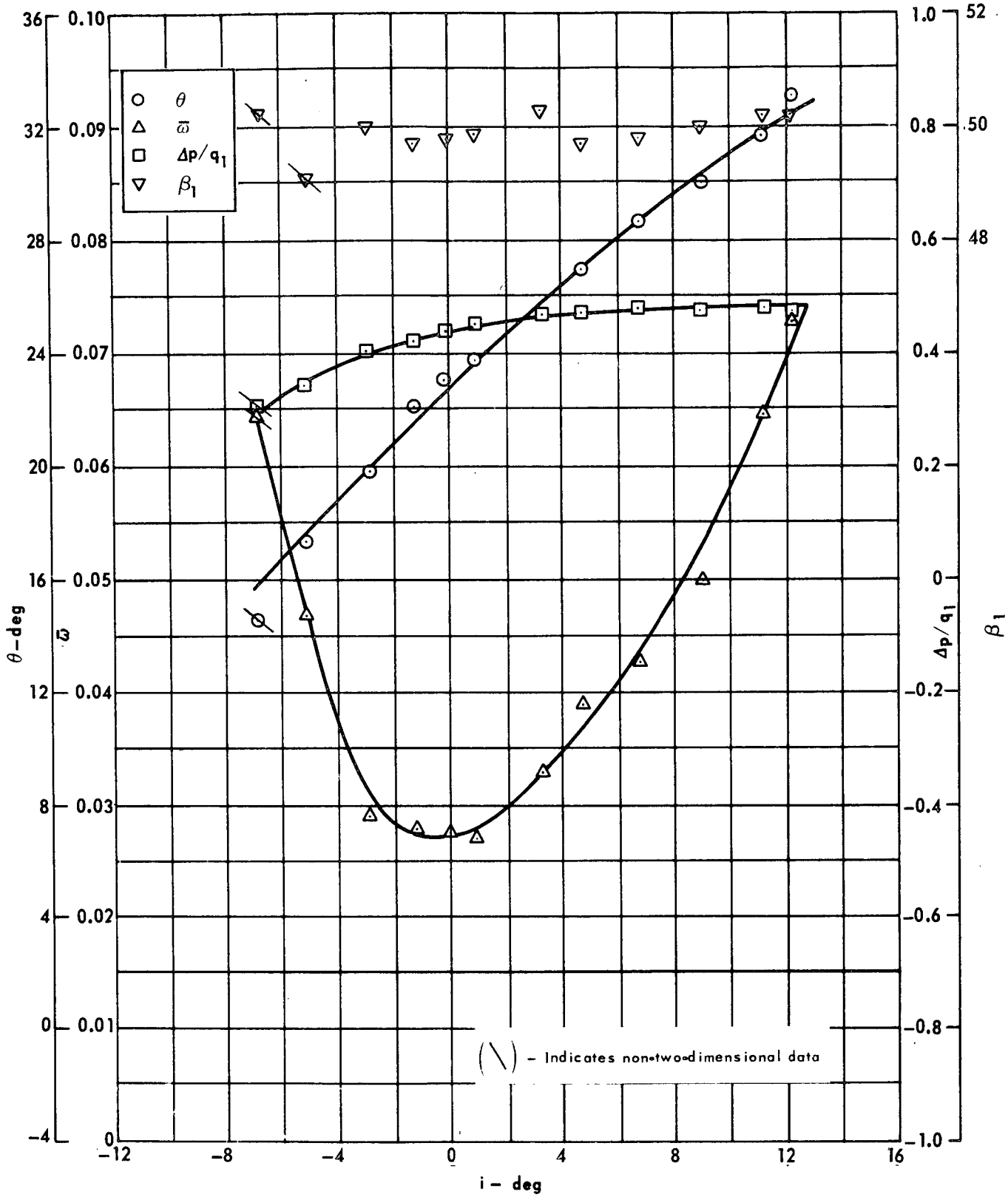

Cascade configuration : $\beta_{1N} = 50$, $\sigma = 1.50$

Double circular–arc profile : $\phi = 30$, $t/c = 0.06$

(a) $\theta, \bar{\omega}, \Delta p/q_1, \beta_1$

Figure 20. – Cascade characteristics as functions of incidence .

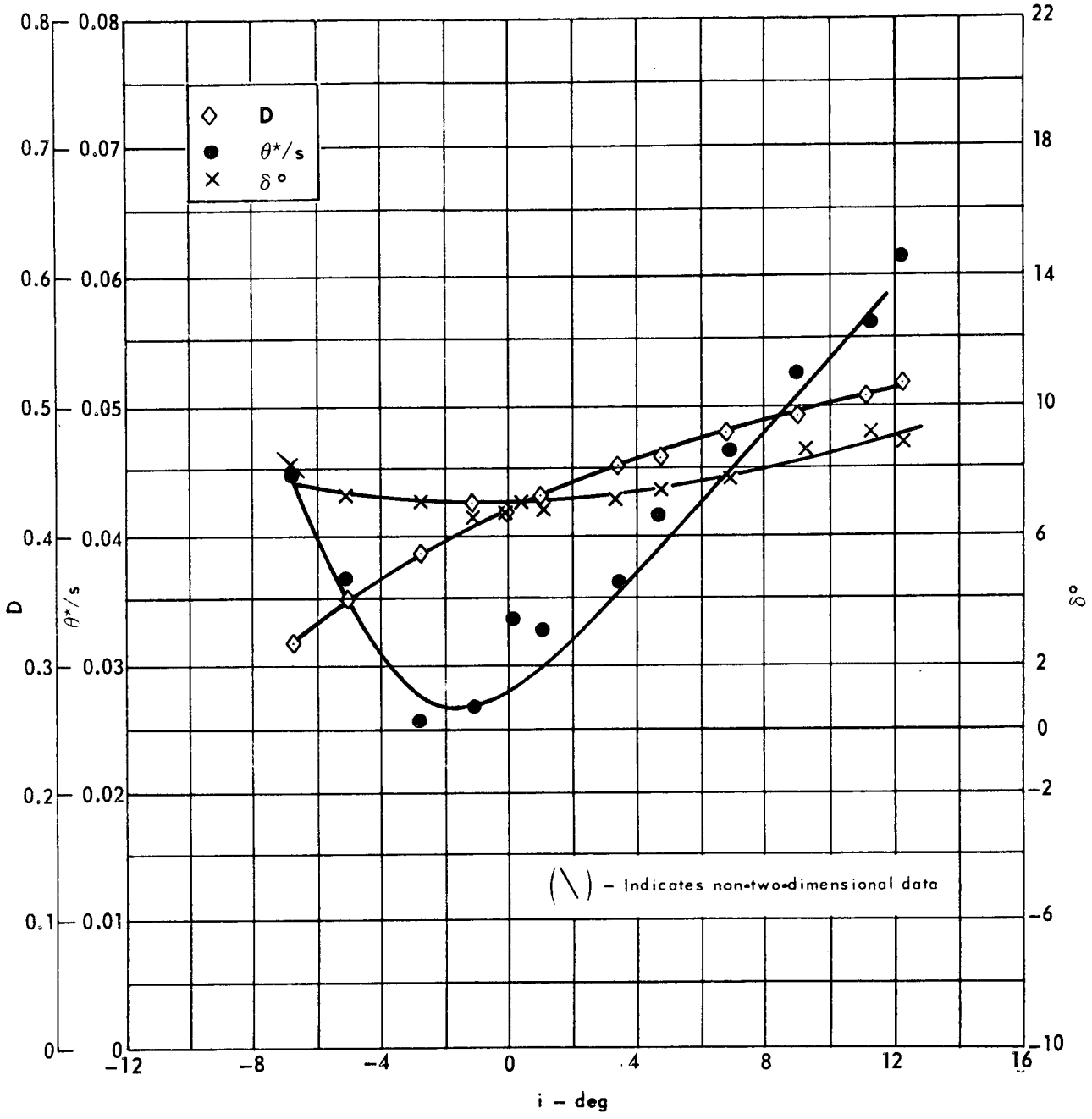

Cascade configuration : $\beta_{1N} = 50$, $\sigma = 1.50$

Double circular-arc profile : $\phi = 30$, $t/c = 0.06$

(b) D, θ^*/s, δ°

Figure 20.. - Concluded.

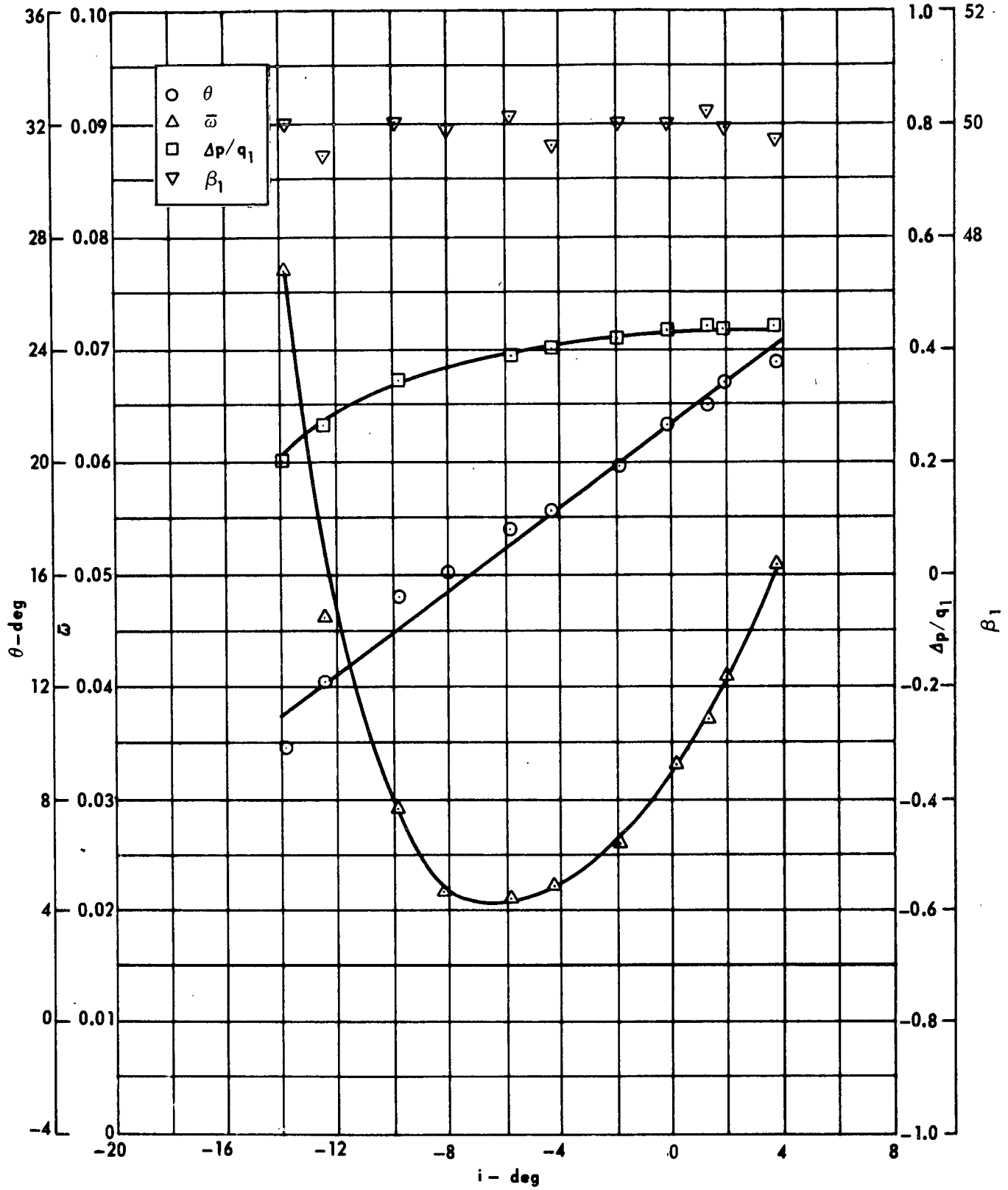

Cascade configuration : $\beta_{1N} = 50$, $\sigma = 0.75$

Double circular–arc profile : $\phi = 40$, $t/c = 0.06$

(a) $\theta, \bar{\omega}, \Delta p/q_1, \beta_1$

Figure 21. – Cascade characteristics as functions of incidence .

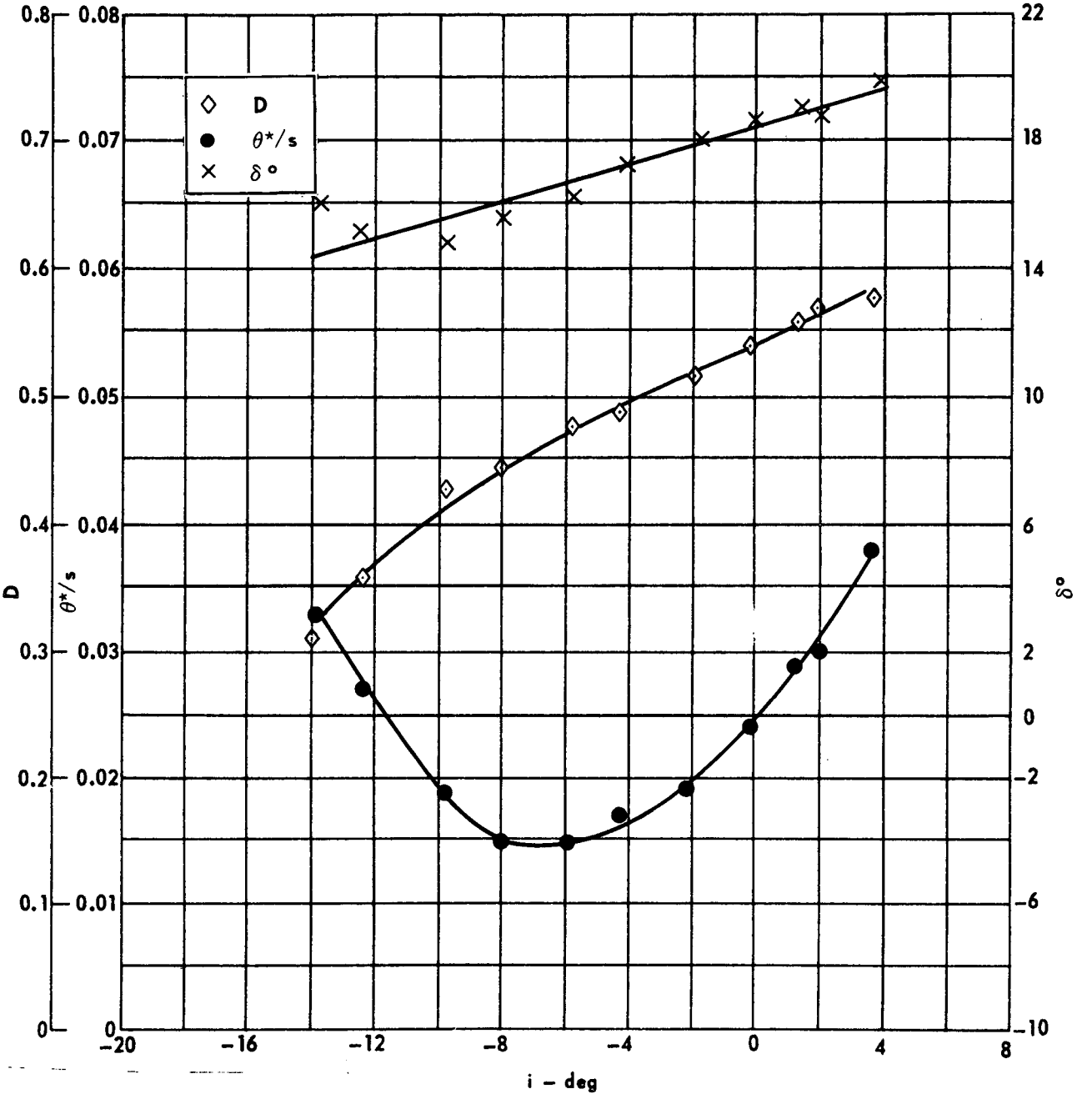

Cascade configuration : $\beta_{1N} = 50$, $\sigma = 0.75$

Double circular–arc profile : $\phi = 40$, $t/c = 0.06$

(b) D, θ^*/s, δ°

Figure 21. – Concluded.

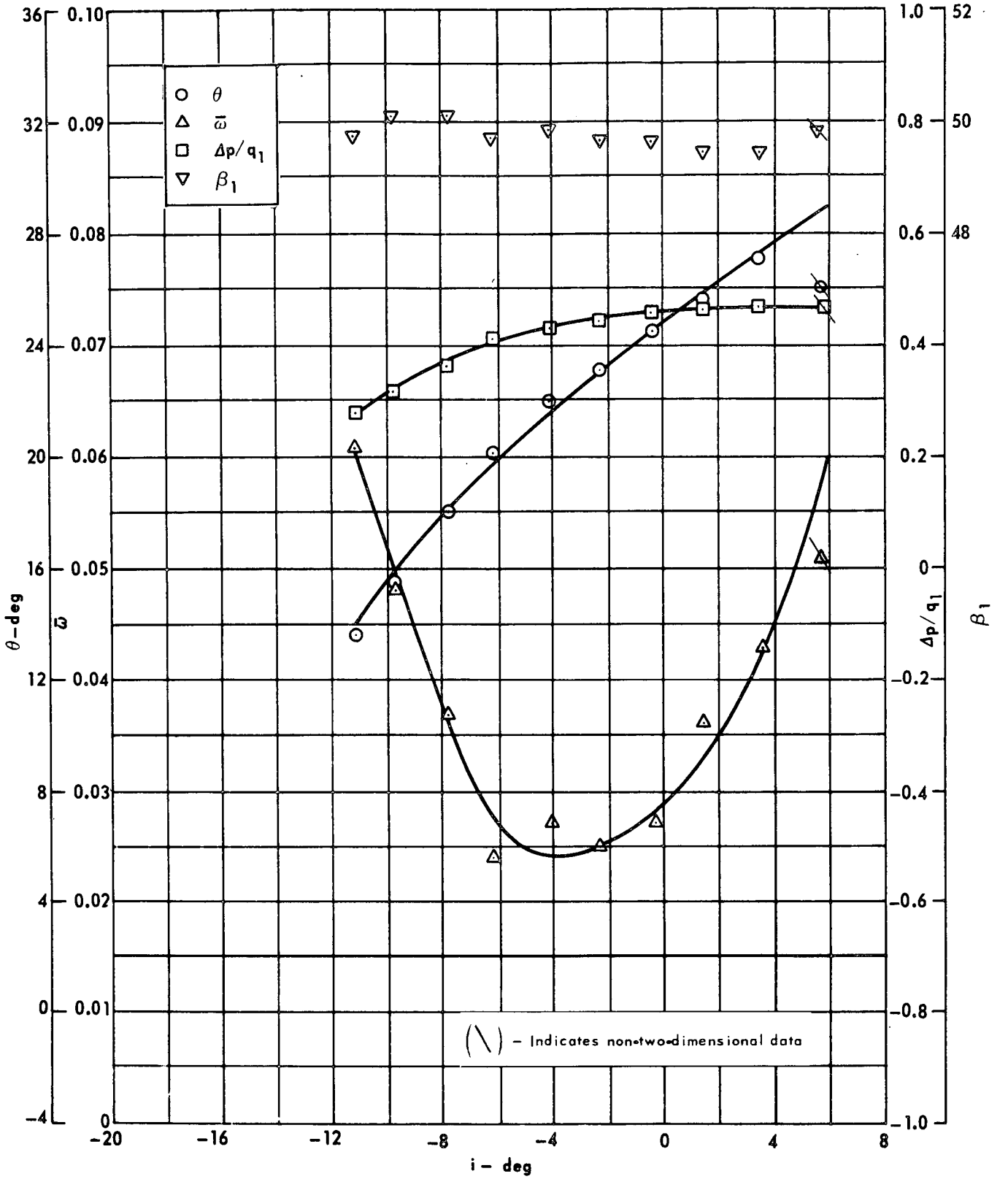

Cascade configuration : $\beta_{1N} = 50$, $\sigma = 1.00$

Double circular-arc profile : $\phi = 40$, $t/c = 0.06$

(a) $\theta, \bar{\omega}, \Delta p/q_1, \beta_1$

Figure 22. – Cascade characteristics as functions of incidence .

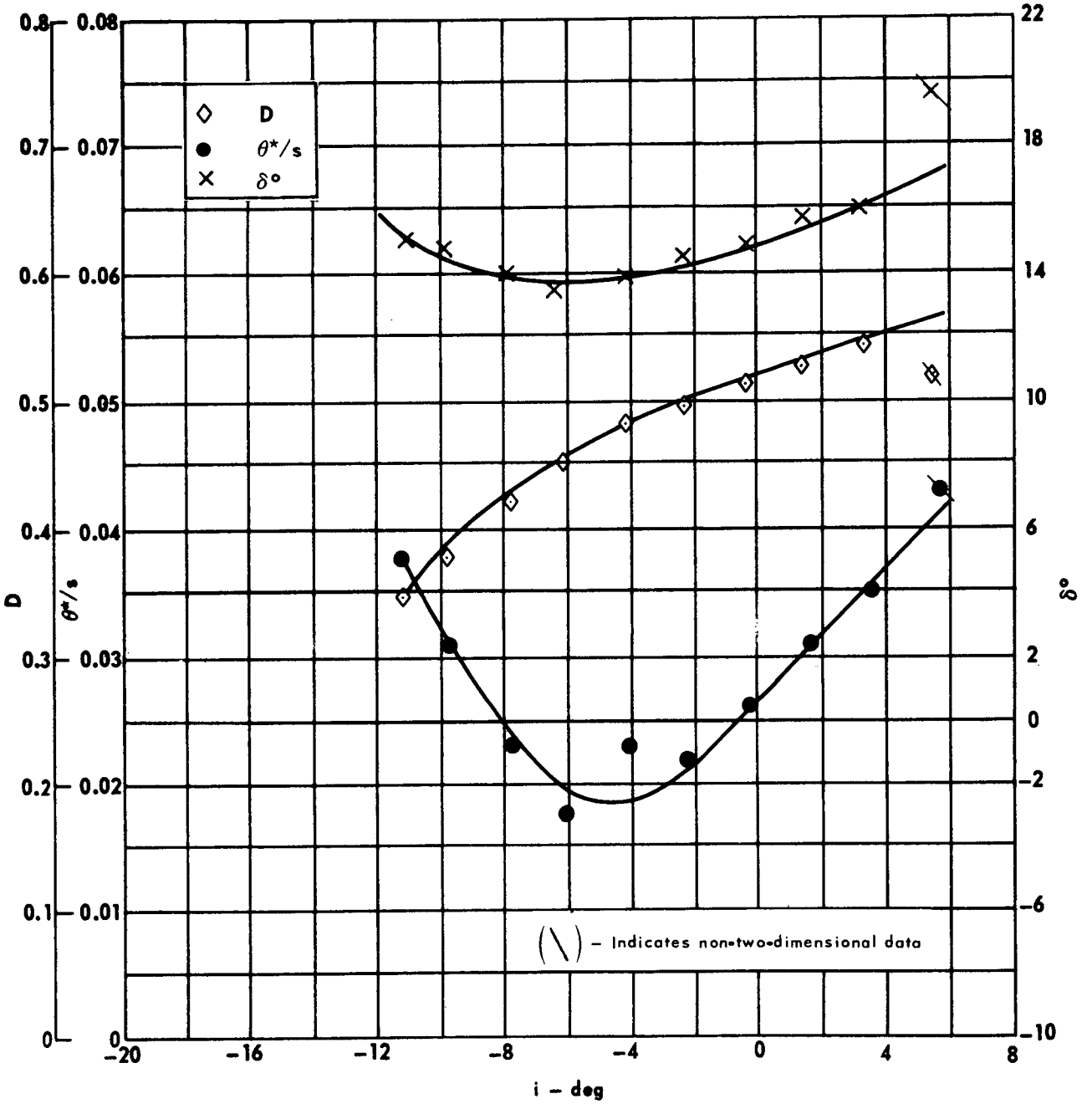

Cascade configuration : $\beta_{1N} = 50$, $\sigma = 1.00$

Double circular-arc profile : $\phi = 40$, t/c = 0.06

(b) D, θ^*/s, δ°

Figure 22. . – Concluded.

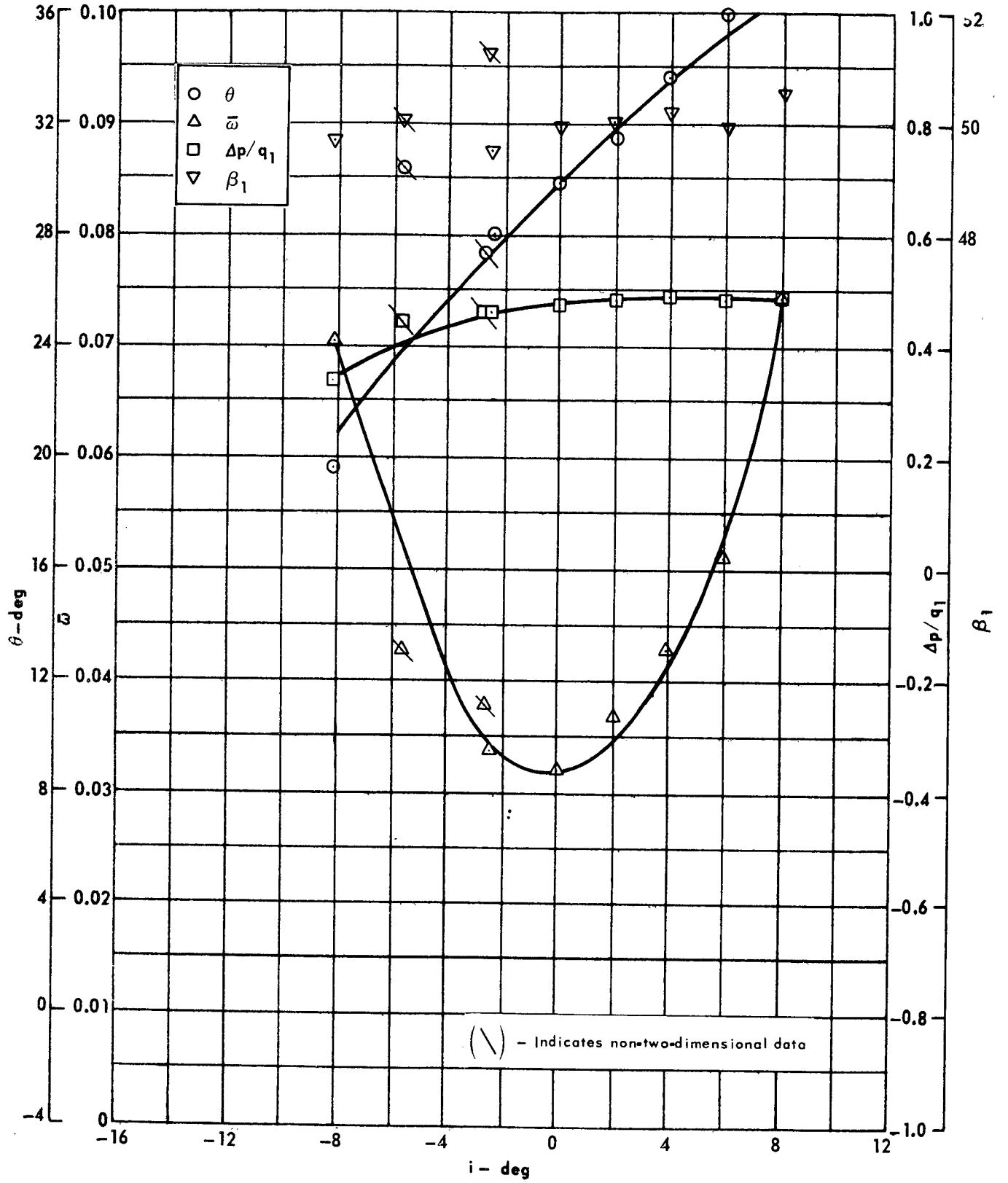

Cascade configuration : $\beta_{1N} = 50$, $\sigma = 1.50$.

Double circular-arc profile : $\phi = 40$, $t/c = 0.06$

(a) $\theta, \bar{\omega}, \Delta p/q_1, \beta_1$

Figure 23. – Cascade characteristics as functions of incidence .

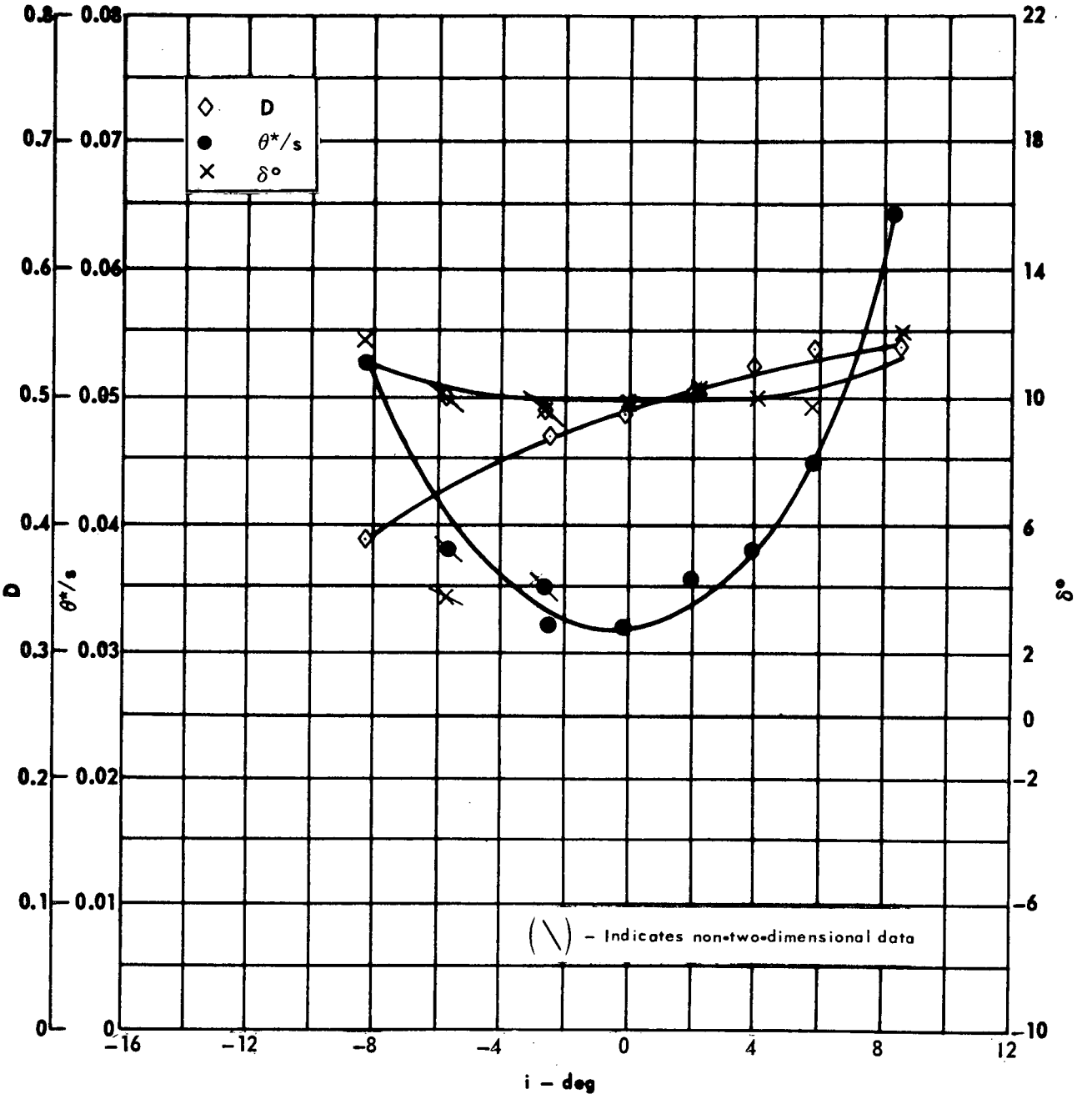

Cascade configuration : $\beta_{1N} = 50$, $\sigma = 1.50$

Double circular-arc profile : $\phi = 40$, $t/c = 0.06$

(b) D, θ^*/s, δ°

Figure 23. – Concluded.

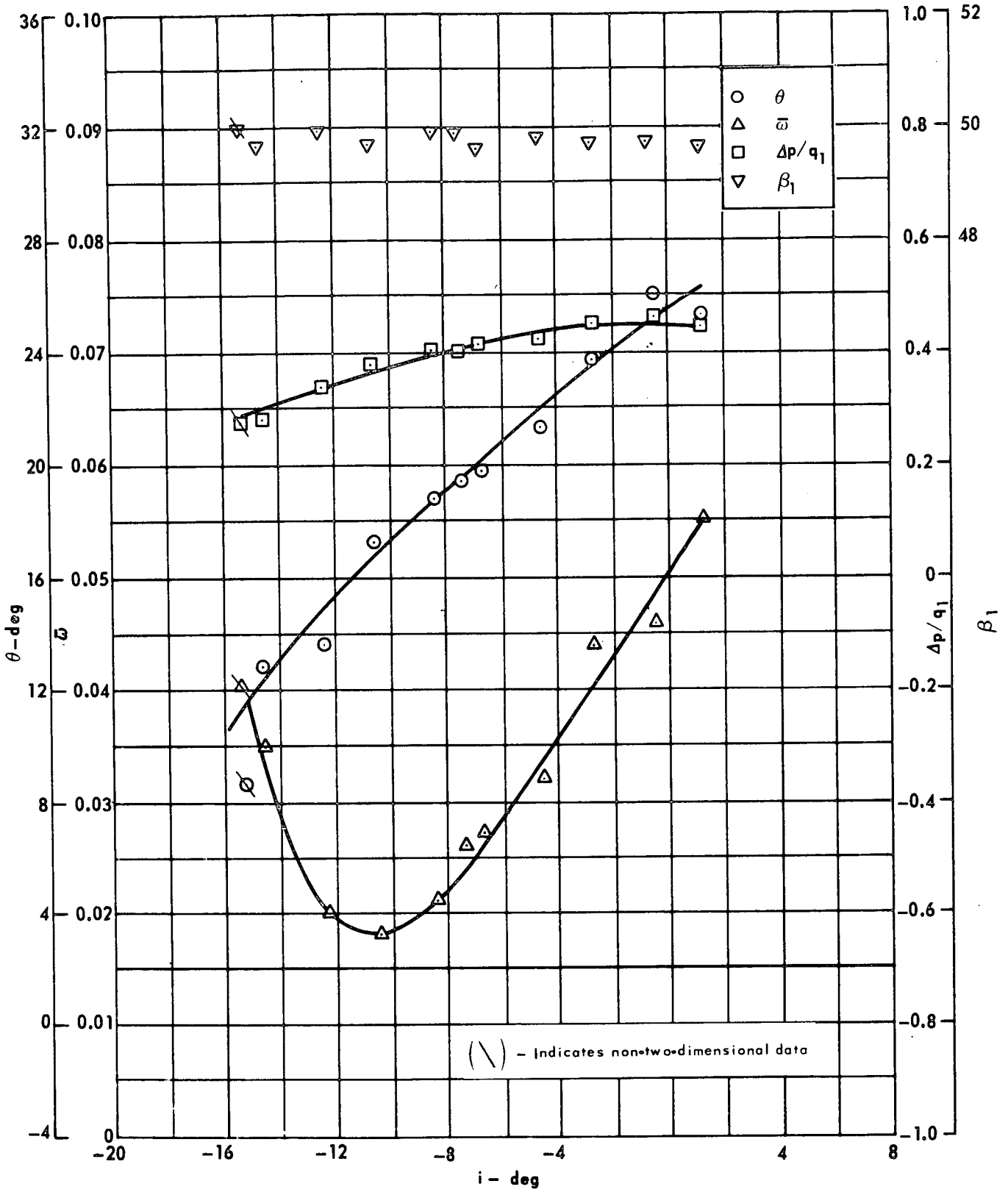

Cascade configuration : $\beta_{1N} = 50$, $\sigma = 0.75$

Double circular-arc profile : $\phi = 45$, $t/c = 0.06$

(a) $\theta, \bar{\omega}, \Delta p/q_1, \beta_1$

Figure 24. – Cascade characteristics as functions of incidence .

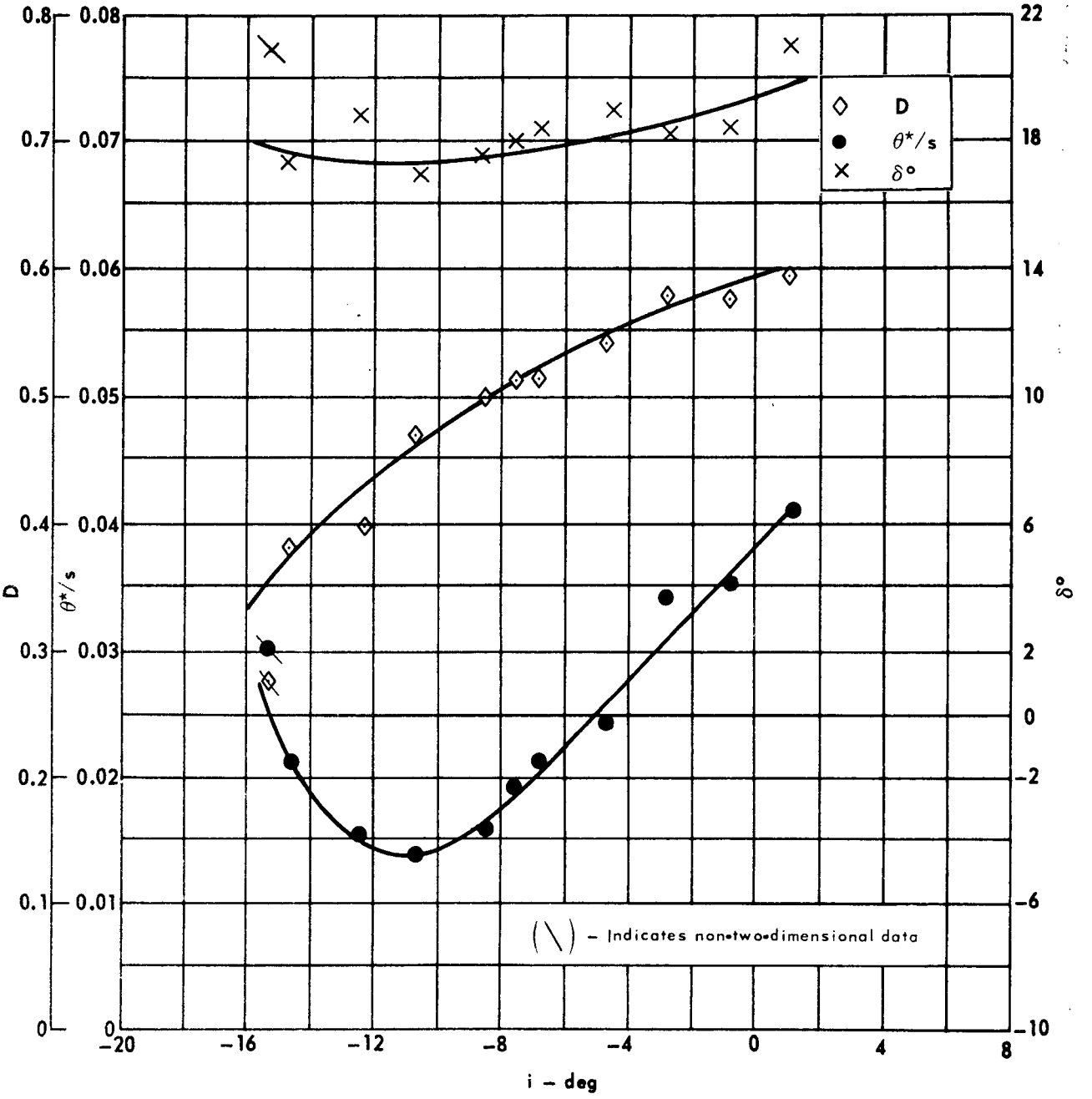

Cascade configuration : $\beta_{1N} = 50$, $\sigma = 0.75$

Double circular-arc profile : $\phi = 45$, $t/c = 0.06$

(b) D, θ^*/s, $\delta°$

Figure 24. – Concluded.

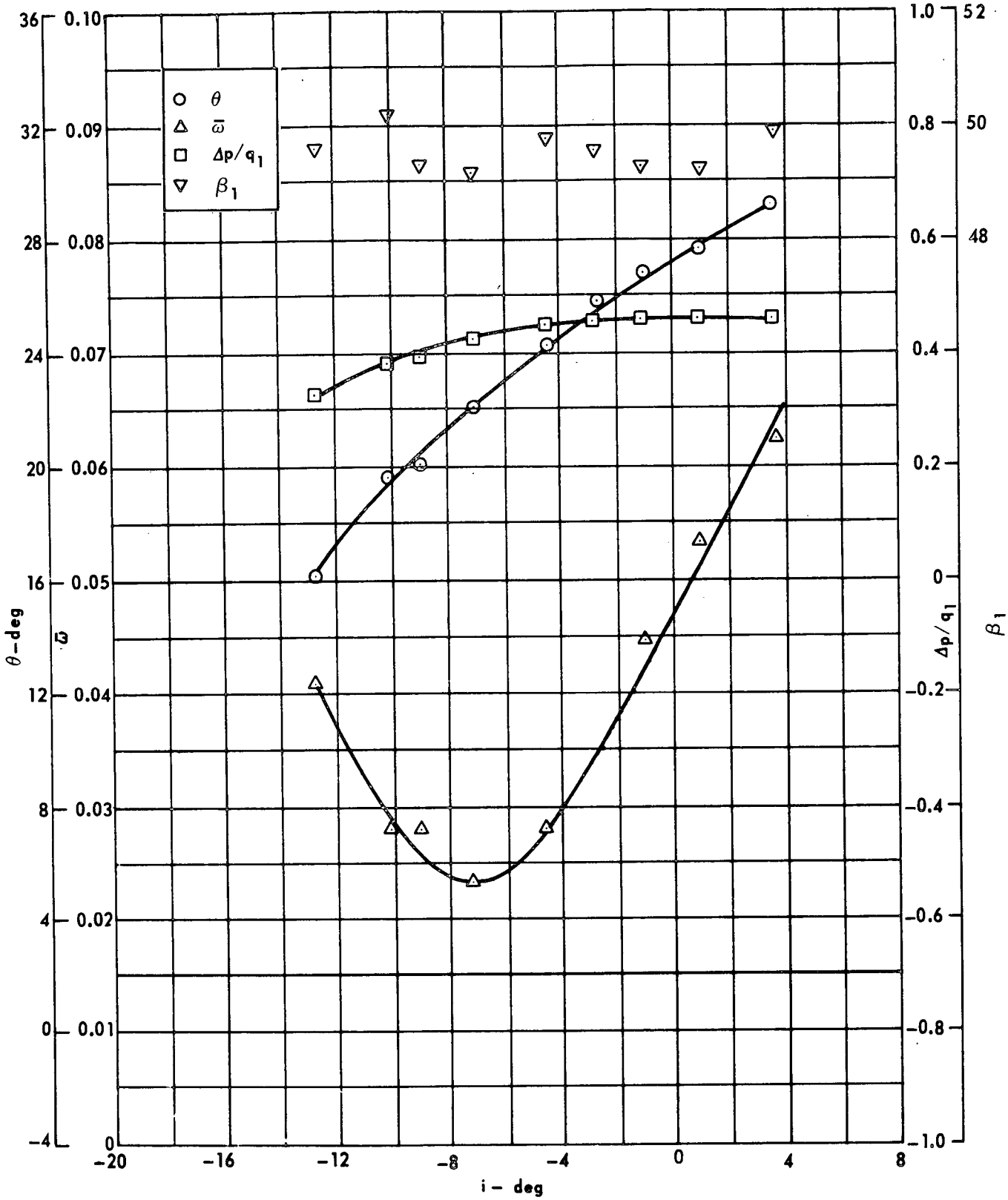

Cascade configuration : $\beta_{1N} = 50$, $\sigma = 1.00$

Double circular–arc profile : $\phi = 45$, $t/c = 0.06$

(a) $\theta, \bar{\omega}, \Delta p/q_1, \beta_1$

Figure 25. – Cascade characteristics as functions of incidence .

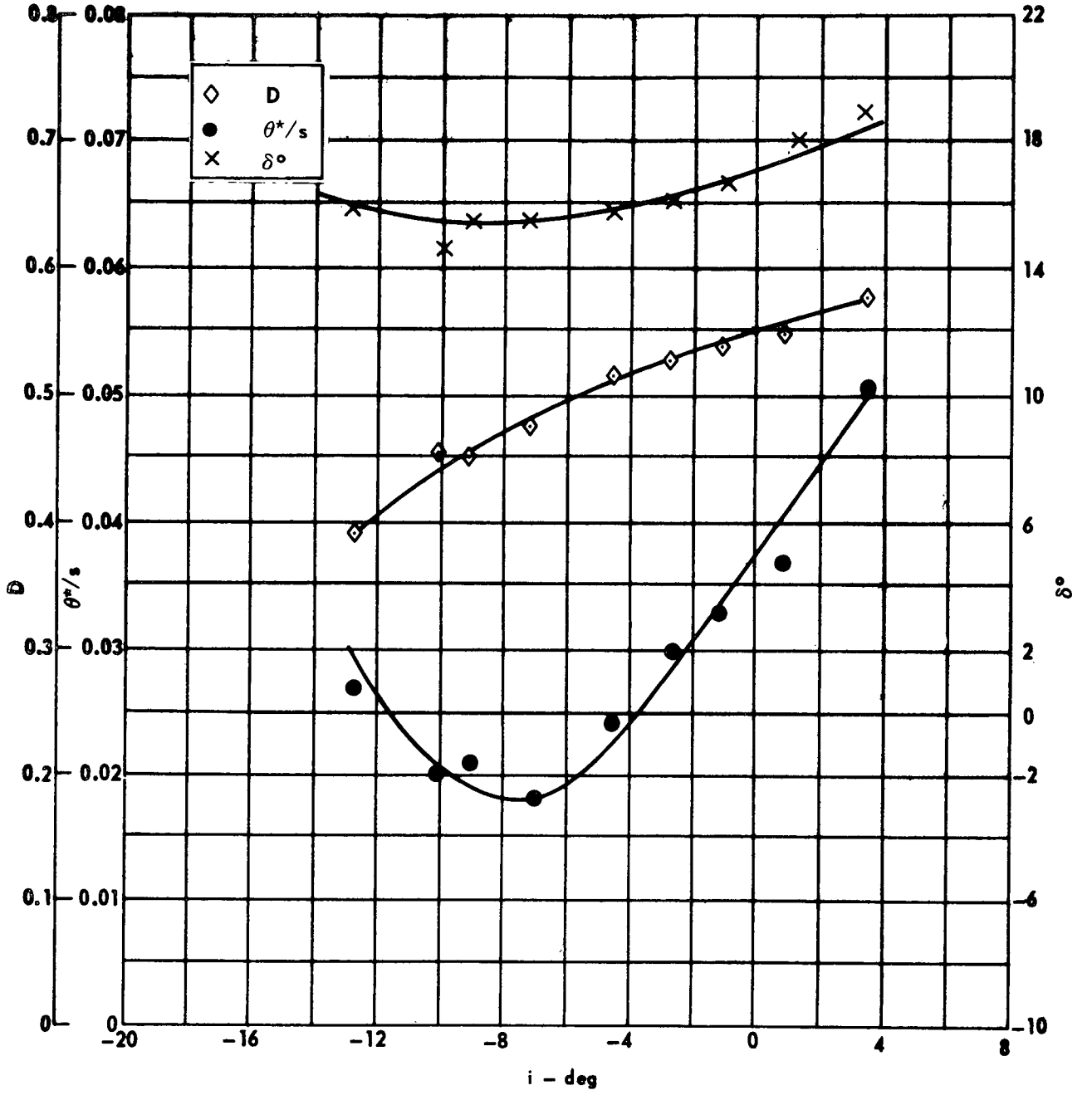

Cascade configuration : $\beta_{1N} = 50$, $\sigma = 1.00$

Double circular–arc profile : $\phi = 45$, t/c = 0.06

(b) D, θ^*/s, δ°

Figure 25. – Concluded.

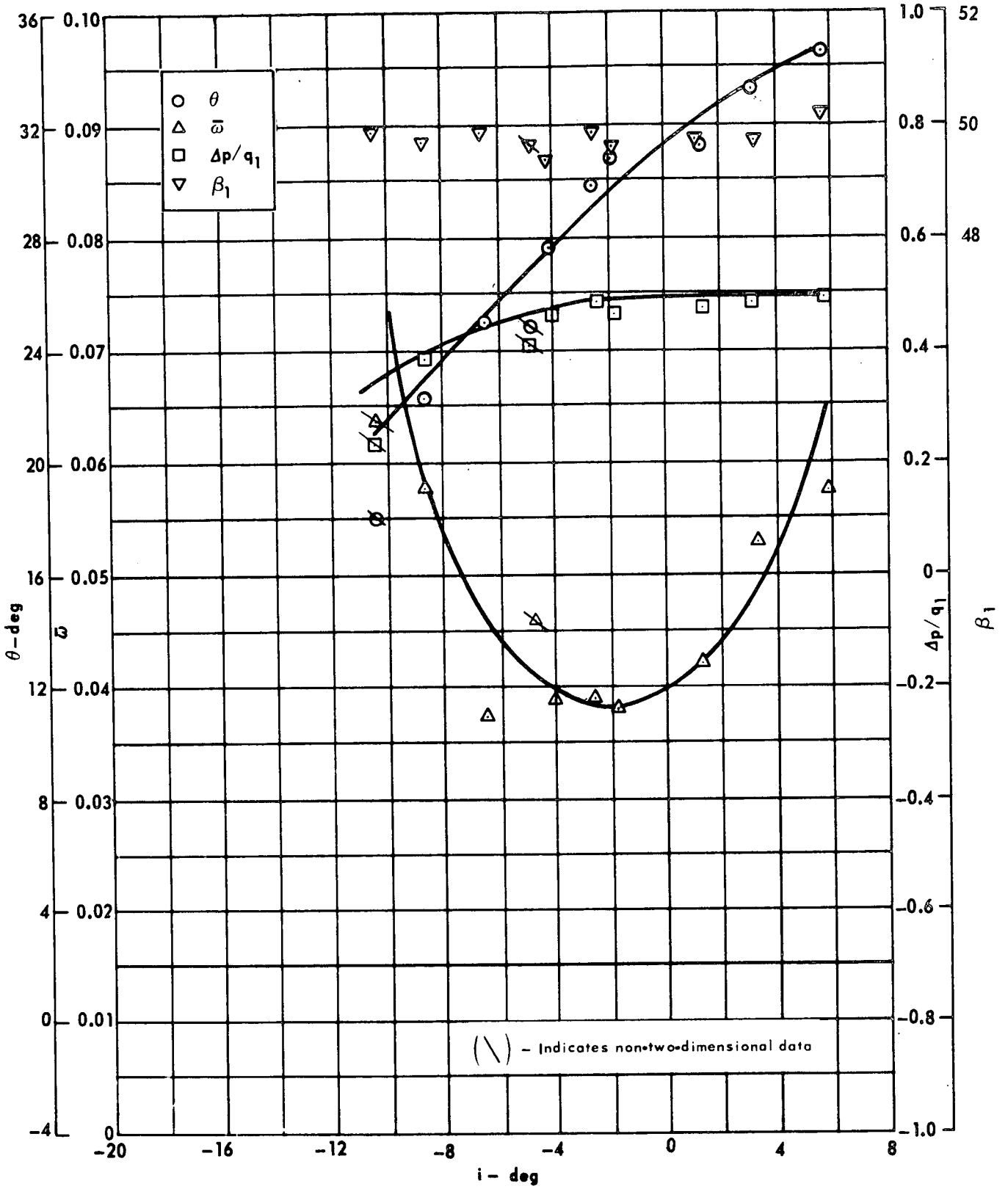

Cascade configuration : $\beta_{1N} = 50$, $\sigma = 1.50$

Double circular–arc profile : $\phi = 45$, $t/c = 0.06$

(a) $\theta, \bar{\omega}, \Delta p/q_1, \beta_1$

Figure 26. – Cascade characteristics as functions of incidence .

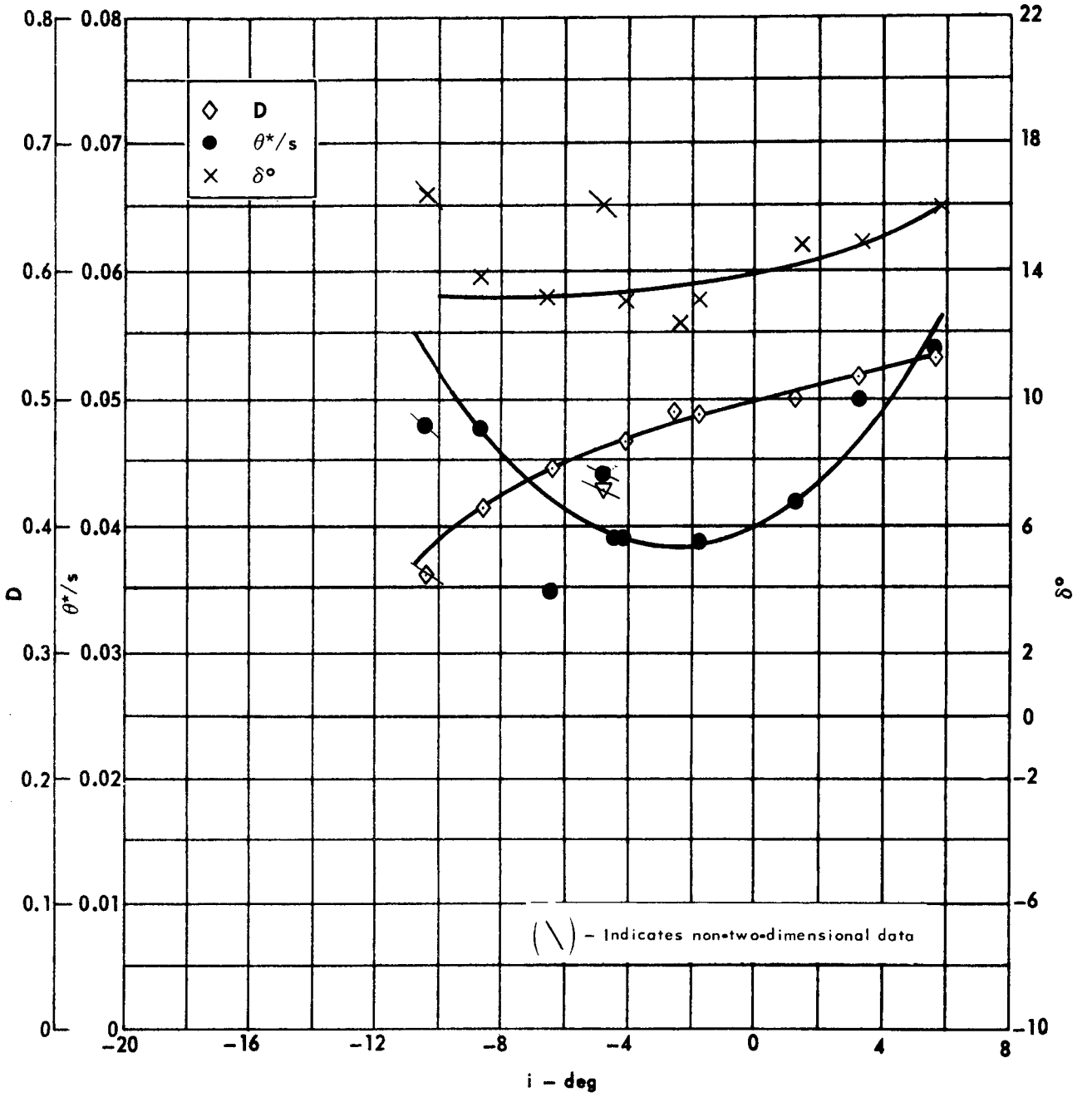

Cascade configuration : $\beta_{1N} = 50$, $\sigma = 1.50$

Double circular–arc profile : $\phi = 45$, $t/c = 0.06$

(b) D, θ^*/s, δ°

Figure 26. – Concluded.

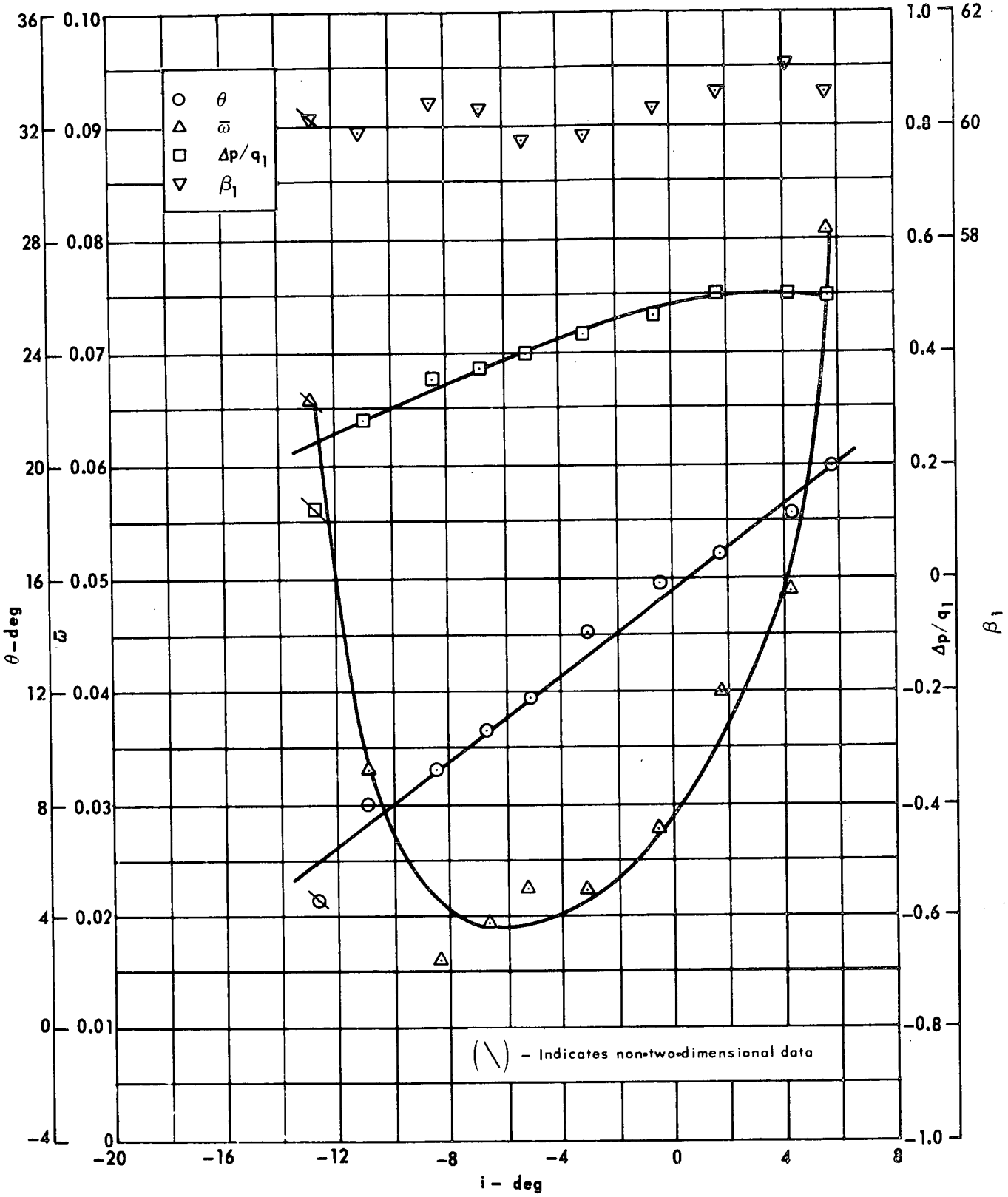

Cascade configuration : $\beta_{1N} = 60$, $\sigma = 0.75$

Double circular–arc profile : $\phi = 30$, $t/c = 0.06$

(a) $\theta, \bar{\omega}, \Delta p/q_1, \beta_1$

Figure 27. – Cascade characteristics as functions of incidence .

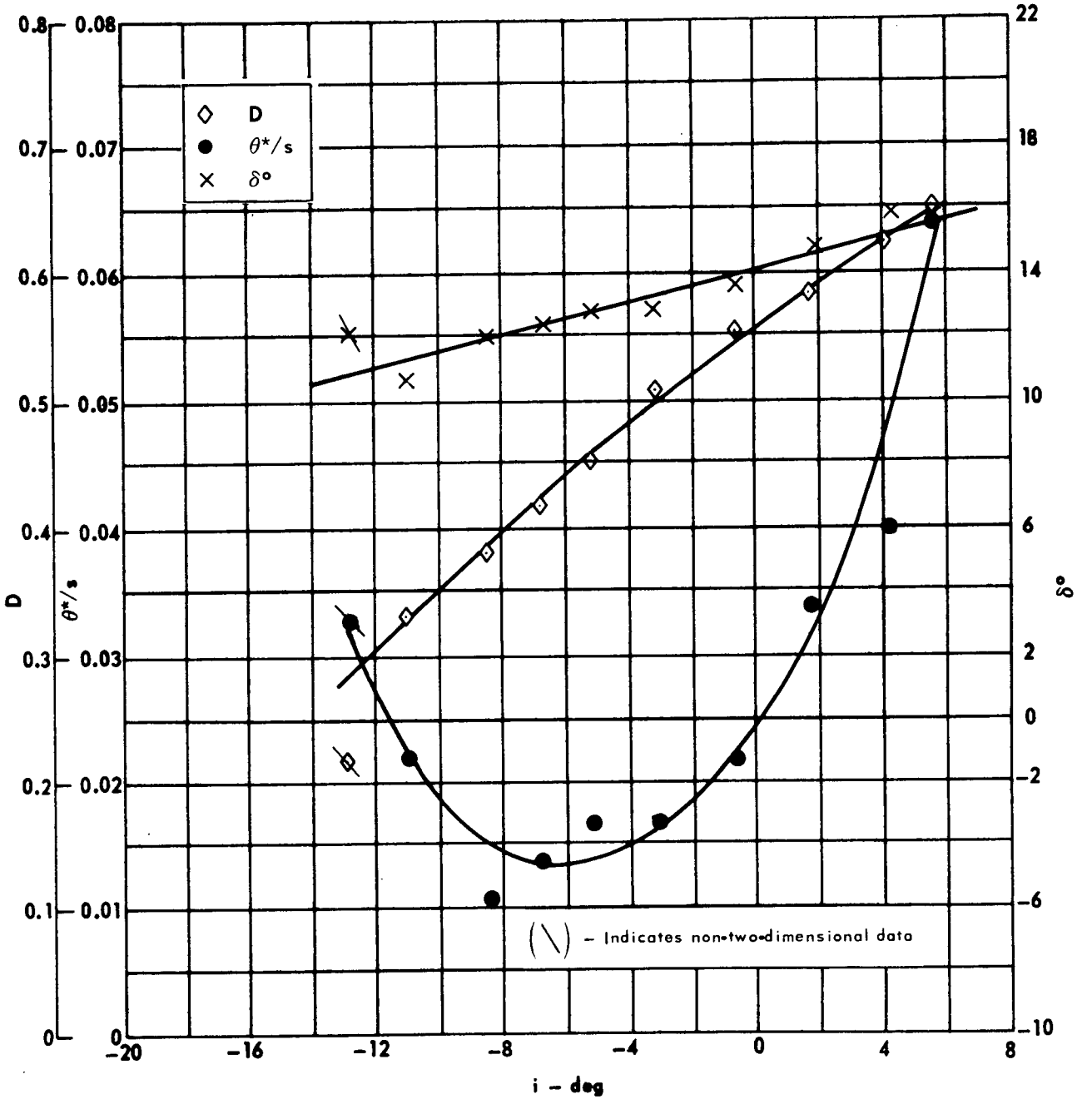

Cascade configuration : $\beta_{1N} = 60$, $\sigma = 0.75$

Double circular–arc profile : $\phi = 30$, $t/c = 0.06$

(b) D, θ^*/s, δ°

Figure 27. – Concluded.

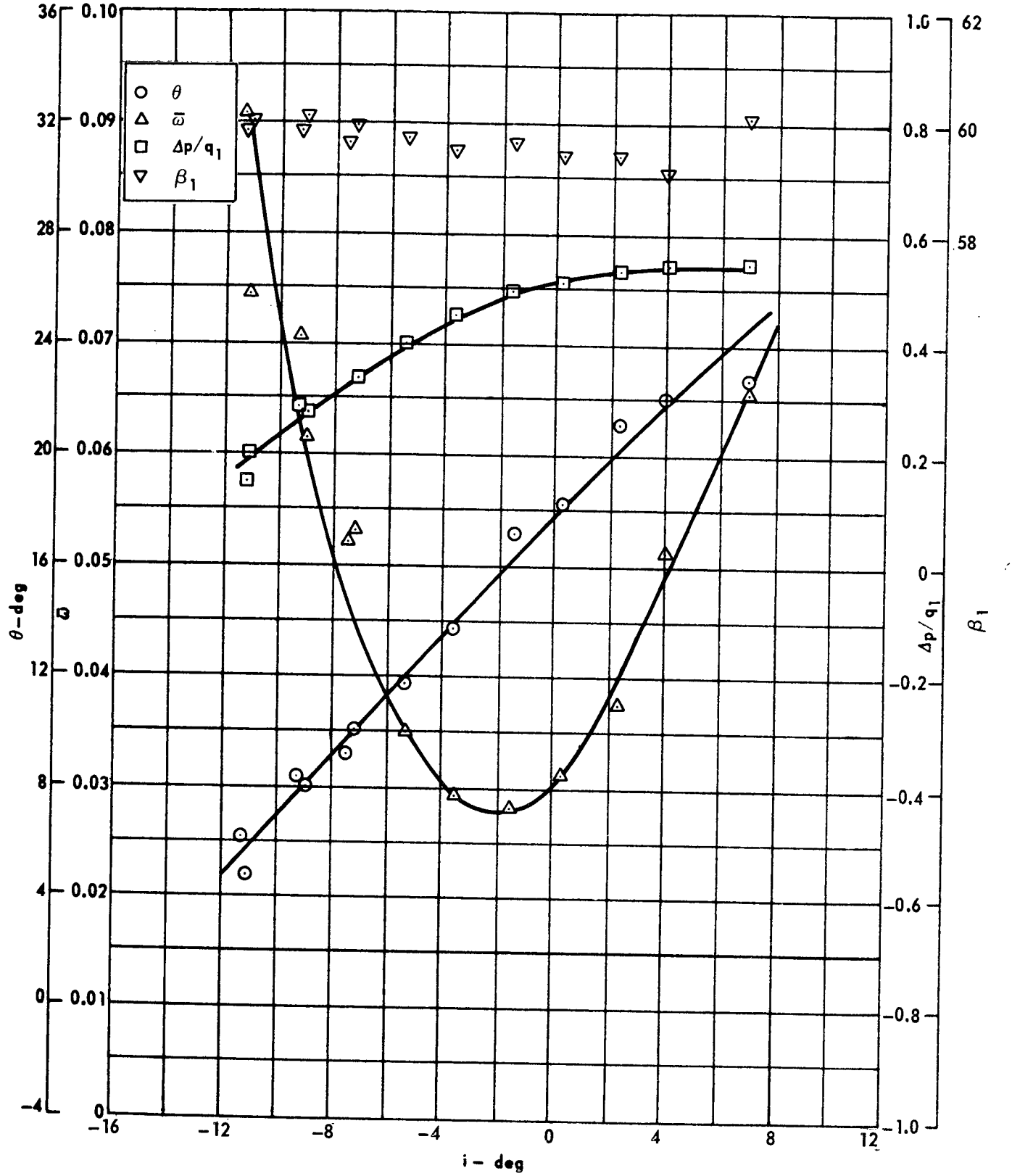

Cascade configuration : $\beta_{1N} = 60$, $\sigma = 1.00$

Double circular-arc profile : $\phi = 30$, $t/c = 0.06$

(a) $\theta, \bar{\omega}, \Delta p/q_1, \beta_1$

Figure 28. – Cascade characteristics as functions of incidence .

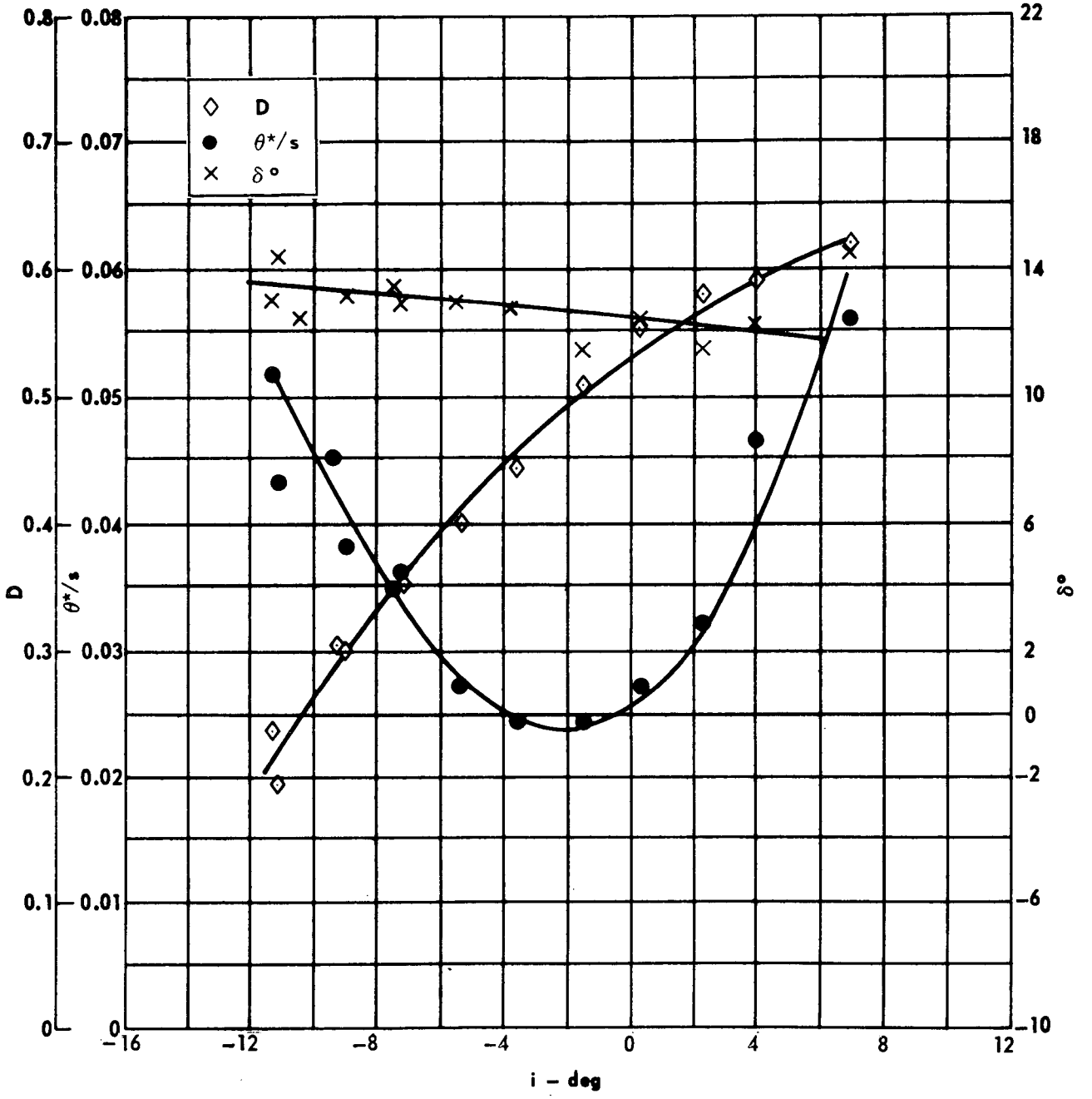

Cascade configuration : $\beta_{1N} = 60$, $\sigma = 1.00$

Double circular–arc profile : $\phi = 30$, $t/c = 0.06$

(b) D, θ^*/s, δ°

Figure 28. – Concluded.

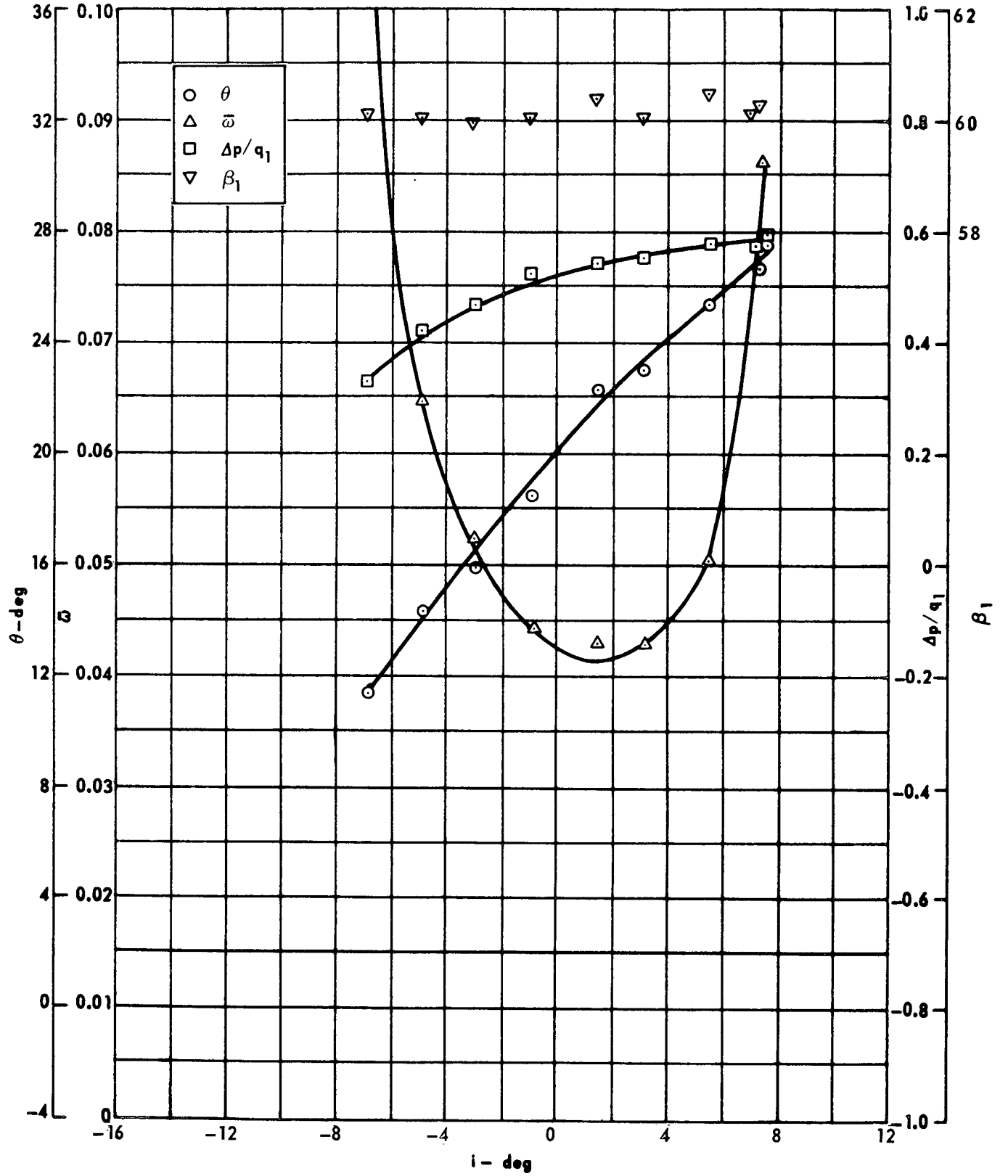

Cascade configuration : $\beta_{1N} = 60$, $\sigma = 1.50$

Double circular-arc profile : $\phi = 30$, $t/c = 0.06$

(a) $\theta, \bar{\omega}, \Delta p/q_1, \beta_1$

Figure 29. – Cascade characteristics as functions of incidence .

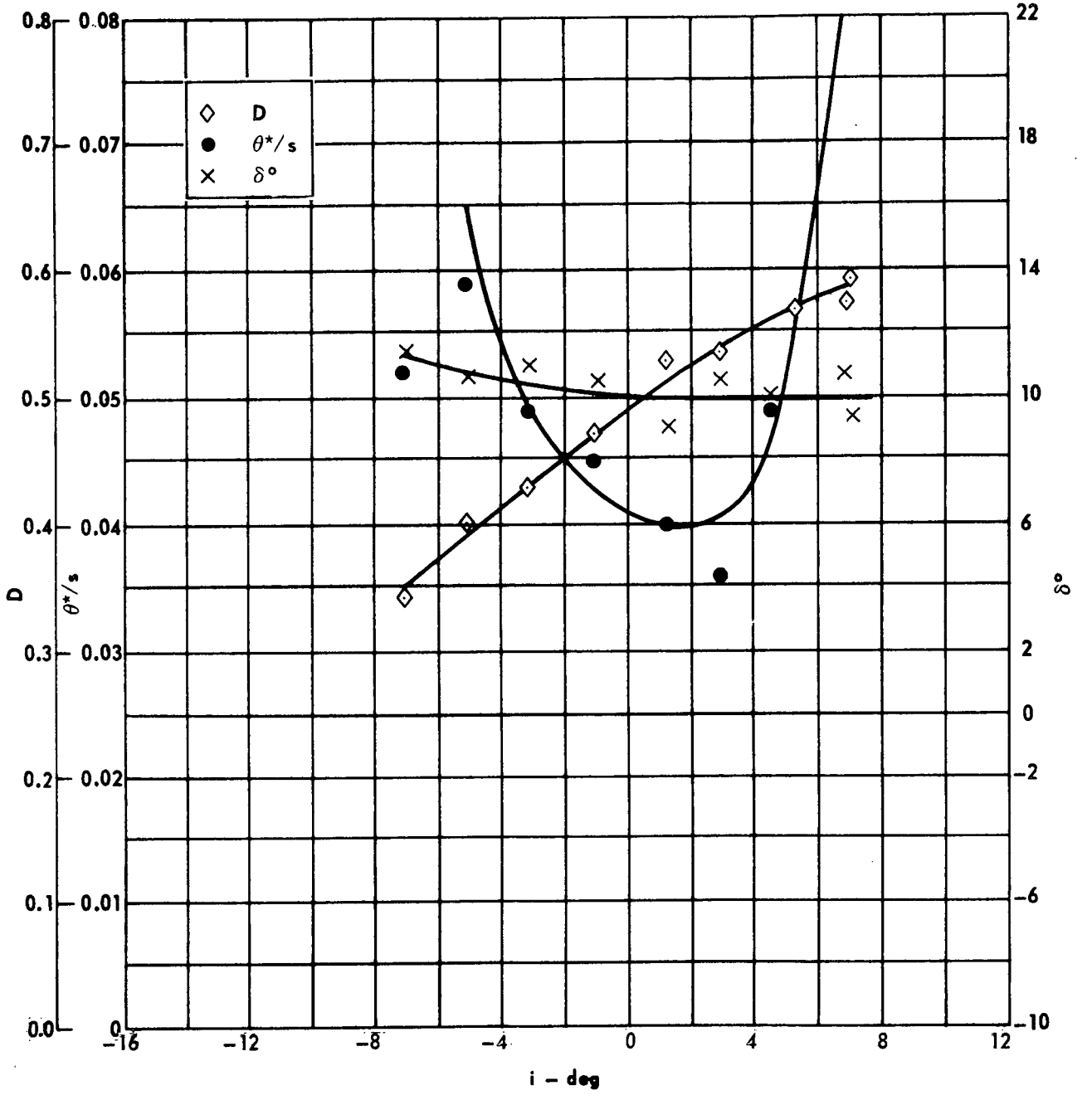

Cascade configuration : $\beta_{1N} = 60$, $\sigma = 1.50$

Double circular–arc profile : $\phi = 30$, $t/c = 0.06$

(b) D, θ^*/s, δ°

Figure 29. – Concluded.

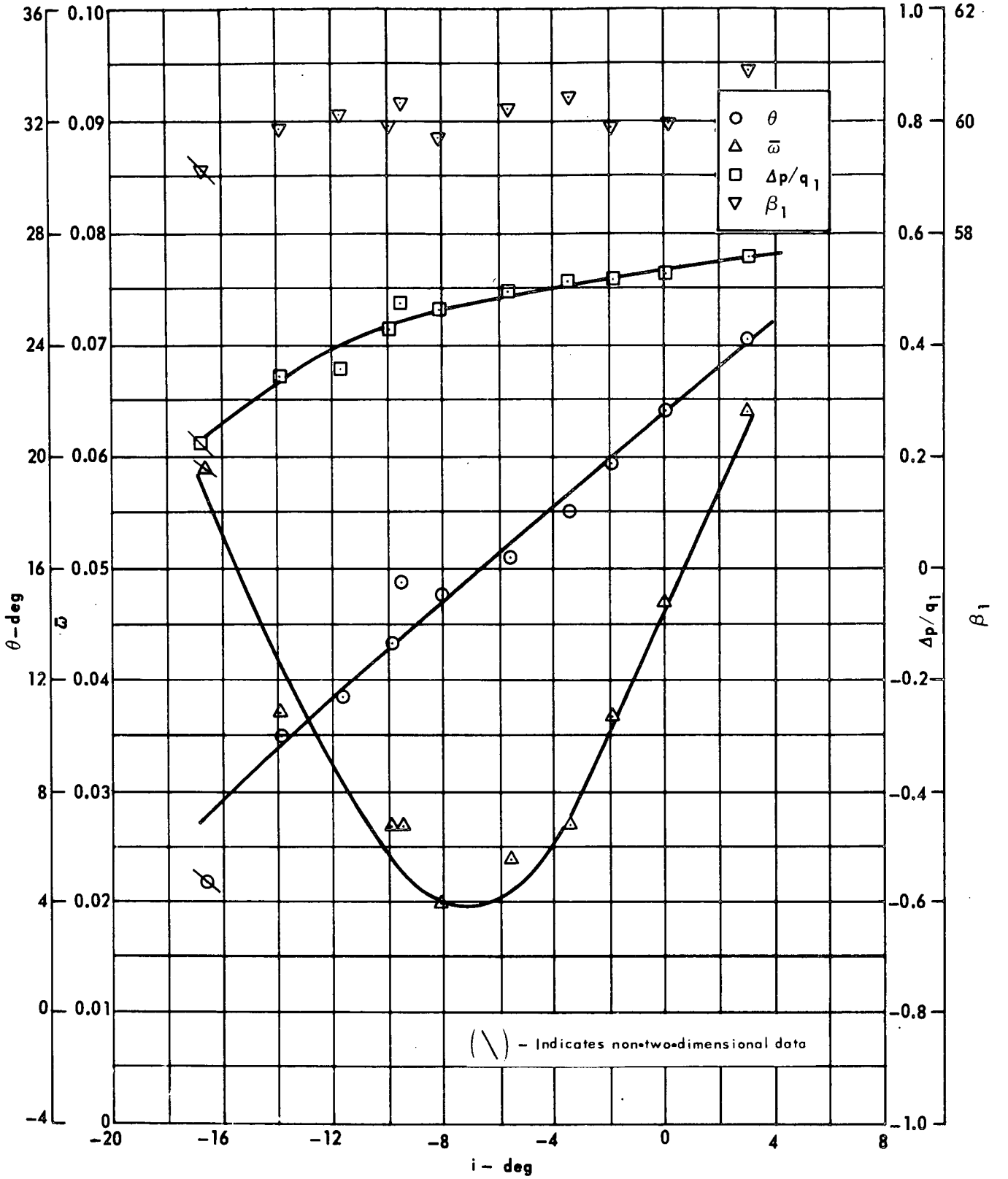

Cascade configuration : $\beta_{1N} = 60$, $\sigma = 0.75$

Double circular-arc profile : $\phi = 40$, $t/c = 0.06$

(a) $\theta, \bar{\omega}, \Delta p/q_1, \beta_1$

Figure 30. – Cascade characteristics as functions of incidence .

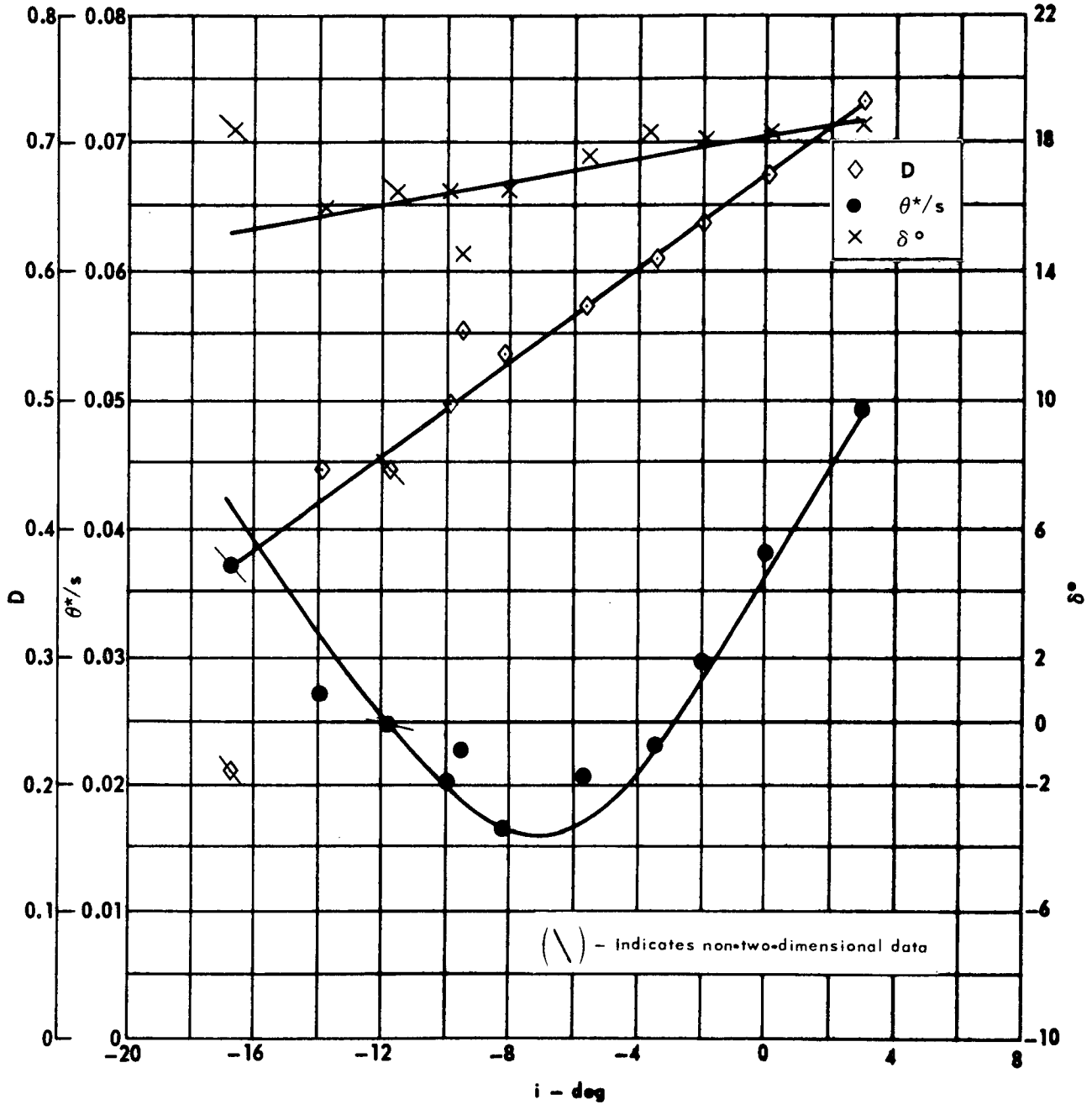

Cascade configuration : $\beta_{1N} = 60$, $\sigma = 0.75$

Double circular-arc profile : $\phi = 40$, $t/c = 0.06$

(b) D, θ^*/s, δ°

Figure 30. – Concluded.

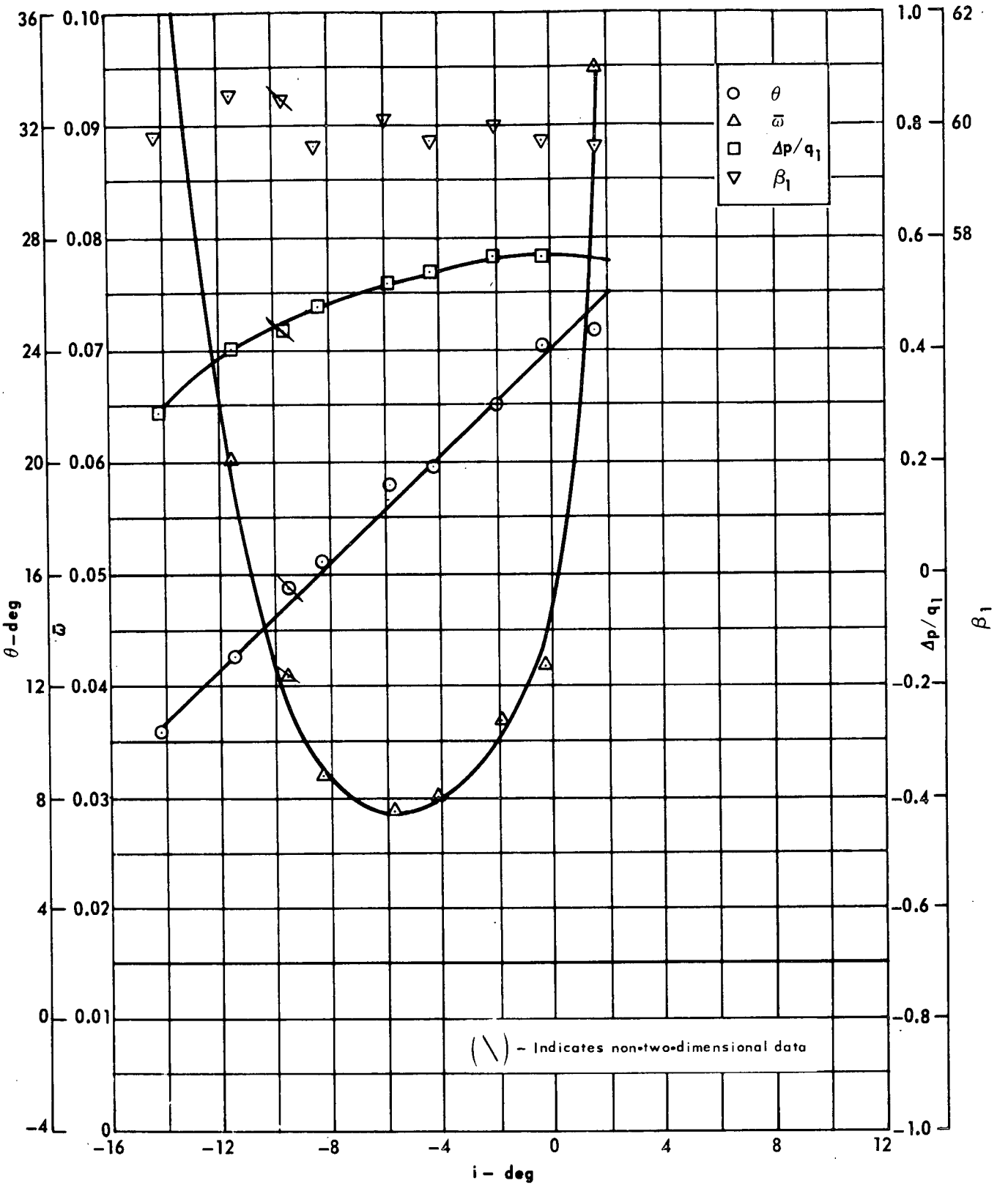

Cascade configuration : $\beta_{1N} = 60$, $\sigma = 1.00$

Double circular-arc profile : $\phi = 40$, $t/c = 0.06$

(a) $\theta, \bar{\omega}, \Delta p/q_1, \beta_1$

Figure 31. – Cascade characteristics as functions of incidence .

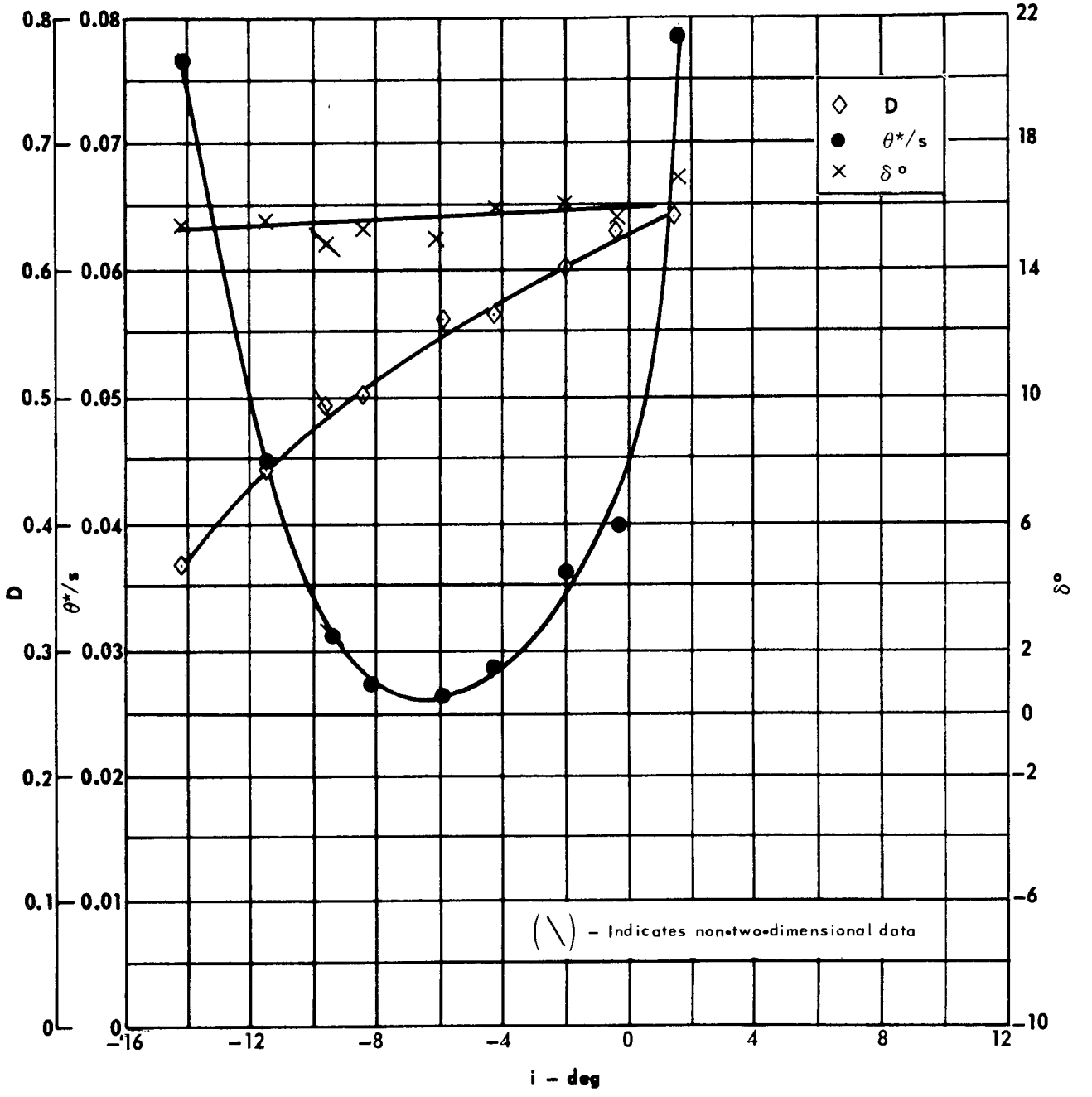

Cascade configuration : $\beta_{1N} = 60$, $\sigma = 1.00$

Double circular–arc profile : $\phi = 40$, $t/c = 0.06$

(b) D, θ^*/s, δ°

Figure 31. – Concluded.

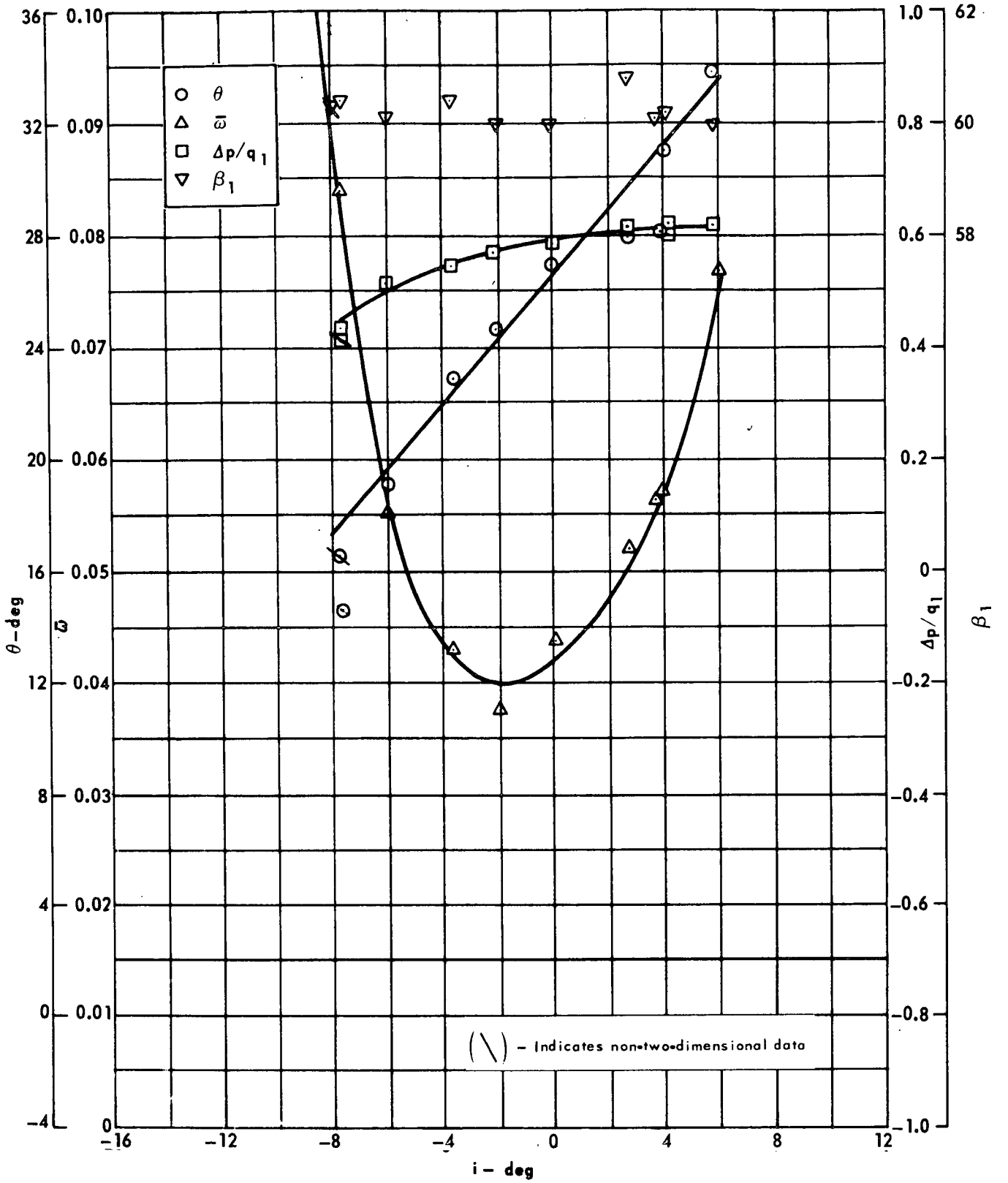

Cascade configuration : $\beta_{1N} = 60$, $\sigma = 1.50$

Double circular–arc profile : $\phi = 40$, $t/c = 0.06$

(a) $\theta, \bar{\omega}, \Delta p/q_1, \beta_1$

Figure 32. – Cascade characteristics as functions of incidence .

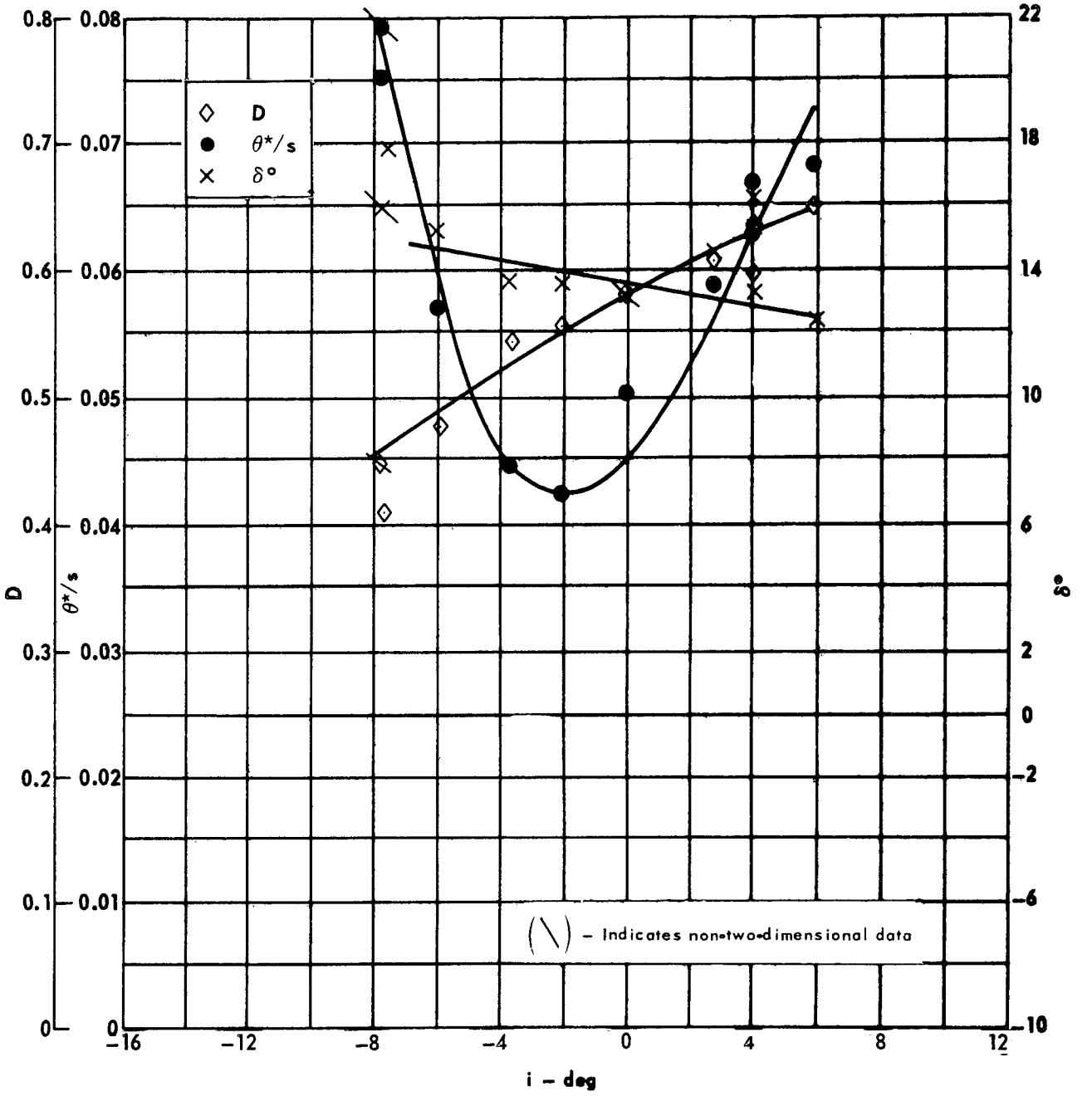

Cascade configuration : $\beta_{1N} = 60$, $\sigma = 1.50$

Double circular–arc profile : $\phi = 40$, t/c = 0.06

(b) D, θ^*/s, δ°

Figure 32. – Concluded.

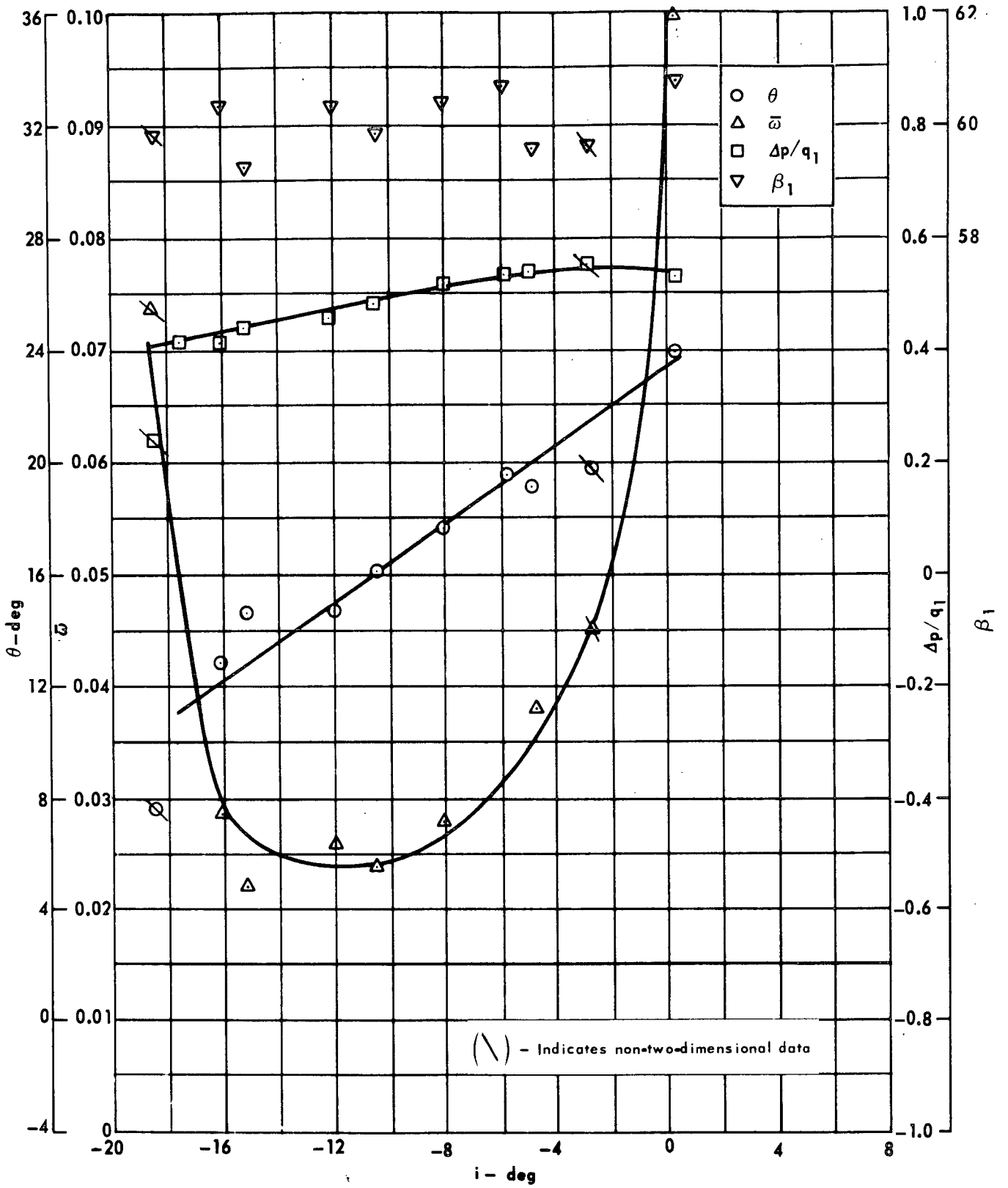

Cascade configuration : $\beta_{1N} = 60$, $\sigma = 0.75$

Double circular-arc profile : $\phi = 45$, $t/c = 0.06$

(a) $\theta, \bar{\omega}, \Delta p/q_1, \beta_1$

Figure 33. – Cascade characteristics as functions of incidence .

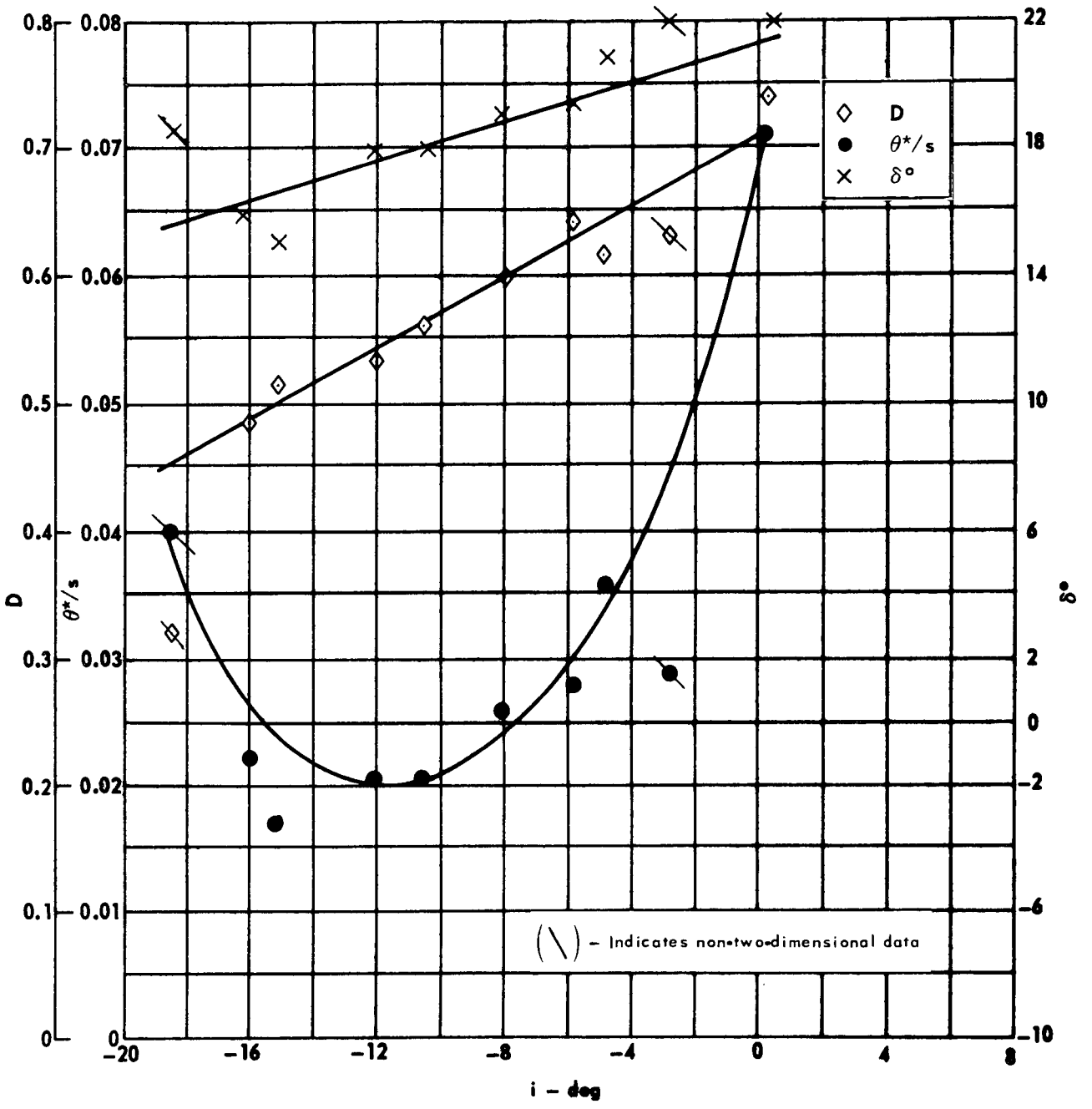

Cascade configuration : $\beta_{1N} = 60$, $\sigma = 0.75$

Double circular-arc profile : $\phi = 45$, $t/c = 0.06$

(b) D, θ^*/s, δ°

Figure 33. – Concluded.

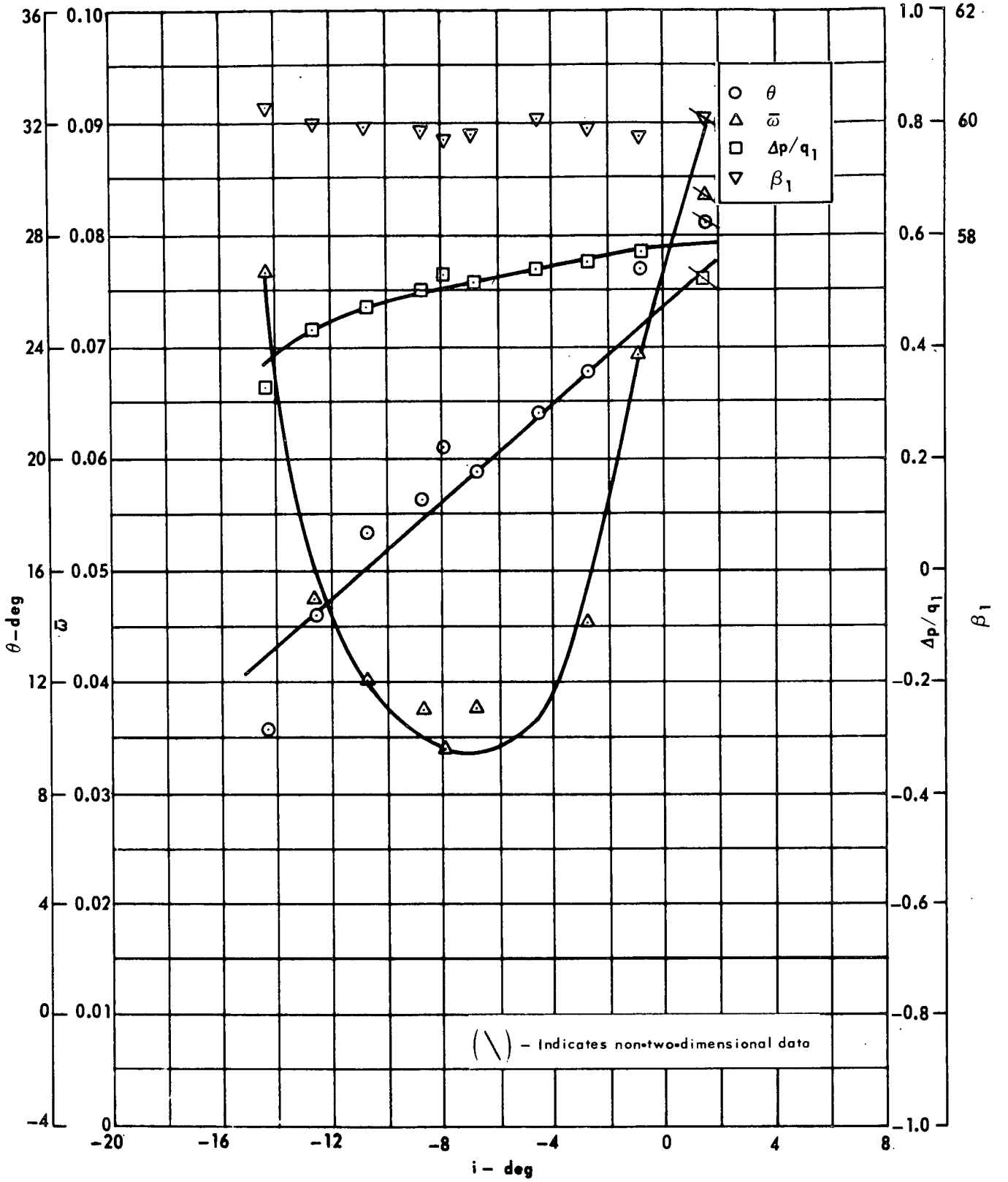

Cascade configuration : $\beta_{1N} = 60$, $\sigma = 1.00$

Double circular–arc profile : $\phi = 45$, $t/c = 0.06$

(a) $\theta, \bar{\omega}, \Delta p/q_1, \beta_1$

Figure 34. – Cascade characteristics as functions of incidence .

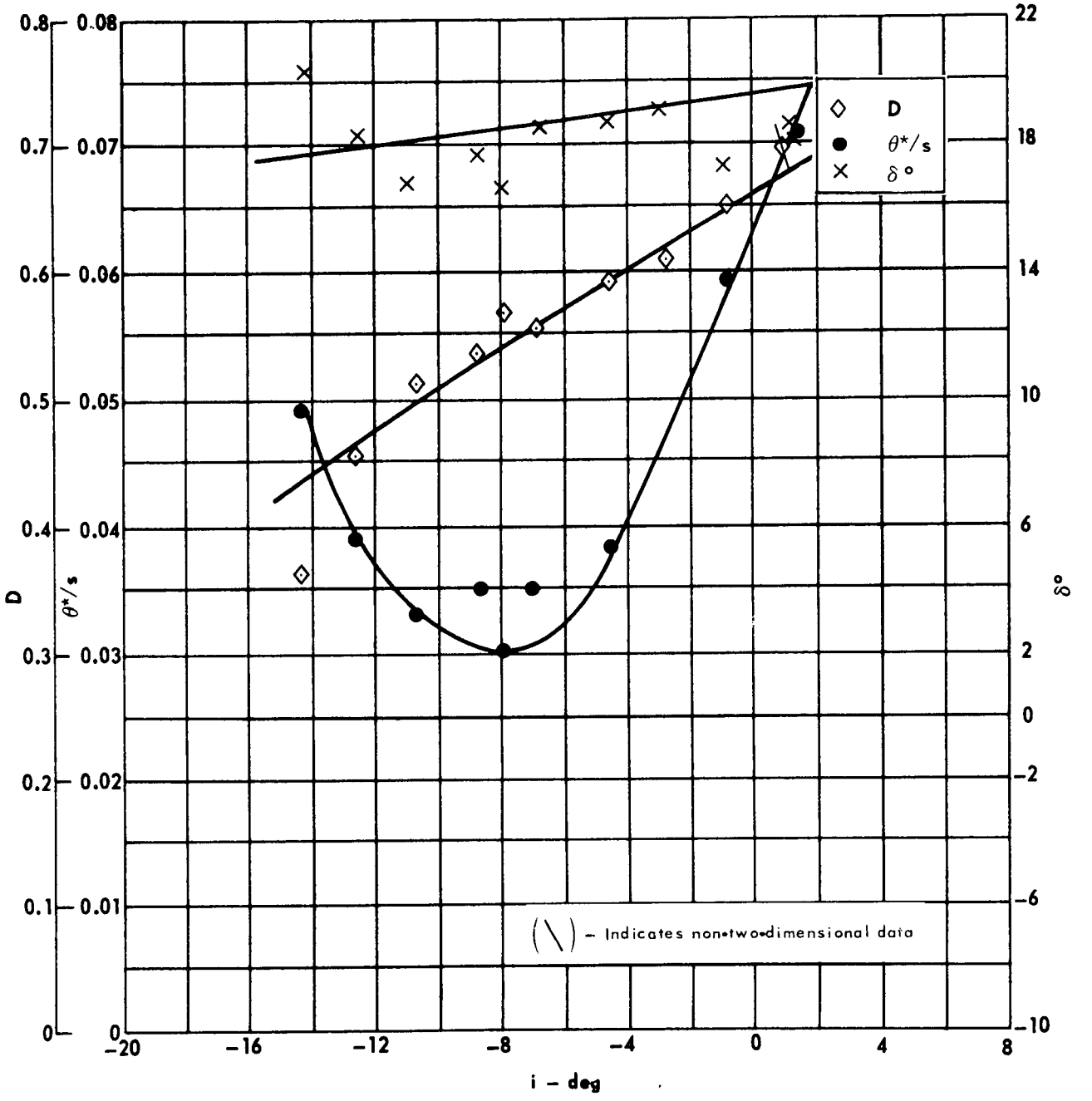

Cascade configuration : $\beta_{1N} = 60$, $\sigma = 1.00$

Double circular-arc profile : $\phi = 45$, $t/c = 0.06$

(b) D, θ^*/s, δ°

Figure 34. – Concluded.

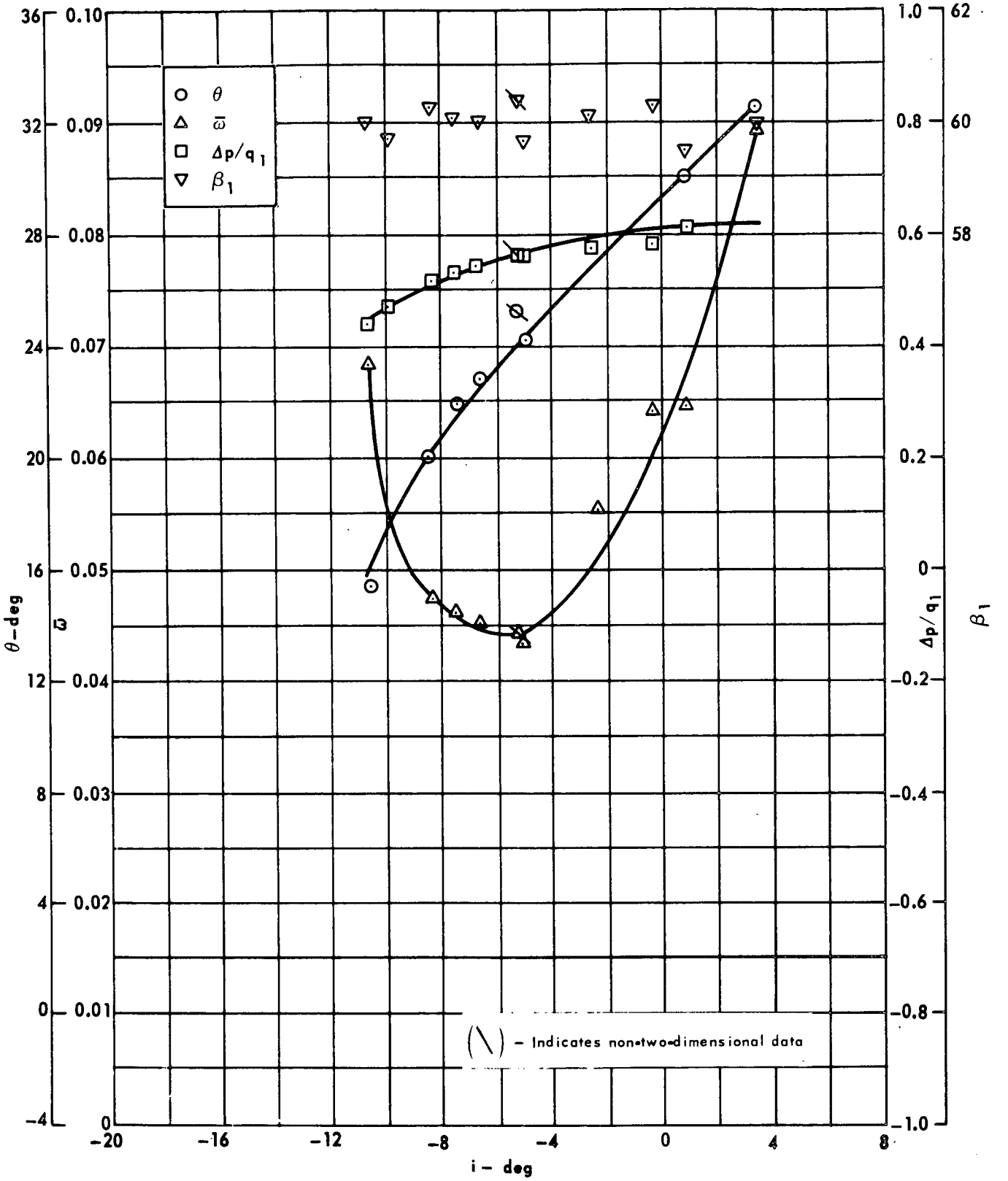

Cascade configuration : $\beta_{1N} = 60$, $\sigma = 1.50$

Double circular–arc profile : $\phi = 45$, $t/c = 0.06$

(a) $\theta, \bar{\omega}, \Delta p/q_1, \beta_1$

Figure 35. – Cascade characteristics as functions of incidence .

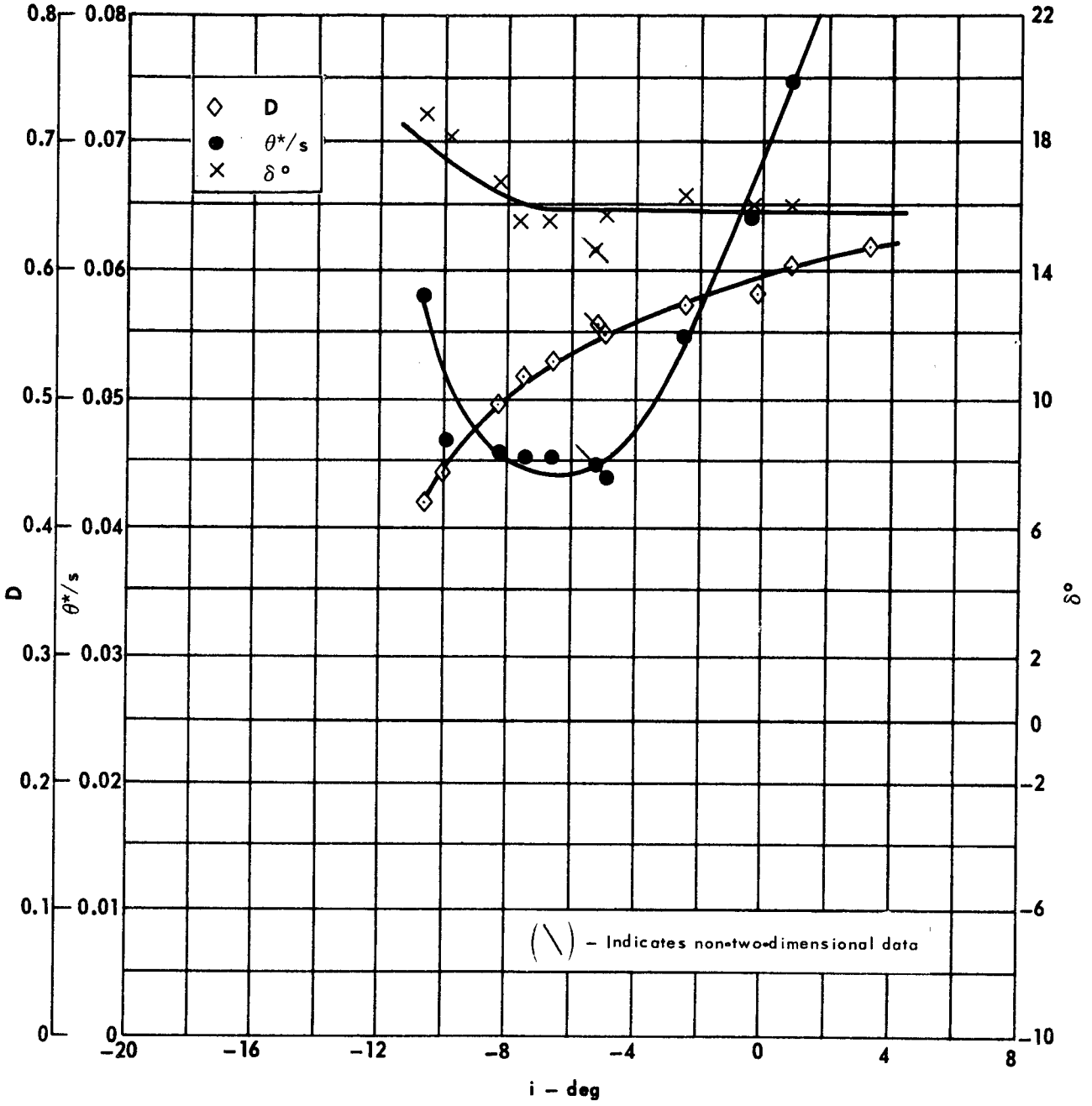

Cascade configuration : $\beta_{1N} = 60$, $\sigma = 1.50$

Double circular-arc profile : $\phi = 45$, $t/c = 0.06$

(b) D, θ^*/s, δ°

Figure 35. – Concluded.

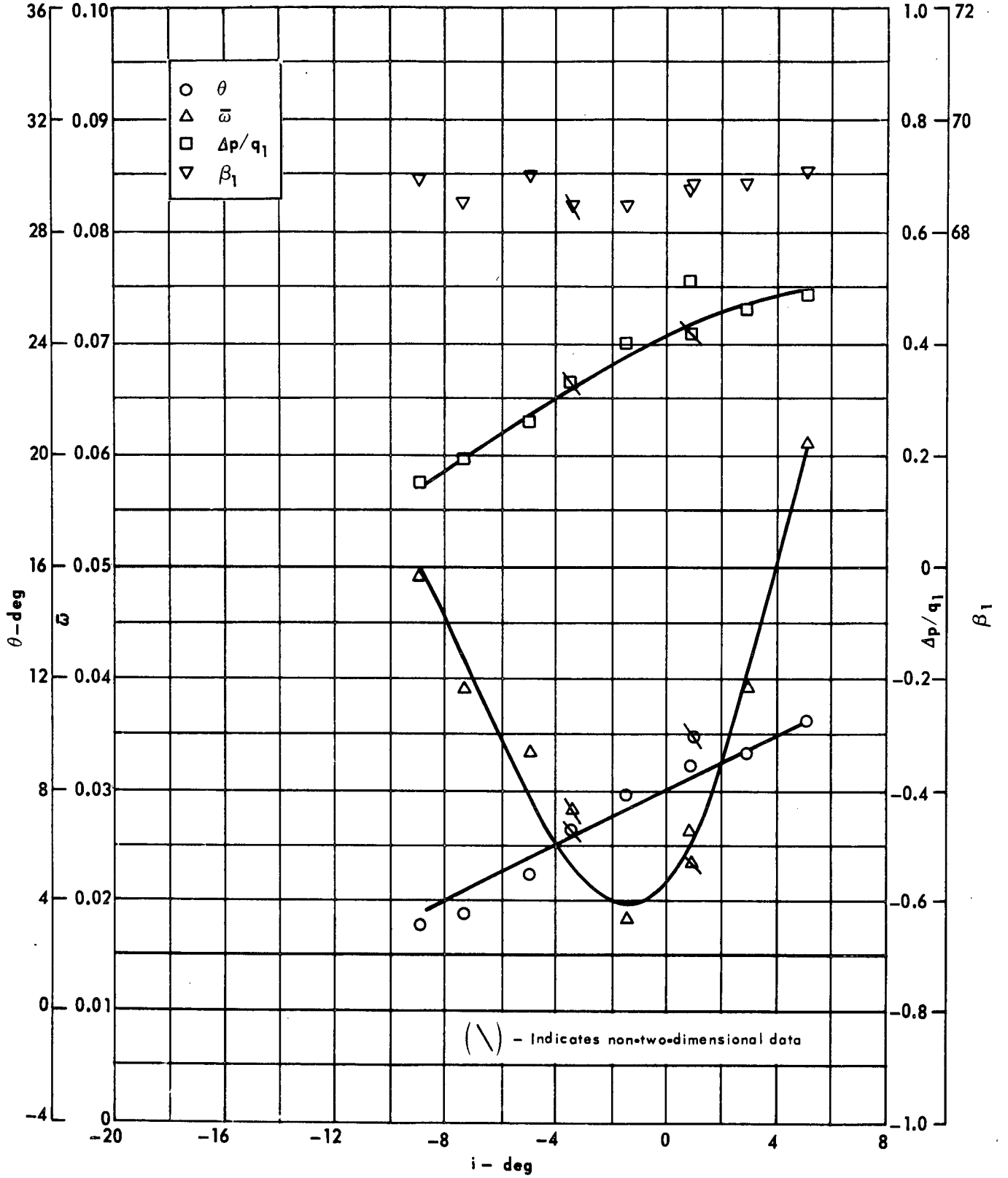

Cascade configuration : $\beta_{1N} = 70$, $\sigma = 0.75$

Double circular-arc profile : $\phi = 20$, $t/c = 0.06$

(a) $\theta, \bar{\omega}, \Delta p/q_1, \beta_1$

Figure 36. – Cascade characteristics as functions of incidence .

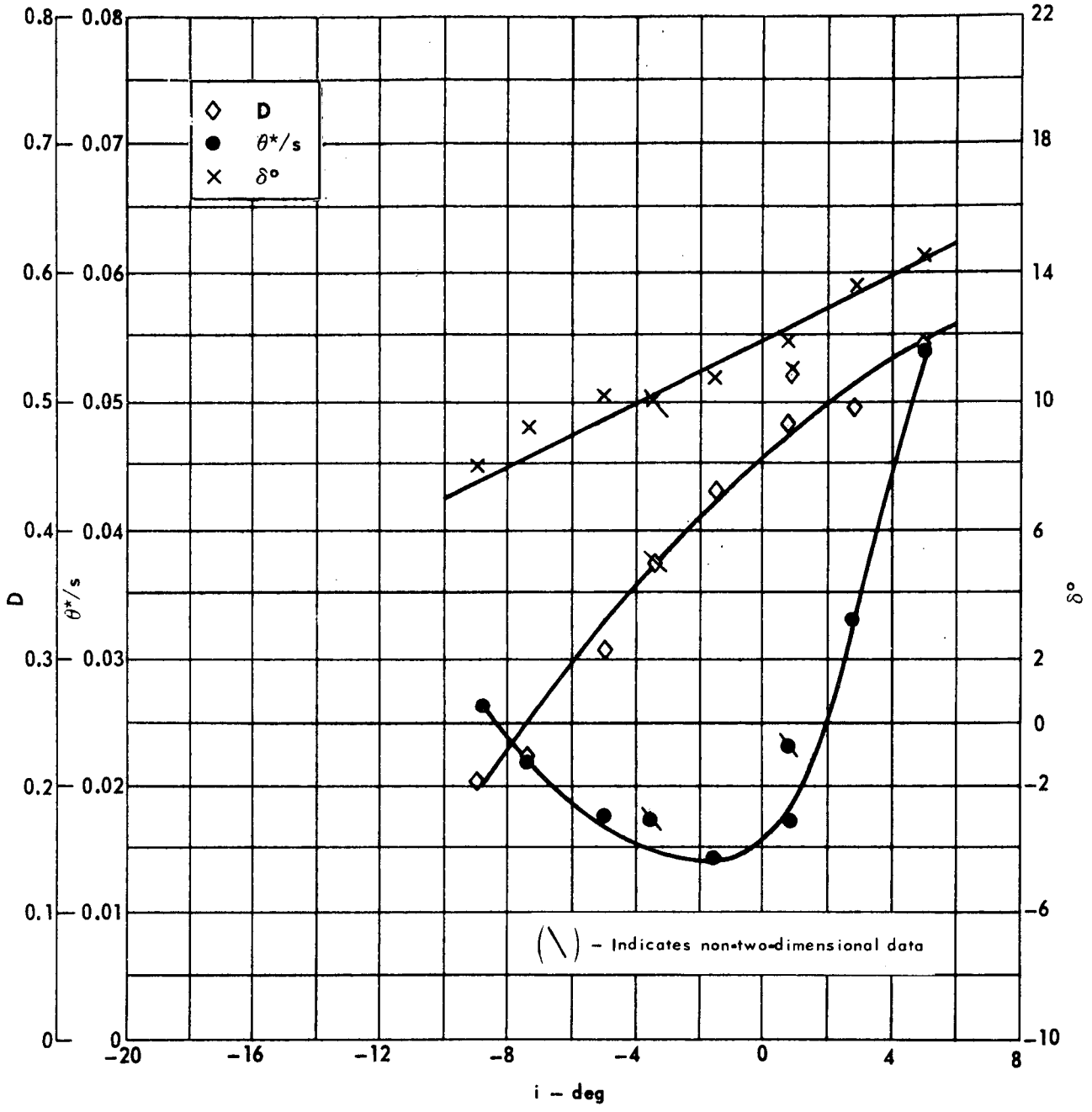

Cascade configuration : $\beta_{1N} = 70$, $\sigma = 0.75$

Double circular-arc profile : $\phi = 20$, $t/c = 0.06$

(b) D, θ^*/s, δ°

Figure 36. – Concluded.

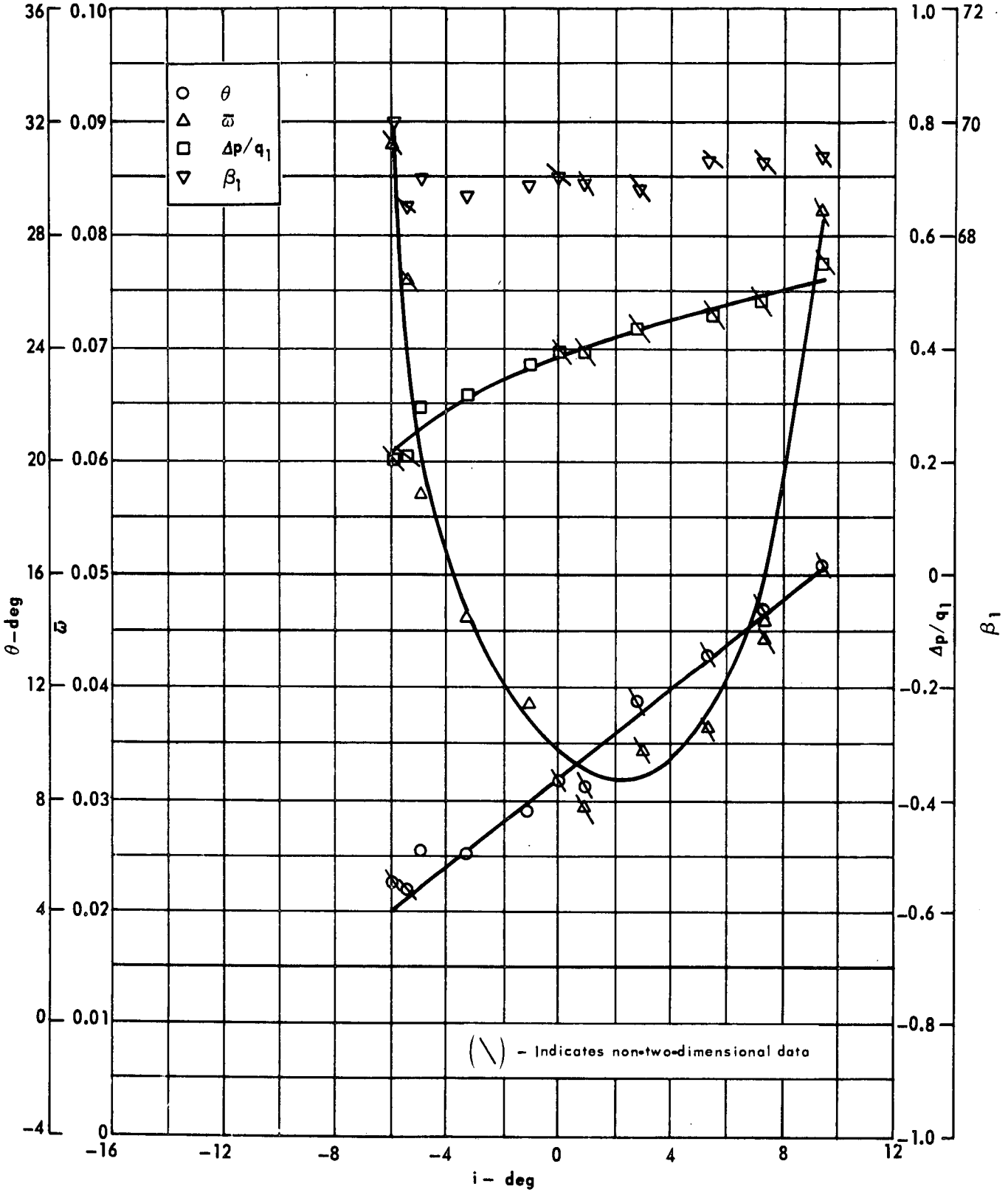

Cascade configuration : $\beta_{1N} = 70$, $\sigma = 1.00$

Double circular-arc profile : $\phi = 20$, $t/c = 0.06$

(a) $\theta, \bar{\omega}, \Delta p/q_1, \beta_1$

Figure 37. – Cascade characteristics as functions of incidence .

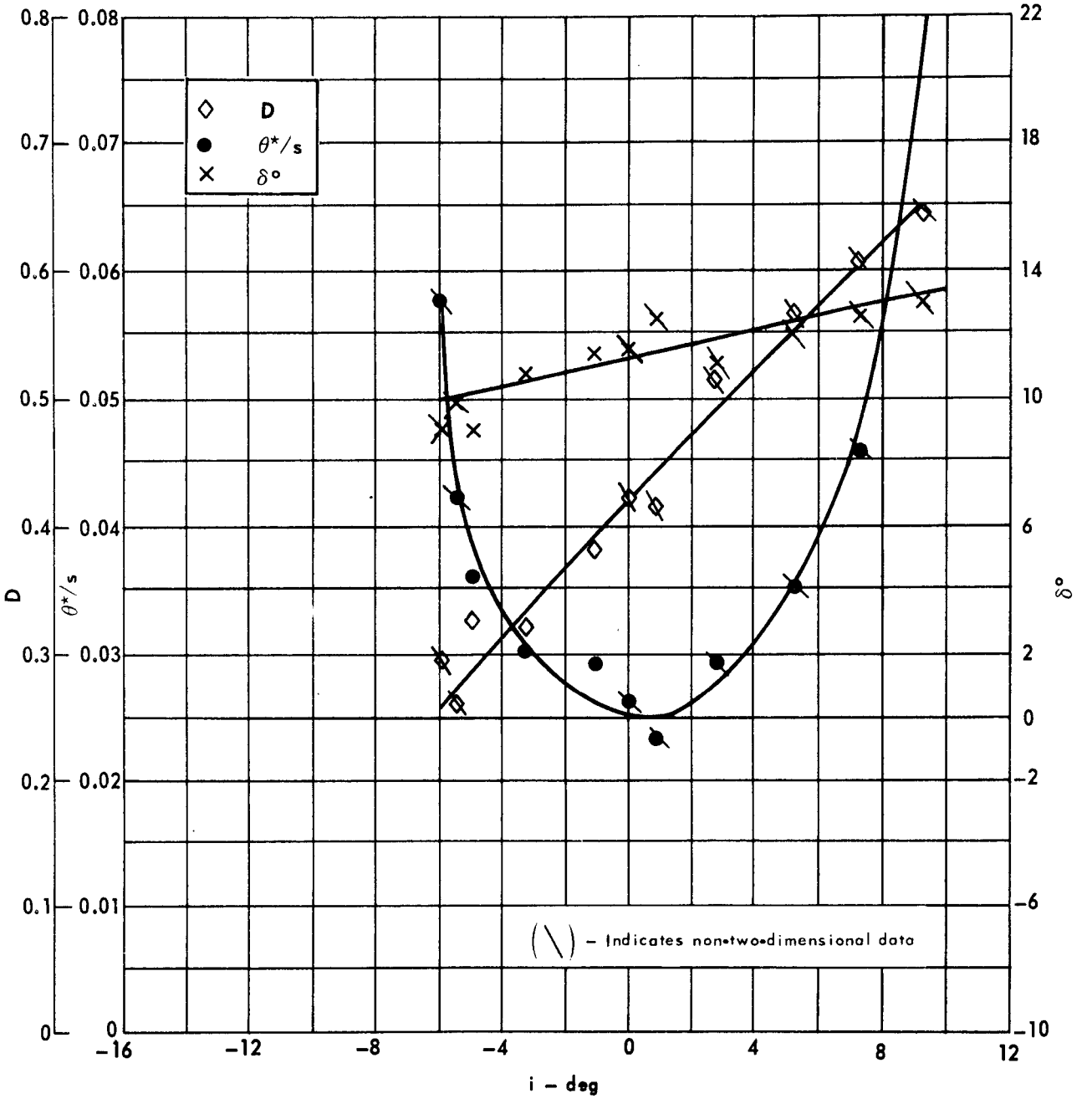

Cascade configuration : $\beta_{1N} = 70$, $\sigma = 1.00$

Double circular–arc profile : $\phi = 20$, $t/c = 0.06$

(b) D, θ^*/s, δ°

Figure 37. – Concluded.

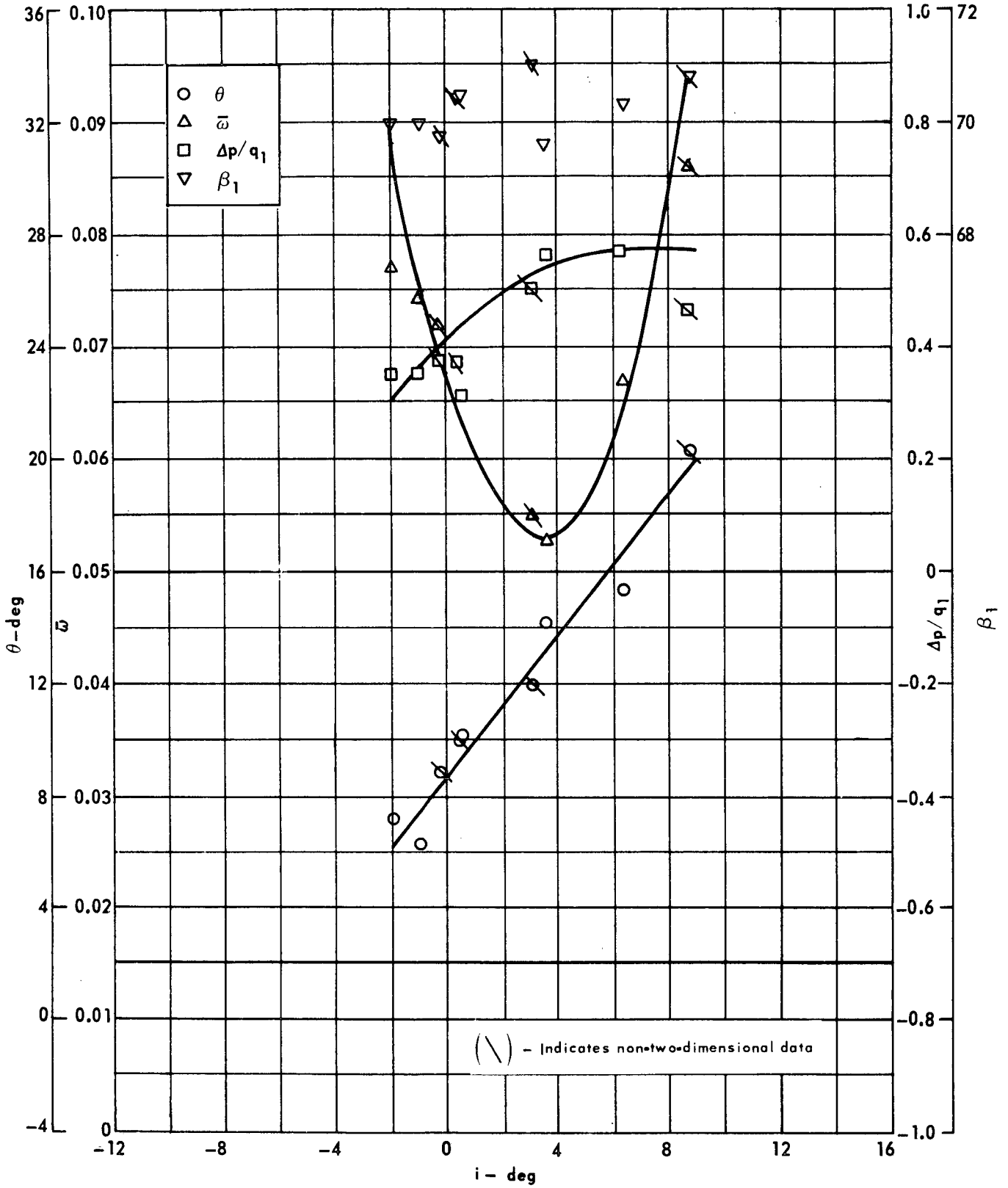

Cascade configuration : $\beta_{1N} = 70$, $\sigma = 1.50$

Double circular–arc profile : $\phi = 20$, $t/c = 0.06$

(a) $\theta, \bar{\omega}, \Delta p/q_1, \beta_1$

Figure 38. – Cascade characteristics as functions of incidence .

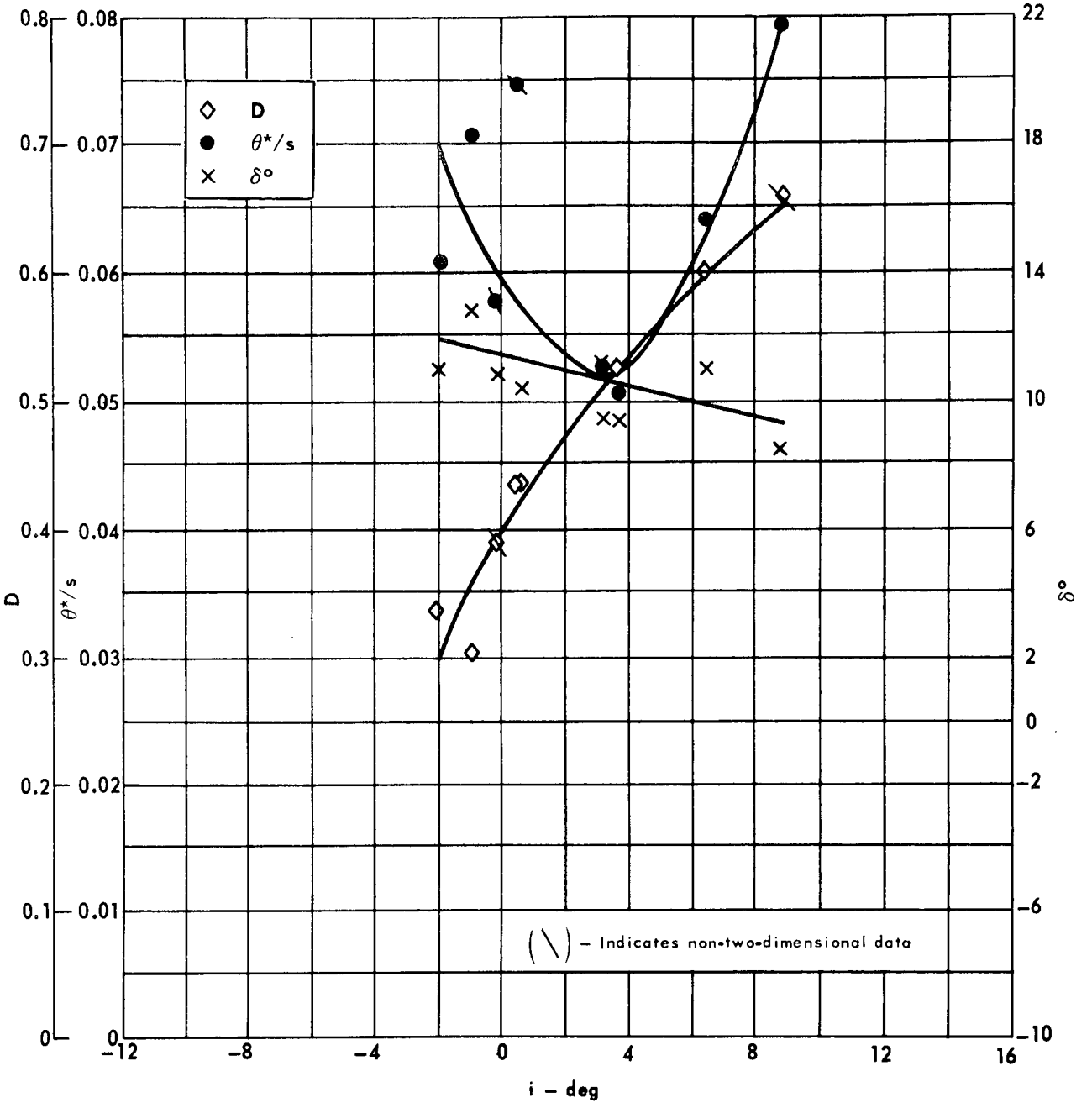

Cascade configuration : $\beta_{1N} = 70$, $\sigma = 1.50$

Double circular–arc profile : $\phi = 20$, $t/c = 0.06$

(b) D, θ^*/s, δ°

Figure 38. – Concluded.

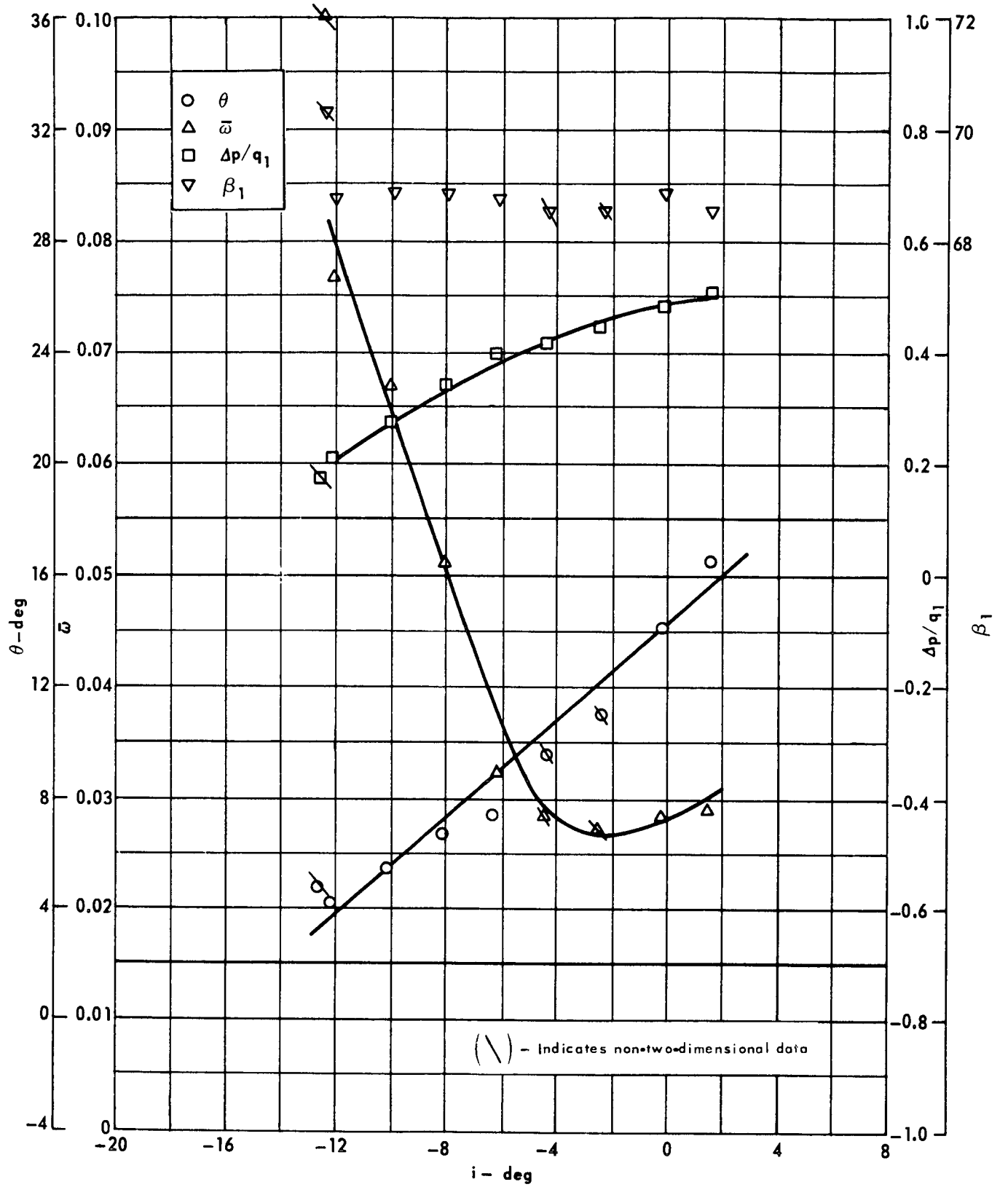

Cascade configuration : $\beta_{1N} = 70$, $\sigma = 0.75$

Double circular-arc profile : $\phi = 30$, $t/c = 0.06$

(a) $\theta, \bar{\omega}, \Delta p/q_1, \beta_1$

Figure 39. – Cascade characteristics as functions of incidence .

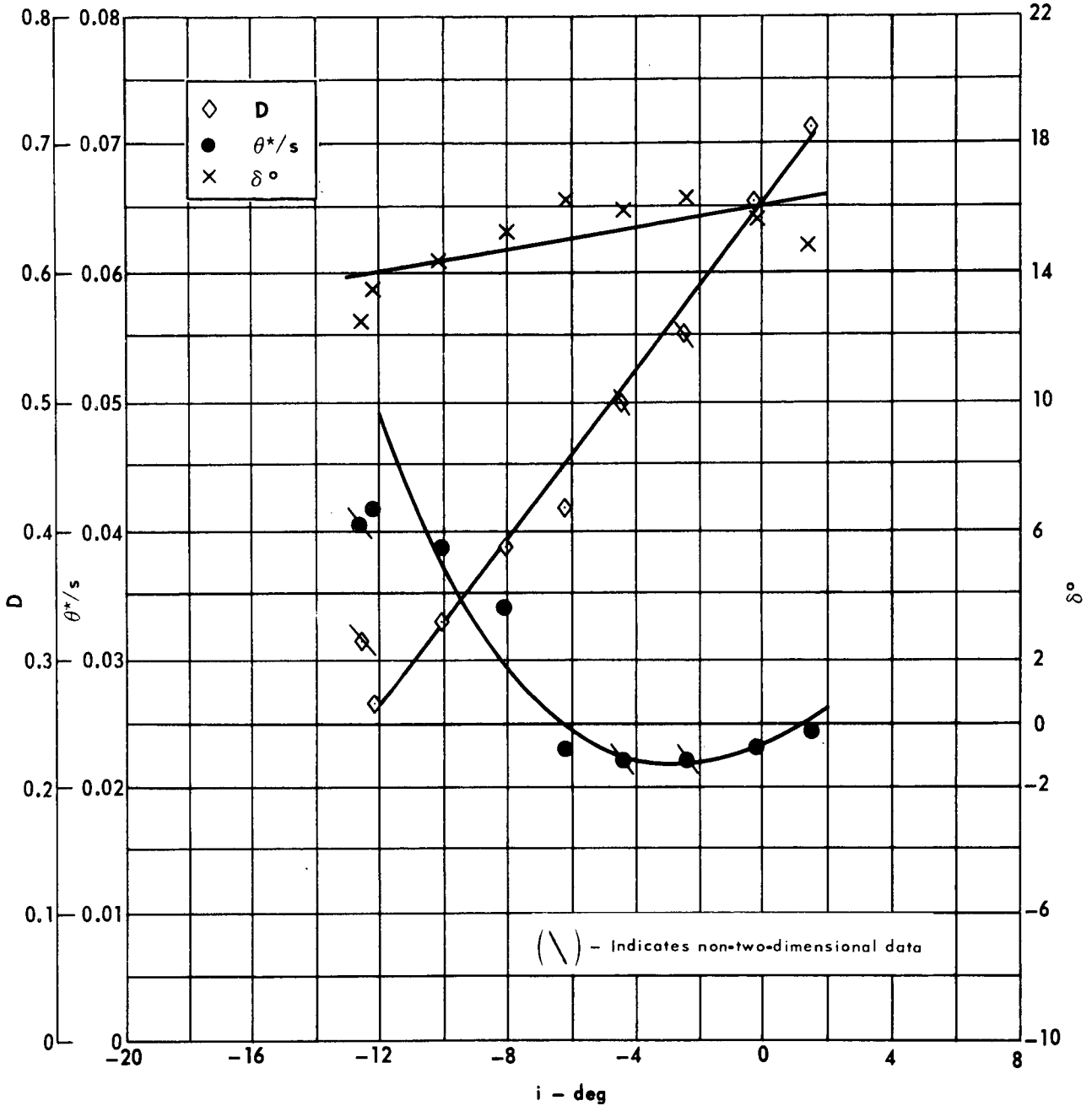

Cascade configuration : $\beta_{1N} = 70$, $\sigma = 0.75$

Double circular–arc profile : $\phi = 30$, $t/c = 0.06$

(b) D, θ^*/s, δ°

Figure 39. – Concluded.

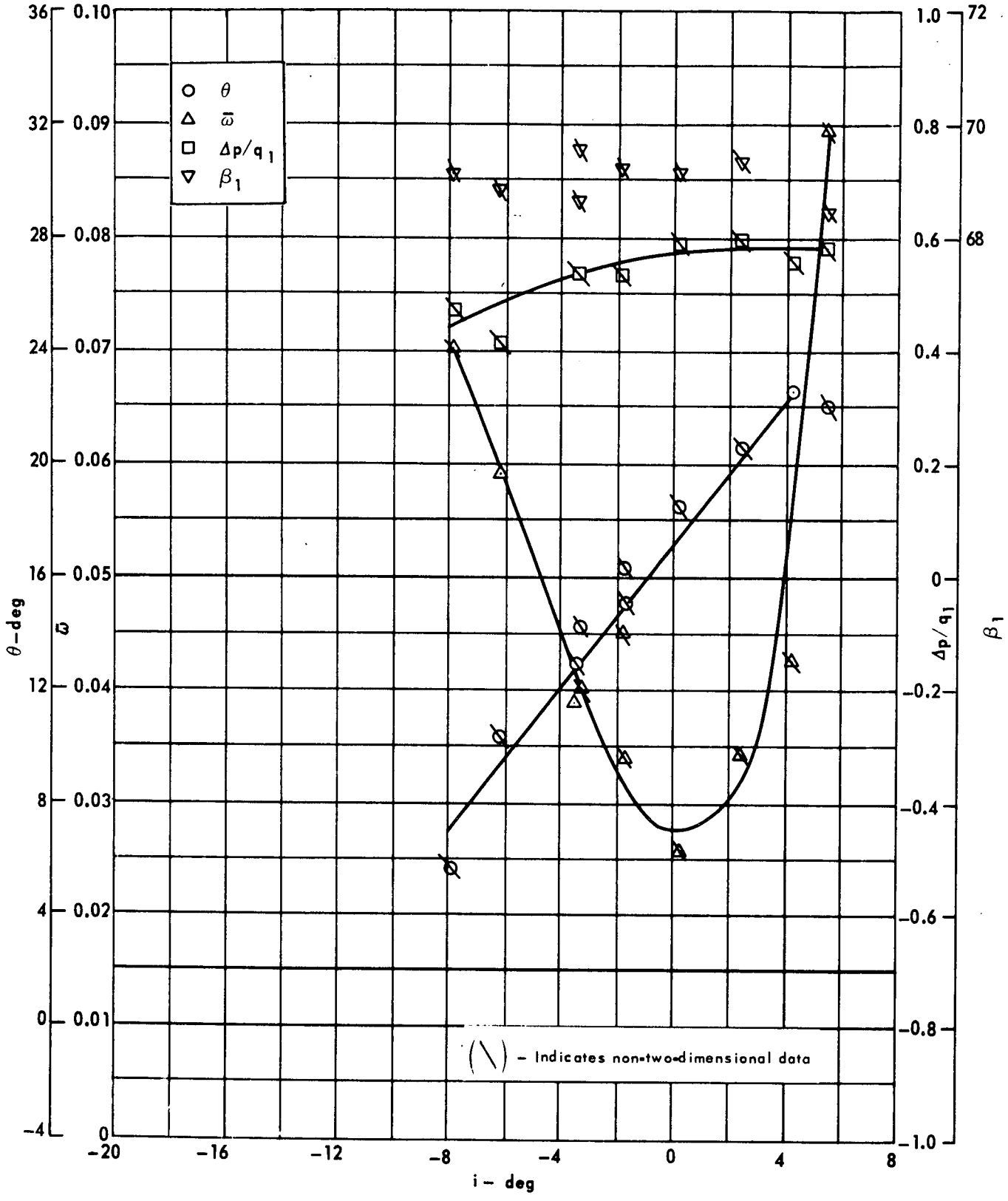

Cascade configuration : $\beta_{1N} = 70$, $\sigma = 1.00$

Double circular–arc profile : $\phi = 30$, $t/c = 0.06$

(a) $\theta, \bar{\omega}, \Delta p/q_1, \beta_1$

Figure 40. – Cascade characteristics as functions of incidence .

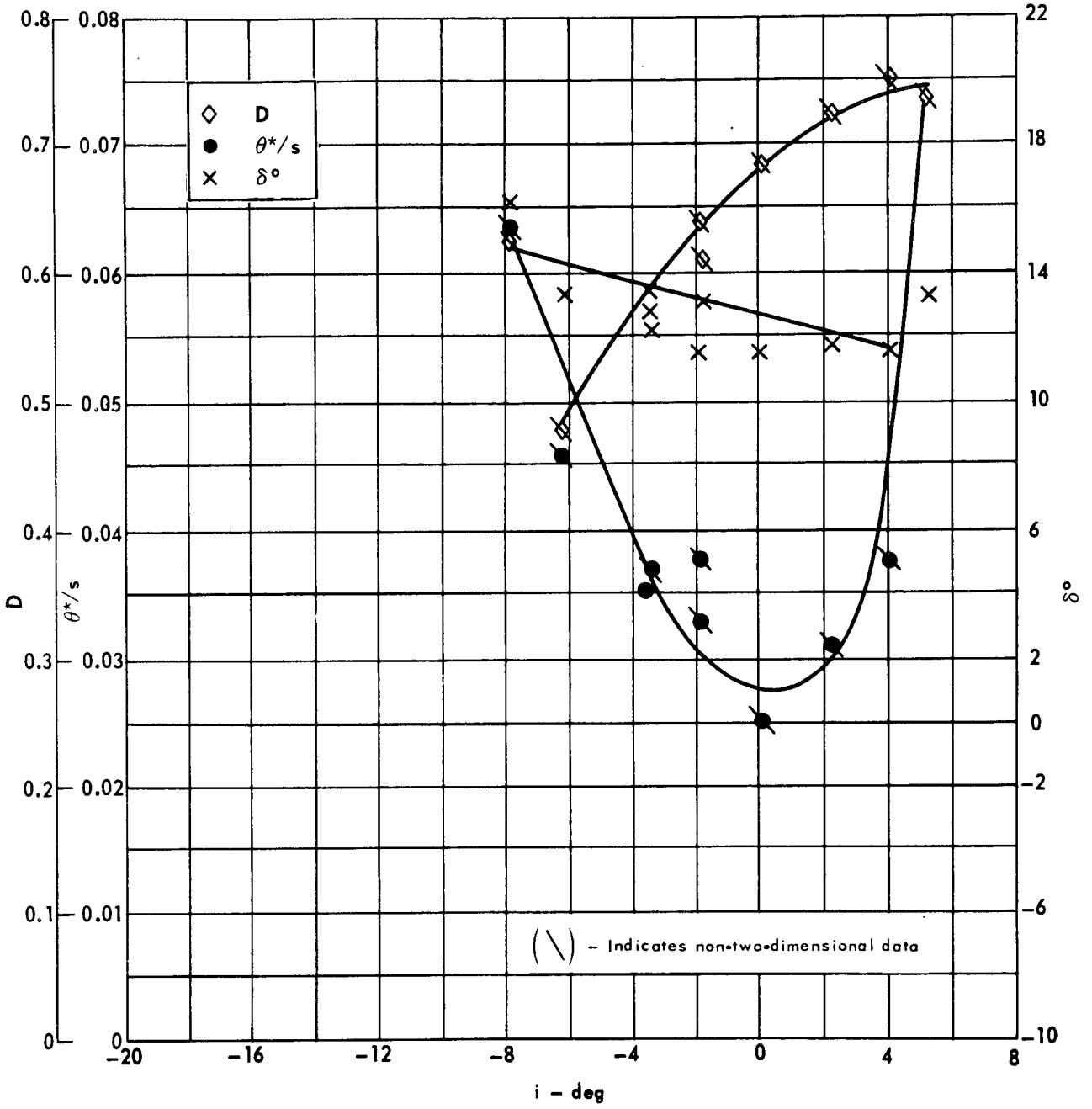

Cascade configuration : $\beta_{1N} = 70$, $\sigma = 1.00$

Double circular-arc profile : $\phi = 30$, $t/c = 0.06$

(b) D, θ^*/s, δ°

Figure 40. – Concluded.

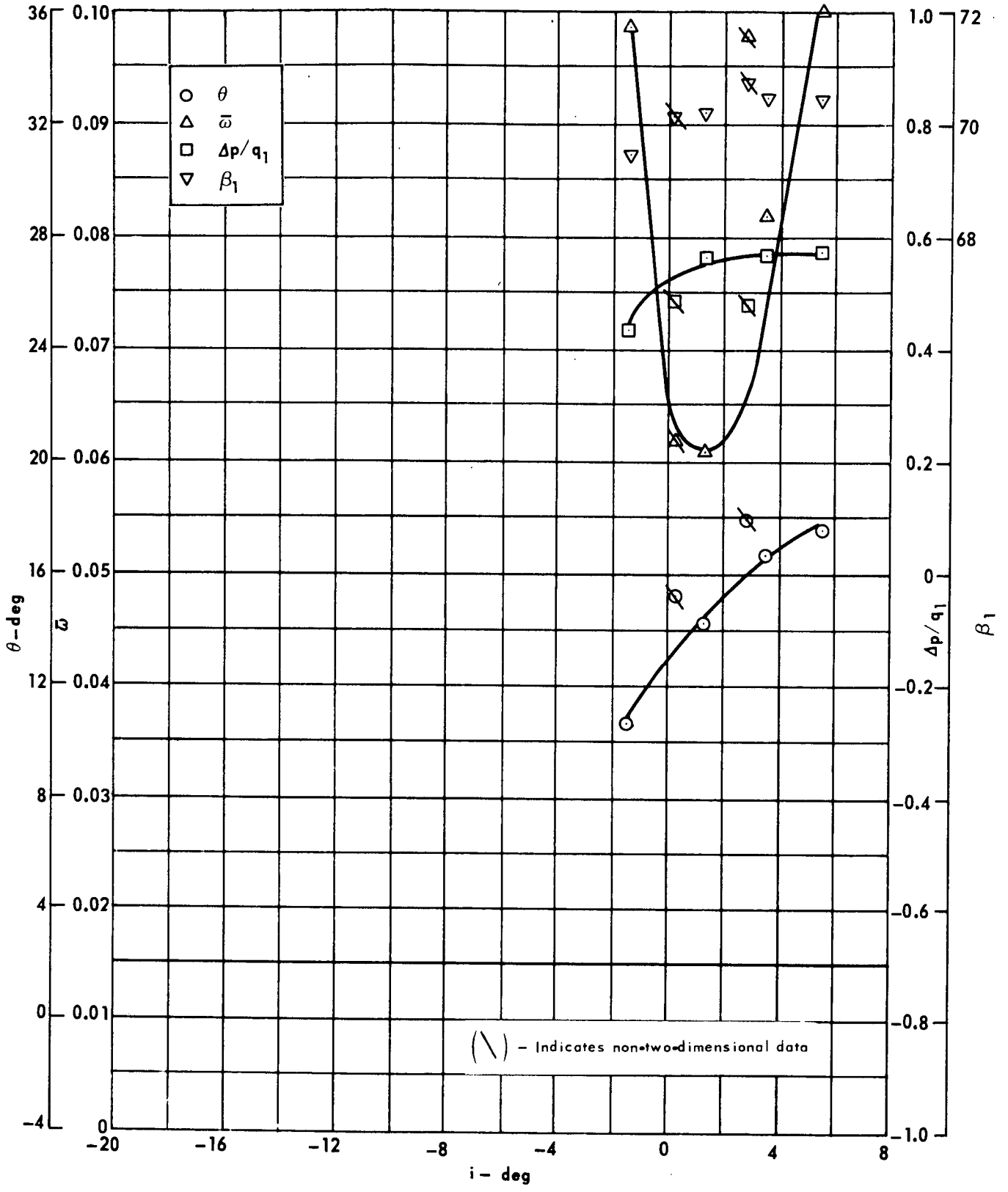

Cascade configuration : $\beta_{1N} = 70$, $\sigma = 1.50$

Double circular-arc profile : $\phi = 30$, $t/c = 0.06$

(a) $\theta, \bar{\omega}, \Delta p/q_1, \beta_1$

Figure 41. Cascade characteristics as functions of incidence .

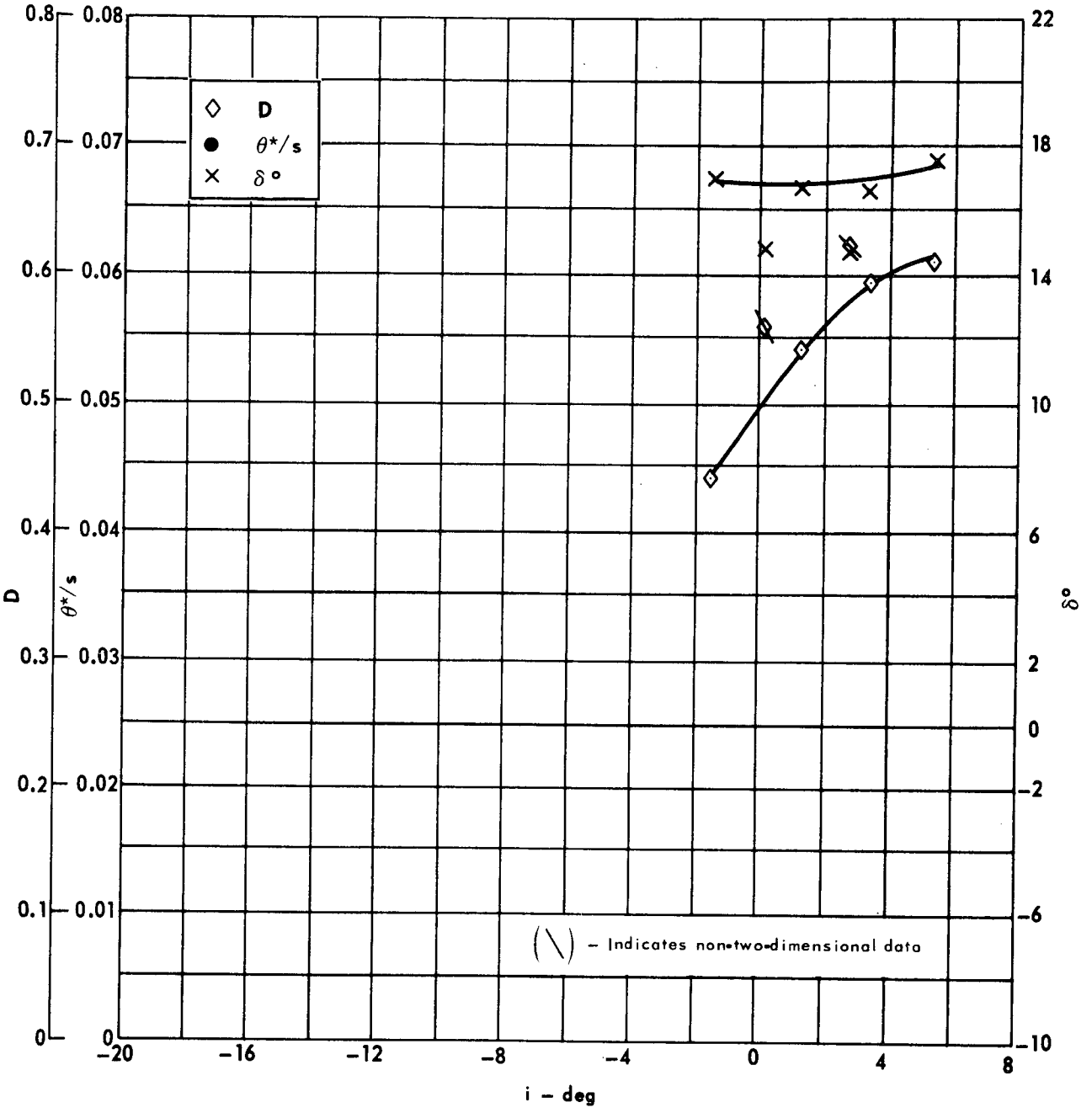

Cascade configuration : $\beta_{1N} = 70$, $\sigma = 1.50$

Double circular–arc profile : $\phi = 30$, $t/c = 0.06$

(b) D, θ^*/s, δ°

Figure 41. – Concluded.

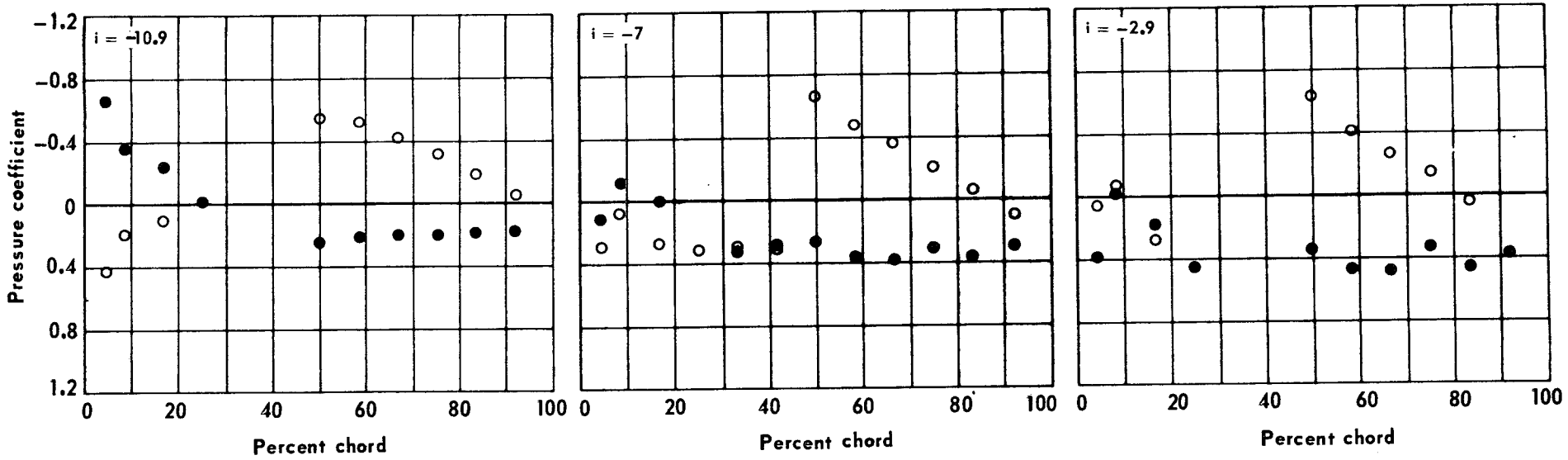

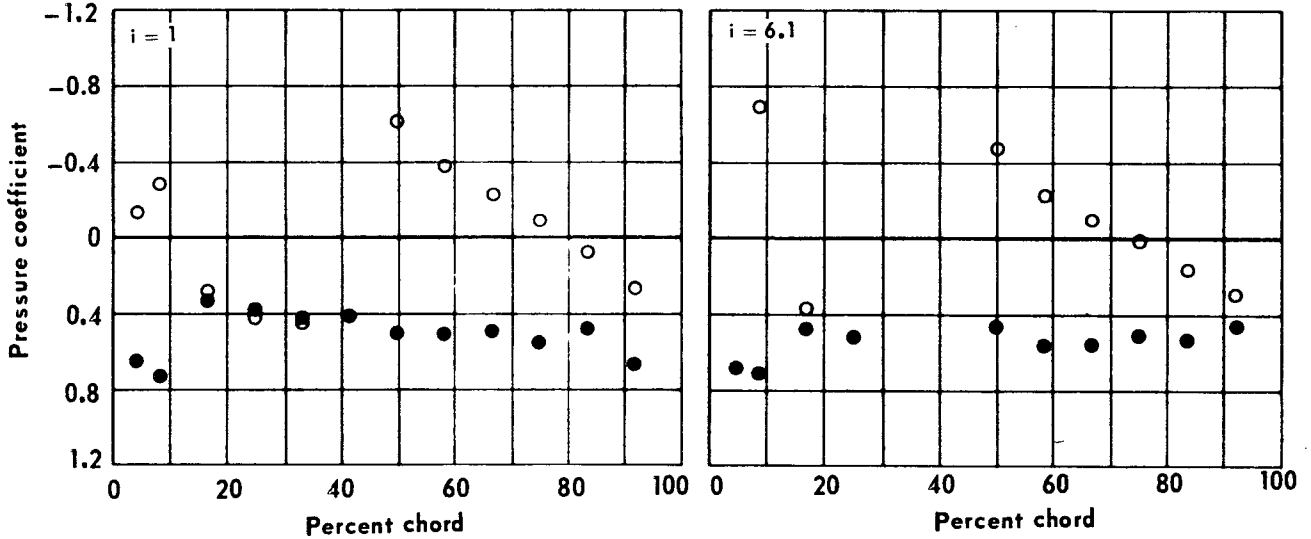

(a) $\beta_{IN} = 50, \phi = 30, \sigma = 0.75$ (Slotted)

Figure 42. – Pressure distribution for double circular–arc hydrofoils.

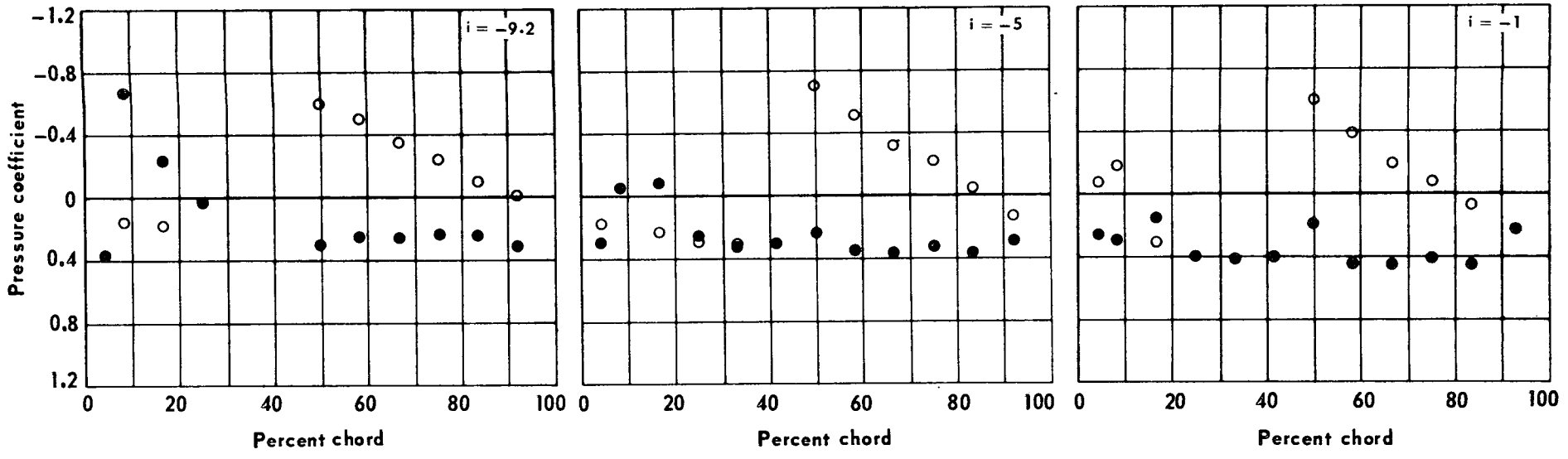

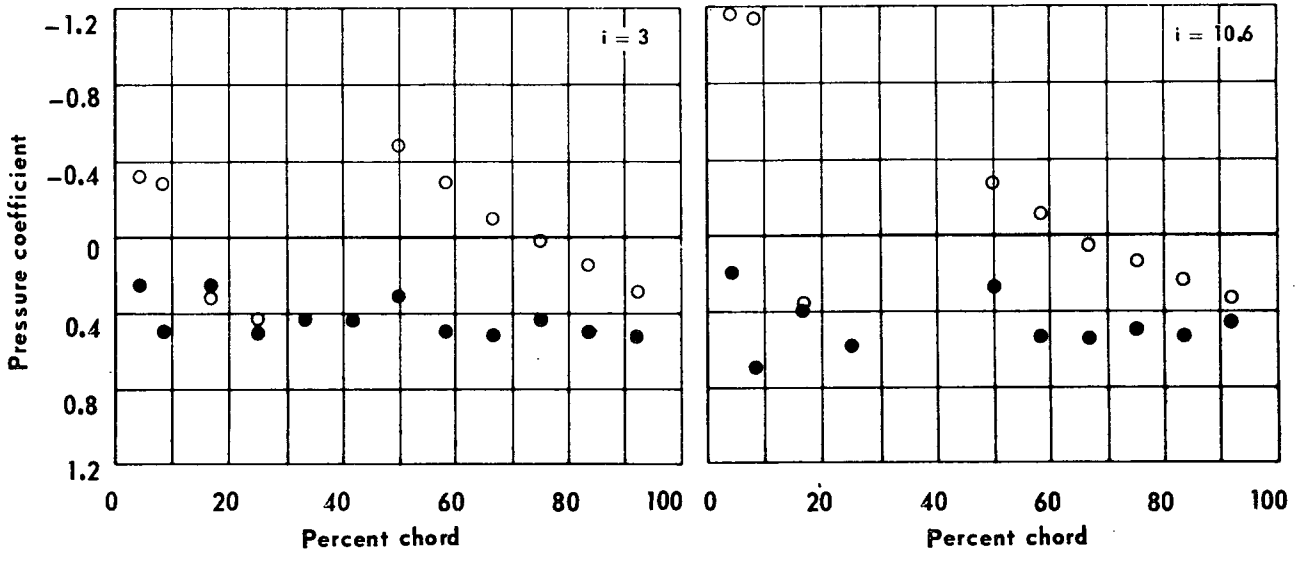

(b) $\beta_{IN} = 50 \cdot \phi = 30 \cdot \sigma = 1.00$ (Slotted)

Figure 42. – Continued.

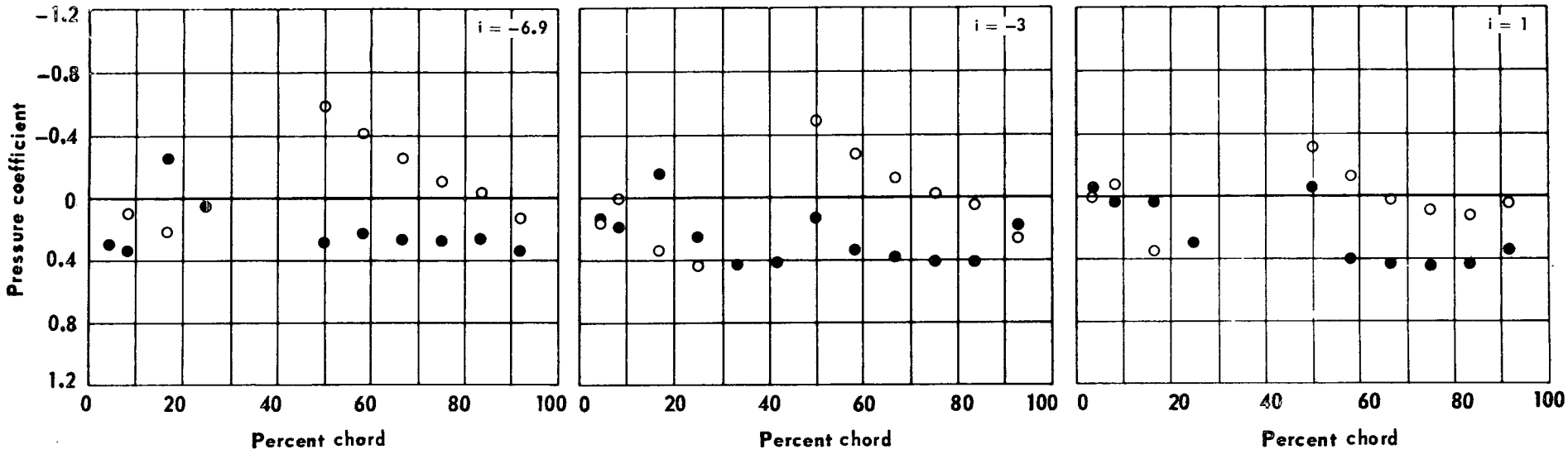

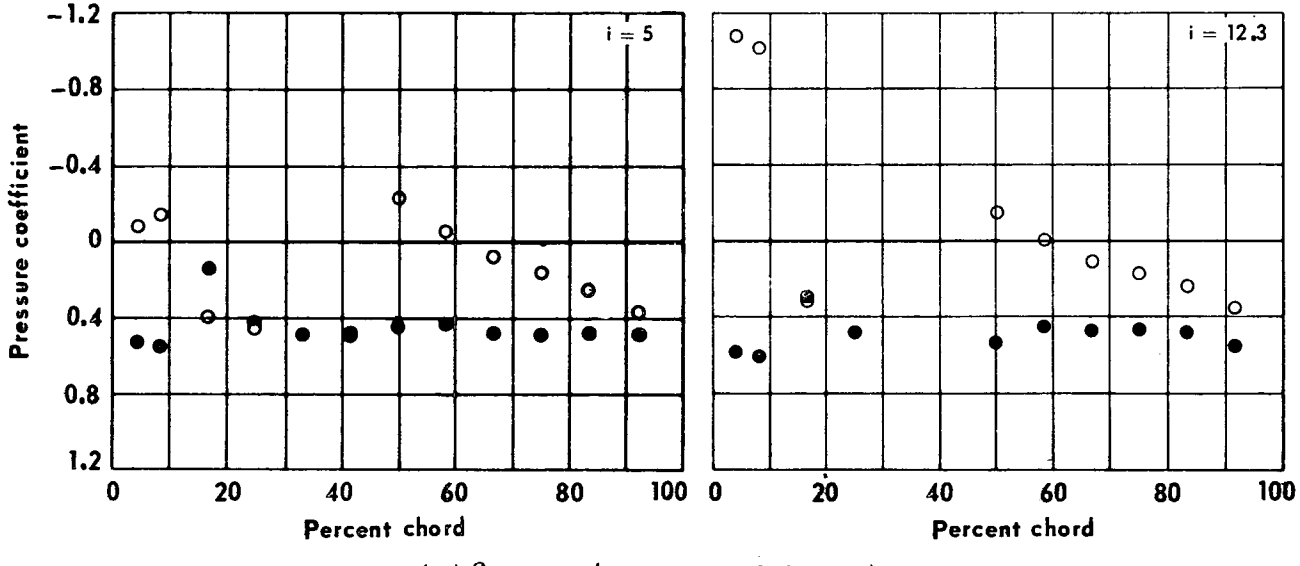

(c) $\beta_{IN} = 50, \phi = 30, \sigma = 1.50$ (Slotted)

Figure 42. – Concluded.

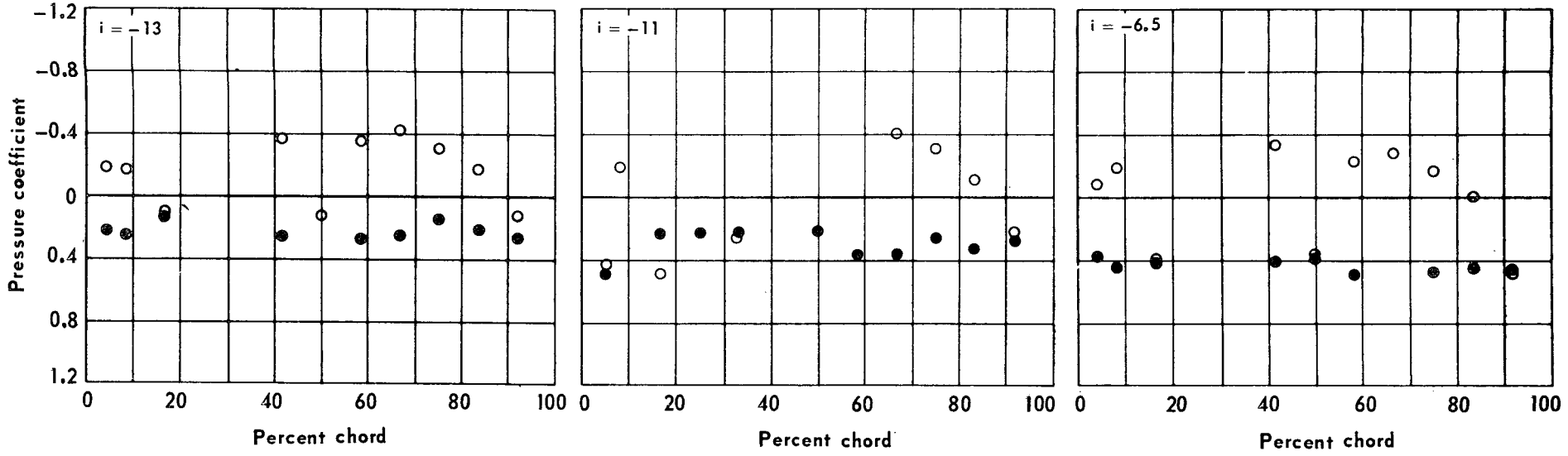

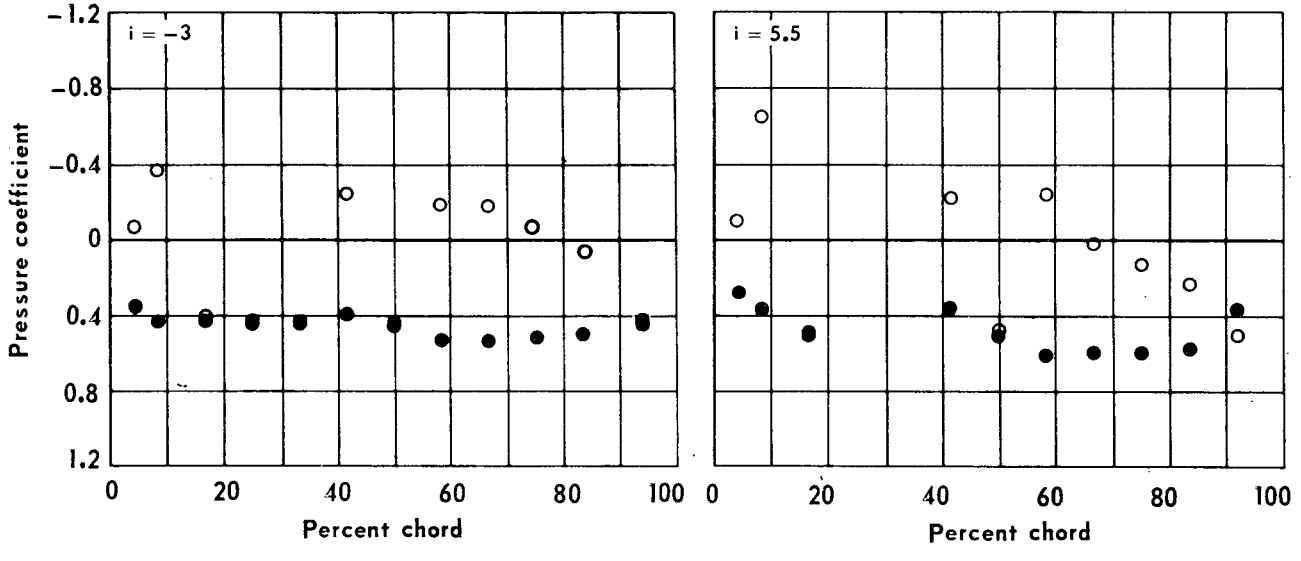

(a) $\beta_{IN} = 60, \phi = 30, \sigma = 0.75$ (Slotted)

Figure 43. – Pressure distribution for double circular–arc hydrofoils.

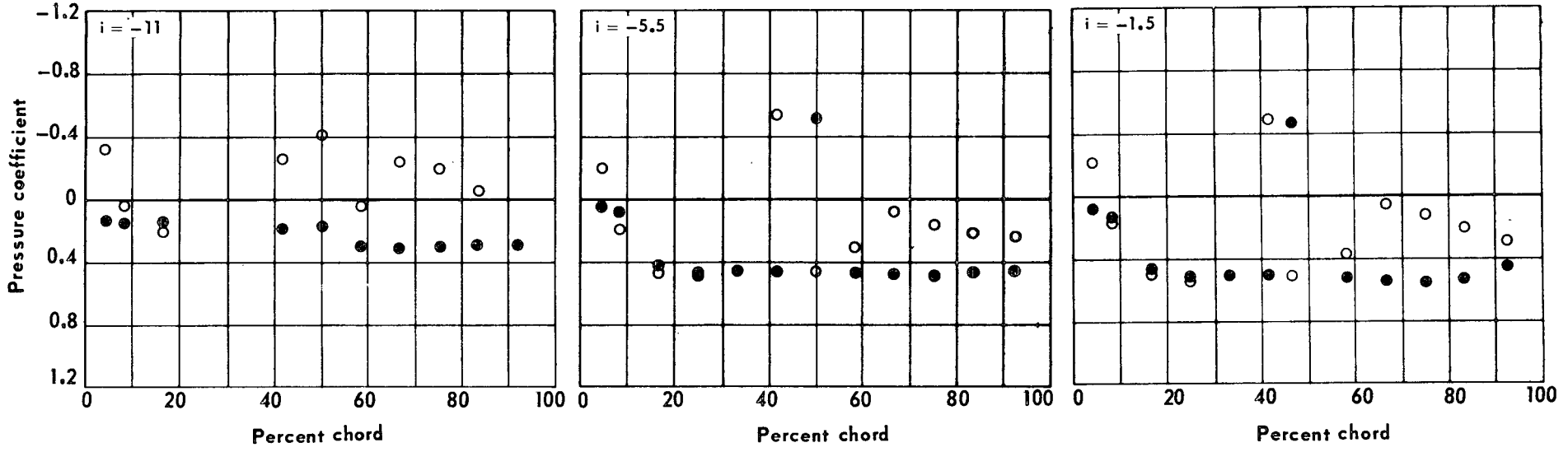

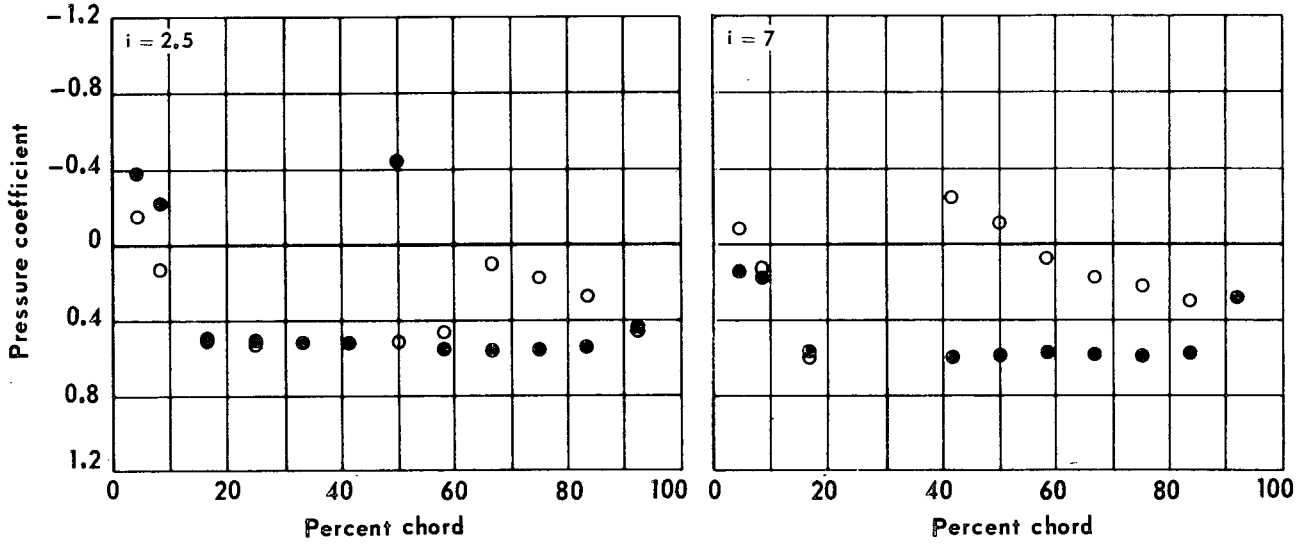

(b) $\beta_{IN} = 60, \phi = 30, \sigma = 1.00$ (Slotted)

Figure 43. – Continued.

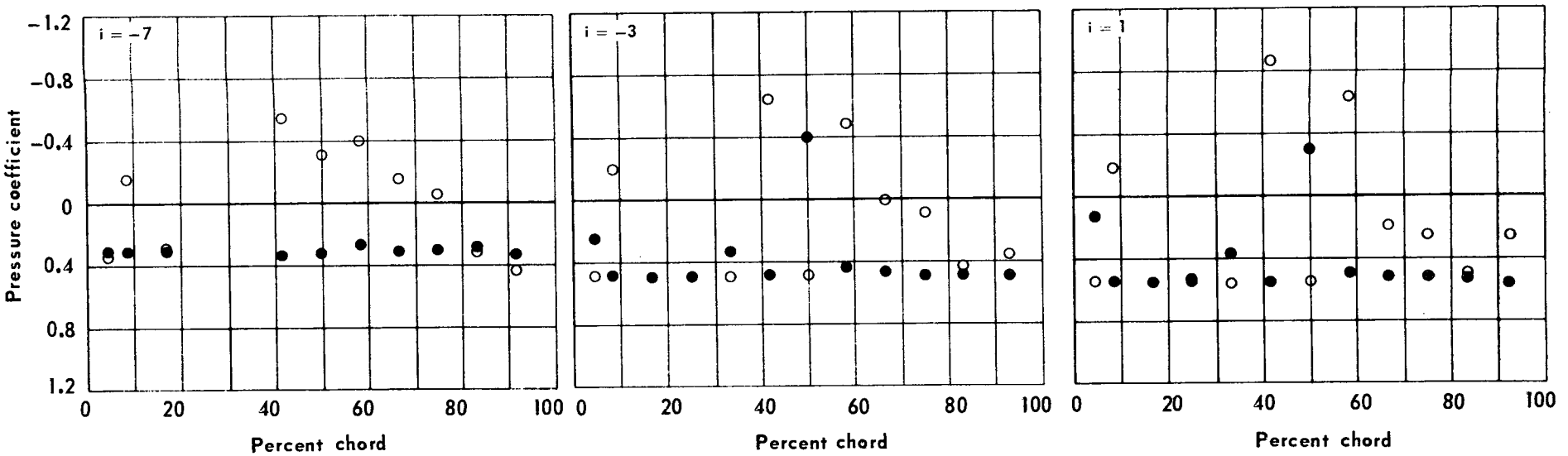

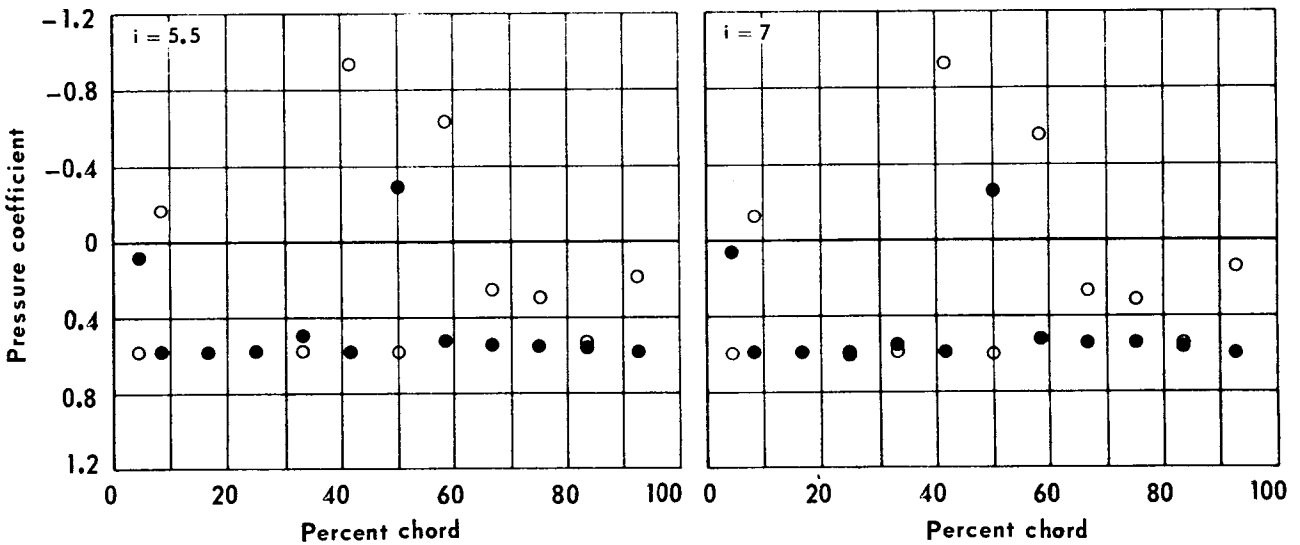

(c) $\beta_{IN} = 60, \phi = 30, \sigma = 1.50$ (Slotted)

Figure 43. – Concluded.

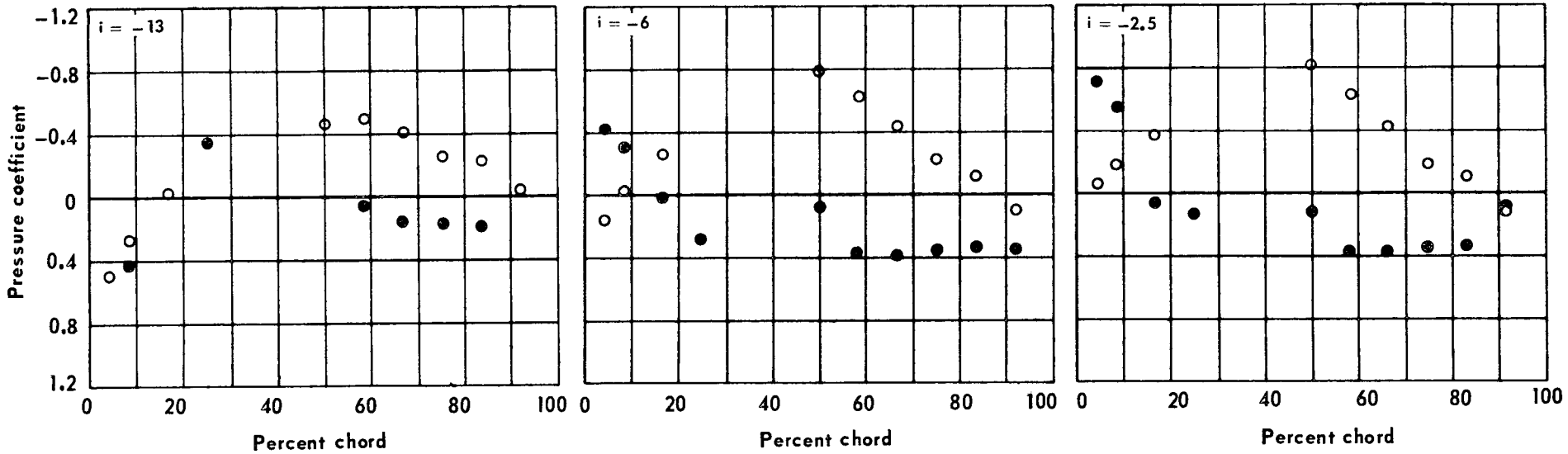

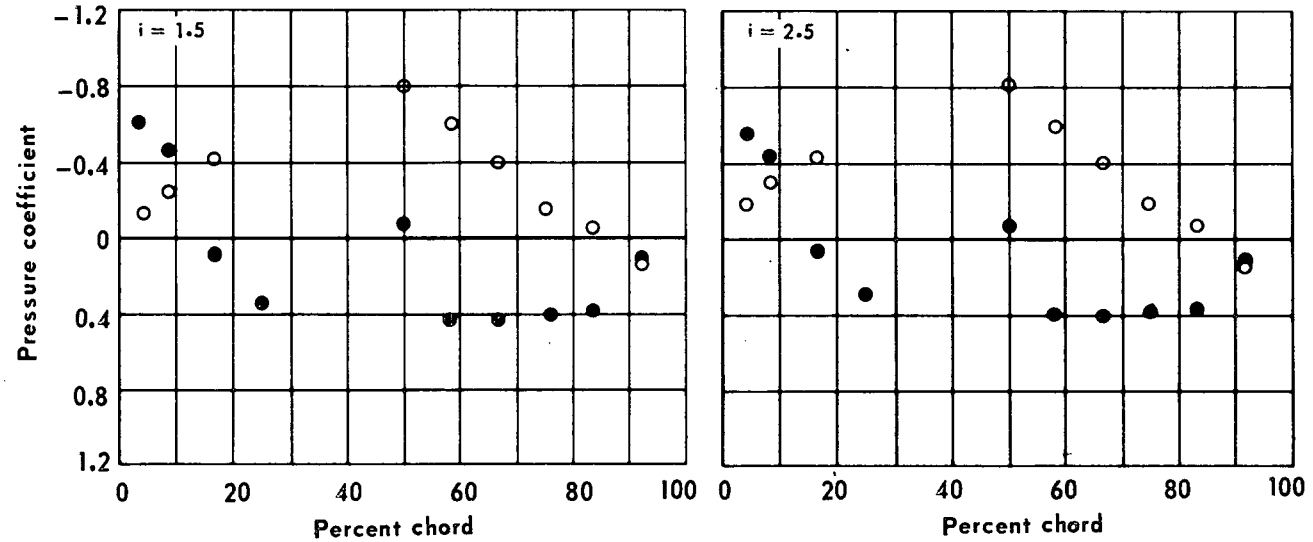

(a) $\beta_{IN} = 70, \phi = 30, \sigma = 0.75$ (Slotted)

Figure 44. – Pressure distribution for double circular–arc hydrofoils.

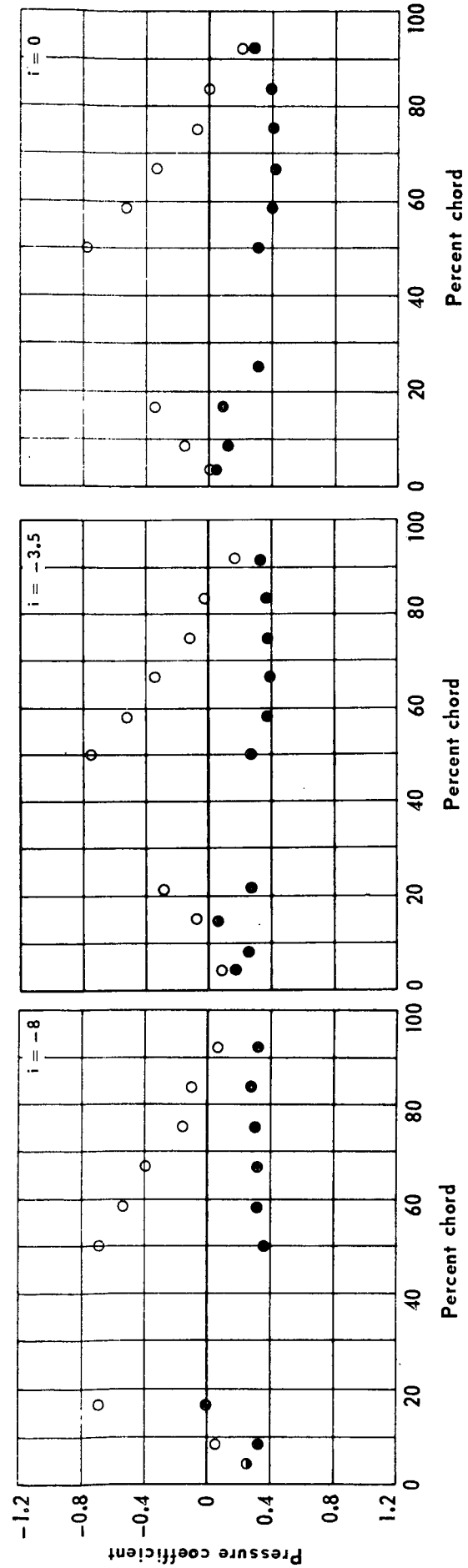

(b) $\beta_{IN} = 70, \phi = 30, \sigma = 1.00$ (Slotted)

Figure 44. – Continued.

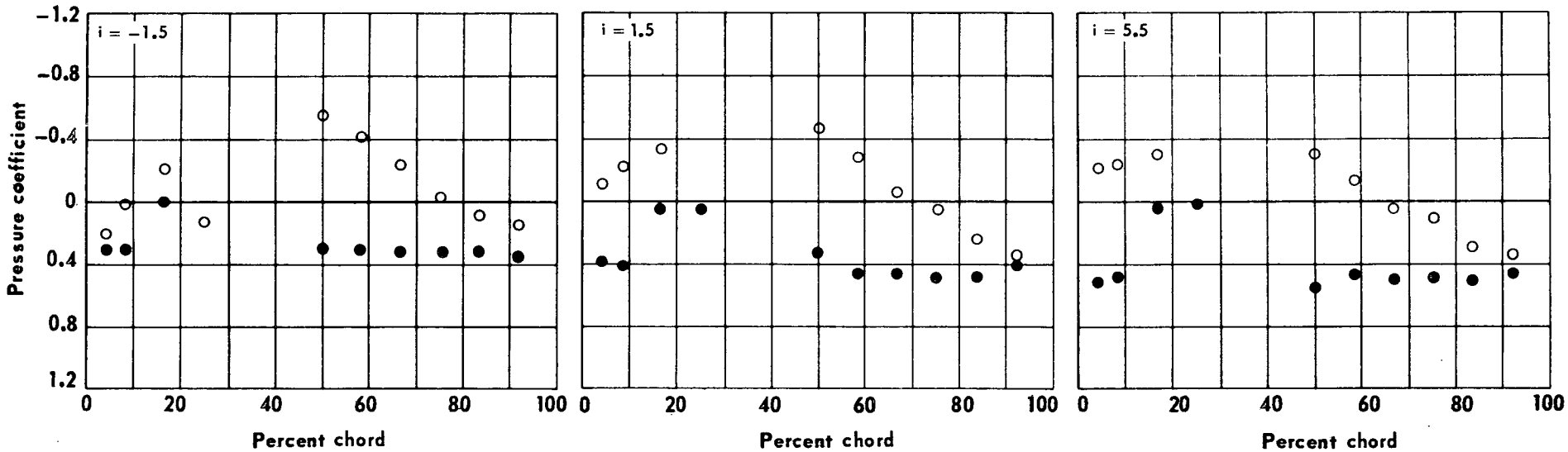

(c) $\beta_{IN} = 70, \phi = 30, \sigma = 1.50$ (Slotted)

Figure 44. – Concluded.

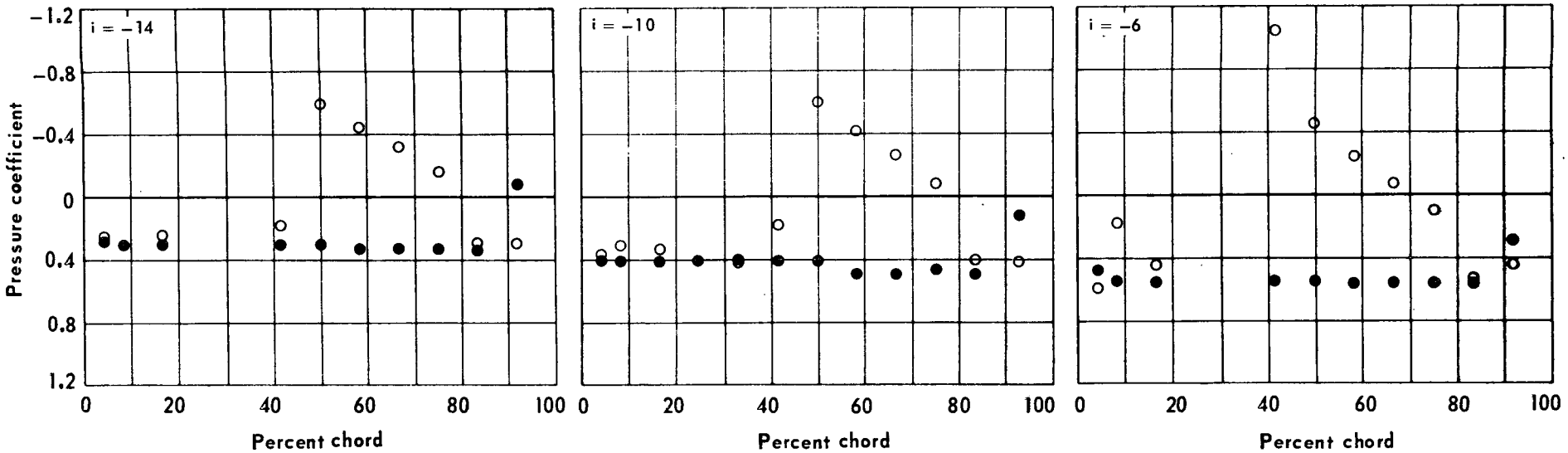

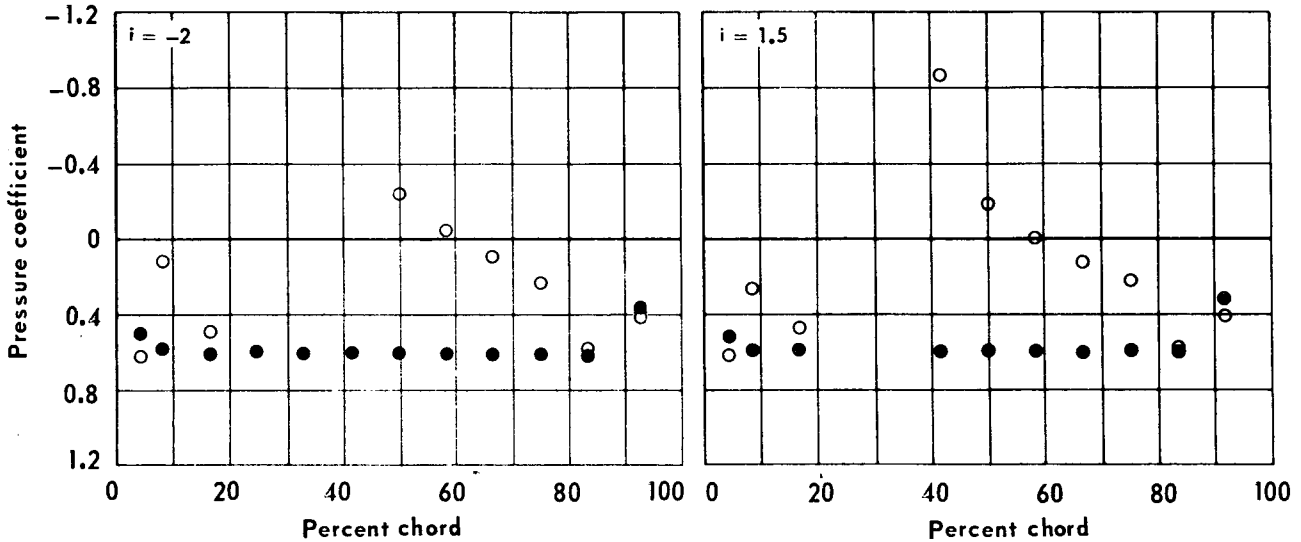

(a) $\beta_{IN} = 60, \phi = 40, \sigma = 1.00$ (Slotted)

Figure 45. – Pressure distribution for double circular–arc hydrofoils.

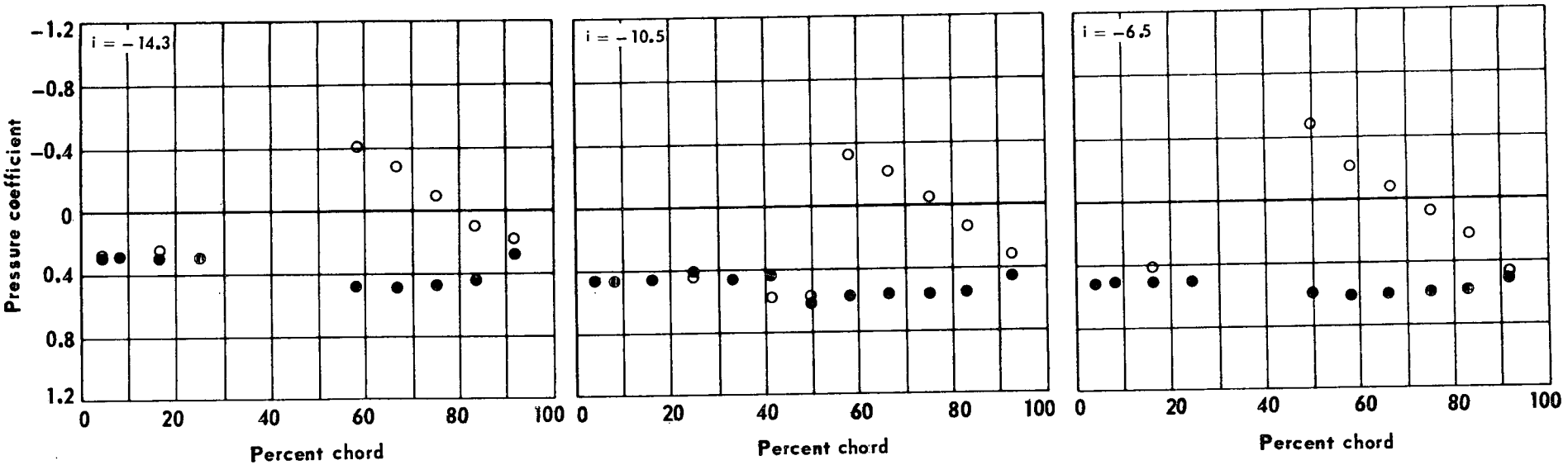

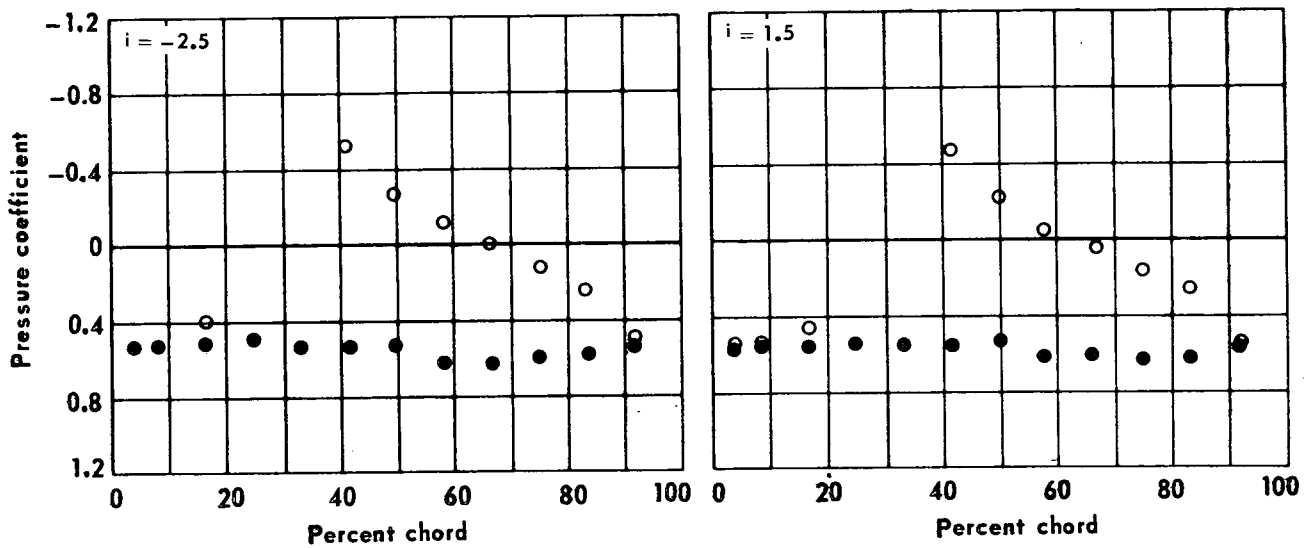

(b) $\beta_{IN} = 60, \phi = 45, \sigma = 1.00$ (Slotted)

Figure 45. – Concluded.

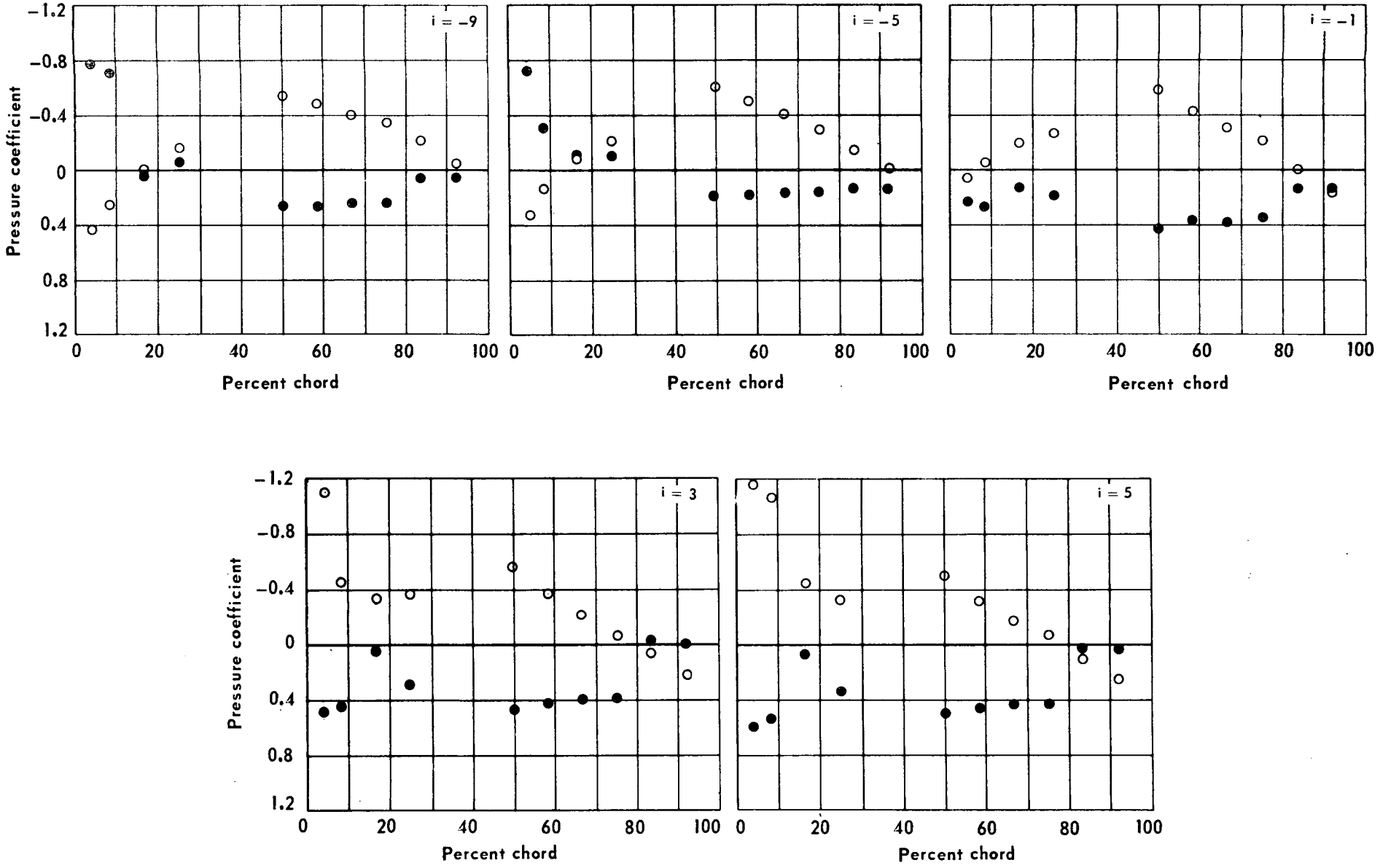

(a) $\beta_{IN} = 70, \phi = 20, \sigma = 0.75$ (Slotted)

Figure 46. – Pressure distribution for double circular–arc hydrofoils.

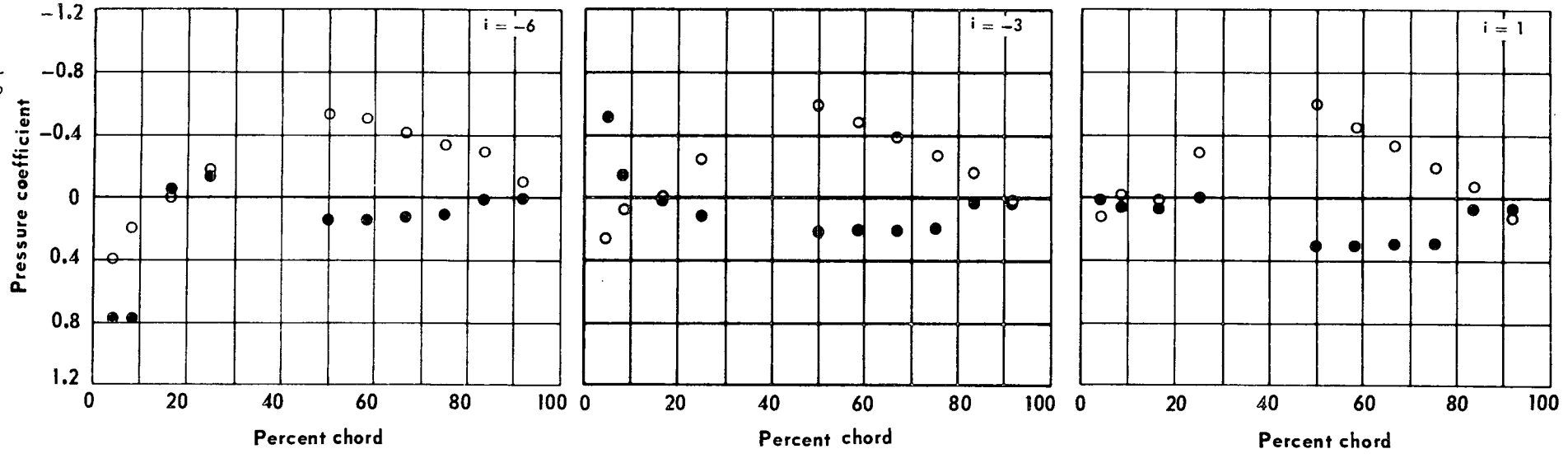

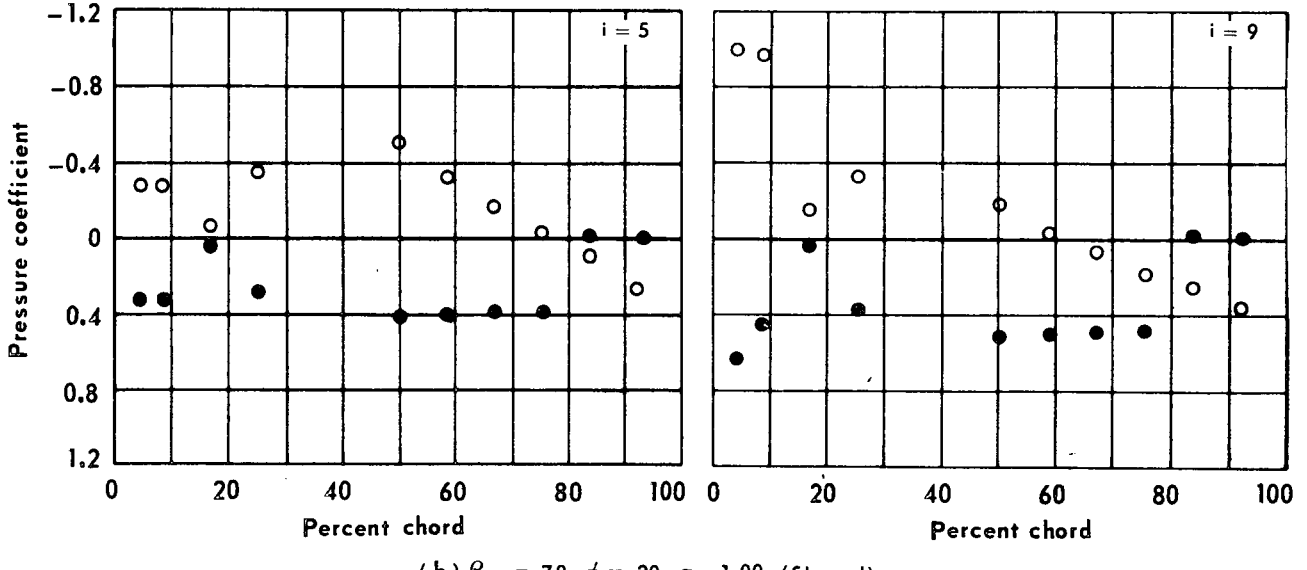

(b) $\beta_{IN} = 70, \phi = 20, \sigma = 1.00$ (Slotted)

Figure 46. – Continued.

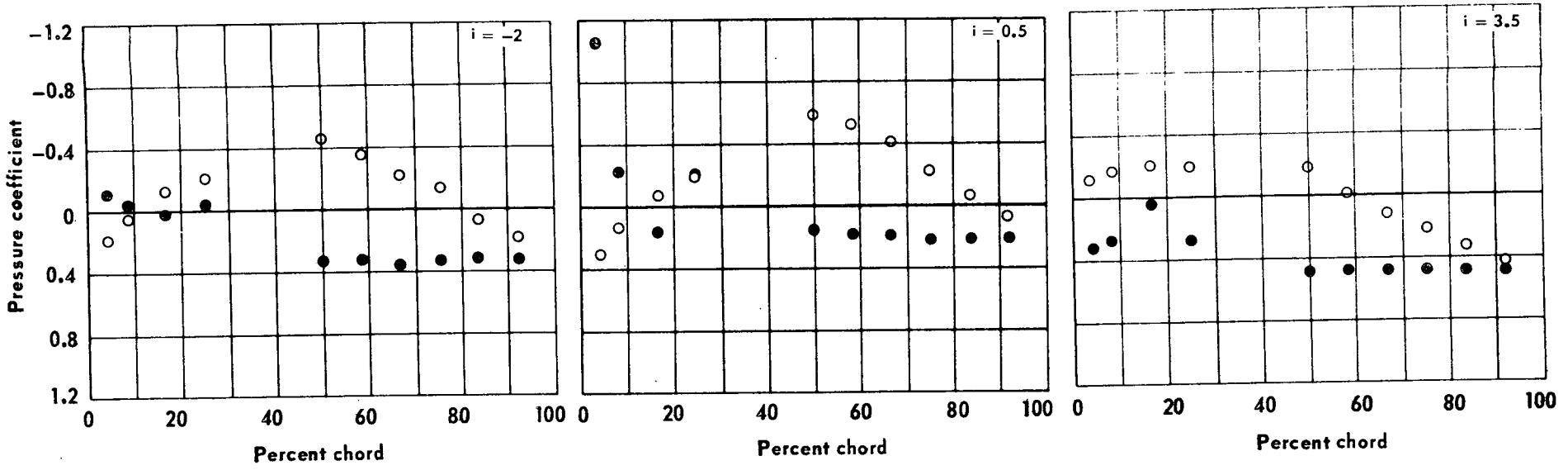

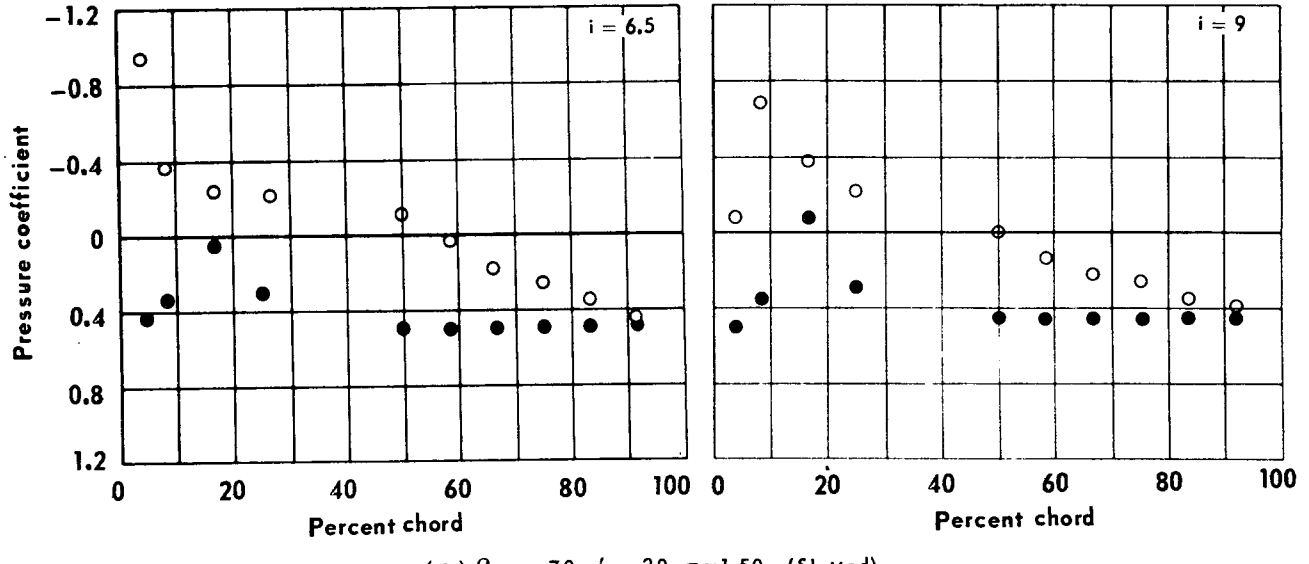

(c) $\beta_{IN} = 70, \phi = 20, \sigma = 1.50$ (Slotted)

Figure 46. – Concluded.

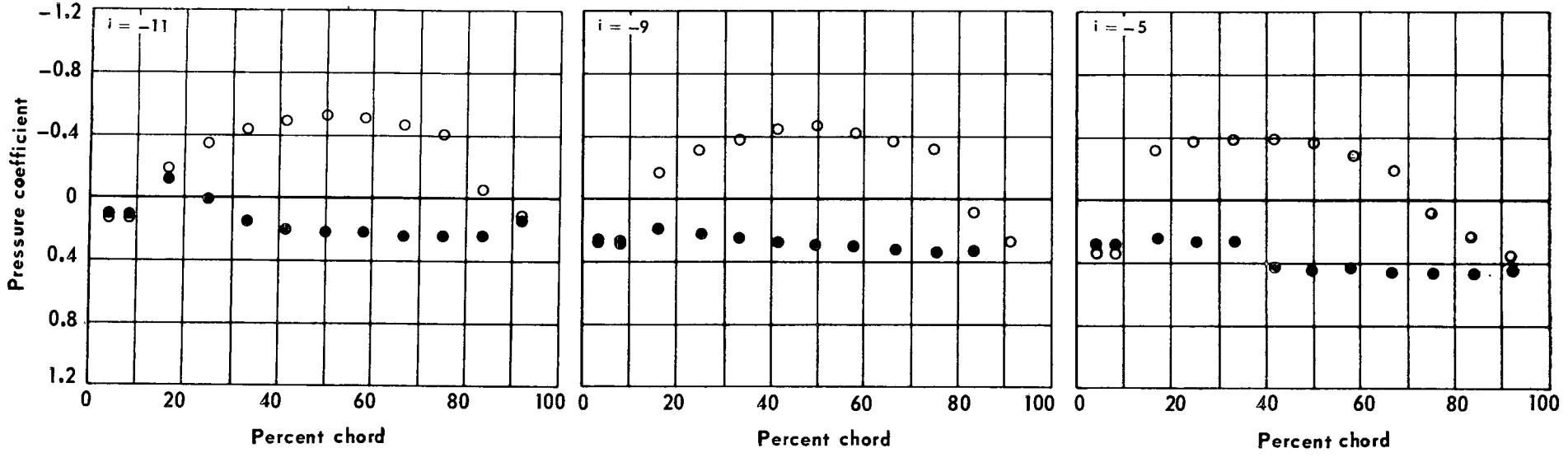

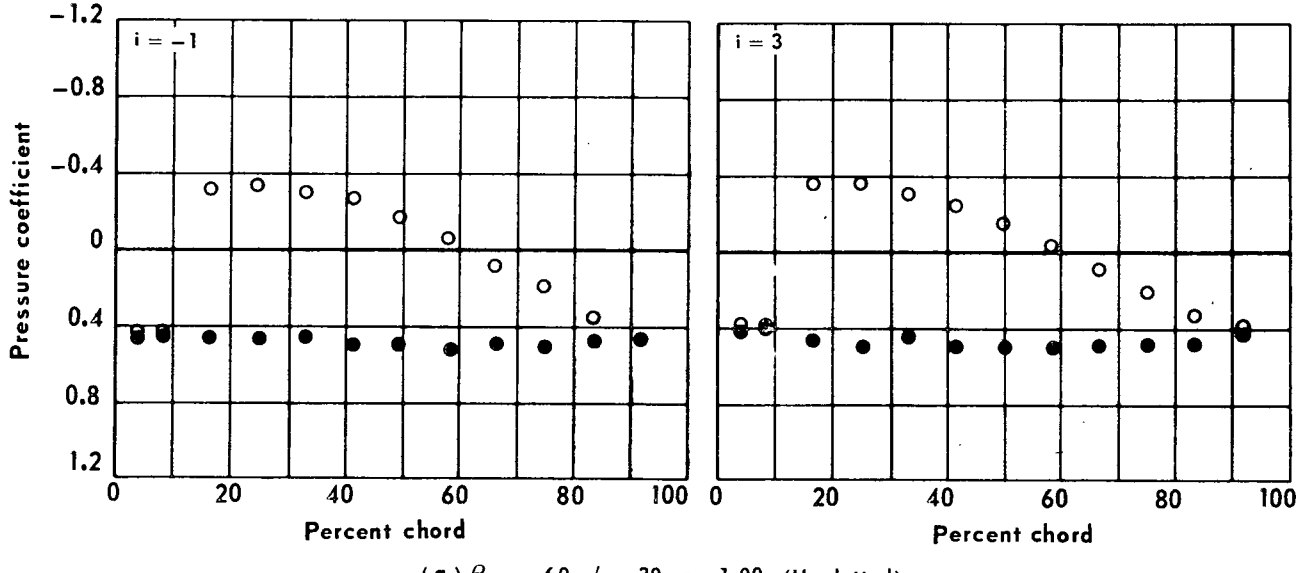

(a) $\beta_{IN} = 60, \phi = 30, \sigma = 1.00$ (Unslotted)

Figure 47. – Pressure distribution for double circular–arc hydrofoils.

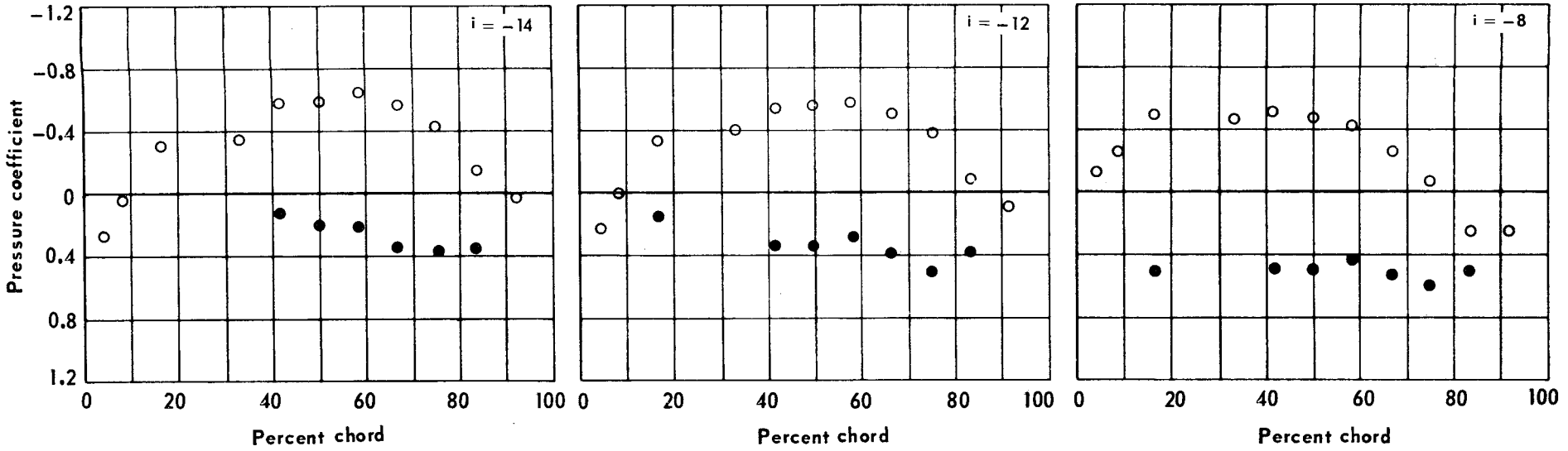

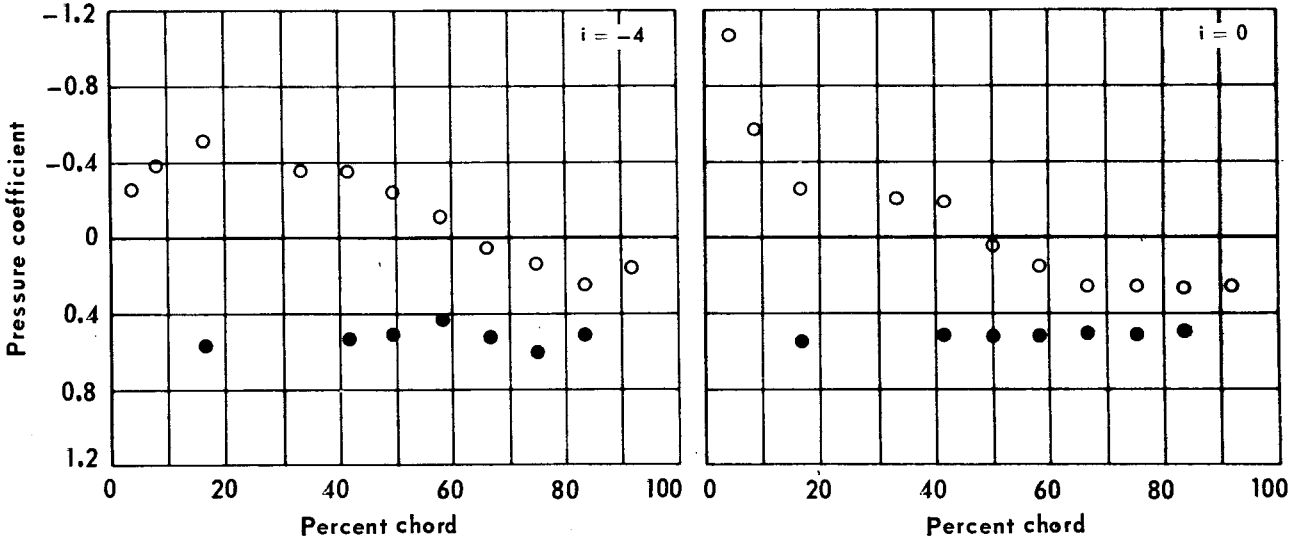

(b) $\beta_{IN} = 60, \phi = 40, \sigma = 1.00$ (Unslotted)

Figure 47. – Continued.

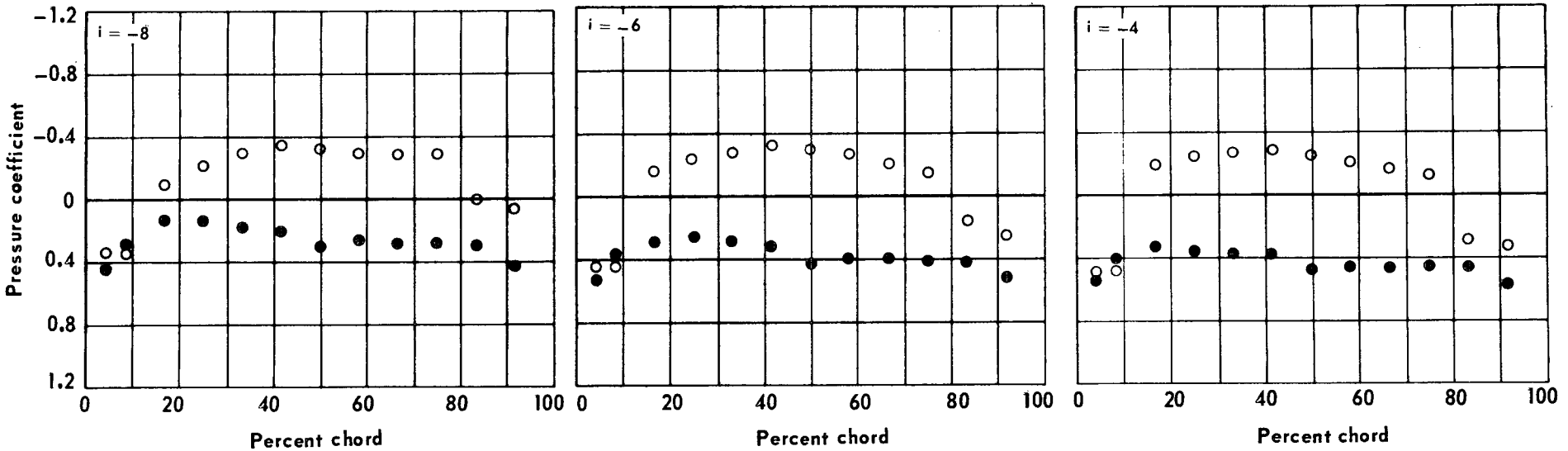

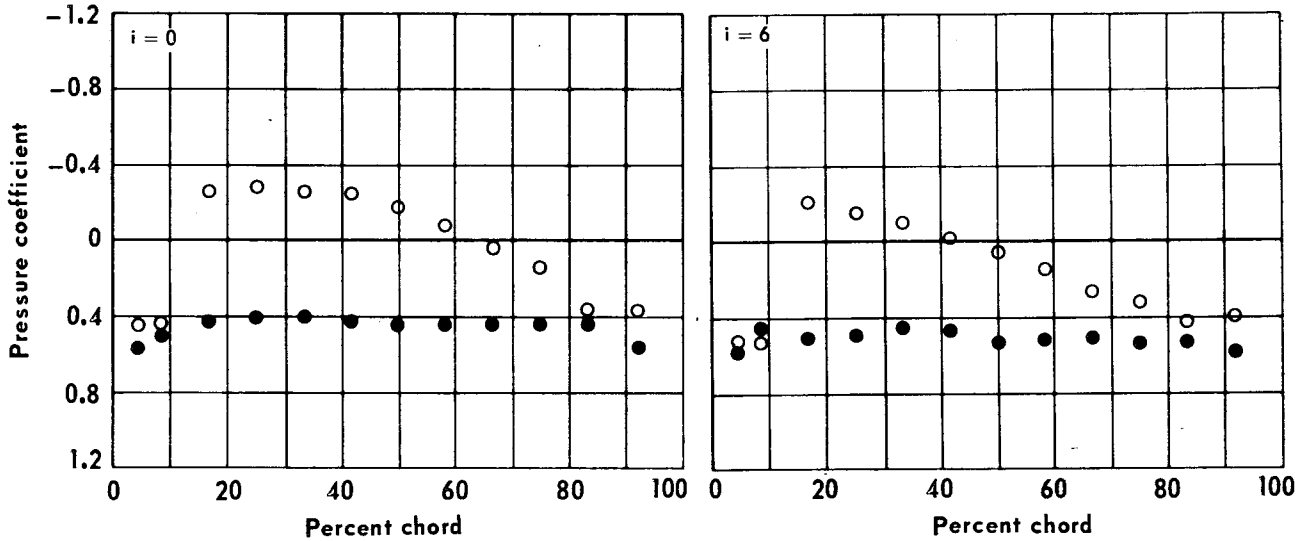

(c) $\beta_{IN} = 70, \phi = 20, \sigma = 1.00$ (Unslotted)

Figure 47. – Continued.

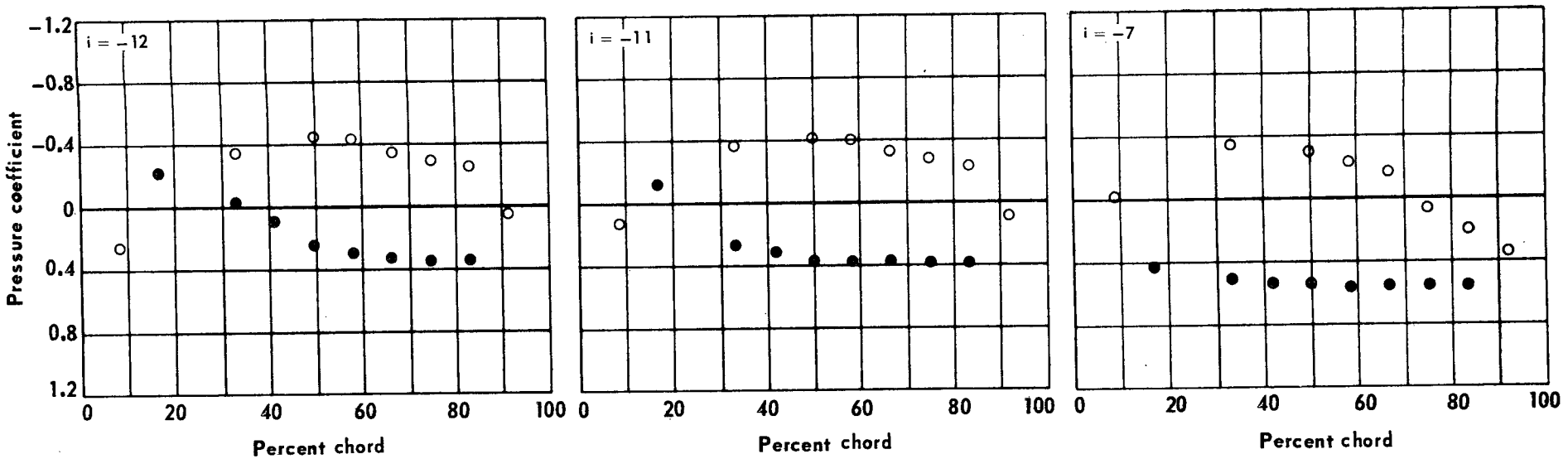

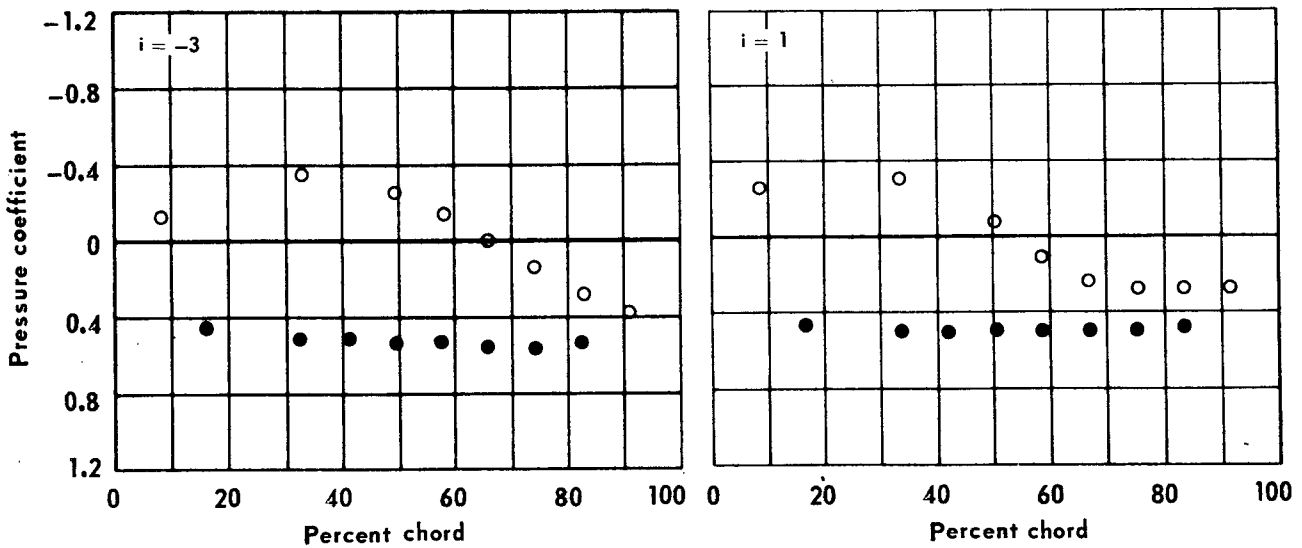

(d) $\beta_{IN} = 70, \phi = 30, \sigma = 1.00$ (Unslotted)

Figure . – Concluded.

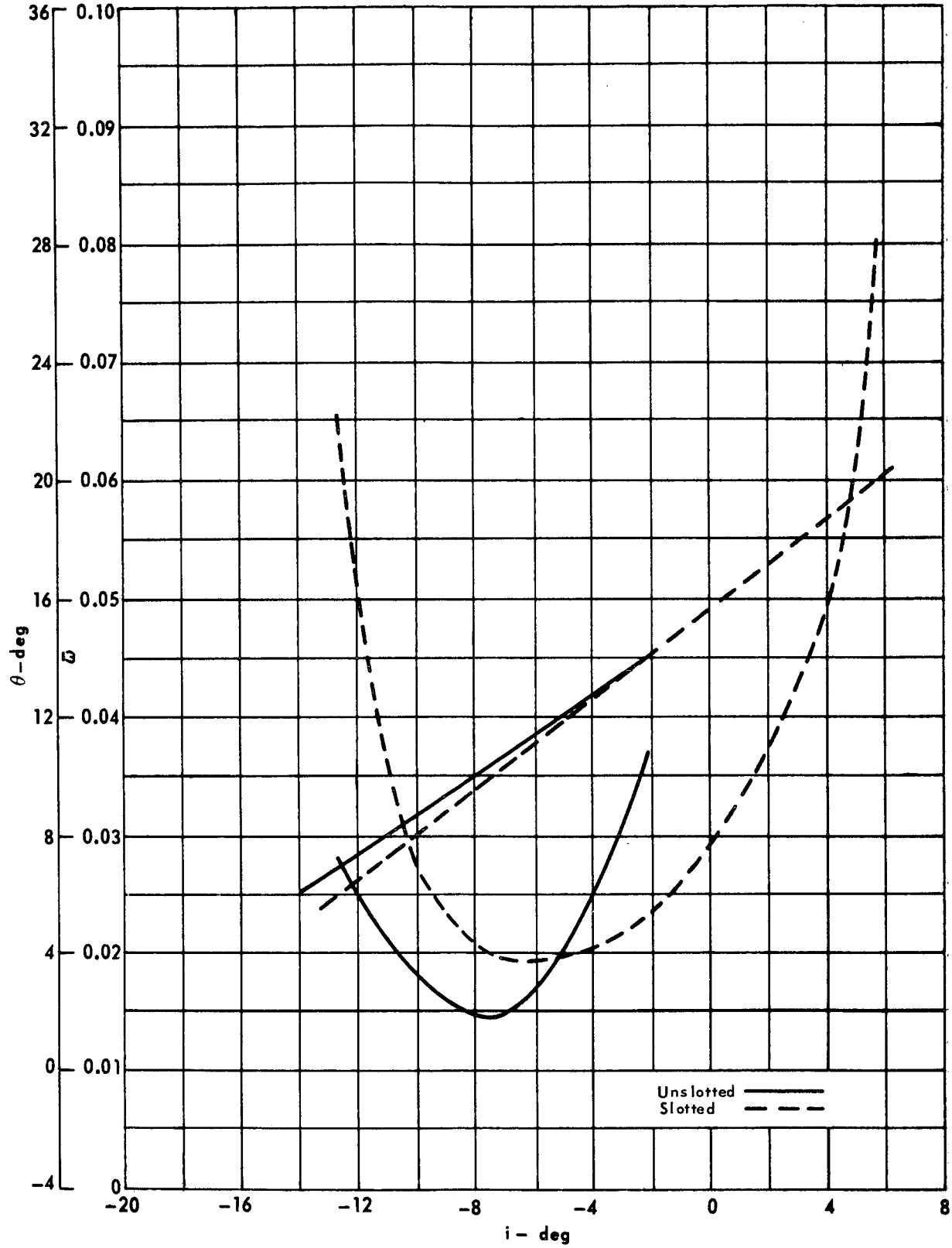

Cascade configuration : $\beta_{1N} = 60$, $\sigma = 0.75$

Double circular–arc profile : $\phi = 30$, $t/c = 0.06$

Figure 48. – Cascade characteristics for slotted and unslotted double circular–arc hydrofoils.

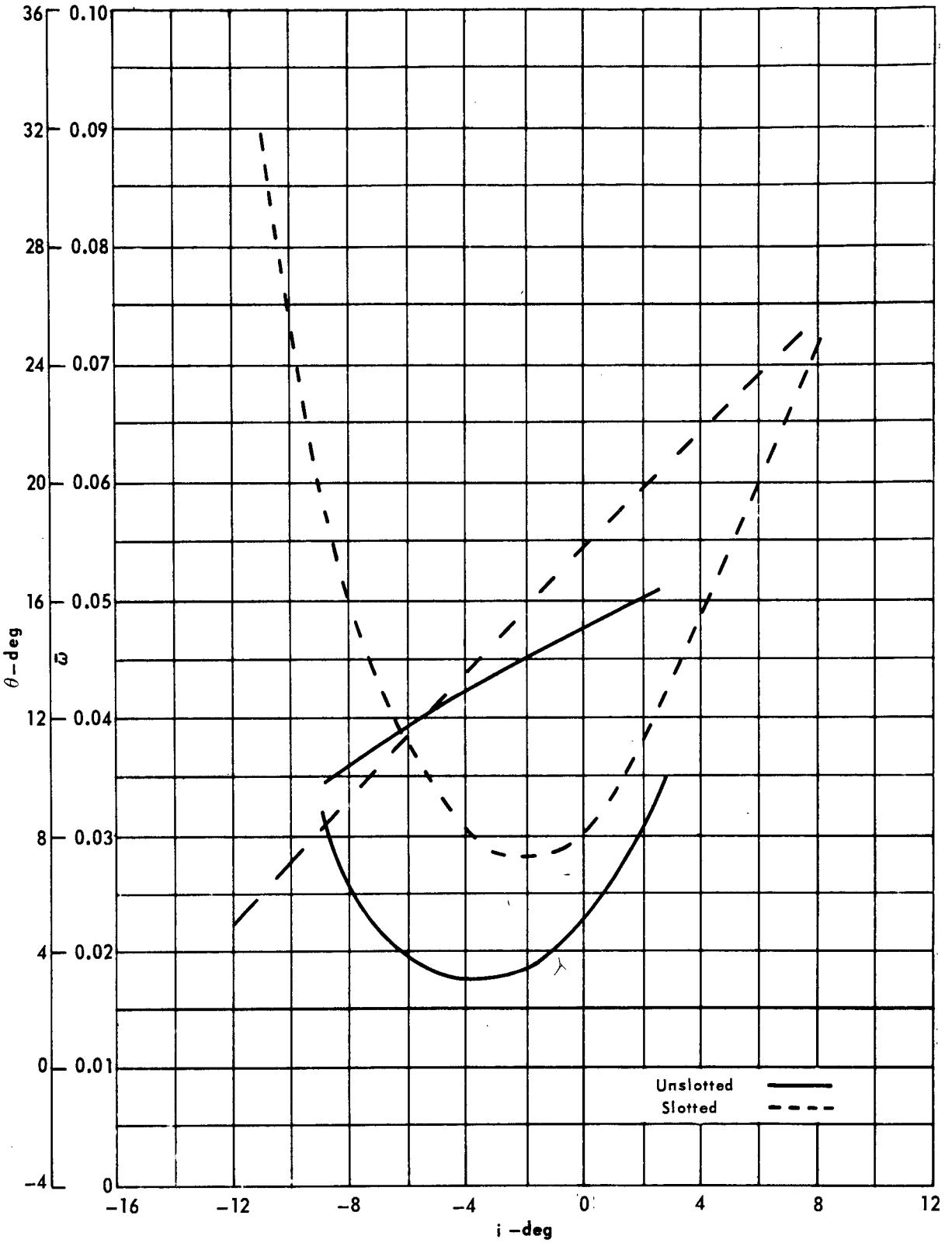

(b) Cascade configuration : $\beta_{1N} = 60$, $\sigma = 1.00$

Double circular–arc profile : $\phi = 30$, $t/c = 0.06$

Figure 48. – Continued.

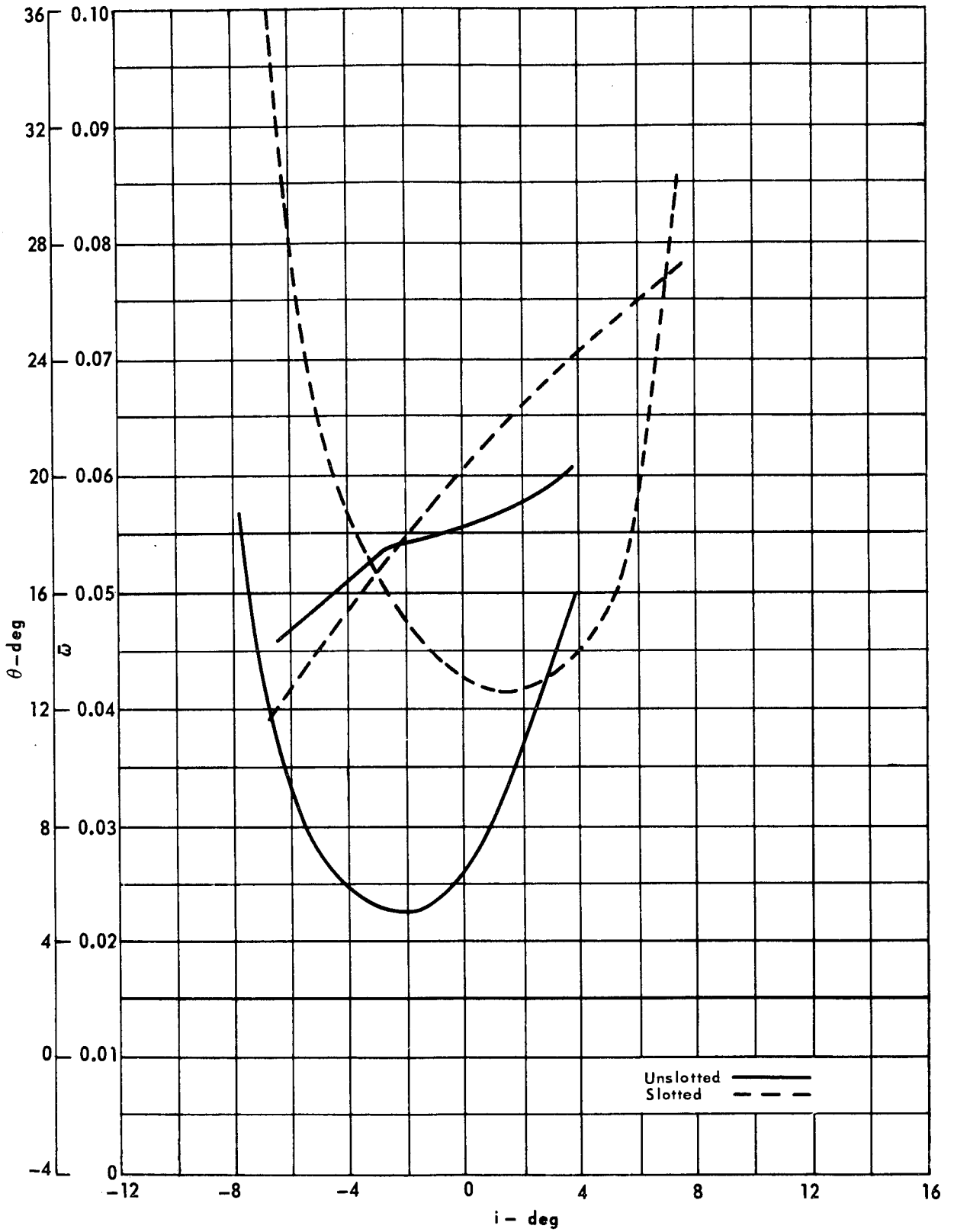

(c) Cascade configuration : $\beta_{1N} = 60$, $\sigma = 1.50$

Double circular–arc profile : $\phi = 30$, $t/c = 0.06$

Figure 48. – Continued.

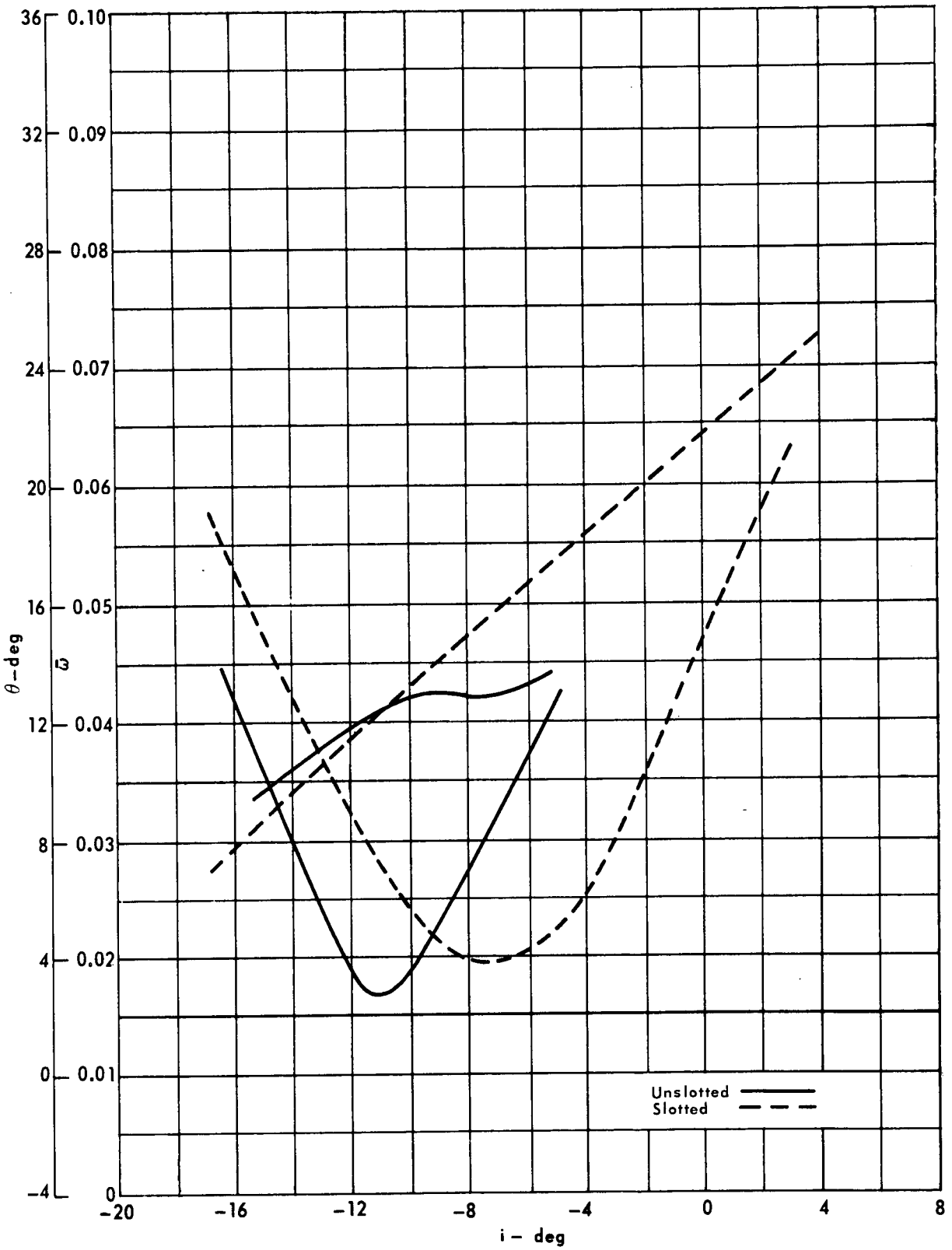

(d) Cascade configuration : $\beta_{1N} = 60$, $\sigma = 0.75$

Double circular–arc profile : $\phi = 40$, $t/c = 0.06$

Figure 48. – Continued.

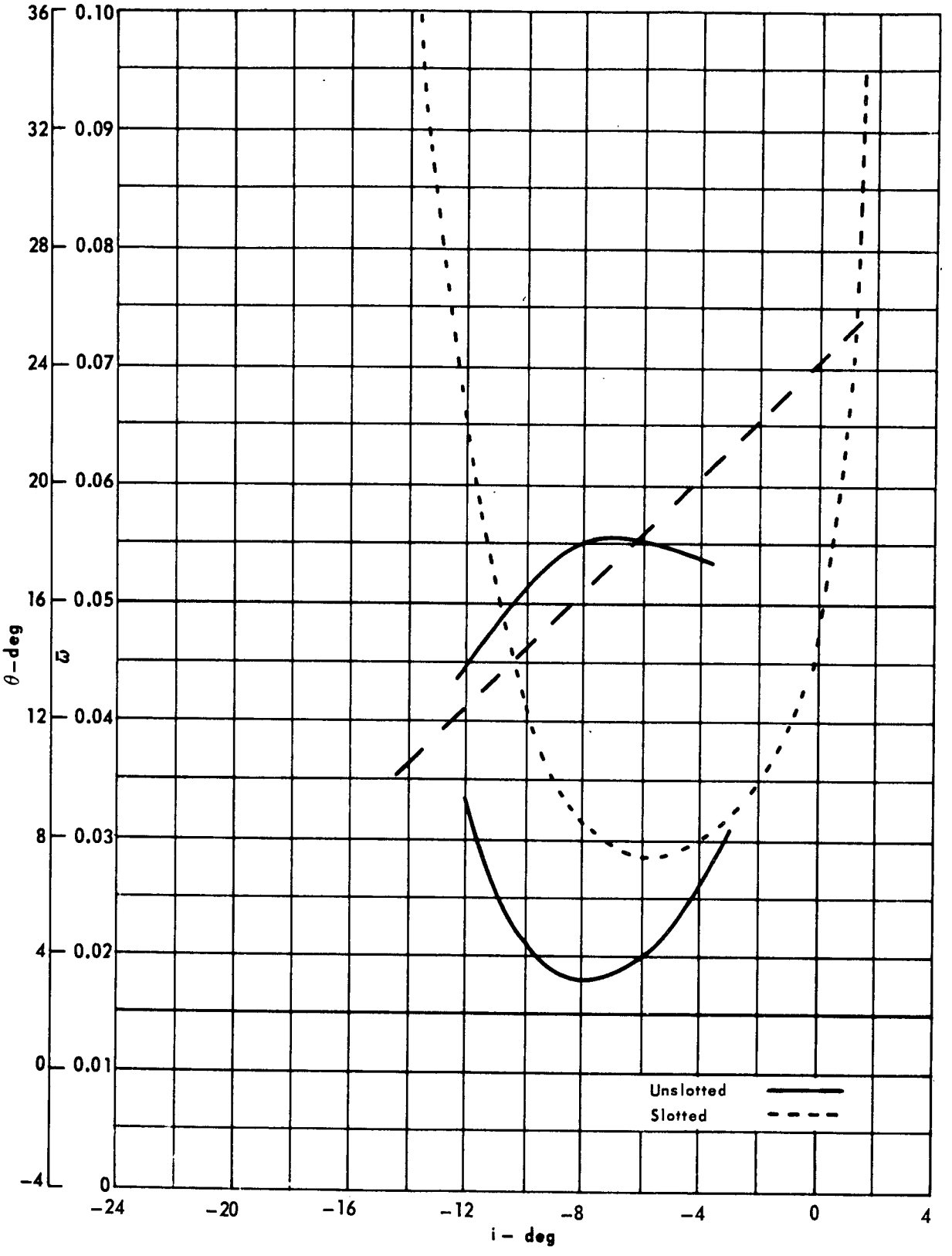

(e) Cascade configuration : $\beta_{1N} = 60$, $\sigma = 1.00$

Double circular–arc profile : $\phi = 40$, $t/c = 0.06$

Figure 48. – Continued.

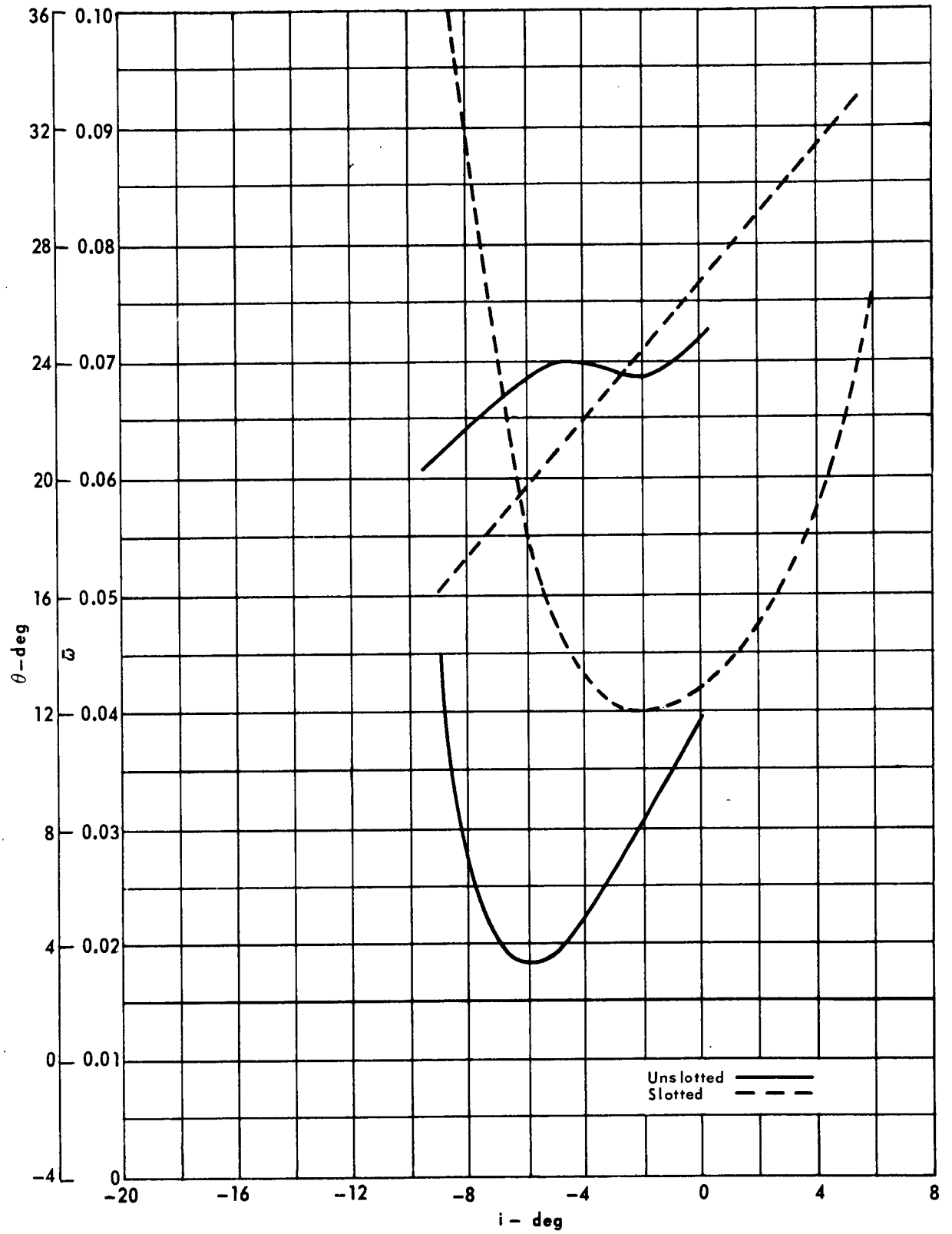

(f) Cascade configuration : $\beta_{1N} = 60$, $\sigma = 1.50$

Double circular-arc profile : $\phi = 40$, $t/c = 0.06$

Figure 48. – Continued.

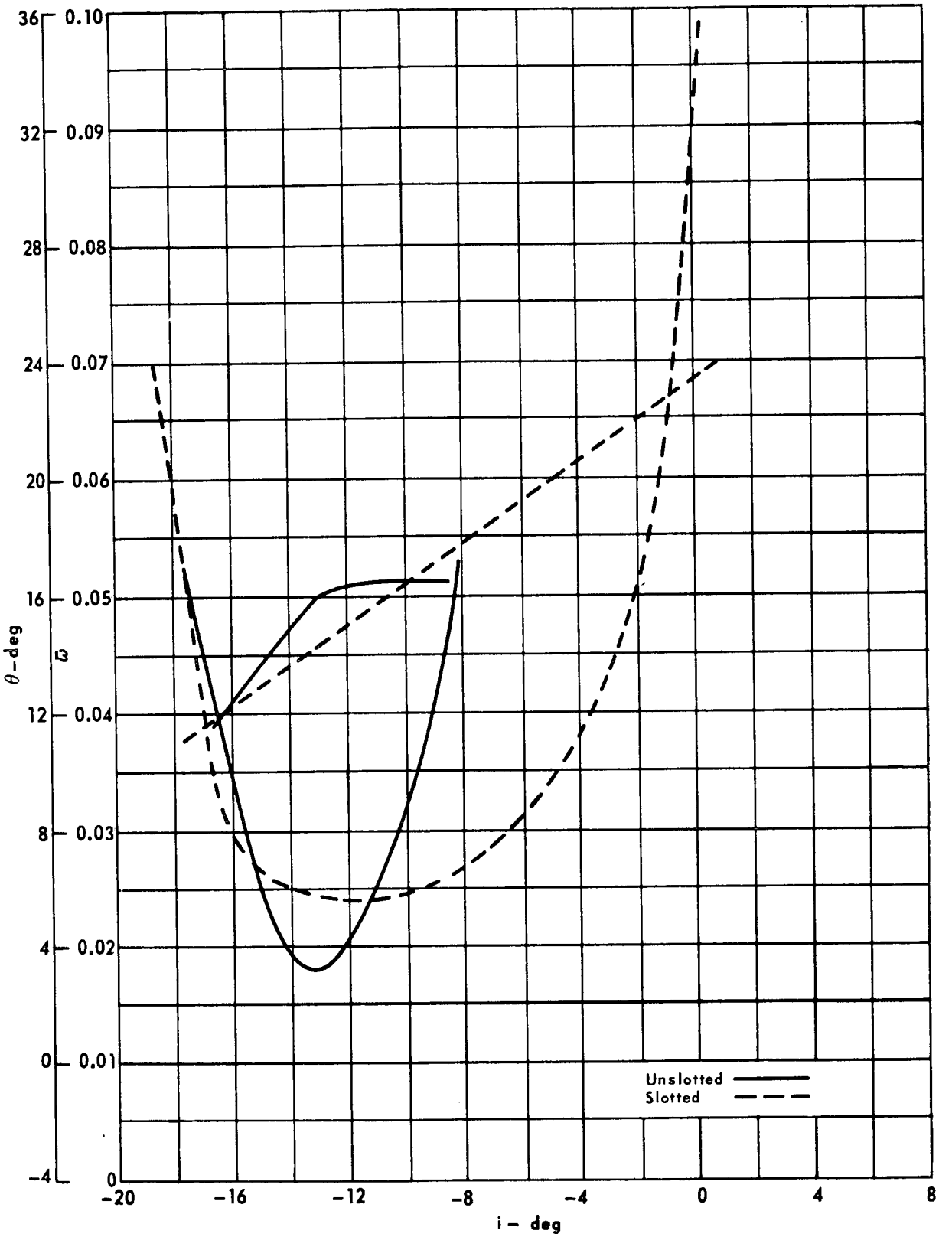

(g) Cascade configuration : $\beta_{1N} = 60$, $\sigma = 0.75$

Double circular–arc profile : $\phi = 45$, $t/c = 0.06$

Figure 48. – Continued.

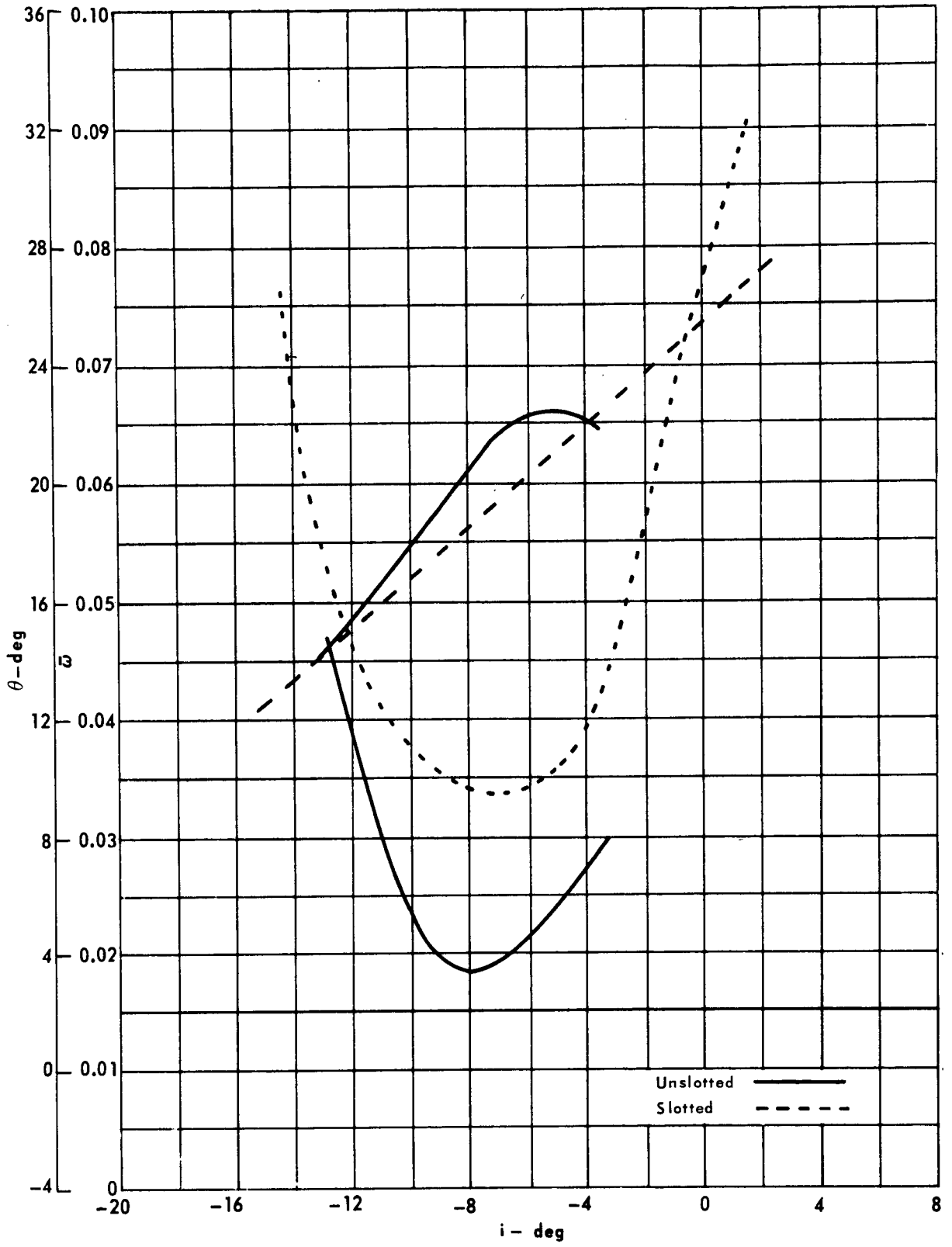

(h) Cascade configuration : $\beta_{1N} = 60$, $\sigma = 1.00$

Double circular–arc profile : $\phi = 45$, $t/c = 0.06$

Figure 48. – Continued.

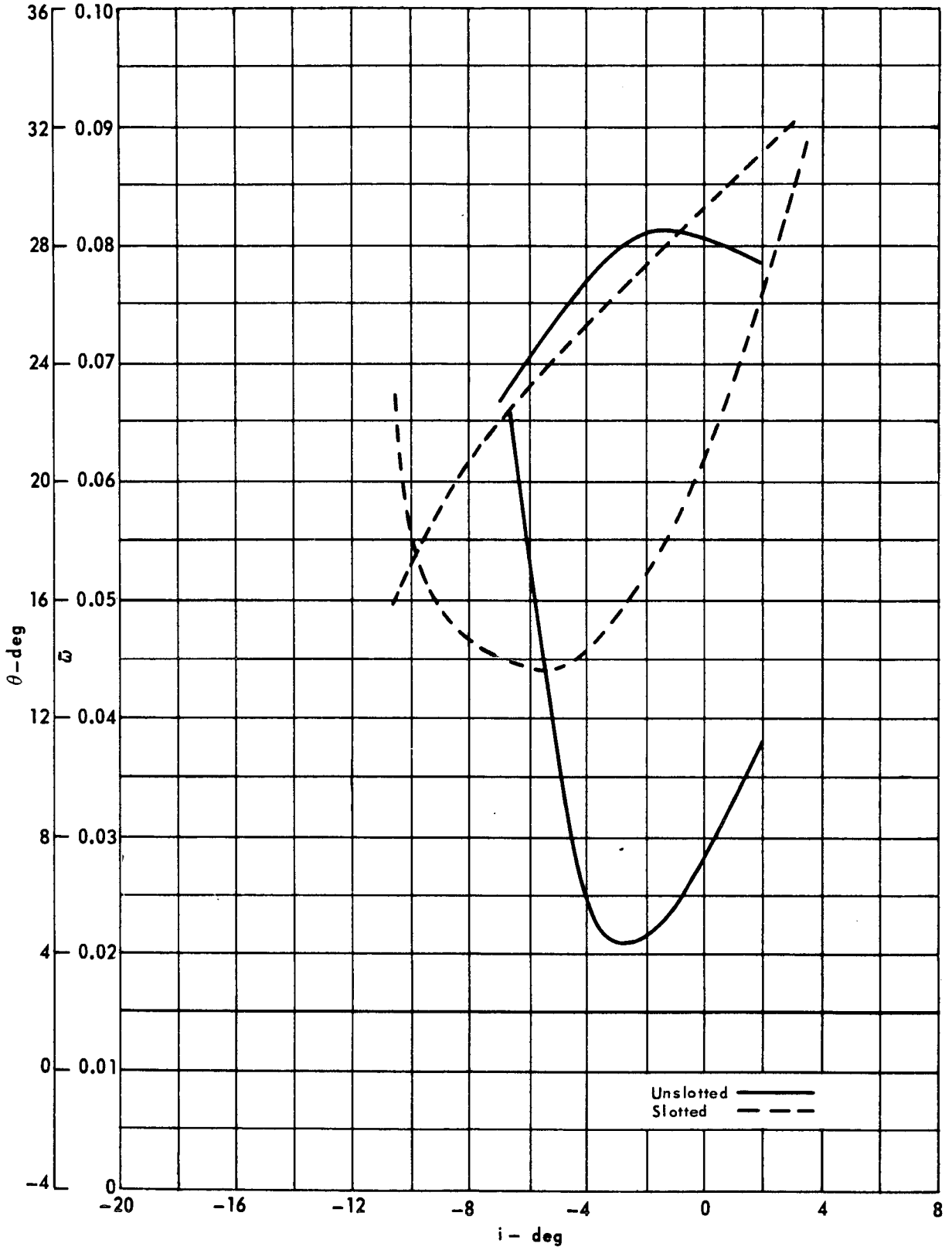

(i) Cascade configuration : $\beta_{1N} = 60$, $\sigma = 1.50$

Double circular-arc profile : $\phi = 45$, $t/c = 0.06$

Figure 48. – Continued.

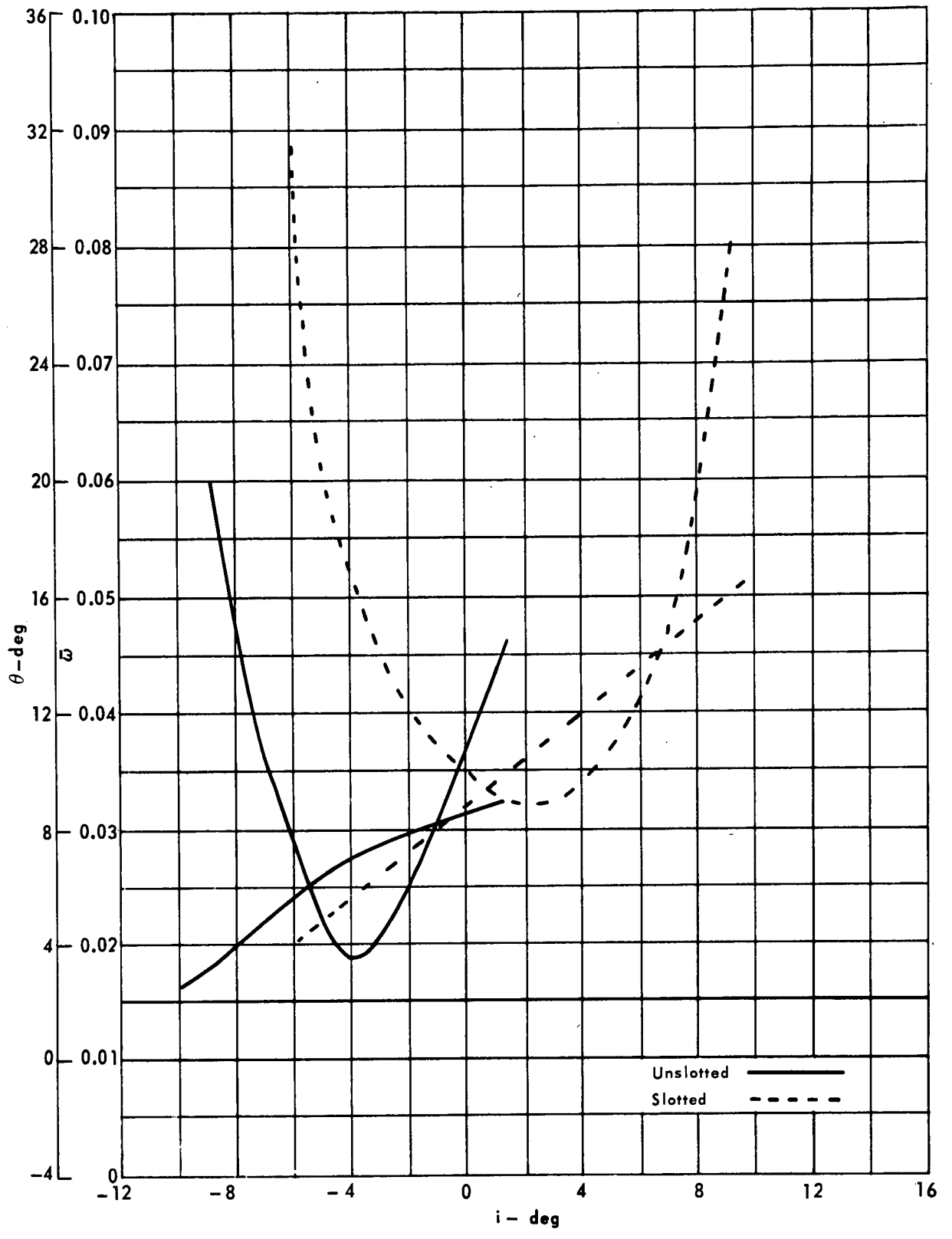

(j) Cascade configuration : $\beta_{1N} = 70$, $\sigma = 1.00$

Double circular–arc profile : $\phi = 20$, $t/c = 0.06$

Figure 48. – Continued.

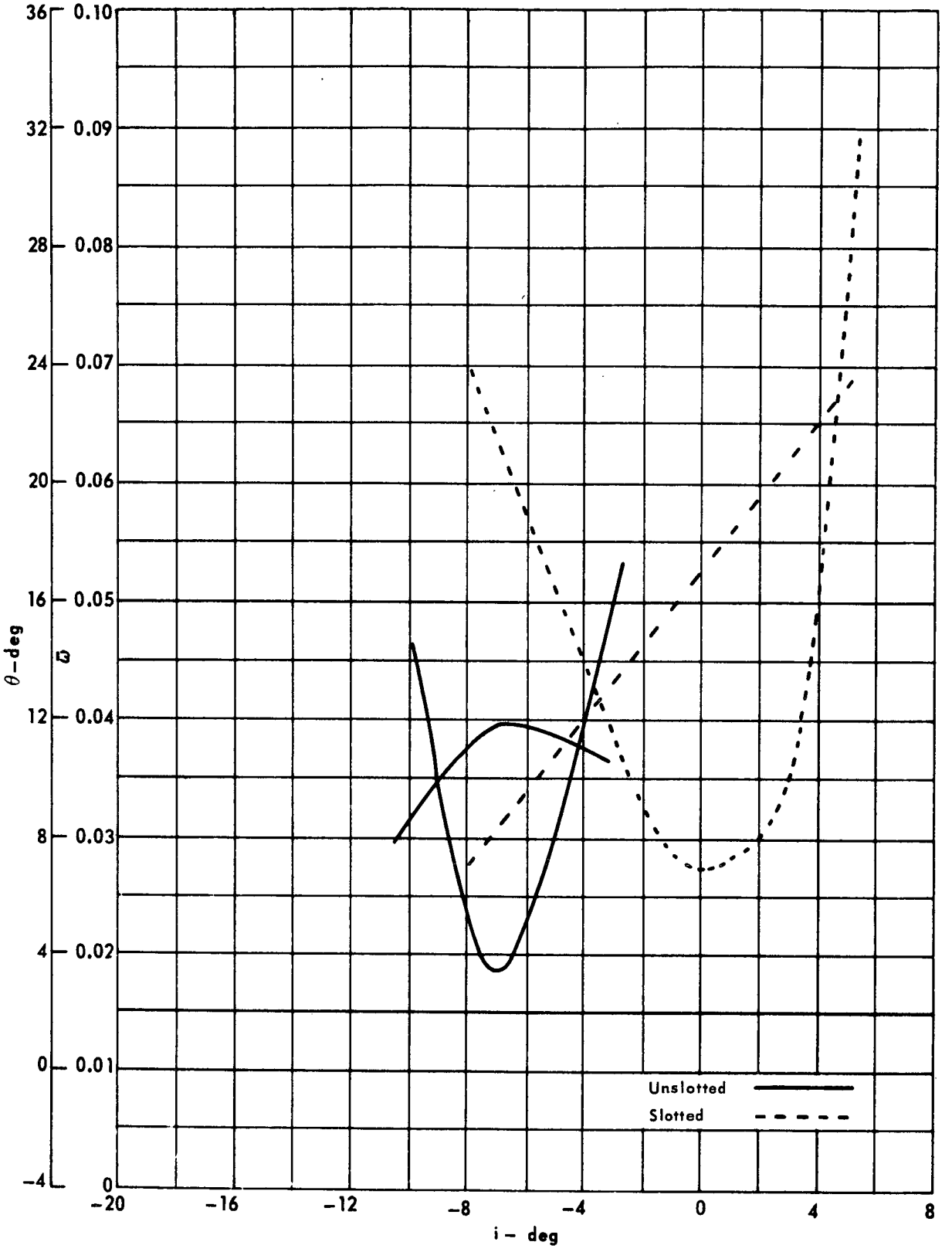

(k) Cascade configuration : $\beta_{1N} = 70$, $\sigma = 1.00$

Double circular-arc profile : $\phi = 30$, $t/c = 0.06$

Figure 48. – Concluded.

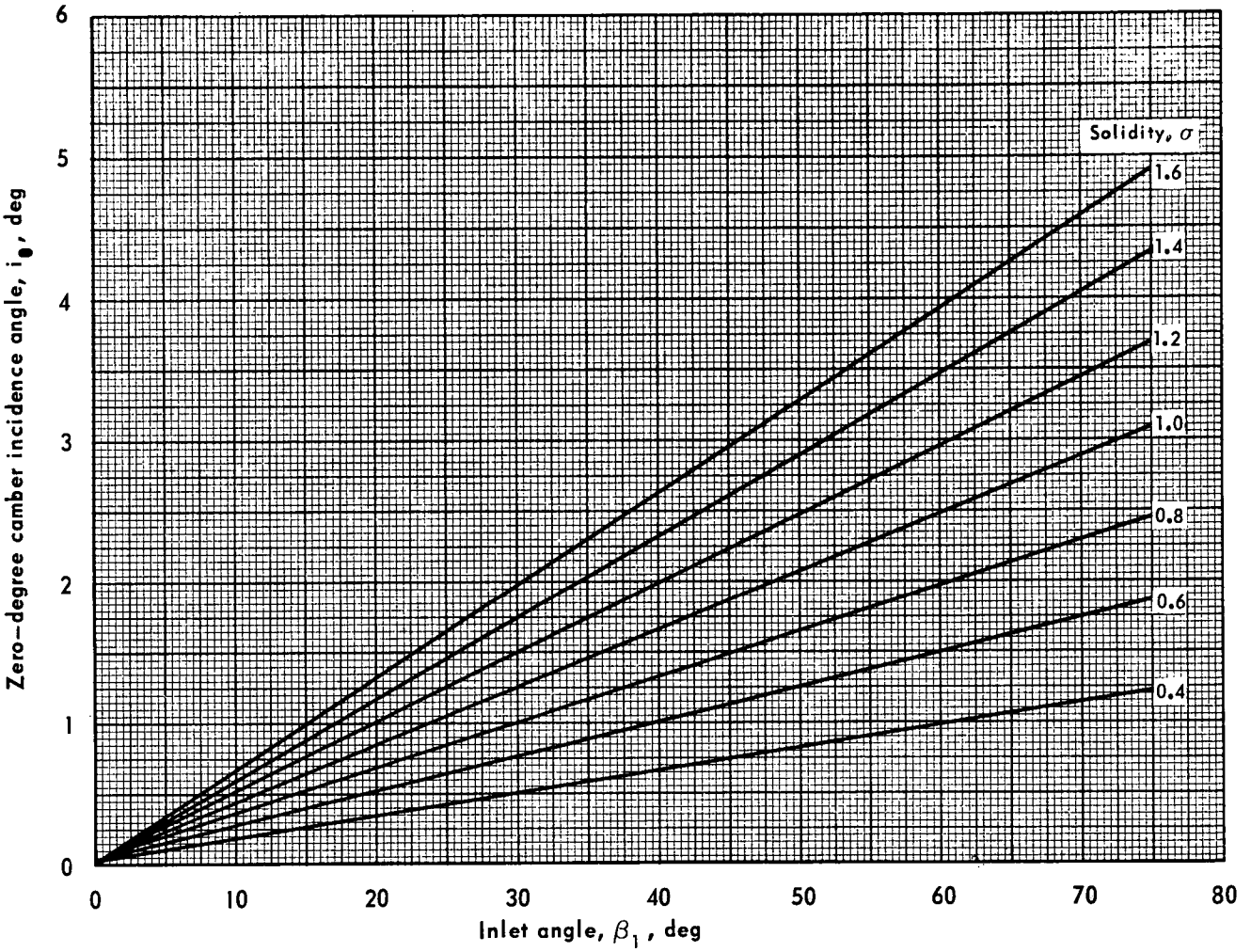

t/c = 0.06

Figure 49. – Reference minimum–loss incidence angle for zero degree camber unslotted double circular–arc hydrofoils .

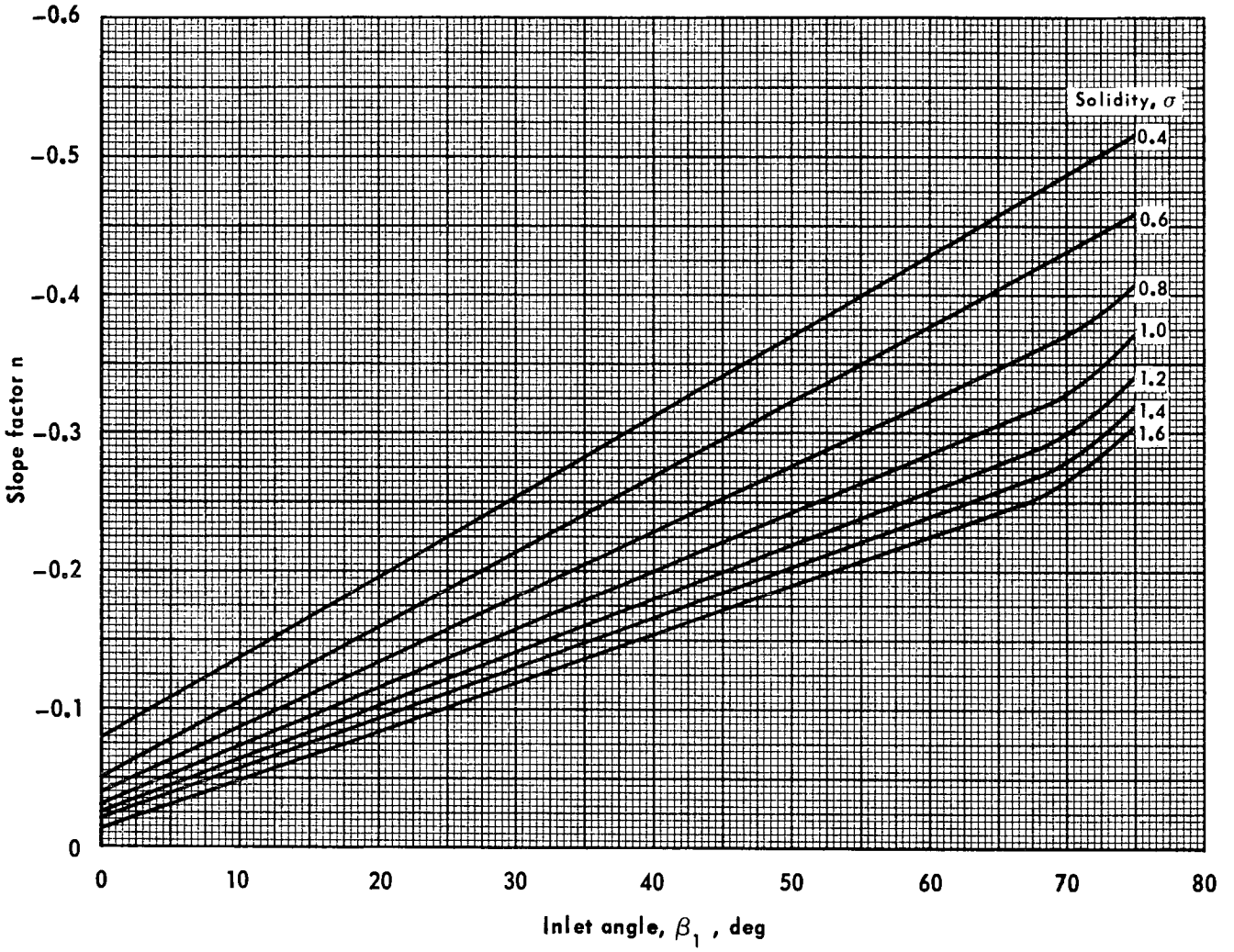

Figure 50. – Slope factor for reference minimum–loss incidence angle (unslotted double circular–arc hydrofoils).

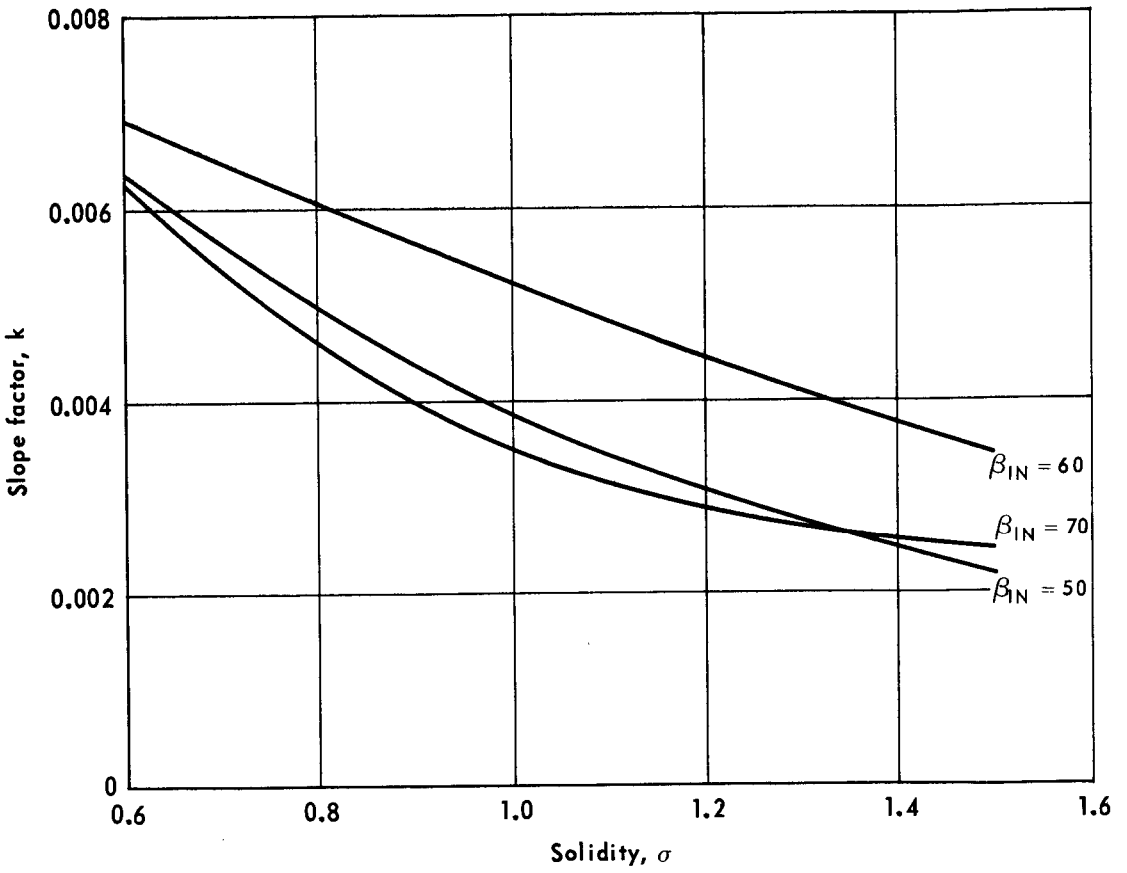

Figure 51. – Slope factor for reference minimum–loss incidence angle (slotted double circular–arc hydrofoils).

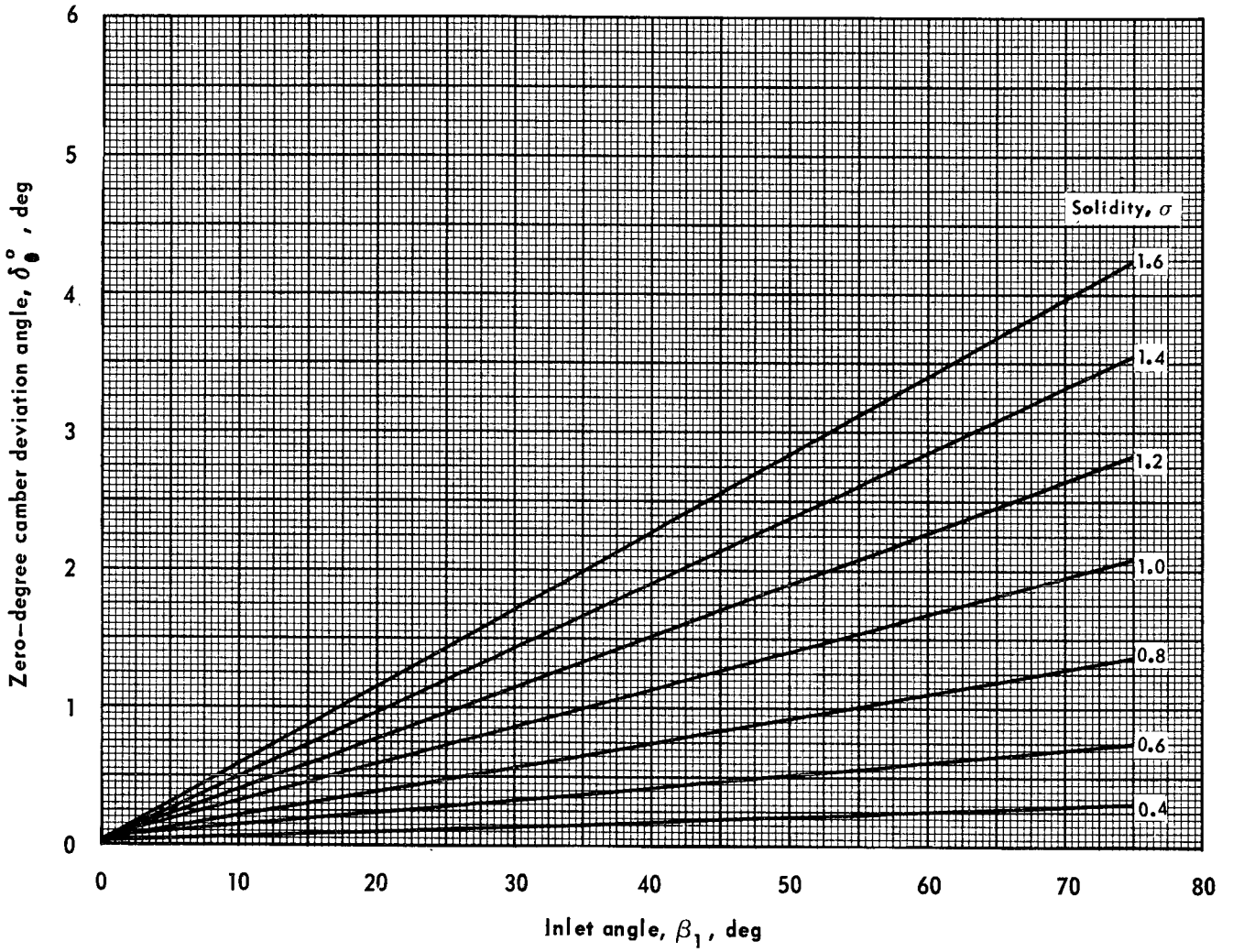

t/c = 0.06

Figure 52. – Reference minimum–loss deviation angle for zero–degree camber unslotted double circular–arc hydrofoils.

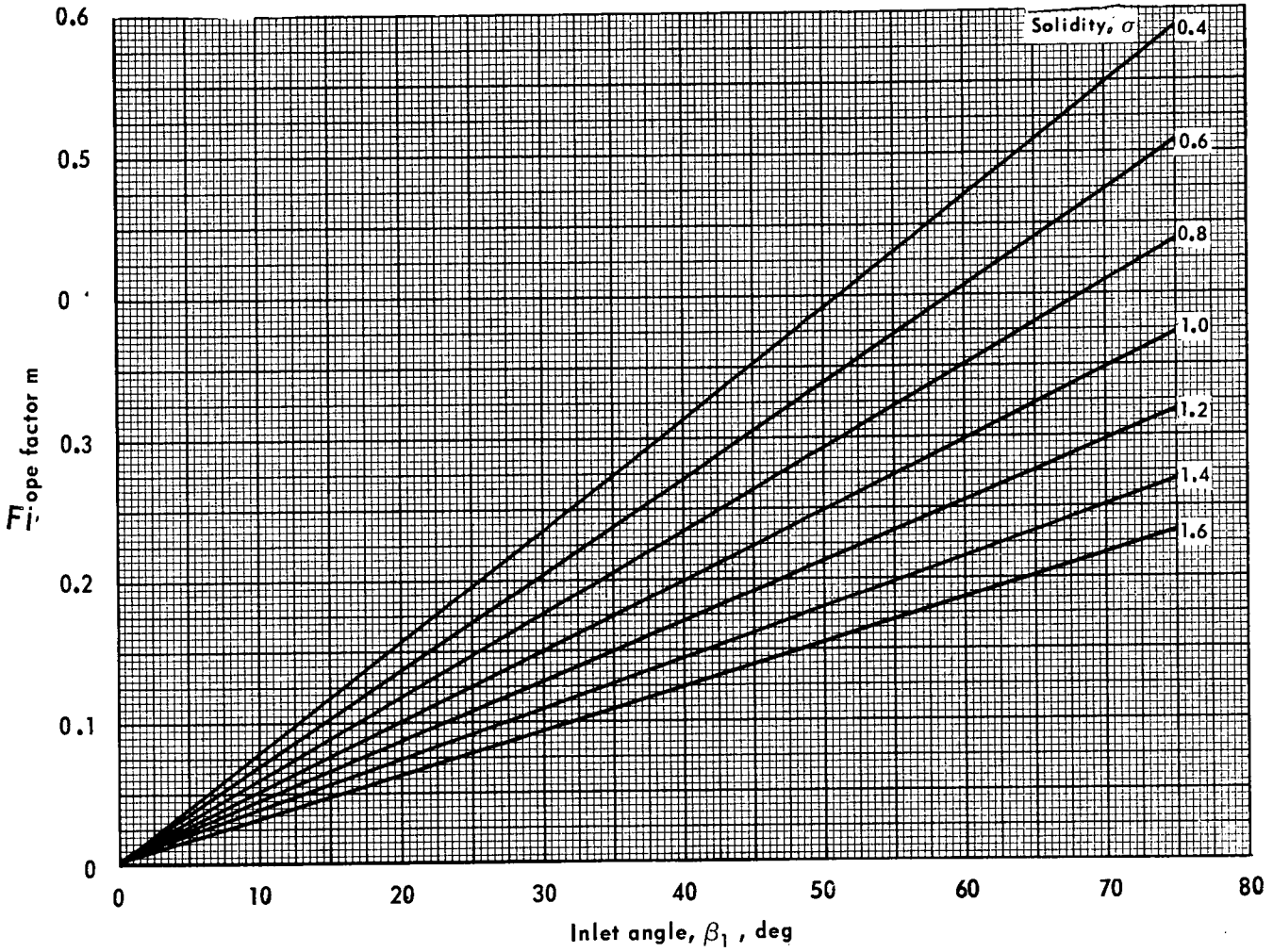

t/c = 0.06

Figure 53. – Slope factor for reference minimum–loss deviation angle (unslotted double circular–arc hydrofoils).

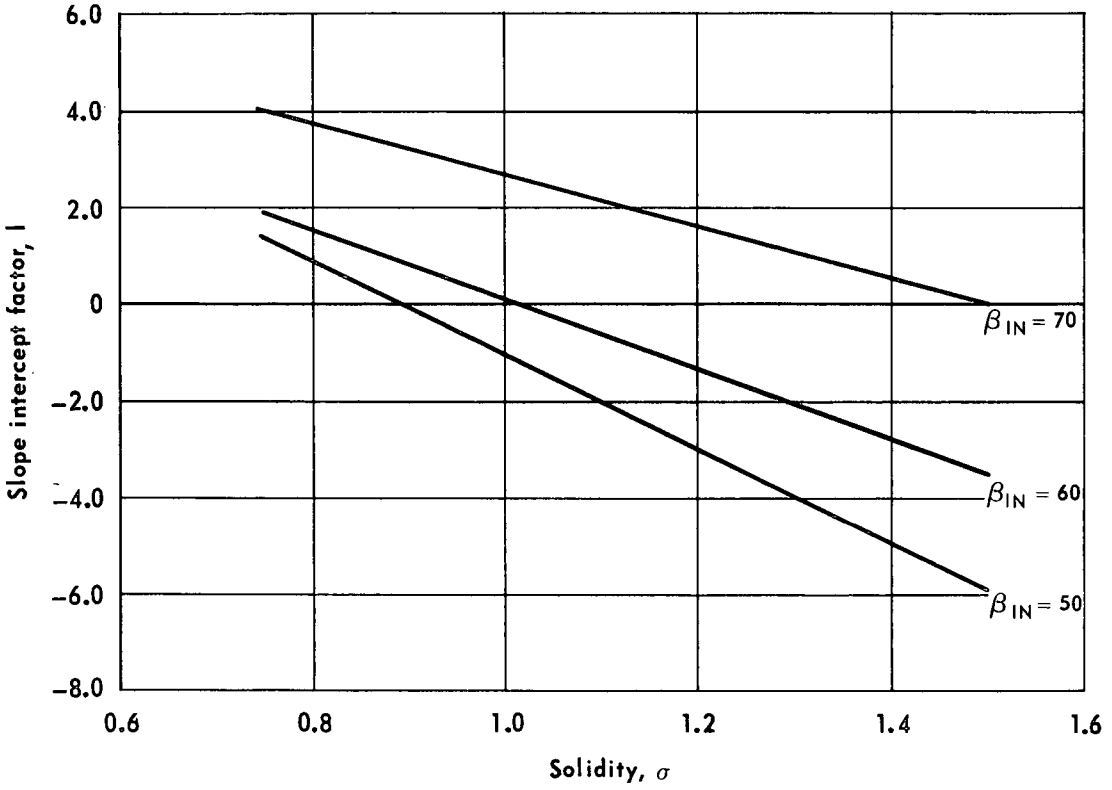

Figure 54. – Slope intercept factor for reference minimum–loss deviation angle (slotted double circular–arc hydrofoils).